ON-CHIP SPIN CONTROL IN SEMICONDUCTOR MICRO- AND NANO- STRUCTURES

Der Fakultät für Ingenieurwissenschaften der
Universität Duisburg-Essen
zur Erlangung des akademischen Grades eines

Doktors der Naturwissenschaften (Dr. rer. nat.)

genehmigte Dissertation

von

Yuansen Chen
aus
Da'ye, Hubei, V.R. China

To my dear parents

致我最亲爱的父母

CONTENTS

SUMMARY

Spin control and spin manipulation are critical issues towards applications of spintronic devices in the future. Since the spin always carries a certain amount of magnetic momentum, an effective magnetic field is required to perform spin control and manipulation. This effective field can be either from one spin-related interaction mechanism, such as exchange interaction, spin-orbit coupling, hyperfine interaction etc., or just from a magnetic field, which is the most straightforward way. Generally macroscopic Helmholtz coils are used to generate a magnetic field, which nevertheless gives poor performance with respect to spatial resolution for addressing local spins and high frequency operation for studying fast/ultrafast spin dynamics.

In this thesis, the dynamics of two localized spin systems are studied in semiconductors. Both types of localized spins couple with the carrier spins. The studies are based on a micro-fabrication technology, which allows one to electrically generate an on-chip switchable magnetic field. The experimental results demonstrate a local spin control and spin manipulation on a micrometer length scale. Further, the underlying physics is addressed from theoretical calculations showing that the local spin environment is critical for the studied spin dynamics.

The method to generate an on-chip magnetic field is established by a two-step electron beam lithography and lift-off technique. Single-turn gold microcoils with variable aperture size ranging from 3 μm to 20 μm are defined on top of semiconductors. Thanks to the minimized coil length scale and the low complex impedance, a switchable magnetic field up to tens of mT can be obtained with a transition time less than 400 ps.

The concept of spin control by a local magnetic field is demonstrated in a $Cd_{1-x}Mn_xTe/(Cd, Mg)Te$ diluted magnetic semiconductor (DMS) quantum well (QW). The Mn^{2+} ion spins are localized and strongly couple with the free carrier spins via *sp-d* exchange interaction. Introducing a current through the coil on top of the semiconductor, an electrically switchable magnetic field can be induced which aligns the Mn^{2+} ion spins in the DMS QW layer. Due to the strong *sp-d* exchange interaction between Mn^{2+} ions and carriers, there is a huge Zeeman energy splitting between carrier spin states. Therefore even a weak magnetic field of a few mT can generate an efficient carrier spin polarization, which can be probed by polarization-resolved magneto-photoluminescence (PL) spectroscopy. A pronounced carrier spin polarization of up to 8.5% is obtained by the current-induced field at liquid helium temperature. The spatial spin distribution directly reflects the locally varying sign and amplitude of the current-induced field. Since the spin relaxation process between Zeeman levels is rather fast compared to the exciton lifetime, the detected PL polarization can directly reflect the magnetization of Mn^{2+} ions. The magnetization process is a convolution of Mn^{2+} spin dynamics induced by the pulsed magnetic field and the phonon dynamics generated by the pulsed current-heating. A method is developed to separate these two contributions. For a DMS QW with high Mn^{2+} concentration of x = 0.067, the spin response to a magnetic field is fast enough so that the phonon dynamics can be determined from the PL polarization dynamics. The phonon lifetime in the studied samples is estimated to be on the order of hundred nanoseconds.

By reducing the repetition period of the electrical pulse to be below the phonon lifetime, a thermal quasi-equilibrium state is established between the Mn^{2+} spin system and the lattice system. This allows one to study the Mn^{2+} spin dynamics on a sub-ns time scale in a weak magnetic field regime of only several mT. In the absence of an external field (B_{ext}), the Mn^{2+} spin dynamics is found to be on the order of hundred picoseconds, which is up to date faster than any reported Mn^{2+} spin response to an external field. In the presence of a certain B_{ext}, the spin dynamics is slowed down. From numerical simulations, it is suggested anisotropic spin interactions, including hyperfine interaction, Mn ion spin coupling with the local strain-induced electrical field and the crystal field, are needed for an interpretation of the observed spin dynamics. At $B_{ext} = 0$ these local interactions can induce strong anti-crossings between Mn^{2+} spin states, and thus induce fast Mn^{2+} spin transitions by the adiabatic relaxation channel on a sub-ns time scale. Since the Zeeman splitting is energetically dominant at a certain B_{ext}, Mn^{2+} spin dynamics is governed by spin-lattice relaxation which is generally much slower.

The second type of localized spins is the nuclear spin in n-GaAs. A pronounced nuclear spin polarization is obtained, via Fermi-contact nucleus-electron spin coupling, by means of injecting spin-polarized electrons. By applying a RF current through the microcoil, optically detected NMR with micrometer resolution is demonstrated in n-GaAs. To trace the variance of the nuclear field namely the Overhauser field, the electron Larmor precession frequency is monitored via time-resolved magneto-optical Kerr rotation. Sweeping the frequency of magnetic field induced by an on-chip microscale current loop, nuclear spin depolarization is achieved for each isotope species (^{69}Ga, ^{71}Ga and ^{75}As). The measured nuclear field amplitude ratios between different isotope species distinctly contradict the theoretically predicted ones. This arises from a non-uniform nuclear spin leakage factor for each nuclear isotope. This is due to the quadrupole relaxation which depolarizes the nuclear spins, and the depolarization level is not uniform for different isotope species. By applying resonance RF pulse sequences, Rabi oscillation of ^{75}As nuclear spins is obtained with an effective dephasing time ~200 μs.

The observed non-fundamental NMR allows one to address the local nuclear spin environment. The local nuclear spin interaction gives rise to admixture of nuclear spin states. Assisted by resonance field-induced spin flip, optically-forbidden NMR is observed at RF of half-harmonics $1/2 f^{\alpha}$, harmonics $2 f^{\alpha}$ and two-mixed ($f^{\alpha 1} + f^{\alpha 2}$), where f^{α} is the RF for fundamental NMR of isotope species α. The measured nuclear spin dynamics is well interpreted as a two-level process between the dynamic nuclear polarization formation and nuclear spin depolarization via RF absorption. By analyzing the nuclear spin depolarization amplitude and the nuclear spin dynamics, it is concluded that the local quadrupole interaction and the current-induced oblique field are dominant perturbations for $2 f^{\alpha}$ and $1/2 f^{\alpha}$ NMR, respectively. The ($f^{\alpha 1} + f^{\alpha 2}$) NMR can be only due to the nuclear dipole-dipole interaction.

1 INTRODUCTION

In present computers, the information bit is represented by the carrier charge. Usually this is realized by utilizing electron charges in semiconductor integrated circuits. The generation, transport and control of electrons are achieved by applying electrical fields on the semiconductor device. With the on-going miniaturization of the semiconductor electronics, a further improvement of the device performance, e.g. lower power consumption and higher computing frequency, becomes more and more challenging [1]. In order to suffice the daily growth of the needed processing capability as illustrated by Moore's law [2], an alternative technology for information processing is urgently required in the next decades.

Apart from the charge property, an electron also has an eigen spin. The electron spin was for the first time experimentally observed during the famous "Stern-Gerlach experiment" in 1922 [3], and it was theoretically demonstrated by Dirac until 1928 [4, 5]. From his theory, the electron spin turns out to be intrinsic as a relativistic quantum effect, and it cannot be explained in context of classical physics. An electron can have a spin state of either "spin up" or "spin down". Each electron spin state corresponds to a certain amount of magnetic moment in a specific direction. As a result, the average electron spin is manifested as magnetization for an ensemble of electrons. The electron spin properties are responsible for most magnetic effects in modern physics [6]. Therefore the magnetic properties can be controlled by tackling the spin degree of freedom. The spin states or magnetization can be used as information bits in applications.

The electron spin degree of freedom has been technologically put into applications in magneto-electronics [7, 8]. Thanks to the discovery of the giant magnetoresistance (GMR) effect [9-11], the information density in the hard drive disks has been increased by more than one order of magnitude[12] in the past decade. The GMR-based read heads of hard disks [13] and magnetic field sensors [14] also have been widely used. Based on the tunneling magnetoresistance (TMR) effect [15, 16], the magnetoresistive random access memory (MRAM) is commercially available since 2006 [17]. Because MRAMs combine advantages of a high integration density, the high speed of a static random access and the non-volatility of a flash memory [18], the trend is likely that new generations of MRAMs will replace the current memory products in the future.

All the available magnetoresistive devices of information storage are hitherto successfully performed in metallic systems [8]. Nevertheless, the metallic structures are not ideal candidates for information processing as the electron density cannot be continuously adjusted and there is no bandgap in metals. These can give poor electronic controllability and function compatibility to most electronic and electro-optical components, which are generally based on semiconductor systems. To understand spin properties in semiconductors thus becomes crucial for potential applications of spin-based information processing. This emerging field is named as semiconductor "spin-electronics" or abbreviated as "spintronics".

Semiconductor spintronic devices are regarded as one of the promising candidates for future information processing [8, 19]. Compared with charge-based electronic devices, they are expected to

obtain several prominent potential advantages [20]. (i) Fast spin control and coherent spin manipulation up to THz frequency scale; (ii) Much lower power consumption during spin control and non-volatility for spin information storage; (iii) Being promising for quantum computing by addressing the spin states of a single carrier or ion in a semiconductor nanostructure.

Towards applications of semiconductor spintronics devices, several fundamental issues are regarded crucial [8]: generation of spin polarization, spin transport, spin control, coherent spin manipulation, and detection of spin states. The spin-polarized carriers have been widely generated by means of polarized optical pumping [21] or electrical injection in semiconductor hybrid structures [22, 23]. Experiments of spin transport [24-26] are usually performed in a spin-field-effect-transistor (spin-FET) of which the architecture prototype is an analog to the conventional charge-based FET design [27]. To control a spin state, a magnetic field or an effective magnetic field is required. An on-chip magnetic field can be generated either from a ferromagnet micro/nanostructure [28-31] or a current loop [32, 33]. An effective field can be obtained by spin-related mechanisms, i.e. exchange interaction [26, 34], and spin-orbit interaction [35] etc. Coherent spin manipulation has been demonstrated up to THz by tailored optical pulsed excitation [36, 37], and up to GHz by pulsed resonance RF excitation [34, 38-40]. The spin states are probed electrically, e.g. via magnetoresistance [41], or optically, e.g. via luminescence polarization [21] or spectral shift [42], and the magneto-optic Kerr/Faraday effect [43].

In order to incorporate magnetic properties into a nonmagnetic semiconductor, one alternative is to introduce magnetic centers in the host semiconductors. A semiconductor doped with magnetic ions is named as diluted magnetic semiconductor (DMS) [44]. In a DMS system, the magnetic ions partly substitute the cations of the host material. Well known host materials like II-VI semiconductors, e.g. CdTe, CdSe, CdS, ZnTe, ZnSe, HgTe, HgSe, ZnO, and III-V semiconductors, e.g. GaAs, InAs, GaN, have been widely utilized, and for the magnetic dopants, Mn, Fe, Co, Cr, V, Eu are often used [42, 44]. The manganese Mn^{2+} ions are the most popular example. This is due to the isoelectronic property of Mn^{2+}-ion in II-VI semiconductors and the large localized magnetic moment, which come from its $3d^5$- electronic shell configuration. Thanks to the highly developed growth technique, excellent DMS samples can be well fabricated from bulk materials [44] and quantum structures [42]. The Mn content can be precisely controlled even up to ~0.7 while the DMS lattice structure is still kept. Recently, novel structures incorporating Mn ions are demonstrated, e.g. single Mn ion in a quantum dot (QD) [45], DMS core-shell nanocrystals [46], and DMS colloidal QDs [47].

The DMS system combines the electrical and optical properties of a nonmagnetic semiconductor with magnetic properties of magnetic ions, i.e. Mn ions. Due to the presence of the band gap in a DMS, the carrier density can be flexibly controlled [26, 48] and electronic state transitions induced by optical excitation are allowed [44]. These facilitate greatly the electrical and optical investigations in DMS systems [41, 42, 44], e.g. carrier transport measurements and photoluminescence studies. More prominent characteristics come from the magnetic properties. Due to the strong exchange interaction, i.e. s-d exchange interaction between Mn ions and electrons and p-d exchange interaction between Mn ions and holes, pronounced carrier spin polarization can be obtained even in a weak

magnetic field. This leads to the often observed giant Zeeman splitting and giant magneto-optic Farady/Kerr rotation [42, 44].

The concept of carrier-induced ferromagnetism [49, 50] gives the idea to control the magnetic phase of Mn ions by tuning the carrier density, i.e. the magnetization can be varied between the anti-ferromagnetism and ferromagnetism. Since the p-d exchange interaction is stronger than the s-d exchange interaction in a typical DMS system, the modulation of hole density is generally used [26, 41, 51-53]. The demonstration of electrical control of ferromagnetism [26] stimulated vast experimental and theoretical investigations in various DMS, which was afterwards expected as one of the most promising material system for spintronic devices. Up to date, convincing results of ferromagnetism control are still below room temperature [54].

The magnetization dynamics of Mn ions depends on the Mn content [42, 55, 56], which determines how fast the Mn ion spins can be controlled and how long they can be coherently manipulated. The longitudinal spin relaxation time, known as spin-lattice relaxation (SLR) time, can vary greatly for different Mn contents. Due to the absence of the orbit spin for a Mn ion in II-VI DMS systems, the spin-phonon coupling between the Mn ion spin and the lattice is rather weak. Thus for a very dilute Mn content, the SLR process is quite long up to a millisecond time scale at liquid helium temperature. Mn^{2+} ion clusters are formed by increasing the Mn content [57, 58]. The SLR process is much faster for a cluster as a result of the Mn-Mn interaction, and via spin diffusion, single Mn ions surrounding are relaxed [59]. As a whole the SLR time is reduced below 100 ns for a Mn content of ~0.1. On a contrary, the transverse spin relaxation time namely the spin-spin relaxation time changes slowly from a low Mn content to a higher value. It is generally between ~10 ps and ~1 ns for different Mn contents [55, 60-62].

In order to accelerate the SLR process, carriers are introduced to provide an extra channel by means of carrier-Mn spin scattering [63] bypassing the relatively slow spin-phonon coupling. Experimental results demonstrate a pronounced SLR acceleration by increasing either the electron [64] or hole density [65]. Further, the magnetization dynamics can be shifted to a nanosecond time scale as a result of the Mn ion spin interaction with the local environment [56].

Similar to the localized electron spin of a Mn ion in a DMS, one nucleus also has a localized spin. The nuclear magnetic moment is generally smaller than the electronic magnetic moment by three orders of magnitude. This leads to a much weaker coupling between the nuclear spins and the local environment. As a consequence, the nuclear SLR time can be long up to even hours or days, and the nuclear spin-spin relaxation time is a few 100 µs or more [66]. Due to the quite long spin lifetime, the nuclear spin states have been suggested for potential applications of information processing by combination with electron spins [67, 68].

Since the nuclear magnetic moment is rather small, the nuclear spin polarization is quite small in a thermal equilibrium state. By making use of non-equilibrium electrons in semiconductors, the nuclear spin polarization can be greatly enhanced as a result of the electron-nucleus Fermi contact hyperfine interaction [69]. This phenomenon is known as Overhauser effect, and the effective nuclear field is usually named Overhauser field. The non-equilibrium electrons can be generated by

optical pumping [70] or electrical injection [71]. Especially optical means has been widely used to address the various subjects of nuclear spin studies in semiconductors [21, 72].

The magnitude of the nuclear field is determined by the strength of the hyperfine interaction and the nuclear isotope abundance [21, 73]. In III-V semiconductors, which are most widely studied, a nuclear spin polarization up to 50% was observed in QDs and the nuclear field of a few Tesla was experimentally determined [73-76]. A complete nuclear spin polarization is limited by nuclear leakage mechanisms [66, 77-79], like nuclear spin-spin interaction, nuclear SLR, nuclear quadrupole relaxation, and nuclear spin diffusion etc. These mechanisms depolarize nuclear spins competing with the hyperfine interaction which polarizes the nuclear spins. This explains why the nuclear polarization obtained in quantum structures is much larger than the value in bulk materials [21, 73]. Generally, an external magnetic field is required to suppress the depolarization mechanisms. In absence of an applied field, dynamic nuclear polarization formation in QDs has been recently demonstrated by using the Knight field [80, 81]. Due to much smaller hyperfine coupling constants, the nuclear field in II-VI semiconductors is much less compared with III-V counterparts. The nuclear field was experimentally determined to be ~10 mT [80, 82, 83].

The coherent manipulation of nuclear spins is achieved by means of the NMR technique [66]. The NMR in semiconductors can be detected by different experimental methods, e.g. highly sensitive detection of nuclear spin polarization from free induction decay signals [72], luminescence depolarization due to the Hanle effect [21, 77, 79, 84, 85], electrical resistance variance in the quantum Hall effect regime [86, 87], or the nuclear field-induced photoluminescence (PL) spectrum shift [88] and the electron spin precession dynamics, the latter probed by time-resolved magneto-optical Faraday/Kerr rotation [89-93]. Quite often, the RF field needed for NMR is produced from a Helmholtz coil [89]. Other approaches include all-optical NMR making use of the Knight field from optically generated spin-polarized electrons [90, 94], or an in-built micro-stripe which has been hitherto used in the ultralow temperature regime of ~50 mK [86]. By tailoring the pulse duration of the resonance RF field, the nuclear spins can be coherently manipulated, and it is known as nuclear Rabi oscillation. As the magnitude of the RF field is limited to ~1 mT in most experiments up to date, the coherent manipulation is typically in a frequency regime of a few kHz.

Recent experimental observations confirm the importance of the local nuclear environment to the nuclear spins in quantum structures, where the nuclear properties are varying on a mesoscopic length scale. The local quadrupole interaction is found so strong that the concept of the nuclear spin temperature cannot be valid [95-97], as well the Knight field is demonstrated non-uniform as a consequence of the inhomogeneous electron wavefunction in a quantum dot [98]. Usually, the local nuclear spin interaction is extracted from either spectral features of the NMR signal, like spectral broadening and spectral shift, or spin-echo type of experiments [66, 86, 89]. In this way, the nuclear spin information is typically analyzed as a result of the total local nuclear spin interaction, e.g. including both dipole-dipole and nuclear quadrupole interaction. As the local perturbations can mix the nuclear spin states, optical-forbidden NMR can thus be induced [99, 100]. This method has not

been often used up to date, since the local nuclear spin interaction is much smaller compared with the nuclear Zeeman energy in most NMR experiments [72].

This thesis is dedicated to address on-chip spin control and spin dynamics of two localized systems in semiconductor micro- and nano-structures. The whole work is based on an on-chip electrical technique, which provides a magnetic field by introducing a current loop on top of the semiconductor. This allows one to demonstrate sub-nanosecond control of Mn ion spin dynamics in a DMS quantum well (QW) and local nuclear spin manipulation in n-GaAs. The thesis is organized as following:

In Chapter 2, the background physics of this work is presented. In the first part, the crystal structure and the band structure of zincblende semiconductors are given. In the next part, the optical selection rules are given for a bulk GaAs system. The fundamental physics of a DMS QW is introduced in the last part. The optical properties are discussed for a QW system, and the magnetic properties of the DMS QW are reviewed.

In Chapter 3, techniques used in this thesis are introduced. At first a microstructure fabrication technology is established to provide an electrically switchable on-chip magnetic field, which is the novel and key technique throughout the whole thesis. This is done by a two-step electron beam lithography and lift-off technique. In the next part, the high-frequency electrical operation is demonstrated by adapting 50 ohm match for the sample and the cryostat. The electrical characterization of the microstructures is presented. The on-chip magnetic field is used for two types of spin-related experiments. To address the magnetization dynamics of Mn^{2+} ions in diluted magnetic semiconductor quantum wells, measurements of the time-resolved photoluminescence polarization degree are performed by means of magneto-luminescence spectroscopy, of which the working principle is given in the third part. In the last part, the time-resolved magneto-optical Kerr rotation technique is presented which is used to monitor the nuclear spin polarization and detect the nuclear magnetic resonance in one n-GaAs sample.

In Chapter 4, the concept of local electrical control of spin polarization is demonstrated by using the on-chip microscale current loop. In the first part, the magnetic properties of the diluted magnetic semiconductor quantum wells are characterized in a static magnetic field. The strong *sp-d* exchange interaction between the carriers and Mn ions gives a large effective exciton *g* factor. The photoluminescence thus shows pronounced polarization in the low field regime. In the second part, a magnetic field is generated by introducing a current through the on-chip microcoil. The switchable magnetic field allows an electrical control of the spin polarization, which is a competing result between the current-induced magnetic field raising the magnetization of Mn ions and the current-generated local heating for the demagnetization. A method is developed to extract the contribution from each mechnism. In the last part, the magnetization dynamics on a sample with a higher Mn content is investigated, and this sample can function as a detector for the phonon dynamics with a nanosecond time resolution.

In Chapter 5, the magnetization dynamics down to zero magnetic field is addressed in diluted magnetic semiconductor quantum wells. In the first part, the interaction of Mn ions with the local environment is introduced and the magnetic properties affected by carriers are discussed. These two

factors can strongly determine the Mn ion magnetization dynamics in the regime of a low magnetic field. Next the experimental results of the magnetization dynamics are presented showing a pronounced dependence on the external magnetic field. This is due to the interplay between the local anisotropic interactions of Mn ions and the Zeeman interaction with the external field. Numerical simulations based on the Lindblad master equation are performed and the theoretical calculations coincide well with the experiment results.

In Chapter 6, nuclear spin polarization and coherent nuclear spin manipulation are studied in one n-GaAs sample. At first a theoretical background is discussed regarding the electron-nucleus hyperfine coupling which controls the dynamic nuclear polarization and the nuclear spin relaxation in a semiconductor. Experimentally the dynamic nuclear field is optically addressed by the time-resolved Kerr rotation technique. The dependence of the nuclear field properties is studied by varying the experimental conditions. By utilizing an on-chip microcoil fabricated atop the semiconductor sample and introducing a radio frequency current through the microcoil to produce a resonance magnetic field, optically detected nuclear magnetic resonance is demonstrated on a length scale of a few micrometers. Further, the Rabi oscillation of ^{75}As nuclear spins is observed.

In Chapter 7, dynamic nuclear magnetic resonance is addressed in n-GaAs, mainly with respect to the observed optically forbidden magnetic resonance absorption. The local nuclear spin interaction is introduced regarding the nuclear magnetic moment and the nuclear quadrupole moment. The multi-spin magnetic resonance is explained according to the local nuclear spin perturbations, and the multi-photon absorption due to the tilted RF excitation is discussed. A two-level model is given for the measured nuclear spin dynamics, describing the interplay between the dynamic nuclear polarization via hyperfine interaction and nuclear spin depolarization due to magnetic resonance absorption. Comparing the characteristic nuclear spin relaxation rate obtained in experiment with master equation simulations, the underlying nuclear spin depolarization mechanism for each resonance is identified.

2 BACKGROUND PHYSICS

This chapter presents the background physics for this work. In the first part, the crystal structure and the band structure of zincblende semiconductors are given. In the next part, the optical selection rules are given for a bulk zincblende semiconductor. The fundamental physics of a diluted magnetic semiconductor (DMS) quantum well (QW) is introduced in the last part. The optical properties are discussed for a QW system, and the magnetic properties of the DMS QW are reviewed.

2.1 Properties of zincblende semiconductors

In this work, the two materials investigated are based on the II-VI binary compound-semiconductor CdTe and the III-V binary compound-semiconductor GaAs. Both semiconductor systems have zincblende crystal geometry, which leads to a similar electronic band structure.

2.1.1 Zincblende lattice structure

The zincblende crystal structure is schematically depicted in FIG 2.1-1. There are two types of atoms in a cubic cell. Each type of atom has a face-center-cubic (fcc) lattice. The two lattices are displaced against each other by a quarter of the space diagonal, so that each atom is tetrahedrally surrounded by four atoms of the other type. The lattice constant a_{Latt} is conventionally defined as the side length of the cubic cell. Each atom has four next neighbours of the other atom type at the corners of a regular tetrahedron at a distance of $\sqrt{3}/4 \cdot a_{\text{Latt}}$, and has twelve next-nearest neighbours of the same atom type at a distance of $\sqrt{2}/2 \cdot a_{\text{Latt}}$.
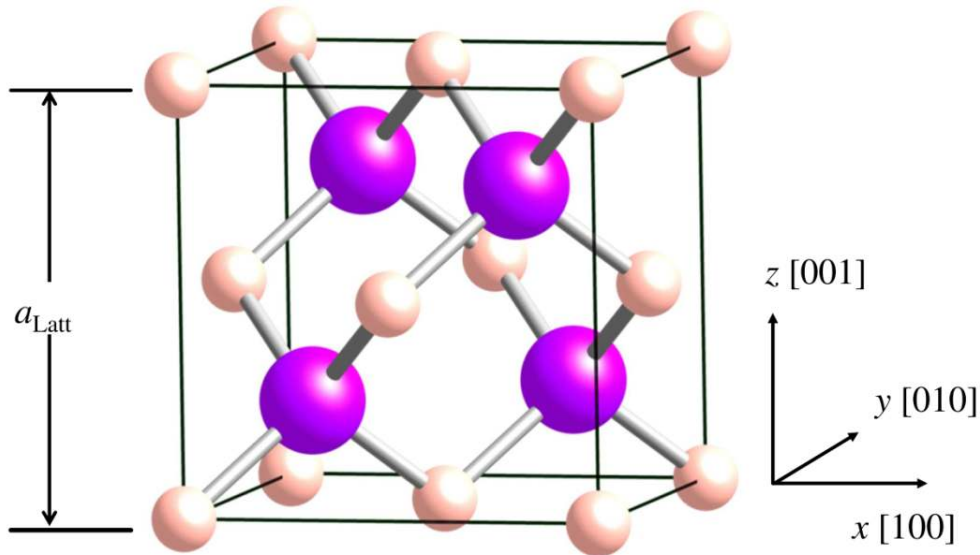
FIG 2.1-1: Unit cell of the zincblende crystal structure. The atom type is specified by an individual color. After Ref.[6].

A Wigner-Seitz cell is defined as the primitive cell in which there is only one lattice point if there is only one atom type in a crystal structure. The Wigner-Seitz cell for an fcc crystal lattice is presented in FIG 2.1-2(a). The counterpart in *k*-space, i.e. the first Brillouin zone, is described in FIG 2.1-2(b).

For an fcc lattice in real space, the first Brillouin zone is body-center-cubic (bcc) in k-space. The symmetry points and the axes are given by Greek letters in FIG 2.1-3. In the origin $k_x = k_y = k_z = 0$, the symmetry point is denoted as Γ.

(a) Wigner-Seitz cell   (b) First Brillouin zone

z [001]   y [010]

lattice real space

x [100]

k_z [001] k_y [010]

lattice k-space

k_x [100]

FIG 2.1-2: Schematic description of (a) the Wigner-Seitz cell for an fcc lattice in real space and (b) the corresponding first Brillouin zone in k-space. After Ref.[6].

FIG 2.1-3: First Brillouin zone of zincblende crystal structure. Symmetry points and axes are indicated by Greek letters. After Ref. [6]

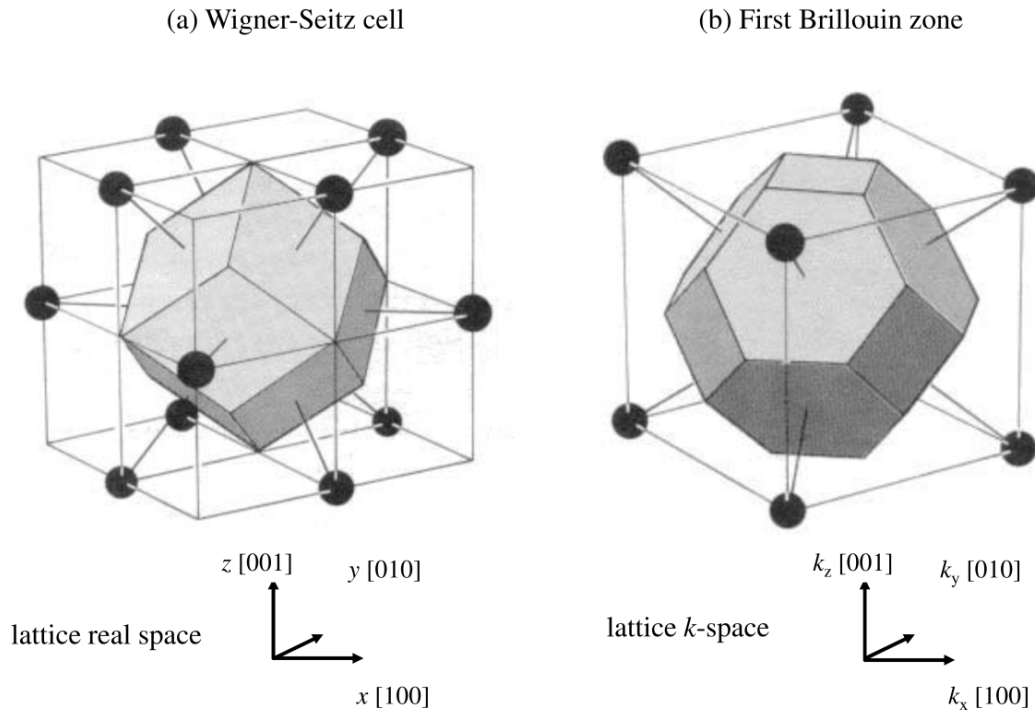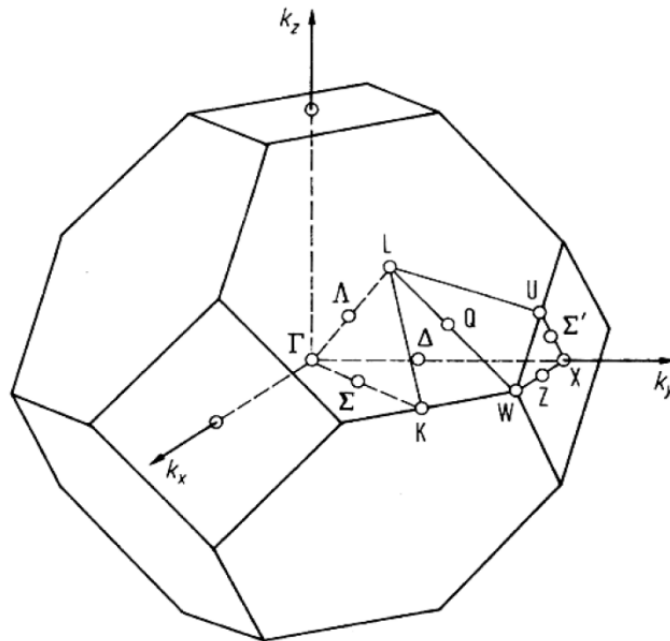In a zincblende binary compound, there are two atoms of different types in one Wigner-Seitz cell. It can be found that the volume of the Wigner-Seitz is $v_{cell} = 1/4 \cdot a_{Latt}^3$. The lattice constants involved in this work are listed in Table 2-1. For a ternary zincblende semiconductor compound, the lattice constant $a_{Latt\text{-}ternary}$ can be given by the Vegard's law [101]

$$a_{Latt\text{-}ternary} = (1-x) \cdot a_{Latt\text{-}binary1} + x \cdot a_{Latt\text{-}binary2} , \qquad (2\text{-}1)$$

in which (1-x) and x are the contents of the binary semiconductor 1 and 2, respectively. The corresponding lattice constants are $a_{Latt\text{-}ternary1}$ and $a_{Latt\text{-}ternary2}$.

Semiconductor material	Lattice constant (Å)
CdTe	6.481 [44]
MnTe	6.334 [44]
MgTe	6.419 [102]
GaAs	5.654 [103]

Table 2-1: Lattice constants for different binary semiconductors with the zincblende crystal structure.

2.1.2 Electronic band structures in zincblende semiconductors

Due to the lattice periodicity and the space symmetry in a crystal system, energy bands are formed [104]. The valence band is the highest range of electron energies in which electrons are normally present at absolute zero temperature, and the proximate band above the valence band is the conduction band. In a direct bandgap semiconductor, most electronic and optical properties are controlled by the energy dispersion at the Γ point in the first Brollouin zone.

For each zincblende semiconductor in Table 2-1, there is a direct energy bandgap at Γ point, i.e. $\boldsymbol{k} = \boldsymbol{0}$. From the group theory, the valence band has *p*-like symmetry and the conduction band has *s*-like symmetry in real space [104]. As a result, four bands are formed [105]: the conduction band (CB), the heavy-hole (HH) valence band, the light-hole (LH) band, and the spin-orbit (SO) split-off valence band. The schematic description of a direct bandgap bulk zincblende semiconductor is given in FIG 2.1-4. Each band has a two-fold degeneracy by considering the electron spin states. As convention, the CB band is denoted as Γ_6, HH and LH bands are denoted as Γ_8, and the SO band is denoted as Γ_7. The energy bandgap E_g is the energy required to excite one electron from the Γ_8 maximum (E_{v0}) to the Γ_6 minimum (E_{c0}), i.e. $E_g = E_{c0} - E_{v0}$. The energy splitting Δ_{SO} from the Γ_8 maximum to the Γ_7 maximum originates from the spin-orbit interaction. Here the Γ_8 maximum is defined as the zero energy level.

In order to determine the energy dispersion relation in the center of the first Brillouin zone, the $\boldsymbol{k} \cdot \boldsymbol{p}$ method based on the four-band Kane model is considered [105]. The Hamiltonian in a zincblende semiconductor is given as

$$\hat{H} = \frac{\hat{p}^2}{2m_0} + \hat{V}(\boldsymbol{r}) + \frac{\hbar}{4m_0^2 c^2} \hat{\boldsymbol{\sigma}} \cdot \nabla V(\boldsymbol{r}) \times \hat{\boldsymbol{p}} \qquad (2\text{-}2)$$

Hereby $\hat{\boldsymbol{p}}$ is the momentum operator, m_0 is the free electron mass, $\hat{V}(\boldsymbol{r})$ is the periodic potential of the lattice at position $\boldsymbol{r}$, the constant c is the light speed in vacuum and the operator $\hat{\boldsymbol{\sigma}}$ is described by the Pauli spin matrix. For an electron, the first term represents the electron kinetic energy. The second term is the periodic potential energy with $V(\mathbf{r}) = V(\mathbf{r} + \boldsymbol{R})$, in where $\boldsymbol{R}$ is the translation vector of the lattice. The last item describes the spin-orbit interaction between the electron spin and the internal electrical field which arises from the bulk inversion asymmetry in the zincblende crystal structure.
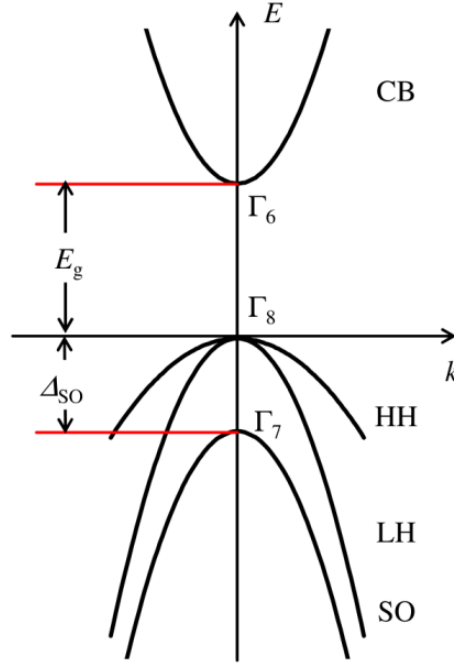
FIG 2.1-4: Schematic description of the band structure of zincblende-type bulk semiconductors in the vicinity of Γ-point.

According to the Bloch theorem, the electron states can be written as

$$\psi_{nk}(\boldsymbol{r}) = u_{nk}(\boldsymbol{r})e^{i k \cdot r} , \qquad (2\text{-}3)$$

where

$$u_{nk}(\boldsymbol{r}) = u_{nk}(\boldsymbol{r} + \boldsymbol{R}) \qquad (2\text{-}4)$$

is a periodic function. Here the index n refers to the band and $\boldsymbol{k}$ is the wave vector. The energy is given by $E = E_n(\boldsymbol{k})$.

By writing the Schrödinger equation for the wavefunction in (2.3), it is obtained

$$\hat{H}\psi_{nk} = \left(\frac{\hat{p}^2}{2m_0} + \hat{V}(\boldsymbol{r}) + \frac{1}{4m_0^2 c^2} \hat{\boldsymbol{\sigma}} \cdot \nabla V \times \hat{\boldsymbol{p}} \right)\psi_{nk}(\boldsymbol{r}) = E_n(\boldsymbol{k})\psi_{nk}(\boldsymbol{r}) \qquad (2\text{-}5)$$

By taking account the definition of the momentum operator, i.e. $\hat{\boldsymbol{p}} = -i\hbar\nabla$, the Schrödinger equation can be rewritten in terms of the periodic function as [105]

$$\left(\hat{H}_0 + \frac{\hbar}{m_0} \boldsymbol{k} \cdot \hat{\boldsymbol{p}} + \frac{\hbar}{4m_0^{\,2}c^2} \hat{\boldsymbol{\sigma}} \cdot \nabla V(\boldsymbol{r}) \times \hat{\boldsymbol{p}} + \frac{\hbar^2}{4m_0^{\,2}c^2} \hat{\boldsymbol{\sigma}} \cdot \nabla V(\boldsymbol{r}) \times \boldsymbol{k} \right) u_{\mathrm{nk}}(\boldsymbol{r}) = E_{\mathrm{n}}'(\boldsymbol{k}) u_{\mathrm{nk}}(\boldsymbol{r}), \qquad (2\text{-}6)$$

with

$$E_{\mathrm{n}}'(\boldsymbol{k}) = E_{\mathrm{n}}(\boldsymbol{k}) - \hbar^2 k^2 / 2m_0 \qquad (2\text{-}7)$$

and

$$\hat{H}_0 = \frac{\hat{p}^2}{2m_0} + \hat{V}(\boldsymbol{r}) \qquad (2\text{-}8)$$

Therefore $E_{\mathrm{n}}(\boldsymbol{k})$ can be obtained by from $E_{\mathrm{n}}'(\boldsymbol{k})$. In the vicinity of the Γ point, the last term on the left side can be neglected [105]. It becomes

$$\left(\hat{H}_0 + \frac{\hbar}{m_0} \boldsymbol{k} \cdot \hat{\boldsymbol{p}} + \frac{\hbar}{4m_0^{\,2}c^2} \hat{\boldsymbol{\sigma}} \cdot \nabla V(\boldsymbol{r}) \times \hat{\boldsymbol{p}} \right) u_{\mathrm{nk}}(\boldsymbol{r}) = E_{\mathrm{n}}'(\boldsymbol{k}) u_{\mathrm{nk}}(\boldsymbol{r}) \qquad (2\text{-}9)$$

To solve the Schrödinger equation above, a right set of basis functions should be chosen, so that the wavefunction $u_{\mathrm{nk}}(\boldsymbol{r})$ can be represented by a linear combination of these functions, i.e.

$$u_{\mathrm{nk}}(\boldsymbol{r}) = \sum_{\mathrm{m}} a_{\mathrm{m}} v_{\mathrm{m}}(\boldsymbol{r}) \qquad (2\text{-}10)$$

Here $\{v_{\mathrm{m}}(\boldsymbol{r})\}$ is the function set, and a_{m} is the corresponding coefficient.

As mentioned above, the conduction band has s-like symmetry and the valence band has p-like symmetry near the Γ point, the basis functions can be chosen according to the orbit spin in each band. By considering the two-fold spin degeneracy, the basis functions are chosen as follows [105],

$$v_1(\boldsymbol{r}) = \left| iS \downarrow \right\rangle, \ v_2(\boldsymbol{r}) = \left| \frac{X - iY}{\sqrt{2}} \uparrow \right\rangle, \ v_3(\boldsymbol{r}) = \left| Z \downarrow \right\rangle, \ v_4(\boldsymbol{r}) = \left| -\frac{X + iY}{\sqrt{2}} \uparrow \right\rangle$$

$$v_5(\boldsymbol{r}) = \left| iS \uparrow \right\rangle, \ v_6(\boldsymbol{r}) = \left| -\frac{X + iY}{\sqrt{2}} \downarrow \right\rangle, \ v_7(\boldsymbol{r}) = \left| Z \uparrow \right\rangle, \ v_8(\boldsymbol{r}) = \left| \frac{X - iY}{\sqrt{2}} \downarrow \right\rangle$$

$$(2\text{-}11)$$

Here the wavefunction $|S\rangle$ is the normalized s-orbit spherical harmonic function. The wavefunctions $|Z\rangle$ and $\left| \mp \frac{X \pm iY}{\sqrt{2}} \right\rangle$ are the p-orbit spherical harmonic functions. These spherical harmonics are the normalized electron wavefunctions of a Hydrogen atom [105]. The electron spin states are denoted by $|\uparrow\rangle$ for spin up and $|\downarrow\rangle$ for spin down. Each basis function is a product of one orbit harmonic function and the spin state wavefunction, e.g. $v_1(\boldsymbol{r}) = \left| iS \downarrow \right\rangle = \left| iS \right\rangle \cdot \left| \downarrow \right\rangle$. The first four basis functions are respectively degenerate with the last four basis functions, i.e. $v_1(\boldsymbol{r})$ is degenerate with $v_5(\boldsymbol{r})$, $v_2(\boldsymbol{r})$ is degenerate with $v_6(\boldsymbol{r})$, $v_3(\boldsymbol{r})$ is degenerate with $v_7(\boldsymbol{r})$ and $v_4(\boldsymbol{r})$ is degenerate with $v_8(\boldsymbol{r})$,.

At the Γ point, the electronic states $\left| X \uparrow \right\rangle$, $\left| X \downarrow \right\rangle$, $\left| Y \uparrow \right\rangle$, $\left| Y \downarrow \right\rangle$, $\left| Z \uparrow \right\rangle$ and $\left| Z \downarrow \right\rangle$ are degenerate and have energy of E_{p} [105], i.e.

$$\hat{H}_0 \left| X \uparrow \right\rangle = E_p \left| X \uparrow \right\rangle, \ \hat{H}_0 \left| X \downarrow \right\rangle = E_p \left| X \downarrow \right\rangle,$$
$$\hat{H}_0 \left| Y \uparrow \right\rangle = E_p \left| Y \uparrow \right\rangle, \ \hat{H}_0 \left| Y \downarrow \right\rangle = E_p \left| Y \downarrow \right\rangle, \tag{2-12}$$
$$\hat{H}_0 \left| Z \uparrow \right\rangle = E_p \left| Z \uparrow \right\rangle, \ \hat{H}_0 \left| Z \downarrow \right\rangle = E_p \left| Z \downarrow \right\rangle,$$

Similarly for the conduction band, the states $\left| S \uparrow \right\rangle$ and $\left| S \downarrow \right\rangle$ are degenerate and have energy of E_s, i.e.

$$\hat{H}_0 \left| S \uparrow \right\rangle = E_s \left| S \uparrow \right\rangle, \ \hat{H}_0 \left| S \downarrow \right\rangle = E_s \left| S \downarrow \right\rangle, \tag{2-13}$$

According to the basis functions in (2.11), the Hamiltonian $\hat{H}_c$ contained in Equation (2.9) can be represented by an 8×8 matrix. It is written as

$$\begin{bmatrix} \hat{H}_c & 0 \\ 0 & \hat{H}_c \end{bmatrix} \tag{2-14}$$

Here $\hat{H}_c$ is a 4×4 matrix, and it is obtained as [105] :

$$H_c = \begin{bmatrix} E_s & 0 & kP & 0 \\ 0 & E_p - \Delta_{SO}/3 & \sqrt{2}\Delta_{SO}/3 & 0 \\ kP & \sqrt{2}\Delta_{SO}/3 & E_p & 0 \\ 0 & 0 & 0 & E_p + \Delta_{SO}/3 \end{bmatrix} \tag{2-15}$$

Here the assumption $k_x = k_y = 0$ is made. The Kane's parameter P and the spin-orbit split-off energy Δ_{SO} are defined as

$$P = -i \frac{\hbar}{m_0} \left\langle S \left| \hat{p}_z \right| Z \right\rangle \tag{2-16}$$

$$\Delta_{SO} = \frac{3\hbar i}{4m_0^2 c^2} \left\langle X \left| \frac{\partial V}{\partial x} \hat{p}_y - \frac{\partial V}{\partial y} \hat{p}_x \right| Y \right\rangle \tag{2-17}$$

By using the definitions $E_s = E_g$ and $E_p = -\Delta_{SO}/3$, the Hamiltonian in (2.15) is rewritten as

$$\hat{H}_c = \begin{bmatrix} E_g & 0 & kP & 0 \\ 0 & -2\Delta_{SO}/3 & \sqrt{2}\Delta_{SO}/3 & 0 \\ kP & \sqrt{2}\Delta_{SO}/3 & -\Delta_{SO}/3 & 0 \\ 0 & 0 & 0 & 0 \end{bmatrix} \tag{2-18}$$

By considering the Hamiltonian H_c for the first four basis functions, the Schrödinger equation in (2.9) is rewritten in the matrix form as

$$\begin{bmatrix} E_g & 0 & kP & 0 \\ 0 & -2\Delta_{SO}/3 & \sqrt{2}\Delta_{SO}/3 & 0 \\ kP & \sqrt{2}\Delta_{SO}/3 & -\Delta_{SO}/3 & 0 \\ 0 & 0 & 0 & 0 \end{bmatrix} \begin{bmatrix} a_1 v_1(\boldsymbol{r}) \\ a_2 v_2(\boldsymbol{r}) \\ a_3 v_3(\boldsymbol{r}) \\ a_4 v_4(\boldsymbol{r}) \end{bmatrix} = E' \begin{bmatrix} a_1 v_1(\boldsymbol{r}) \\ a_2 v_2(\boldsymbol{r}) \\ a_3 v_3(\boldsymbol{r}) \\ a_4 v_4(\boldsymbol{r}) \end{bmatrix} \tag{2-19}$$

There are four eigenvalues for the energy E'. By taking account Equation (2.7), the energy $E_n(\boldsymbol{k})$ for $\boldsymbol{k} \approx 0$ can be obtained as

$$\text{CB}: E_c(k) \approx E_g + \frac{\hbar^2 k^2}{2m_{\text{eff-CB}}}, \quad \text{with} \frac{1}{m_{\text{eff-CB}}} = \frac{1}{m_0} + \frac{2P^2(E_g + 2\Delta_{\text{SO}}/3)}{\hbar^2 E_g(E_g + \Delta_{\text{SO}})} \tag{2-20}$$

$$\text{HH}: E_{\text{HH}}(k) \approx \frac{\hbar^2 k^2}{2m_{\text{eff-HH}}}, \quad \text{with} \ \frac{1}{m_{\text{eff-HH}}} = \frac{1}{m_0} \tag{2-21}$$

$$\text{LH}: E_{\text{LH}}(k) \approx \frac{\hbar^2 k^2}{2m_{\text{eff-LH}}}, \quad \text{with} \frac{1}{m_{\text{eff-LH}}} = \frac{1}{m_0} - \frac{4P^2}{3\hbar^2 E_g} \tag{2-22}$$

$$\text{SO}: E_{\text{SO}}(k) \approx -\Delta_{\text{SO}} + \frac{\hbar^2 k^2}{2m_{\text{eff-SO}}}, \quad \text{with} \frac{1}{m_{\text{eff-SO}}} = \frac{1}{m_0} - \frac{2P^2}{3\hbar^2(E_g + \Delta_{\text{SO}})} \tag{2-23}$$

The effective mass for each electronic state is given by Equation (2.20) ~ (2.23). To note, the Kane's model gives an inaccurate description for the effective electronic mass of the HH band, i.e. see Equation (2.21). This can be fixed by the eight-band Luttinger-Kohn's model [105].

The coefficient set $\{a_m\}$ for each E' can be determined. The corresponding wavefunctions are

$$\text{CB}: u_{1k}(\boldsymbol{r}) \approx \left| iS \downarrow \right\rangle \tag{2-24}$$

$$\text{HH}: u_{2k}(\boldsymbol{r}) \approx \left| -\frac{X + iY}{\sqrt{2}} \uparrow \right\rangle \tag{2-25}$$

$$\text{LH}: u_{3k}(\boldsymbol{r}) \approx \frac{1}{\sqrt{3}} \left| \frac{X - iY}{\sqrt{2}} \uparrow \right\rangle + \sqrt{\frac{2}{3}} \left| Z \downarrow \right\rangle \tag{2-26}$$

$$\text{SO}: u_{4k}(\boldsymbol{r}) \approx \sqrt{\frac{2}{3}} \left| \frac{X - iY}{\sqrt{2}} \uparrow \right\rangle - \frac{1}{\sqrt{3}} \left| Z \downarrow \right\rangle \tag{2-27}$$

For the corresponding degenerate electronic states, the wavefunctions are

$$\text{CB}: u_{5k}(\boldsymbol{r}) \approx \left| iS \uparrow \right\rangle \tag{2-28}$$

$$\text{HH}: u_{6k}(\boldsymbol{r}) \approx \left| \frac{X - iY}{\sqrt{2}} \downarrow \right\rangle \tag{2-29}$$

$$\text{LH}: u_{7k}(\boldsymbol{r}) \approx -\frac{1}{\sqrt{3}} \left| \frac{X + iY}{\sqrt{2}} \downarrow \right\rangle + \sqrt{\frac{2}{3}} \left| Z \uparrow \right\rangle \tag{2-30}$$

$$\text{SO}: u_{8k}(\boldsymbol{r}) \approx \sqrt{\frac{2}{3}} \left| \frac{X + iY}{\sqrt{2}} \downarrow \right\rangle + \frac{1}{\sqrt{3}} \left| Z \uparrow \right\rangle \tag{2-31}$$

Now consider the electronic states in terms of the spin states. The electron spin state is represented by $|s, m_s>_s$, in which s is the electron spin and m_s is the spin component along an arbitrary z-axis. It is written as

$$\left|\uparrow\right\rangle = \left|1/2, 1/2\right\rangle_s, \quad \left|\downarrow\right\rangle = \left|1/2, -1/2\right\rangle_s \tag{2-32}$$

The orbital spin state is represented by by $|l, m_l>_l$, in which l is the electron orbit spin and m_l is the spin component along the z-axis. It is obtained

$$\left|S\right\rangle = \left|0,0\right\rangle_l, \quad \left|-\frac{X+iY}{\sqrt{2}}\right\rangle = \left|1,1\right\rangle_l, \quad \left|\frac{X-iY}{\sqrt{2}}\right\rangle = \left|1,-1\right\rangle_l, \quad \left|Z\right\rangle = \left|1,0\right\rangle_l \tag{2-33}$$

By denoting the orbital angular momentum operator as $\hat{\boldsymbol{L}}$ and the spin angular momentum operator as $\hat{\boldsymbol{S}}$, the operator of the total angular momentum written as $\hat{\boldsymbol{J}} = \hat{\boldsymbol{L}} + \hat{\boldsymbol{S}}$. The corresponding projection operators hold $\hat{J}_z = \hat{L}_z + \hat{S}_z$. By performing the following operations

$$\begin{aligned}
\hat{J} u_{nk}(\boldsymbol{r}) &= \hat{L} u_{nk}(\boldsymbol{r}) + \hat{S} u_{nk}(\boldsymbol{r}) = j\hbar u_{nk}(\boldsymbol{r}) \\
\hat{J}_z u_{nk}(\boldsymbol{r}) &= \hat{L}_z u_{nk}(\boldsymbol{r}) + \hat{S}_z u_{nk}(\boldsymbol{r}) = m_j \hbar u_{nk}(\boldsymbol{r})
\end{aligned} \tag{2-34}$$

the electronic states $u_{nk}(\boldsymbol{r})$ can be represented by the spin states $|j, m_j>_j$. They are summarized as

$$\begin{aligned}
\mathrm{CB}: u_1 &= i\left|1/2, -1/2\right\rangle_j = \left|iS\downarrow\right\rangle, \\
u_5 &= i\left|1/2, 1/2\right\rangle_j = \left|iS\uparrow\right\rangle; \\
\mathrm{HH}: u_2 &= \left|3/2, 3/2\right\rangle_j = \left|-\frac{X+iY}{\sqrt{2}}\uparrow\right\rangle, \\
u_6 &= \left|3/2, -3/2\right\rangle_j = \left|\frac{X-iY}{\sqrt{2}}\downarrow\right\rangle; \\
\mathrm{LH}: u_3 &= \left|3/2, -1/2\right\rangle_j = \frac{1}{\sqrt{3}}\left|\frac{X-iY}{\sqrt{2}}\uparrow\right\rangle + \sqrt{\frac{2}{3}}\left|Z\downarrow\right\rangle, \\
u_7 &= \left|3/2, 1/2\right\rangle_j = -\frac{1}{\sqrt{3}}\left|\frac{X+iY}{\sqrt{2}}\downarrow\right\rangle + \sqrt{\frac{2}{3}}\left|Z\uparrow\right\rangle; \\
\mathrm{SO}: u_4 &= \left|1/2, -1/2\right\rangle_j = \sqrt{\frac{2}{3}}\left|\frac{X-iY}{\sqrt{2}}\uparrow\right\rangle - \frac{1}{\sqrt{3}}\left|Z\downarrow\right\rangle, \\
u_8 &= \left|1/2, 1/2\right\rangle_j = \sqrt{\frac{2}{3}}\left|\frac{X+iY}{\sqrt{2}}\downarrow\right\rangle + \frac{1}{\sqrt{3}}\left|Z\uparrow\right\rangle.
\end{aligned} \tag{2-35}$$

Here the state $u_{nk}(\boldsymbol{r})$ is denoted as u_n.

For an accurate band structure calculation, the specific atomic parameters should be taken into consideration [105]. FIG 2.1-5 gives the calculated band structure [106] for bulk CdTe (a) and GaAs (b). From experimental data [103], $E_g(\mathrm{CdTe}) = 1.475$ eV, $\Delta_{SO}(\mathrm{CdTe}) = 0.952$ eV, $E_g(\mathrm{GaAs}) = 1.424$ eV at room temperature. At a temperature of 1.7 K, $\Delta_{SO}(\mathrm{GaAs}) = 0.3464$ eV is determined.
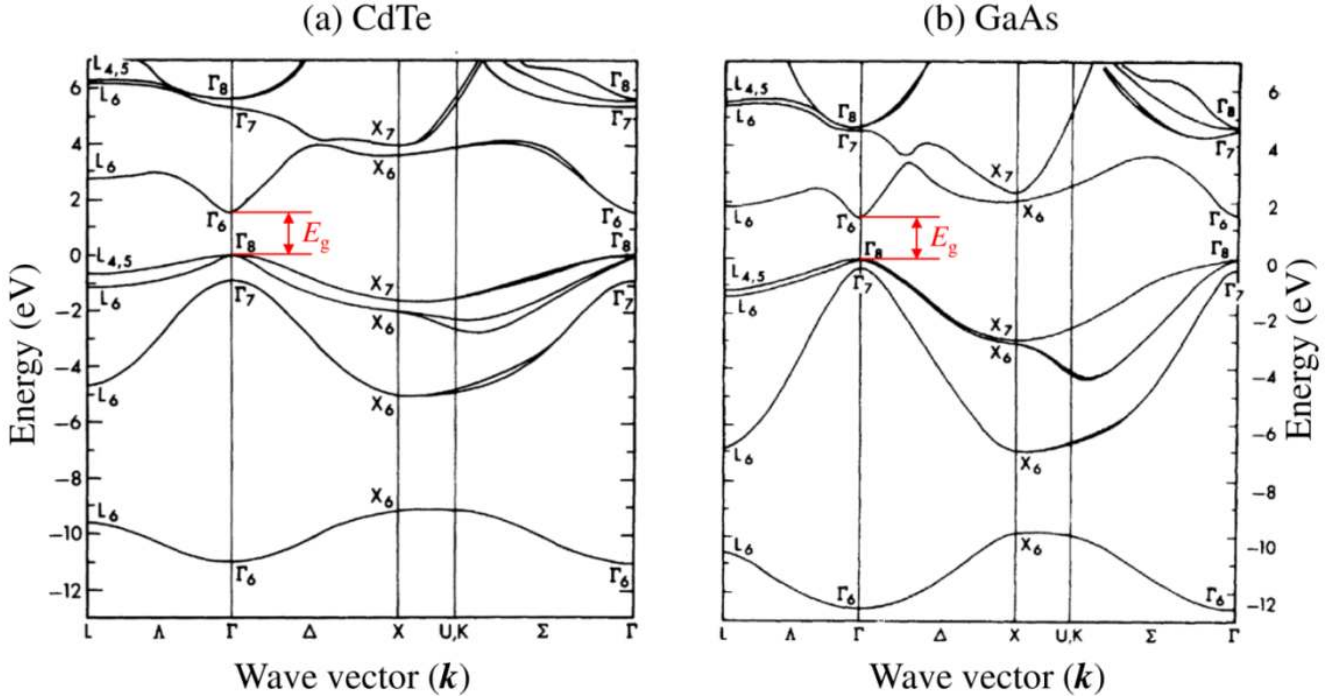
FIG 2.1-5: Calculated band structure adopted from Ref. [106]. (a) bulk CdTe; (b) bulk GaAs.

2.2 Optical orientation in zincblende semiconductors

Due to the direct nature of the band structure in zincblende semiconductors, optical excitation can induce electronic transitions from the valence band to the conduction band in the vicinity of Γ point. Polarized optical excitation, namely optical orientation, has been widely used to generate spin-polarized electrons for spin-related phenomena studies in semiconductors. Quite systematical investigations are summarized in Ref. [21] for III-V semiconductors.

The resonant optical excitation is considered at the Γ point. This means that the excitation energy $\hbar\omega_{\text{exc}}$ is equal to the electronic bandgap energy E_{g}, i.e. $E_{\text{g}} = \hbar\omega_{\text{exc}}$. An optically-induced electronic transition process can be treated as a state transition induced by the electrical dipole Hamiltonian operator $\hat{H}_{\text{Dip}}$ of the light. It is defined as

$$\hat{H}_{\text{Dip}} = e\hat{r} \cdot \hat{E} \tag{2-36}$$

The electrical field vector E of the optical excitation is denoted as

$$E(t) = E_x(t) + E_y(t) \cdot e^{i\theta} \tag{2-37}$$

Here it is considered the light wave vector is along the z-axis direction (see Section A3). The electrical field component along x-axis and y-axis are respectively represented as $E_x(t)$ and $E_y(t)$, and the phase retardation is given by θ. It can be found:

In case of σ^+-polarized excitation, i.e. $|E_x(t)| = |E_y(t)|$ and $\theta = \pi/2$,

$$\hat{\boldsymbol{H}}_{\text{Dip}}(\sigma^+) = e(\hat{x}E_x + i\hat{y}E_y) = \gamma(\hat{X} + i\hat{Y}) \tag{2-38}$$

Here γ is constant determined by the spherical harmonic function [105].

In case of σ^--polarized excitation, i.e. $|\boldsymbol{E}_\text{x}(t)| = |\boldsymbol{E}_\text{y}(t)|$ and $\theta = -\pi/2$,

$$\hat{\boldsymbol{H}}_{\text{Dip}}(\sigma^-) = e(\hat{x}E_x - i\hat{y}E_y) = \gamma(\hat{X} - i\hat{Y}) \tag{2-39}$$

In case of linearly-polarized excitation, i.e. $|\boldsymbol{E}_\text{x}(t)| = |\boldsymbol{E}_\text{y}(t)|$ and $\theta = 0$,

$$\hat{\boldsymbol{H}}_{\text{Dip}}(\pi) = e(\hat{x}E_x + \hat{y}E_y) = \gamma(\hat{X} + \hat{Y}) \tag{2-40}$$

It could be found that σ^+-polarized excitation can induce a transition from the state $|3/2, -3/2\rangle_j$ to the state $i|1/2, -1/2\rangle_j$, as there is

$$\langle 1/2, -1/2 | \hat{\boldsymbol{H}}_{\text{Dip}}(\sigma^+) | 3/2, -3/2 \rangle = \gamma \left\langle S\downarrow \left| \hat{X} + i\hat{Y} \right| \frac{X - iY}{\sqrt{2}} \downarrow \right\rangle = \sqrt{2}\gamma \langle S | \hat{X} | X \rangle \tag{2-41}$$

Also the σ^+-polarized excitation can induce a transition from the state $|3/2, -1/2\rangle_j$ to the state $i|1/2, 1/2\rangle_j$, as there is

$$\langle 1/2, 1/2 | \hat{\boldsymbol{H}}_{\text{Dip}}(\sigma^+) | 3/2, -1/2 \rangle = \gamma \left\langle S\uparrow \left| \hat{X} + i\hat{Y} \right| \frac{X - iY}{\sqrt{6}} \uparrow + \sqrt{\frac{2}{3}} Z \downarrow \right\rangle = \sqrt{\frac{2}{3}}\gamma \langle S | \hat{X} | X \rangle \tag{2-42}$$

As well, the σ^+-polarized excitation can induce a transition from the state $|1/2, -1/2\rangle_j$ to the state $i|1/2, 1/2\rangle_j$, as there is

$$\langle 1/2, 1/2 | \hat{\boldsymbol{H}}_{\text{Dip}}(\sigma^+) | 1/2, -1/2 \rangle = \gamma \left\langle S\uparrow \left| \hat{X} + i\hat{Y} \right| \sqrt{\frac{2}{3}} \frac{X - iY}{\sqrt{2}} \uparrow - \frac{1}{\sqrt{3}} Z \downarrow \right\rangle = \sqrt{\frac{4}{3}}\gamma \langle S | \hat{X} | X \rangle \tag{2-43}$$

The transition probability is proportional to the square of the calculated values from (2.41) ~ (2.43). Therefore the relative transition strength is 1:1/3:2/3. For the calculations, it has been used $\langle S | \hat{X} | X \rangle = \langle S | \hat{Y} | Y \rangle = \langle S | \hat{Z} | Z \rangle$ by considering the spherical symmetry of S function.

Similarly, state transitions induced by σ^--polarized excitation and by linearly-polarized excitation can be calculated. The transition paths and the relative strengths are summarized in FIG 2.2-1.

Since Γ_7 is split from Γ_8 due to the spin-orbit interaction, the state transitions from SO band to CB band can be neglected in case of a resonant excitation from Γ_8 to Γ_6. If the excitation is $\sigma^\pm$-polarized, the state transitions $|3/2, \mp 3/2\rangle_j \rightarrow |1/2, \mp 1/2\rangle_j$ and $|3/2, \mp 1/2\rangle_j \rightarrow |1/2, \pm 1/2\rangle_j$ are both induced, and the electron spin polarization is given as

$$P_{\text{opt}} = \pm \frac{p_{|1/2,1/2\rangle_j} - p_{|1/2,-1/2\rangle_j}}{p_{|1/2,1/2\rangle_j} + p_{|1/2,-1/2\rangle_j}} = \pm \frac{1 - 1/3}{1 + 1/3} = \pm 50\% \,, \tag{2-44}$$

where the transition probability to the spin state $|1/2, 1/2\rangle_j$ and $|1/2, -1/2\rangle_j$ are respectively given by $p_{|1/2, 1/2\rangle_j}$ and $p_{|1/2, -1/2\rangle_j}$. This gives an upper-limit spin polarization by optical orientation in a bulk zincblende semiconductor, i.e. GaAs. The obtained electron spin polarization is generally smaller than this value as a result of different spin relaxation mechanisms [21]. In quantum structures, the

optically generated spin polarization can be up to 100%, since the LH band is not degenerate with the HH band anymore and only the state transition $|3/2, -3/2>_j \rightarrow |1/2, -1/2>_j$ is allowed in the case of resonant excitation.
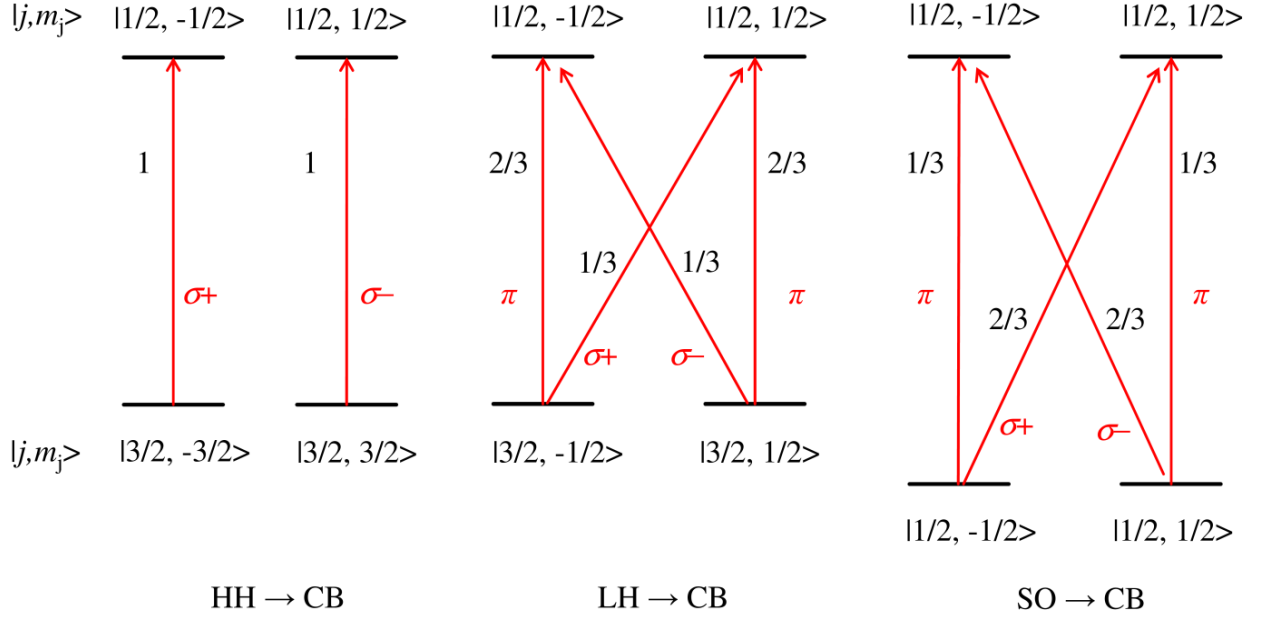

FIG 2.2-1: Allowed optical transitions from valence band to conduction band by different polarizations. The relative transition strength is indicated.

2.3 II-VI diluted magnetic semiconductors

Diluted magnetic semiconductors (DMS) are semiconducting alloys whose lattice is made up in part of substitutional magnetic ions [107]. The host materials can be IV-VI, II-VI and III-VI semiconductors [54] and the magnetic centers are typically of transition metals or rare-earth elements, e.g. Mn, Cr and Eu. Since the DMS system pertain both semiconducting electronic properties and magnetic properties, it has obtained great interest over decades. From the aspect of fundamental physics, it is interesting to understand the basic physics of the magnetic centers [42, 44, 108], such as magnetic ordering and the magnetization dynamics. On the other hand, the DMS is regarded as one promising candidate for future applications of spintronic devices [41, 54], especially after the successful demonstration of electrically controllable ferromagnetism [26].

In this thesis, the DMS investigations are performed in heterostructures made of II-VI semiconductors belonging to telluride family, i.e. single $Cd_{1-x}Mn_xTe/Cd_{1-y}Mg_yTe$ quantum wells (QW). Here x and y are the mole fraction of Mn and Mg, respectively. The study focus is mainly concerning to the magnetization dynamics of the Mn^{2+} ions acting as paramagnetic centers. Thanks to the superb optical quality of the grown samples [109], the magnetic properties are optically addressed by means of photoluminescence spectroscopic measurements. In the following, basic characteristics of the studied DMS QW are given.

2.3.1 Bandgap of a DMS QW

For the studied $Cd_{1-x}Mn_xTe/Cd_{1-y}Mg_yTe$ heterostructures, both crystal alloys are ensured to favor the zinc-blende structure, so that the compounds still have direct bandgap structures at the Γ point of the first Brillouin zone. By using the virtual crystal approximation approach [107], the bandgap for a bulk $Cd_{1-x}Mn_xTe$ DMS can be well described by

$$E_g(x) = (1-x)E_g(CdTe) + xE_g(Mn\,Te),$$ (2-45)

in which $E_g(CdTe)$ and $E_g(MnTe)$ are the energy bandgaps for CdTe and MnTe, respectively. Here the bandgap is referred to the energy splitting between the Γ_8 valence band and the Γ_6 conduction band. The Γ_7 split-off band is omitted for the studied (Cd, Mn)Te system. In the liquid helium temperature, it has been determined as $E_g(CdTe) = 1.606$ eV [107] and $E_g(MnTe) = 3.198$ eV [110]. The above relation can be simplified as

$$E_g(x) = 1.606 + 1.592x \text{ [eV]}$$ (2-46)

For the $Cd_{1-y}Mg_yTe$ alloys, the energy bandgap dependence is experimentally summarized as [111]

$$E_g(y) = 1.606 + 1.700y + 0.3y^2 \text{ [eV]}$$ (2-47)

To determine the actual band structure of QW heterostructure, the offset of the valence band between the QW layer and the barrier layer should be taken into account. It is described by the valence band discontinuity parameter α_V, which is used to define the depth of the trapping potential V_V in the valance band. The relation is given as

$$V_V = \alpha_V(E_B - E_Q)$$ (2-48)

Here E_B is the bandgap of the barrier layers and E_Q is the bandgap of the QW layer. In FIG 2.3-1(a), the QW band alignment for a positive value of α_V is schematically depicted. The potential confinement in the conduction band and the valence band both happen in the QW region, which is known as the type-I QW structure. The studied $Cd_{1-x}Mn_xTe/Cd_{1-y}Mg_yTe$ QW is this type and the value of α_V has been experimentally determined around to be around 0.3 [112].

The higher barrier potential can confine the electron wavefunction mainly in the QW layer. The layer thickness is typically on the nanometer length scale. As a result of the quantum mechanical effect, the electron momentum is of discrete levels in the growth direction (z-axis direction) [113]. As shown in FIG 2.3-1(b), the energy level of the conduction (valence) band is not on the band minimum (maximum), but higher (lower) by a certain amount. The discrete momentum in the growth direction is

$$k_z = \frac{n\pi}{L_z}, \text{with } n = 1, 2, 3\cdots,$$ (2-49)

in which L_z is the thickness of the QW layer and n is the quantum number. The corresponding discrete subband kinetic energy level is

$$E_{\text{kin}}(n) = \frac{\pi^2 \hbar^2}{2m_{\text{eff-z}}L_z^2}n^2 + \frac{\hbar^2}{2m_{\text{eff-xy}}}k_{\parallel}^2, \text{with } n = 1, 2, 3 \cdots \qquad (2\text{-}50)$$

Hereby, $\hbar$ is the reduced Planck constant, $m_{\text{eff-z}}$ is the effective electron (hole) mass in the conduction (valence) band in the z-axis direction, $m_{\text{eff-xy}}$ is the effective electron (hole) mass in the conduction (valence) band in the in-plane (xy plane) direction, and $k_{\parallel}$ is the continuous in-plane component of the electronic wave vector. As a rough estimation of the quantized kinetic energy in the studied (Cd, Mn)Te QW sample, by using parameters $n = 1$, $k_{\parallel} = 0$, $L_z = 12$ nm, and $m_e \approx 0.094 \cdot m_0$ in CdTe [103, 114] for the electron in the conduction band with m_0 as the free electron mass, $E_{\text{kin-e}} \approx 28$ meV is obtained. Similarly for holes in the valence band, by using $m_{\text{eff-z-hh}} \approx 0.72 \cdot m_0$ for the heavy hole and $m_{\text{eff-z-lh}} \approx 0.13 \cdot m_0$ for the light hole in the valence band, $E_{\text{kin-hh}} \approx 3.6$ meV and $E_{\text{kin-lh}} \approx 20$ meV are respectively obtained. To note, the electronic wavefunction penetration in the barrier layer is not considered here. This kinetic energy difference between the heavy hole and the light hole causes the non-degeneracy at the Γ point of the valence band.
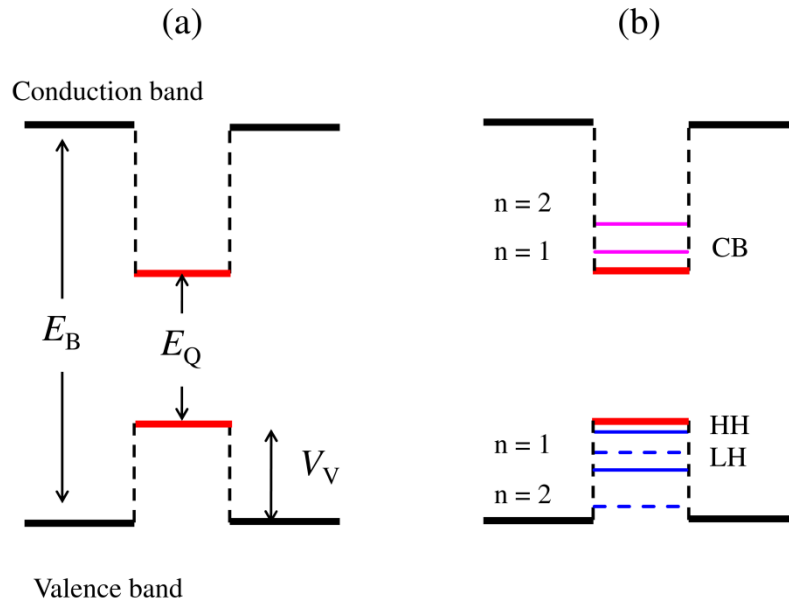

FIG 2.3-1: (a) Band alignment in a type-I quantum well heterostructure; (b) Discrete kinetic energy levels due to spatial confinement at the Γ point. CB band: magenta solid line; HH band: blue solid line; LH band: blue dashed line.

Apart from the electronic confinement, there is universally lattice mismatch between the barrier material and the QW material. Since the QW thickness is generally chosen to be much below the critical relaxation thickness [115], finite strain is generated, i.e. a crystal field is in presence. As a result of the spin-orbit interaction, the LH subband is lowered compared with the HH subband in the QW layer [116].

As a consequence of effective mass difference and the strain-induced spin-orbit interaction, the energy splitting ΔE_{hl} between the heavy HH (blue solid line) and LH (blue dashed line) is indicated in FIG 2.3-1(b). In the QW of the studied $Cd_{1-x}Mn_xTe/Cd_{1-y}Mg_yTe$ heterostructures in which x is between 0.024 and 0.067 and y is equal to 0.3, ΔE_{hl} is estimated ~20 meV from measurements in

similar structures [109, 112]. Here, the non-degeneracy between the HH subband and the LH subband is dominated by the electronic confinement.

For spectroscopic measurements, the photoluminescence (PL) is collected originating from the QW layer. The photoluminescence comes after the recombination of excitons, quasi-particles composed of electron-hole pairs. The excitons are bound states due to the Coulomb interaction between electrons and holes. A schematic description is given in FIG 2.3-2 for the exciton creation.
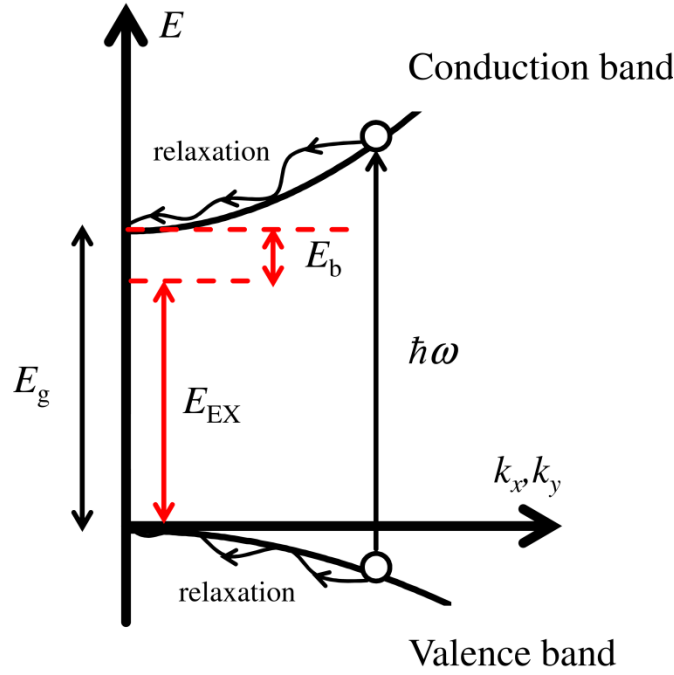

FIG 2.3-2: Picture of exciton generation. For energy terms, $\hbar\omega$: excitation energy; E_b: exciton binding energy; E_{EX}: exciton energy; E_g: semiconductor energy bandgap. After Ref. [117]

The photon excitation ($\hbar\omega$) lifts the electrons from the valence band to the conduction band, and thus electron-hole pairs are generated after energy relaxation. One electron and one hole can be bound to form a neutral exciton (X) with a binding energy E_b, which reduces the total energy of the electron-hole pair. Based on the semi-classical Bohr model, the exciton binding energy can be written as

$$E_b(n) = \frac{1}{8\pi\varepsilon_0\varepsilon_r} \frac{e^2}{a_{B,eff}(n)}, \text{ with } a_{B,eff}(n) = n^2 \frac{4\pi\varepsilon_0\varepsilon_r\hbar^2}{m_{EX}e^2}, \tag{2-51}$$

in which ε_0 is the vacuum dielectric constant, ε_r is the dielectric permittivity, e is the electron charge and n is an integer for the level of the exciton state. The effective Bohr radius is denoted as $a_{B,eff}(n)$, in which m_{EX} is the reduced mass for the exciton. It is described by $m_{EX}^{-1} = m_{eff\text{-}e\text{-}xy}^{-1} + m_{eff\text{-}h\text{-}xy}^{-1}$, where $m_{eff\text{-}e\text{-}xy}$ and $m_{eff\text{-}h\text{-}xy}$ are the in-plane effective mass of the electron and the hole, respectively. The formation possibility of the exciton state ($n = 1$) is generally much larger than the other states ($n > 1$), therefore the photoluminescence is dominated by the recombination of excitons with n = 1. For

excitons (n =1) in bulk CdTe system, $E_b \approx 10.5$ meV and $a_{B,eff} \approx 7.6$ nm have been experimentally determined [118, 119]. In the QW system, the strong spatial confinement could enhance the electron-hole interaction to give rise to higher binding energy than the value in bulk system [120, 121]. In (Cd, Mn)Te/(Cd, Mg)Te heterostructures, the PL intensity from the light-hole excitons was observed much weaker than PL intensity of heavy-hole excitons [109].

Further, if the sample is doped, a charged exciton (trion) can be formed [122]. For instance, in the case of *n*-type doping, negatively charged trions (X^-) composed of two electrons and one hole can be generated [123], while for p-type doping, the positively charge trion (X^+) is obtained [124]. For CdTe-based systems, these two types of trions have been both clearly observed in quantum structures in the past two decades [123, 124]. The trion binding energy is typically larger than the neutral exciton by a few meV. Usually the trion PL intensity is higher than neutral excitons at liquid helium temperature [125].

2.3.2 Magnetic properties of a DMS QW in a static magnetic field

In II-VI DMS systems like $Cd_{1-x}Mn_xTe$ alloys, the magnetic atoms (Mn) occupy randomly the cation positions (Cd), and thus the outer $4s^2$ electrons contribute to the interatomic binding with the anions (Te). The manganese atoms then function as ionic centers, i.e. Mn^{2+} ions, which have the $3d^5$ electronic shell configuration.

According to the Hund rules, all the five 3d-electron spins are aligned parallel to occupy the lowest energetic state [6]. Therefore the orbital spin is $L = 0$, and the effective spin of one Mn^{2+} ion is $S = 5/2$. The Mn ions can be expected to be relatively clean localized magnetic centers, since the spin-orbit coupling between the Mn ions and the static/dynamic crystal field is rather small in a perfect solid crystal [108]. For an isolated Mn^{2+} ion, the ground spin state is of six-fold degeneracy, in which the spin components are S_z = -5/2, -3/2, ..., +5/2 along an arbitrary defined *z*-axis direction. The excited states contain one or more electron spins antiparallel to the ground state, e.g., it requires 2.2 eV of energy to flip one electron spin. For optical excitation below this energy level, the Mn^{2+} ion spin can be regarded always in the ground state.

- **Magnetization of Mn ions in a DMS**

The magnetic system is described by a macroscopic magnetization ***M***, which could be treated as the mean value of the spin $<S_z>$ averaged over all the Mn^{2+} ions in the thermal equilibrium state. In a magnetic field ***B***$_{ext}$ which is defined along the z-axis direction, the degeneracy of the six-fold Mn^{2+} ion spin states is removed, and the energetic sublevels are equally separated by the Zeeman energy splitting [44]. For a $Cd_{1-x}Mn_xTe$ DMS sample, the equilibrium magnetization of Mn^{2+} ions can be written as

$$M(B_{ext}, T_{bath}) = -g_{Mn}\mu_B N_0 x < S_z >, \qquad (2-52)$$

in which g_{Mn} is the Lande g factor of the Mn ion, μ_B is the Bohr magneton, N_0 is the number of crystalline elementary cells per unit volume, and T_{bath} is the sample temperature. For a system of isolated Mn ions which are treated as paramagnetic centers, e.g. in extremely diluted case with $x <<$ 0.01 [44], the average spin $<S_z>$ can be expressed by the Brillouin function

$$< S_z >= -\frac{5}{2} B_{5/2}(\frac{5}{2} \frac{g_{Mn}\mu_B B_{ext}}{k_B T_{bath}}) \quad \text{with}$$

$$B_J(q) = \frac{2J+1}{2J} \coth(\frac{2J+1}{2J} q) - \frac{1}{2J} \coth(\frac{1}{2J} q) \tag{2-53}$$

in which k_B is the Boltzmann constant, and $B_J(q)$ is the Brillouin function of Jth order. For the Mn^{2+} ion spin, J is equal to 5/2. In the regime of a higher Mn concentration, the Mn ions cannot be treated as isolated anymore, since the d-d exchange interaction can couple neighbouring Mn ions with each other. The d-d interaction is antiferromagnetic, from which the mean spin $<S_z>$ is expected to become less. In the range of liquid helium temperature, Mn concentration ($x < 0.67$) and $B_{ext} < 5$ T, the magnetization can be described by a modified Brillouin function [121, 126]

$$M(B_{ext}, T_{bath}) = -g_{Mn}\mu_B N_0 x < S_z >= \frac{5}{2} g_{Mn}\mu_B N_0 x_{eff} B_{5/2}\left(\frac{5}{2} \frac{g_{Mn}\mu_B B_{ext}}{k_B(T_{bath}+T_0)}\right)$$

$$< S_z >= -S_{eff} B_{5/2}\left(\frac{5}{2} \frac{g_{Mn}\mu_B B_{ext}}{k_B(T_{bath}+T_0)}\right) \tag{2-54}$$

Here x_{eff} is the effective Mn concentration, and the effective Mn spin temperature is $T_{eff} = T_{bath} + T_0$. A smaller value than x is expected for x_{eff} due to formation of Mn clusters [44, 127], e.g. Mn ion pairs, Mn ion triangles and so on, in which the Zeeman interaction is suppressed by the much stronger d-d interaction and thus contribute less spin polarization. As a result, the saturated mean spin is less than 5/2, and it is denoted as an effective Mn^{2+} ion spin $S_{eff} = 5/2 \cdot x_{eff}/x$. The antiferromagnetic d-d interaction makes the Mn ions have a higher spin temperature than the sample temperature by T_0 (with a positive value). Based on Monte Carlo simulations [127] and experiment investigations [121], empirical formulae can be given to describe experimental data for the bulk $Cd_{1-x}Mn_xTe$ system as

$$S_{eff}(x) = 0.0179 + 0.653 \cdot e^{-43.35x} + 1.807 \cdot e^{-6.192x}$$

$$T_0 = \frac{35.37 \cdot x}{1+2.752 \cdot x} \tag{2-55}$$

Their dependence of the Mn concentration is depicted in FIG 2.3-3. Monotonically the effective spin decreases with increasing the Mn concentration and the spin temperature parameter T_0 increases, both of which basically originate from enhanced d-d exchange interaction for higher Mn contents.

For the $Cd_{1-x}Mn_xTe$ QW structures, the spectroscopic measurements [109, 120, 128, 129] generally show deviations from the empirical formula given above. The effective Mn^{2+} ion spin deviates by a small fraction , while the temperature parameter T_0 differs by factor a two or so [129].
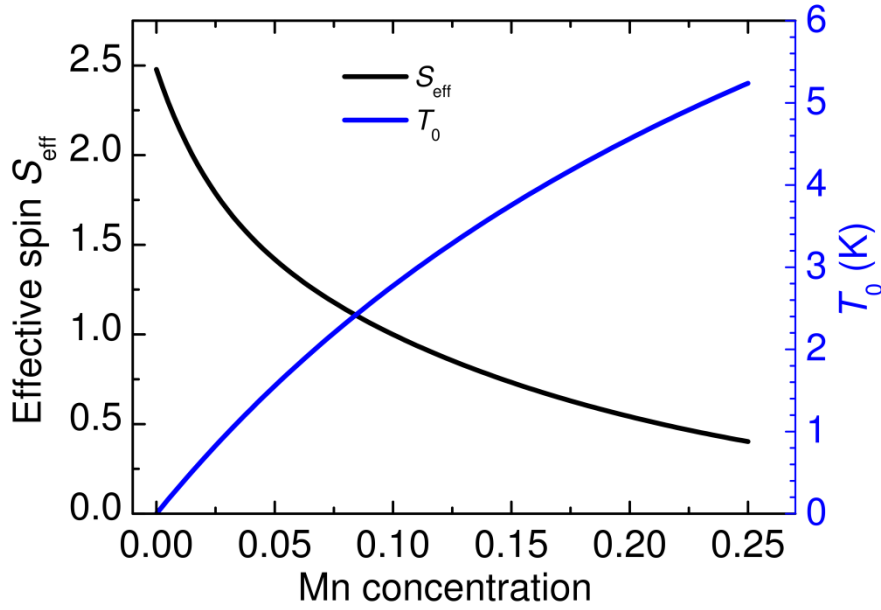
FIG 2.3-3: Calculated effective spin S_{eff} (black line) and T_0 (blue line) versus the Mn concentration in a bulk $Cd_{1-x}Mn_xTe$ system. The plotting is from Equation (2.55) with experimental data from Ref. [121].

Concerning the d-d exchange interaction between Mn ions, it is described by the Heisenberg spin Hamiltonian [130, 131]

$$\hat{H}_{\text{d-d}} = -\sum_{i \neq j} J^{dd}(\boldsymbol{R}_{ij})\hat{S}_i \cdot \hat{S}_j \tag{2-56}$$

Thereby $\hat{S}_i$ and $\hat{S}_j$ are the spin operators for the two Mn ions located at $\boldsymbol{R}_i$ and $\boldsymbol{R}_j$, respectively. $J^{dd}(\boldsymbol{R}_{ij})$ is the exchange interaction constant. The exchange processes are categorized into three types [107]: two-hole processes, one-hole-one-electron, and two-electron processes. The two-hole processes known as superexchange mechanism is the dominant one with a contribution of ~95% to the whole $H_{\text{d-d}}$. The one-hole-one-electron processes, i.e. the Bloembergen-Rowland interaction and the Ruderman-Kittel-Kasuya-Yosida (RKKY) interaction, account for only ~5%, while the two-electron processes are negligible.

The exchange interaction decreases strongly with increasing distance between Mn ions. It has been demonstrated both the nearest-neighbor exchange process (described by J_{NN}) and the next-nearest-neighbor exchange process (described by J_{NNN}) are antiferromagnetic, and thus $H_{\text{d-d}}$ gives antiferromagnetic coupling as a whole. Typically, J_{NN} is approximately five times larger than J_{NNN}. In a $Cd_{1-x}Mn_xTe$ DMS system, J_{NN} was experimentally determined about -0.54 meV [132], and $J_{NNN} \sim$ -0.095 meV [133].

- *sp-d* **exchange interaction**

The prominent magnetic properties in a DMS [44, 107], e.g. the giant magneto-optic rotation and the giant Zeeman effect, originate from the exchange interaction between the Mn ions and carriers, i.e. *s-d* exchange interaction between Mn ions and *s*-like electrons (conduction band Γ_6), and *p-d*

exchange interaction between Mn ions and *p*-like electrons (valence band Γ_7 and Γ_8). The Hamiltonian can be described as

$$\hat{H}_{ex}^{\ s,p-d} = \sum_{\boldsymbol{R}_i} J^{s,p-d}(\boldsymbol{r} - \boldsymbol{R}_i) \hat{\boldsymbol{S}}_i \cdot \hat{\boldsymbol{s}},$$ (2-57)

Here $\boldsymbol{R}_i$ is the location of the *ith* Mn ion, and $\boldsymbol{r}$ is the electron coordinate. $\hat{\boldsymbol{S}}_i$ is the Mn^{2+} ion spin operator, $\hat{\boldsymbol{s}}$ is the electron spin operator. The *sp-d* exchange interaction constant is denoted as $J^{s,p-d}(\boldsymbol{r} - \boldsymbol{R}_i)$. Since the electronic wavefunction spans over a large number of lattice sites which are partly occupied by Mn ions with a concentration x, the summation can be treated in terms of the virtual crystal field approximation. The item $J^{s,p-d}(\boldsymbol{r} - \boldsymbol{R}_i)$ can be replaced by $xJ^{s,p-d}(\boldsymbol{r} - \boldsymbol{R})$, where $\boldsymbol{R}$ is each lattice site in the crystal. Further, the mean Mn^{2+} ion spin $<S_z>$ is used to replace the spin over all the Mn sites and the contribution from the electron spin is the z-component s_j. With these assumptions, the *sp-d* exchange interaction can be simplified as

$$H_{ex}^{\ s,p-d} = x \langle S_z \rangle s_j \sum_{\boldsymbol{R}} J^{s,p-d}(\boldsymbol{r} - \boldsymbol{R})$$
$$= -N_0 I^{s,p-d} x \langle S_z \rangle s_j$$ (2-58)

Here $I^{s,p-d}$ is the integral for *s-d* or *p-d* exchange interaction, which are conventionally denoted as α and $\beta/3$, respectively. In the $Cd_{1-x}Mn_xTe$ DMS system, it has been experimentally determined $N_0\alpha = 0.22$ eV and $N_0\beta = -0.88$ eV. Therefore the coupling between Mn ions and electrons of the conduction band is ferromagnetic while it is antiferromagnetic for the electron of the valence band.

The different coupling types and strengths are raised from the origin of each exchange interaction between the band electrons and $3d^5$ electrons of Mn ions [107, 134]. There are two competing exchange effects. A positive contribution is from the Coulomb exchange interaction, which favors aligning the electron spin parallel to the Mn^{2+} ion spin, and thus it gives the ferromagnetic coupling. A negative source is due to the hybridization of the $3d^5$ electrons with the band electrons. The *s-d* hybridization between the electrons of the conduction band and the Mn ions is forbidden by considering the *s*-type electron wavefunction symmetry, while *p-d* hybridization between the electrons of the valence band and the Mn ions is allowed to contribute a strong and dominant negative contribution as antiferromagnetic coupling. As a whole, the *s-d* exchange interaction gives a positive integral value and the *p-d* exchange interaction a negative value.

Using Equation (2.58), the change of the energy level for each subband can be explicitly expressed. For the Γ_6 conduction band, it gives

$$E_{\Gamma_6} = -m_s N_0 \alpha \cdot x \langle S_z \rangle, \text{with } m_s = \pm \frac{1}{2}$$ (2-59)

For the Γ_8 valence band, it gives

$$E_{\Gamma_8} = -\frac{N_0 \beta}{3} m_j \cdot x \langle S_z \rangle, \text{with } m_j = \pm \frac{3}{2}(\text{HH}), m_j = \pm \frac{1}{2}(\text{LH}),$$ (2-60)

in which the heavy-hole and the light-hole subband are respectively clarified by HH and LH.

- **Giant Zeeman splitting in a DMS**

As a consequence of the *sp-d* exchange interaction, the carriers (electrons or hole) manifest quite abnormal effects in a DMS system compared with nonmagnetic counterparts. The Mn ions are magnetized in a magnetic field, and via *sp-d* exchange interaction, the band structure is greatly modified as indicated by Equations (2.59) and (2.60). Consider the two conduction subbands, the energy levels are

$$E_l(m_s = +\frac{1}{2}) = E_g + (l+\frac{1}{2})\hbar\omega_c + \frac{1}{2}(g_e\mu_B B_{ext} - N_0\alpha \cdot x\langle S_z\rangle)$$
$$E_l(m_s = -\frac{1}{2}) = E_g + (l+\frac{1}{2})\hbar\omega_c - \frac{1}{2}(g_e\mu_B B_{ext} - N_0\alpha \cdot x\langle S_z\rangle)$$

(2-61)

Hereby *l* indicates the *l*th Landau energy level in presence of the external field B_{ext}, ω_c is the cyclotron frequency and g_e is the electron Lande *g* factor. The last term is spin dependent, with a sum of the electron Zeeman energy induced by B_{ext} and the energy shift caused by the exchange interaction with Mn ions. The energy splitting between these two spin sublevels is

$$\Delta E_{\Gamma 6} = E_l(m_s = +\frac{1}{2}) - E_l(m_s = -\frac{1}{2})$$
$$= g_e\mu_B B_{ext} - N_0\alpha \cdot x\langle S_z\rangle = g_{eff-e}\mu_B B_{ext}$$

(2-62)

Here g_{eff-e} is the effective Lande *g* factor of the electron. From Equation (2.61) and (2.62), it is obtained

$$g_{eff-e} = g_e - N_0\alpha \cdot x\langle S_z\rangle/(\mu_B B_{ext}) = g_e + \frac{N_0\alpha \cdot xS_{eff}}{\mu_B B_{ext}}B_{5/2}(q), \text{with } q = \frac{5}{2}\frac{g_{Mn}\mu_B B_{ext}}{k_B(T_{bath}+T_0)}$$

(2-63)

In the regime of a weak magnetic field, i.e. $q << 1$, the Brillouin function can be approximated [107]

$$B_{5/2}\left(\frac{5}{2}\frac{g_{Mn}\mu_B B_{ext}}{k_B(T_{bath}+T_0)}\right) \approx \frac{7}{6}\frac{g_{Mn}\mu_B B_{ext}}{k_B(T_{bath}+T_0)}$$

(2-64)

In this case, the effective Lande *g* factor can be simplified as

$$g_{eff-e} = g_e + \frac{7}{6}\frac{g_{Mn}N_0\alpha \cdot xS_{eff}}{k_B(T_{bath}+T_0)},$$

(2-65)

which is field independent. By using the relations in Equation (2.55) for a $Cd_{1-x}Mn_xTe$ system, $g_{Mn} \approx$ 2 [44], $g_e \sim$ -1 [135] and $T_{bath} = 5$ K, the effective electron *g* factor is calculated, as presented in FIG 2.3-4 (black line). Generally it is larger than the electron factor by one order of magnitude,[1] and it has a positive sign due to the *s-d* ferromagnetic coupling. The maximum value happens at the Mn concentration of $x \sim 0.1$.

---

[1] The calculationns in FIG 2.3-4 give upper limits for the effective *g* factor. In the low field regime, the local Mn^{2+} ion anisotropic spin interaction such as hyperfine interaction and spin-lattice coupling induced by strain or local crystal field, and magnetic fluctuations can depolarize the magnetization of the Mn ions. As a result, the *sp-d* exchange interaction is reduced giving a smaller effective g factor for electrons and holes.

Similarly the energy splitting between spin sublevels in the HH valence band is

$$\Delta E_{\Gamma 8\text{-HH}} = g_{\text{HHe}}\mu_B B_{\text{ext}} - N_0\beta \cdot x\langle S_z\rangle = g_{\text{eff-HHe}}\mu_B B_{\text{ext}} \tag{2-66}$$

Hereby, g_{HHe} denotes the electron g factor in the HH valence band, and $g_{\text{eff-HHe}}$ the effective electron g factor. Because the corresponding hole spin always takes an opposite sign with the electron spin of the valence band, the effective Lande g factor of the heavy hole in the low field regime is

$$g_{\text{eff}-hh} = -g_{\text{eff-HHe}} = g_{hh} - \frac{7}{6}\frac{g_{\text{Mn}}N_0\beta \cdot xS_{\text{eff}}}{k_B(T_{\text{bath}}+T_0)} \tag{2-67}$$

Again by using parameters above except $g_{hh} \sim 0$, the effective hole g factor is calculated as presented in FIG 2.3-4 (blue line). It has a larger magnitude than the electron by a factor of about four. The maximum value happens at a same Mn concentration as for the case of the electron.

Since the carrier g factor values are typically smaller by orders of magnitude than the effective g factors, they could be neglected as an approximation in most cases.

Similar calculations and approximations can be made for the LH valence band. As a summary, the energy splitting in between each subband can be written as

$$\Delta E_{\Gamma 6} \approx -N_0\alpha \cdot x\langle S_z\rangle$$
$$\Delta E_{\Gamma 8\text{-HH}} \approx -N_0\beta \cdot x\langle S_z\rangle \tag{2-68}$$
$$\Delta E_{\Gamma 8\text{-LH}} \approx -\frac{N_0\beta}{3} \cdot x\langle S_z\rangle$$

The effective g factor of the electron, the heavy hole and the light hole can be approximated as

$$g_{\text{eff}-e} = \frac{7}{6}\frac{g_{\text{Mn}}N_0\alpha \cdot xS_{\text{eff}}}{k_B(T_{\text{bath}}+T_0)}$$
$$g_{\text{eff}-hh} \approx -\frac{7}{6}\frac{g_{\text{Mn}}N_0\beta \cdot xS_{\text{eff}}}{k_B(T_{\text{bath}}+T_0)} \tag{2-69}$$
$$g_{\text{eff}-lh} \approx -\frac{7}{18}\frac{g_{\text{Mn}}N_0\beta \cdot xS_{\text{eff}}}{k_B(T_{\text{bath}}+T_0)}$$
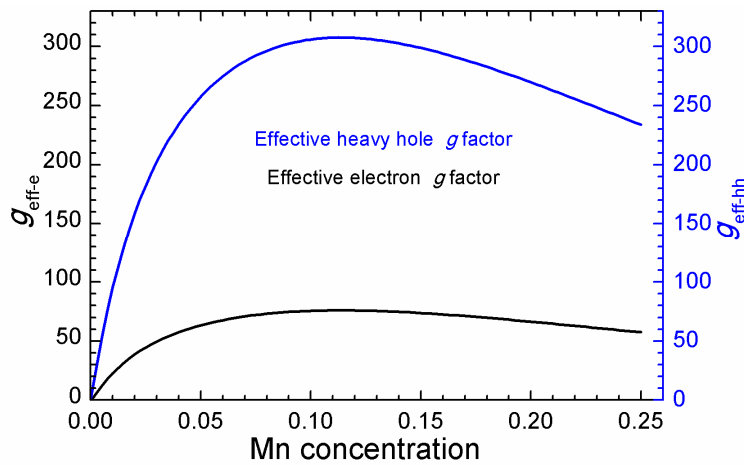

,

FIG 2.3-4: Calculated effective g factor of the electron (black line) and effective g factor of the heavy hole (blue line) versus the Mn concentration in a $Cd_{1-x}Mn_xTe$ system. The sample temperature $T_{\text{bath}} = 5$ K is used.

The energy band structure of the conduction band and the valence band at the Γ point is presented in FIG 2.3-5. Due to the positive effective g factor for the electron, the spin state of $m_s = -1/2$ is in the lower energy level in the Γ_6 band. On the contrary, the electron spin state of $m_j = -3/2$ occupies the highest energy level in the Γ_8 band as a result of its negative effective g factor (to note, the corresponding hole spin is: $m_h = +3/2$, and the effective g factor of the heavy hole is positive).
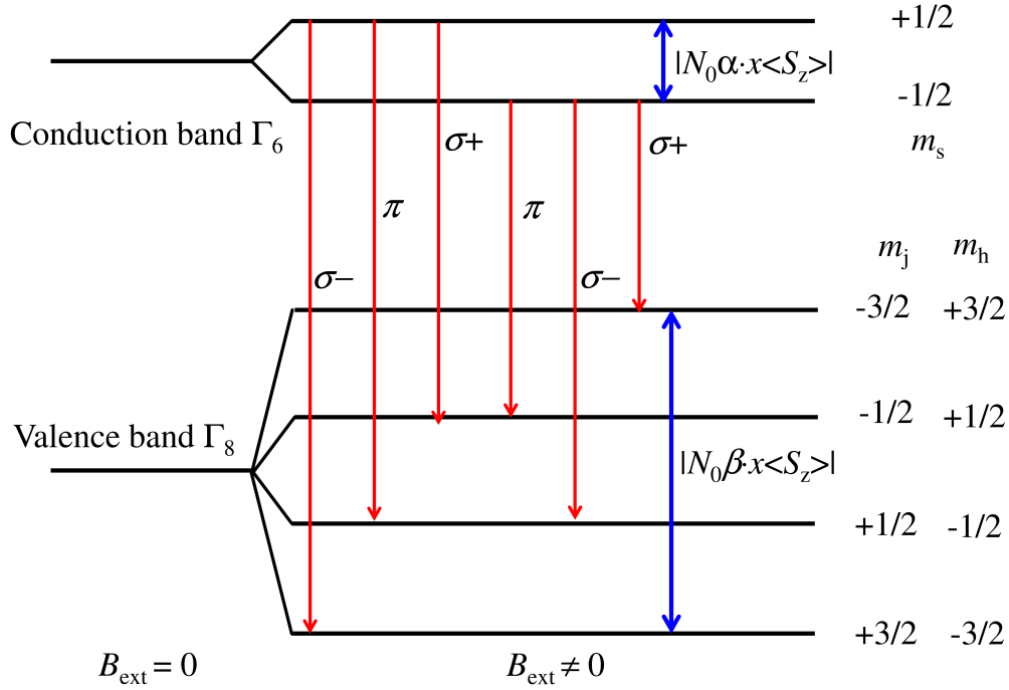

FIG 2.3-5: Energy band structure manifesting giant Zeeman energy splitting as a result of *sp-d* exchange interaction. The blue arrow indicates the maximum energy splitting within each band. The red arrows indicate the optical transitions from the conduction band to the valence band. The polarization of the optical emission is marked for each transition process.

Spin states			Optical polarization	Energy (relative to zero field position)	Relative transition strength
m_s	m_j	(m_h)			
+1/2	+3/2	(-3/2)	σ^-	$-1/2 \cdot N_0(\alpha - \beta) \cdot x \langle S_z \rangle$	3
+1/2	+1/2	(-1/2)	π	$-1/2 \cdot N_0(\alpha - \beta/3) \cdot x \langle S_z \rangle$	2
+1/2	-1/2	(+1/2)	σ^+	$-1/2 \cdot N_0(\alpha + \beta/3) \cdot x \langle S_z \rangle$	1
-1/2	+1/2	(-1/2)	σ^-	$+1/2 \cdot N_0(\alpha + \beta/3) \cdot x \langle S_z \rangle$	1
-1/2	-1/2	(+1/2)	π	$+1/2 \cdot N_0(\alpha - \beta/3) \cdot x \langle S_z \rangle$	2
-1/2	-3/2	(+3/2)	σ^+	$+1/2 \cdot N_0(\alpha - \beta) \cdot x \langle S_z \rangle$	3

Table 2-2: Transition energy and strength for each process marked in FIG 2.3-5. To note, $\langle S_z \rangle$ is negative.

Assisted by one photon emission, one electron can transit from the conduction band to the valence band.[2] According to the optical selection rules $|m_s - m_j| = 0$ or 1, the polarization of the optical

---

[2] The reversed process can be done via one photon absorption. The relevant parameters are the same as in Table 2.2.

emission is marked along each transition process. The photon with helicity of +1 is denoted as σ^+ namely right-circularly polarized; the photon with helicity of -1 is denoted as σ^- namely left-circularly polarized; and the photon with helicity of 0 is denoted as π namely linear-circularly polarized. The transition energy and strength is summarized [44] and presented in Table 2-2.

- **Photoluminescence polarization in a DMS QW**

Due to the giant Zeeman energy splitting in a DMS system, appreciable carrier spin polarization is generated even in a weak magnetic field. For photon-excited carriers in a DMS structure, if carrier spin relaxation process is fast enough so that carriers get polarize before their annihilations, a polarized PL emission is expected resulting from recombination of spin-polarized carriers. The carrier spin relaxation arising from *sp-d* exchange interaction is very fast with a time constant of $\tau_s \sim$ 1 ps [136], while the exciton lifetime τ_{exc} is generally much longer, e.g. $\tau_{exc} \sim$ 100 ps for a $Cd_{1-x}Mn_xTe$ QW structure at liquid helium temperature [125]. In the studied $Cd_{1-x}Mn_xTe$ QW, since the PL intensity from the heavy-hole excitons is dominant over the light-hole excitons, the PL polarization degree is considered here only for the previous one.

The PL discussed here is from the bright excitons. First, the PL polarization is considered for the heavy-hole neutral excitons. A schematic description is given in FIG 2.3-6 in the exciton picture. The PL polarization degree is defined as

$$\rho_{PL} = \frac{I^{\sigma^+} - I^{\sigma^-}}{I^{\sigma^+} + I^{\sigma^-}}, \qquad (2\text{-}70)$$

where I^{σ^+} and I^{σ^-} are the intensity values of the σ^+- polarized and σ^-- polarized photoluminescence, respectively.
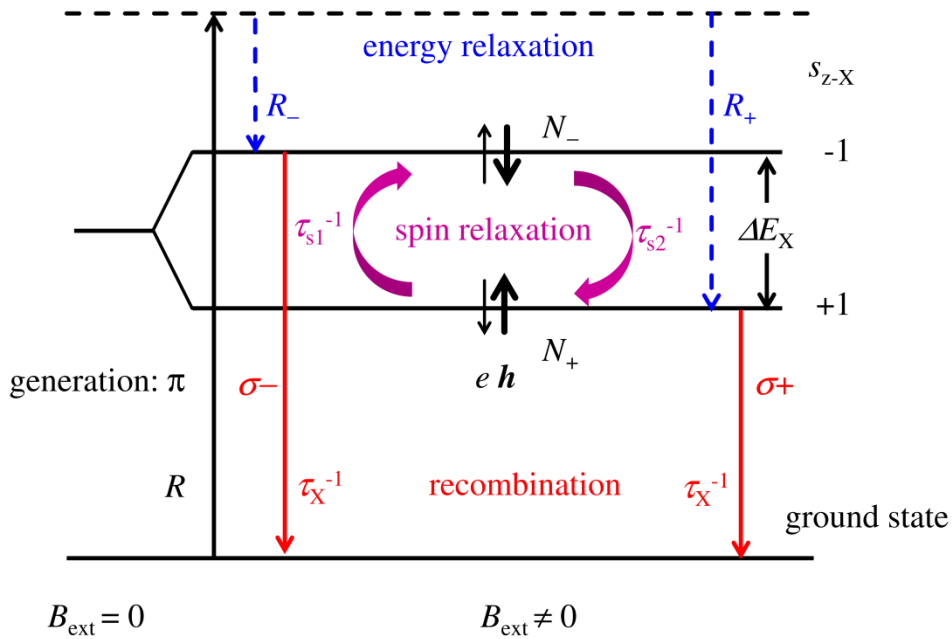

FIG 2.3-6: Schematic description of the PL polarization from the neutral excitons (*X*). The energy splitting between the exciton subbands is ΔE_X. After the exciton recombination, there is no carrier left.

The electron-hole pairs are optically generated by a linearly-polarized (π) excitation with the generation rate as R. The excitation is typically on a non-resonant energy level, and thus the carriers and excitons undergo energy relaxation processes which are treated as a whole energy relaxation process in this work [117]. It is assumed the formation time constant is the same for the exciton with a total spin of -1 and the exciton with a total spin of +1. The previous is denoted as $X(-1)$ and $X(+1)$ for the latter. The exciton spin is defined as the sum of the electron spin (e, the thin arrow) and the hole spin (h, the thick arrow). Since the energy relaxation can be approximated as spin-independent for the studied sample, the generation rate R_- for exciton $X(-1)$ is treated as equal to the generation rate R_+ for exciton $X(+1)$, i.e. $R_+ = R_- = R/2$. As well, the lifetime of $X(-1)$ and $X(+1)$ are also treated as same here, and it is denoted as τ_X which is in the order of several 100 ps.

Before the exciton recombination, the excitons relax into a dynamical equilibrium state. The relaxation channel is dominated by the sp-d exchange interaction in the DMS system, and the spin relaxation time is expected to be a few picoseconds for the non-resonant excitation [136]. The relaxation rate from $X(+1)$ to $X(-1)$ is τ_{s1}^{-1}, and it is τ_{s2}^{-1} for the reverse process. Suppose the Zeeman energy splitting between $X(+1)$ and $X(-1)$ is ΔE_X. Then it is obtained $\tau_{s1}^{-1}/\tau_{s2}^{-1} = \exp(-\Delta E_X/k_B T_X)$ by considering the Boltzmann factor in the thermodynamic equilibrium at the temperature T_X which is the effective exciton temperature. The population of $X(+1)$ and $X(-1)$ exciton is respectively described by $N_+(t)$ and $N_-(t)$ at the time t. The rate equation is written as

$$\frac{dN_+(t)}{dt} = R_+ - \frac{N_+(t)}{\tau_X} + \frac{N_-(t)}{\tau_{s2}} - \frac{N_+(t)}{\tau_{s1}}$$
$$\frac{dN_-(t)}{dt} = R_- - \frac{N_-(t)}{\tau_X} + \frac{N_+(t)}{\tau_{s1}} - \frac{N_-(t)}{\tau_{s2}} \tag{2-71}$$

In the dynamic equilibrium state, i.e. $dN_+(t)/dt = dN_-(t)/dt = 0$, it is obtained

$$\frac{N_+}{N_-} = \frac{\dfrac{R_+}{R_-}\dfrac{\tau_{s1}}{\tau_X} + \left(1+\dfrac{R_+}{R_-}\right)\dfrac{\tau_{s1}}{\tau_{s2}}}{\dfrac{\tau_{s1}}{\tau_X} + \left(1+\dfrac{R_+}{R_-}\right)} \tag{2-72}$$

The PL intensity after exciton recombination is directly proportional to the exciton number in the dynamic equilibriums state, i.e. $I^{\sigma+} \propto N_+$ and $I^{\sigma-} \propto N_-$. The PL polarization degree of the neutral excitons in Equation (2.70) is rewritten as

$$\rho_{PLX} = \rho_X = \frac{N_+ - N_-}{N_+ + N_-} = \frac{\left(\dfrac{R_+}{R_-}-1\right)\dfrac{\tau_{s1}}{\tau_X} + \left(1+\dfrac{R_+}{R_-}\right)\left(\dfrac{\tau_{s1}}{\tau_{s2}}-1\right)}{\left(\dfrac{R_+}{R_-}+1\right)\dfrac{\tau_{s1}}{\tau_X} + \left(1+\dfrac{R_+}{R_-}\right)\left(\dfrac{\tau_{s1}}{\tau_{s2}}+1\right)} \tag{2-73}$$

For the neutral excitons, using the facts: $R_+ = R_-$ and $\tau_{s1}^{-1}/\tau_{s2}^{-1} = \exp(-\Delta E_X/k_b T_X)$, the equation above is simplified

$$\rho_{PLX} = \frac{1 - \dfrac{\tau_{s2}}{\tau_{s1}}}{\dfrac{\tau_{s2}}{\tau_X} + \left(1 + \dfrac{\tau_{s2}}{\tau_{s1}}\right)} = \frac{1}{1 + \tau_s / \tau_X} \rho_{0X},$$

(2-74)

$$\text{with } \tau_s = \frac{\tau_{s1}\tau_{s2}}{\tau_{s1} + \tau_{s2}} \text{ and } \rho_{0X} = \frac{e^{\Delta E_X/2k_B T_X} - e^{-\Delta E_X/2k_B T_X}}{e^{\Delta E_X/2k_B T_X} + e^{-\Delta E_X/2k_B T_X}} = \tanh\left(\frac{\Delta E_X}{2k_B T_X}\right)$$

Hereby, ρ_{0X} is regarded as the PL polarization if the exciton lifetime is infinite $\tau_X \to \infty$, and τ_s is the spin relaxation time for establishing the dynamic equilibrium between the two subbands. Therefore the factor τ_s/τ_X determines the actual saturation level of the PL polarization degree, which gains larger values for faster spin relaxation. Due to the fact $\tau_s \ll \tau_X$, the PL polarization is also a reflection of the exciton temperature T_X, which reflects the energy relaxation process.

Further, by checking the optical transition energy listed in Table 2-2, it could be found the exciton energy splitting is

$$\Delta E_X = -N_0(\alpha - \beta) \cdot x < S_z >$$

(2-75)

To note, the leakage of the wavefunction into the non-magnetic barrier should be taken in account for a QW structure. The full expression of (2.75) is $\Delta E_x = -N_0(\delta_e \alpha - \delta_h \beta) \cdot x < S_z >$, in which δ_e and δ_h are respectively the probability of the electron and the hole confined in the QW. In a typical (Cd,Mn)Te/(Cd,Mg)Te heterostructure, $\delta_e \approx \delta_h \approx 0.98$ [63]. They are both approximated as unity in a general case. Also, the magnetic fluctuation is here neglected, e.g. see Ref. [137]. Therefore the PL polarization described by Equation (2.74) is thus an upper limit value

The pronounced energy splitting due to sp-d exchange interaction is a result of the Mn^{2+} ion spin polarization $<S_z>$. The relation between the PL polarization and the Mn^{2+} ion spin polarization can be expressed as

$$\rho_{0X} = \tanh\left(-\frac{N_0(\alpha - \beta) \cdot x}{2k_B T_X} < S_z >\right)$$

(2-76)

Clearly, the PL polarization is a direct consequence of the spin polarization of Mn^{2+} ions, or the magnetization of the Mn ions by taking into account Equation (2.52).

In the low field regime for weak magnetization of Mn ions, e.g. $B_{ext} \sim 100$ mT, by considering Equation (2.62), (2.66) and (2.68), the exciton energy splitting can be represented in terms of the effective carrier g factor

$$\Delta E_X \approx \Delta E_{\Gamma 6} + \Delta E_{\Gamma 8\text{-HH}} \approx \left(g_{\text{eff-e}} + g_{\text{eff-hh}}\right)\mu_B B_{ext}$$

(2-77)

It can be seen, the heavy-hole neutral exciton takes a giant effective g factor as

$$g_{\text{eff-hhX}} = g_{\text{eff-e}} + g_{\text{eff-hh}},$$

(2-78)

which is positive since the effective electron g factor and the effective hole *g* factor are both positive, e.g. see calculations in FIG 2.3-4. This large effective exciton *g* factor indicates pronounced PL polarization even at a weak magnetic field.

As a whole, by combining Equation (2.69) and (2.74), the PL polarization degree can be approximated as

$$\rho_{PLX} = \frac{1}{1+\tau_s/\tau_X} \tanh(\zeta), \text{with } \zeta = \frac{7}{12} \cdot \frac{g_{Mn}\mu_B B_{ext}}{k_B(T_{bath}+T_0)} \cdot \frac{xS_{eff}(N_0\alpha - N_0\beta)}{k_B T_X} \tag{2-79}$$

In an even weaker field regime where the exciton energy splitting is much less than the exciton thermal energy, e.g. $B_{ext} < 10$ mT, there is $\tanh(\zeta) \approx \zeta$. The PL polarization can be explicitly expressed as

$$\rho_{PLX} \approx \frac{7}{12} \cdot \frac{1}{1+\tau_s/\tau_X} \cdot \frac{g_{Mn}\mu_B B_{ext}}{k_B(T_{bath}+T_0)} \cdot \frac{xS_{eff}(N_0\alpha - N_0\beta)}{k_B T_X} \tag{2-80}$$

In order to make it more clear, Equation (2.80) can be rewritten from (2.76) as

$$\rho_{PLX} \approx -\frac{1}{1+\tau_s/\tau_X} \frac{N_0(\alpha-\beta)\cdot x}{2k_B T_X} <S_z>, \text{with } <S_z> \approx -\frac{7}{6} \cdot S_{eff} \frac{g_{Mn}\mu_B B_{ext}}{k_B(T_{bath}+T_0)} \tag{2-81}$$

This indicates that the PL polarization is linearly proportional to the spin polarization of the Mn ions, i.e. $\rho_{PLX} \propto <S_z>$.

Again, since the exciton spin relaxation time is much shorter than the exciton lifetime as well the energy relaxation time, the dynamic PL polarization $\rho_{PL}(t)$ is determined the Mn^{2+} ion spin dynamics and the exciton effective temperature. It gives

$$\rho_{PLX}(t) \sim \frac{<S_z(t)>}{T_X(t)} \tag{2-82}$$

If the Mn^{2+} ion spin dynamics is much slower than the exciton energy relaxation, e.g. on the time scale above 100 ps, a mean and constant effective exciton temperature can be used. In this case, the exciton temperature can be regarded equal to the lattice temperature, i.e. $T_X(t) = T_{Latt}(t)$. The dynamic PL polarization directly represents Mn ion spin dynamics, i.e. magnetization dynamics of Mn ions, and the lattice temperature in the DMS system,

$$\rho_{PLX}(t) \sim <S_z(t)> \cdot T_{Latt}(t)^{-1} \sim M(B_{ext}, T_{Latt}, t) \cdot T_{Latt}(t)^{-1} \tag{2-83}$$

Now, the PL polarization from the positively charged exciton (or trion, X^+) is considered. One trion is a quasi-particle composed of one electron and two holes. The trions can appear in the *p*-type doped sample, in which there are pre-existing holes. A schematic presentation is given in FIG 2.3-7. This case is valid in the field regime[3] where the *p-d* exchange interaction energy is less than the exciton

---

[3] In the high field regime, the dissociation energy is suppressed by the *p-d* exchange interaction. The two holes can take a same spin. See Ref. [109, 138]

binding energy, so that the spins of both hole are always antiparallel. In addition, it is assumed that the density of the optically generated carriers is much less than the doping density of the holes, so the optical excitation negligibly affects the total carrier density.

The treatment is the same as for the neutral exciton. The denotations are similar, but with minor differences. One trion containing an electron with spin +1/2 is denoted as $X_+(+1/2)$, and $X_+(-1/2)$ means the trion with the electron spin -1/2. The dynamical populations are $N_{t-}(t)$ and $N_{t+}(t)$, respectively. The trion energy splitting at excited states is now ΔE_{exX+}, and the hole splitting is ΔE_{gsX+}. For the p-doping system, the population of the preexisting hole is N_1 for $m_h = +3/2$ on a higher energy level and N_2 for $m_h = -3/2$ on the lower (see FIG 2.3-5). The energy splitting between these subbands is denoted as ΔE_{hh}. By considering the Boltzmann statistics, the population relation is

$$N_1 / N_2 = e^{-\Delta E_{hh}/k_B T_{hh}} , \tag{2-84}$$

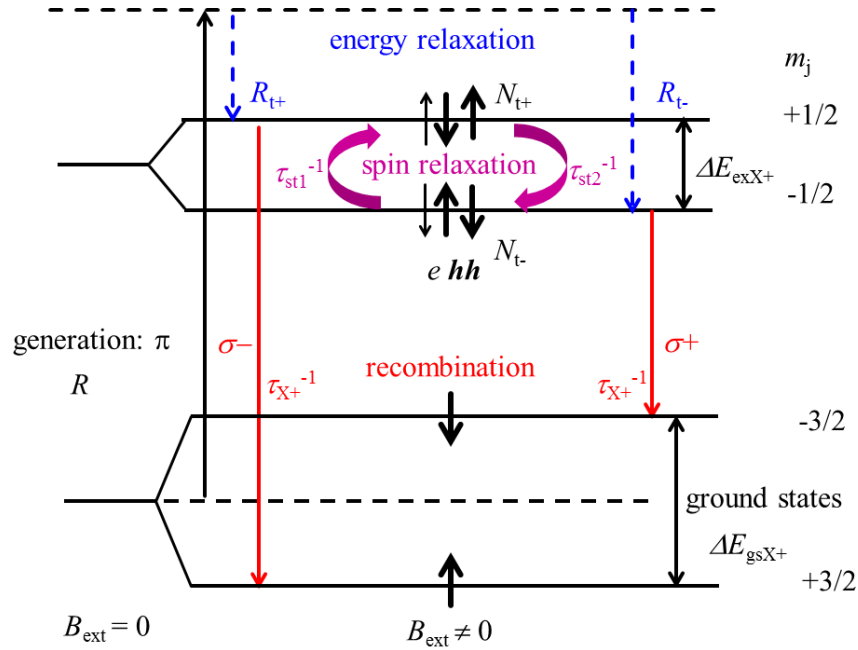where T_{hh} is the temperature for the holes.

FIG 2.3-7: Schematic description of the PL polarization from the positively charged excitons ($X+$). The energy splitting is ΔE_{exX+} at excited states and ΔE_{gsX+} at ground states. After one exciton recombination, there is one hole left.

After the annihilation of the trions, one hole is present compared with no left carrier for one neutral exciton. For the trion $X_+(+1/2)$, the hole with spin +3/2 remains after the exciton recombination. In the case of $X_+(-1/2)$, the remained hole is with spin -3/2. The lifetime of $X_+(+1/2)$ and $X_+(-1/2)$ are also treated as same here, and it is denoted as τ_{X+}.

The dynamics of trions is quite like the neutral exciton. A same rate equation of Equation (2.71) can be directly applied for the trions. Then the PL polarization can be similarly rewritten from Equation (2.73). By taking into account the probability distribution of the ground states [21], the trion PL polarization is obtained as

$$\rho_{\text{PLX}+} = \frac{N_{\text{t}-} - N_{\text{t}+}}{N_{\text{t}-} + N_{\text{t}+}} = \frac{\left(\dfrac{R_{\text{t}-}}{R_{\text{t}+}} - 1\right)\dfrac{\tau_{\text{st1}}}{\tau_{\text{X}+}} + \left(1 + \dfrac{R_{\text{t}-}}{R_{\text{t}+}}\right)\left(\dfrac{\tau_{\text{st1}}}{\tau_{\text{st2}}} - 1\right)}{\left(\dfrac{R_{\text{t}-}}{R_{\text{t}+}} + 1\right)\dfrac{\tau_{\text{st1}}}{\tau_{\text{X}+}} + \left(1 + \dfrac{R_{\text{t}-}}{R_{\text{t}+}}\right)\left(\dfrac{\tau_{\text{st1}}}{\tau_{\text{st2}}} + 1\right)} \tag{2-85}$$

Similarly the relation between τ_{st1}^{-1} and τ_{st2}^{-1} is given by $\tau_{\text{st1}}^{-1}/\tau_{\text{st2}}^{-1} = \exp(-\Delta E_{\text{X}+}/k_B T_{\text{X}+})$, in which $T_{\text{X}+}$ is the trion temperature and $\Delta E_{\text{X}+}$ is the energy splitting. Rather, the generation rate $R_{\text{t}+}$ of $X(+1/2)$ and $R_{\text{t}-}$ of $X(-1/2)$ are not equal anymore. It could be assumed the formation of a trion is a binding process between the optically generated electron-hole pairs and one pre-existing hole, i.e. $X(+1/2)$ is a consequence of the neutral exciton $X(-1)$ and a hole with spin $+3/2$, and $X(-1/2)$ is a consequence of $X(+1)$ and a hole with spin $-3/2$. Therefore it is approximated that the trion generation rate is proportional to the population of the hole which is needed to form the trion, i.e. $R_{\text{t}+} \propto N_1$ and $R_{\text{t}-} \propto N_2$. By considering Equation (2.84), it comes out

$$R_{\text{t}-} / R_{\text{t}+} = N_2 / N_1 = e^{\Delta E_{hh}/k_B T_{\text{hh}}} \tag{2-86}$$

The trion energy is determined by the optical transition summarized in Table 2-2. It could be seen that for PL of the same circular polarization, the transition energy is the same between $X+$ and X. The energy splitting between the discussed trion states is the same as the case of neutral excitons, and it gives

$$\Delta E_{\text{X}+} = \Delta E_{\text{exX}+} + \Delta E_{\text{gsX}+} = \Delta E_{\text{X}} \approx \Delta E_{\Gamma 6} + \Delta E_{\Gamma 8-\text{HH}} \approx \left(g_{\text{eff-e}} + g_{\text{eff-h h}}\right)\mu_B B_{\text{ext}} \tag{2-87}$$

Similar to the expression in (2.74), the X_+ PL polarization can be obtained

$$\rho_{\text{PLX}_+} = \frac{\rho_{0X_+} + \rho_{\text{hh}} \cdot \tau_{\text{st}} / \tau_{\text{X}_+}}{1 + \tau_{\text{st}} / \tau_{\text{X}_+}},$$

$$\text{with } \tau_{\text{st}} = \frac{\tau_{\text{st1}}\tau_{\text{st2}}}{\tau_{\text{st1}} + \tau_{\text{st2}}}, \ \rho_{0X_+} = \tanh\left(\frac{\Delta E_{\text{X}_+}}{2k_B T_{\text{X}_+}}\right) \text{ and } \rho_{\text{hh}} = \tanh\left(\frac{\Delta E_{\text{hh}}}{2k_B T_{\text{hh}}}\right) \tag{2-88}$$

Here the hole spin polarization is defined as $\rho_{\text{hh}} = (N_2 - N_1)/(N_2 + N_1)$. In the case of $\tau_{\text{st}} \ll \tau_{\text{X}+}$, the expression of $\rho_{\text{PLX}+}$ is the same as ρ_{PLX}, the neutral exciton polarization. As a result, the PL polarization from the trions represents the same information of the magnetic dynamics and the effective trion temperature. The relation in (2.82) and (2.83) can be validly applied for the trions as

$$\rho_{\text{PLX}_+}(t) \sim \frac{<S_z(t)>}{T_{\text{X}_+}(t)}$$

$$\rho_{\text{PLX}_+}(t) \sim \ <S_z(t)> \cdot T_{Latt}(t)^{-1} \ \sim M(B_{\text{ext}}, T_{Latt}, t) \cdot T_{Latt}(t)^{-1}, \text{ for } t > \tau_{\text{X}_+} \tag{2-89}$$

For a p-doped sample, the PL comes both from the neutral excitons and the trions. The energy of the latter is smaller than the previous by a few meV, which is within the PL spectral width of each.

For the PL measurement, although the detected PL polarization is a mixture of the neutral exciton polarization and the trion polarization, the magnetization and effective exciton (X/X_+) temperature are monitored in a same way. As a whole, it can be stated the PL polarization is a direct reflection of the magnetic ion spin relaxation and the exciton effective temperature

$$\rho_{\mathrm{PL}}(t) \sim \frac{<S_z(t)>}{T_{\mathrm{X},\mathrm{X}_+}(t)}$$

$$\rho_{\mathrm{PL}}(t) \sim \; <S_z(t)> \cdot T_{Latt}(t)^{-1} \; \sim M(B_{\mathrm{ext}}, T_{Latt}, t) \cdot T_{Latt}(t)^{-1}, \; \text{for} \; t > \tau_{\mathrm{X},\mathrm{X}_+}$$

(2-90)

Here ρ_{PL} is the PL polarization from both types of excitons.

3 EXPERIMENTAL TECHNIQUES

This chapter introduces techniques used in this thesis. A microstructure fabrication technology is established to provide an electrically switchable on-chip magnetic field, which is the novel and key technique throughout the whole thesis. This is done by a two-step electron beam lithography and lift-off technique. These two steps are for patterning electrical contact pads which provide electric connections to a voltage source and microcoils which generate magnetic fields, respectively. In the next part, the high-frequency electrical operation is demonstrated by adapting 50 ohm match for the sample and the cryostat. The electrical characterizations of the microstructures are presented. The on-chip magnetic field is put into applications for two types of spin-related experiments. To address the magnetization dynamics of Mn^{2+} ions in diluted magnetic semiconductor quantum wells, measurements of the time-resolved photoluminescence polarization degree are performed by means of magneto-luminescence spectroscopy, of which the working principle is given in the third part. In the last part, the time-resolved magneto-optical Kerr rotation technique is used to monitor the nuclear spin polarization and detect the nuclear magnetic resonance in a n-GaAs sample.

3.1 Microstructure fabrications on top of a semiconductor

There are two factors to obtain an electrically switchable on-chip magnetic field. On one hand metal microstructures with optimum geometry are designed to generate a magnetic field, of which the out-of-plane component is dominant. On the other hand, conductive pads are made to provide reliable electrical connections to external voltage sources.

To generate magnetic field dominant in out-of-plane direction, the coil-like geometry is utilized. A schematic description is given in FIG 3.1-1(a). The semiconductor cap layer thickness is typically several 10 nm. The structure dimension is on a micrometre length scale by considering optical access and metal-induced strain. Then for a current flow through the microcoil, the magnetic field is dominant in the out-of-plane direction while the in-plane field is negligible in the microcoil center. From the numerical simulation results shown in FIG 3.1-1(b), the z-component of current-induced magnetic field is ~10 mT for I = 120 mA in the coil center, while the x-component of current-induced magnetic field is almost negligible as presented in (c).

As a current can contribute Ohmic heating in the metal, resulting a local heating of the active semiconductor layer, microcoil structure geometry with neighbouring metal pads is used to dissipate excess heating for some used microcoils. To avoid possible deteriorations of the studied semiconductor optical properties (*e.g.* Chromium is quite diffusive, and makes poor optical properties by diffusion into semiconductors), the deposited metals are chosen as Gold (Au).

The other factor is to achieve electrical connections between the microcoil and an external voltage source. This is achieved by a wire-bonding technique between on-chip metal pads and external sample holder pads. To realise reliable wire-bonding, it normally demands strong adhesion between the on-chip bonding pads and semiconductors. The bonding pads are made of triple metal layers,

Chromium (Cr), Palladium (Pd) and Au in the sequence of deposition. These multi-layered pads demonstrate excellent adhesion properties on top of different semiconductors. Therefore it is used as the standard layer structure for wire-bonding in this work. By considering the complex impedance under high-frequency operation and the feasibility of performing wire bonding, the pad area is typically around $300 \times 300 \ \mu m^2$. The bonding pads connect the microcoil and the external sample holder pads, which are connected with SMA/SMB cables via thermal soldering.

Because the two kinds of structures mentioned above are made of different metal layers, the whole microstructure fabrications for one sample are divided into two steps. The first step deals with wire-bonding pads and marker definitions, and the second for microcoil structures. Each step is done by a standard microstructure protocol, based on electron beam lithography (EBL) and lift-off technique.
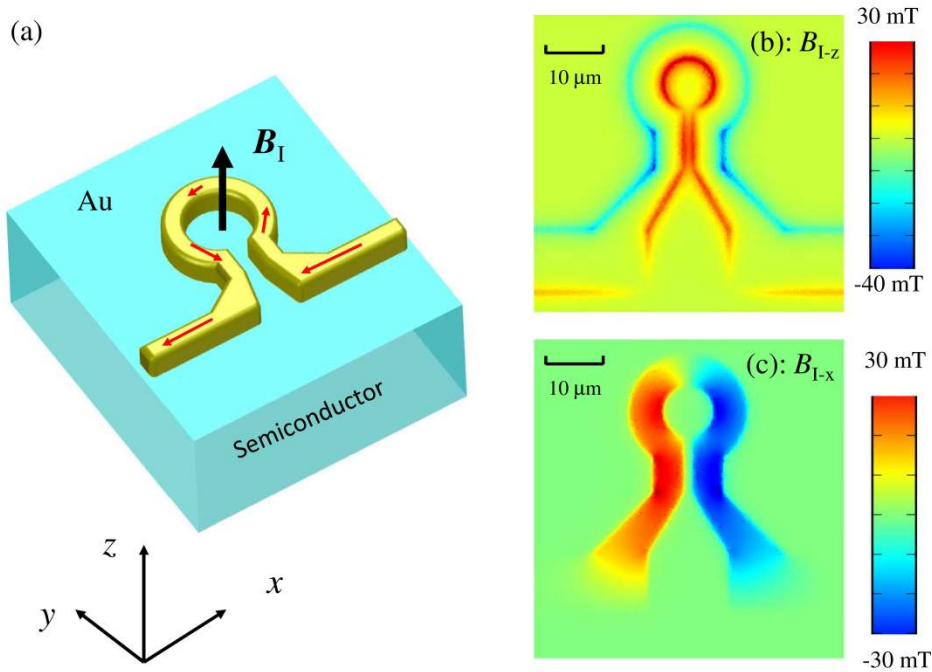
FIG 3.1-1: (a) Schematic description of an Au-microcoil on a semiconductor; (b) Numerical simulation for out-of-plane component $B_{I\text{-}z}$ of the current-induced magnetic field; (c) Numerical simulation for x-component $B_{I\text{-}x}$. For simulations: $I =$ 120 mA, coil inner diameter: 8.5 μm, coil width: 5.5 μm, depth: -70 nm below semiconductor surface.

Typically the sample is cut into ~5 mm $\times$ 5 mm piece from a large wafer, and then the sample is cleaned by a standard protocol to remove possible dirties on the semiconductor surface (see Section A1). To pattern the required two-types of microstructures on top of the semiconductor, the following protocol is used as standard, as well schematically described in FIG 3.1-2.

S1-A. By spin-coating with a rotation speed of 3000 ~ 6000 rpm, the positive resist Poly methyl methacrylate (PMMA) in Chlorbenzen of a concentration of 7% (AR-P 671.07, ALLRESIST) is dispersed atop the semiconductor, so that a PMMA layer is formed with a thickness of approximately 780 ~ 1200 nm. Afterwards, the sample is baked on a hotplate under a temperature of 160°C for 2 minutes;

S1-B. The microstructure layout is designed with the Elphy Quantum software package (Raith GmbH), and the mask is exposed by a well-focused scanning electron microscop (SEM, SUPRA 25, Zeiss). Detailed parameters of EBL process can be found in Section A2;

S1-C. The exposed PMMA mask is dissolved by using the developer solvent (AR 600-56, ALLRESIST) for 80 seconds, and the sample is rinsed by Isopropanol for 80 seconds;

S1-D. Three layers of metals are deposited by the metal coating system (E306A Coating System, Edwards). A Cr layer with 15 nm thickness is deposited via electron beam evaporation, and then a Pd layer of 50 nm thickness is evaporated by means of thermal evaporation. Finally 300 nm Au is deposited again by thermal evaporation. As there are two boats for thermal evaporation and one boat for electron beam evaporation inside the coating system, these three steps can be done without opening the chamber. The sample is taken out after one hour for cooling.

S1-E. The sample is fixed by a pair of wood tweezers and immersed into a beaker with Pyrrolidon solvent. The beaker is heated on a hot plate with a set temperature of 85°C (the liquid temperature is around 50°C). After ~70 min heating, the beaker is put into a water pool of the ultrasonic cleaner. Level 2 of the ultrasonic source is used for ~20 seconds, and then the sample is rinsed with Isopropanol for 1 minute.

Steps (S1-A) to (S1-E) are for fabricating the bonding-wire pads.

For patterning microcoil structures, similar steps are used as indicated from (S2-A) to (S2-E).

S2-A. A new mask is defined using the same procedure as (S1-A);

S2-B. The microstructure layout is again designed and exposed as (S1-B), but with different structure layouts and exposure electron beam current amplitude. Details can be found in Section A2;

S2-C. The exposed PMMA mask is dissolved by the PMMA developer solvent for 70 seconds, and the sample is rinsed by Isopropanol for 70 seconds;

S2-D. In the same coating system, an Au layer with 250 ~ 360 nm thickness is done by thermal evaporation. The sample is taken out after half an hour for cooling.

S2-E. The sample is fixed by a pair of wood tweezers and immersed into a beaker with Pyrrolidon solvent. The beaker is heated on a hot plate with a set temperature of 80°C. After 35 min heating, the beaker is put into a water pool of the ultrasonic cleaner. Level 1 of the ultrasonic source is used for ~20 seconds, and then the sample is rinsed with Isopropanol for 1 minute.

In a whole, Section A2 gives detailed conditions and parameters for each processing step. FIG 3.1-3 shows the SEM micrograph of the fabricated microstructures on top of a semiconductor. They include wire-bonding pads, microcoil structures, markers to identify structures, crosses to define same structure positions between different EBL procedures, and sample names.

FIG 3.1-4 presents four typical microcoil structures. For the microcoils in (a), (b) and (c), the inner aperture size of the coil ranges from 3 µm to 20 µm, and the coil width from 2 µm to 10 µm. The metal pad around the coil in structure (d) is designed to dissipate current-generated local heating [139].

After the microstructure fabrication, the sample is fixed by conductive glue (G302, PLANO) on a copper plate served as the sample holder. After around 15 minutes, an insulation plastic sheet with

copper pads is pasted by the same glue on top of the sample holder. After another 15 minutes, the whole sample ensemble is ready for wire-bonding. FIG 3.1-5 presents the schematics for a sample before wire-bonding.

The wire-bonding is done with an Au wire of 25 µm diameter. The bonding is performed by an automatic and semi-auto ball bonder (5610, F&K Delvotec). The Au wires are bonded on both the on-chip Cr/Pd/Au pads and the copper pads on the plastic sheet. On the latter, the electrical cable soldering is made afterwards. The length of the bonded wires is on the order of millimetres, which allows high-frequency operation electrically on the sample.
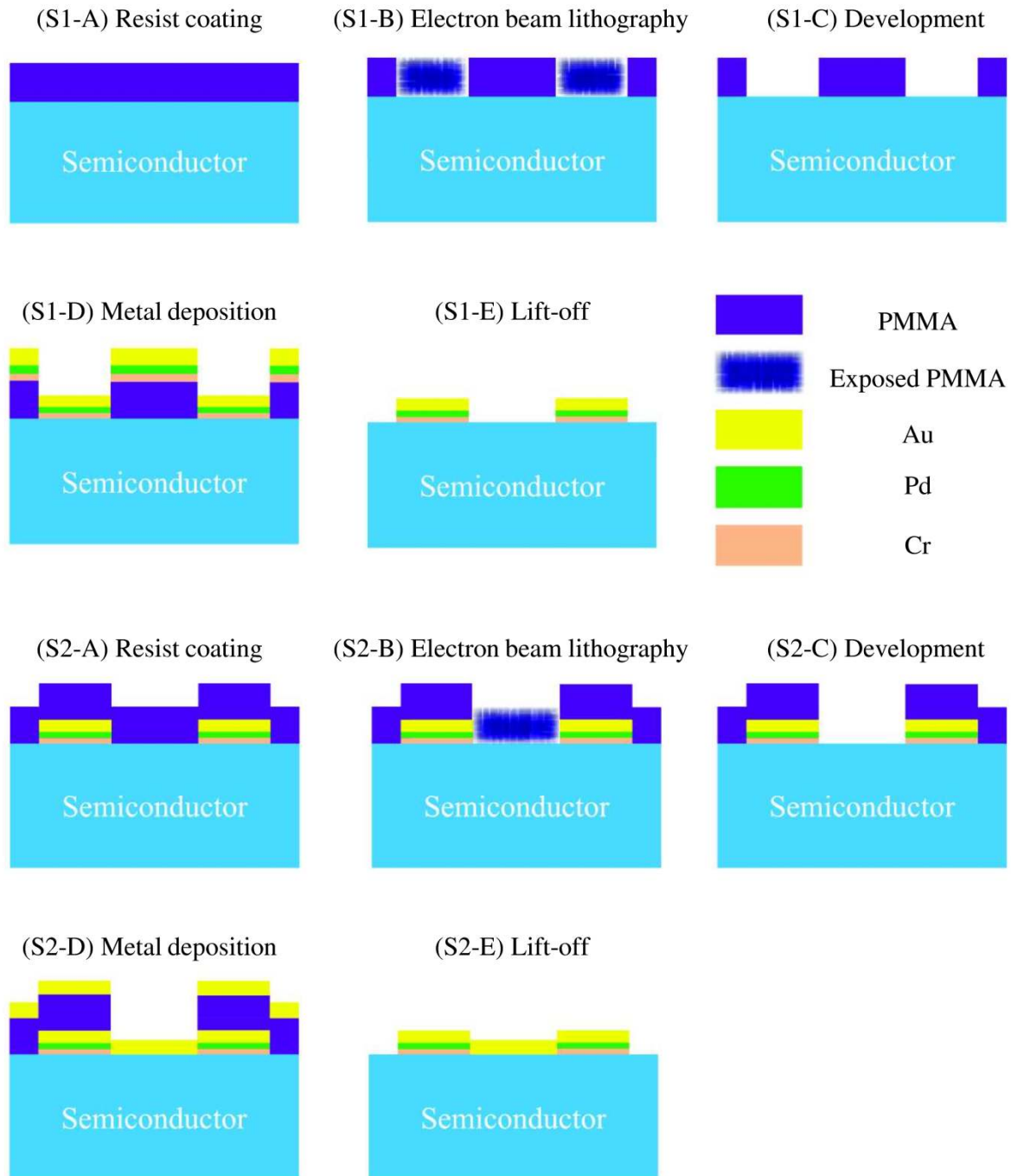
FIG 3.1-2: Side view of microstructure fabrication processes on a semiconductor. The set of processing steps (S1-A) ~ (S1-E) are for fabrication of wire-bonding pads, and steps (S2-A) ~ (S2-E) are for fabrication of microcoil structures.
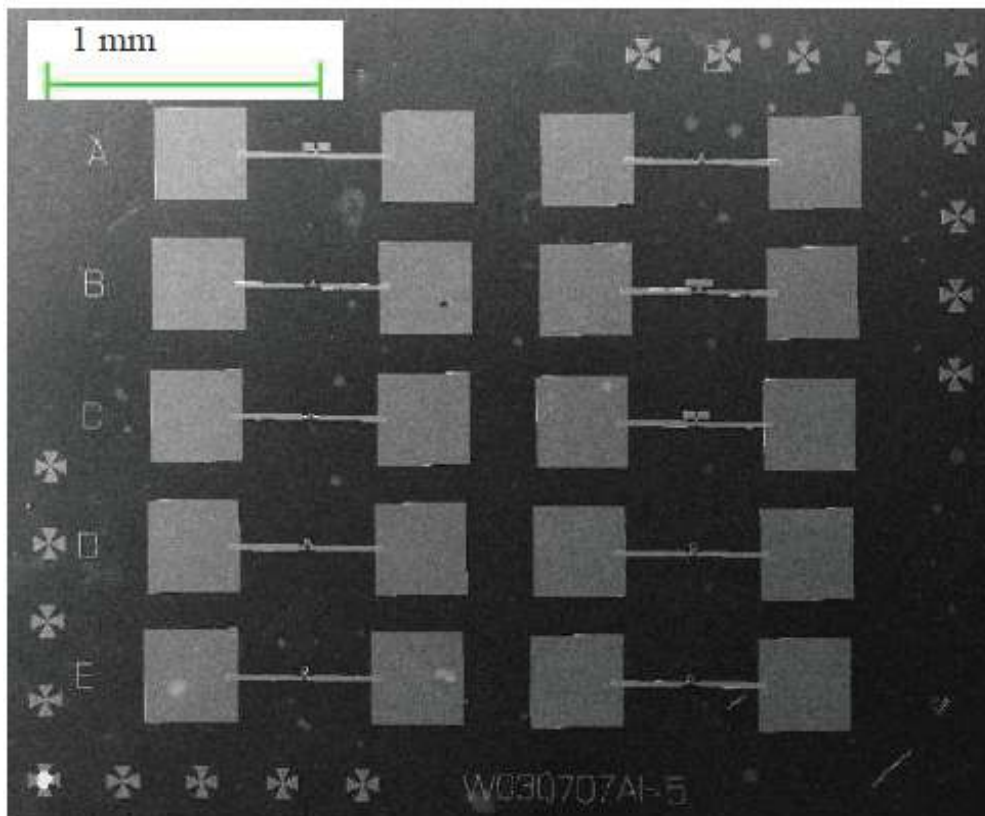
FIG 3.1-3: SEM micrograph of the whole fabricated microstructures on a semiconductor after processing steps from (S1-A) to (S2-E).
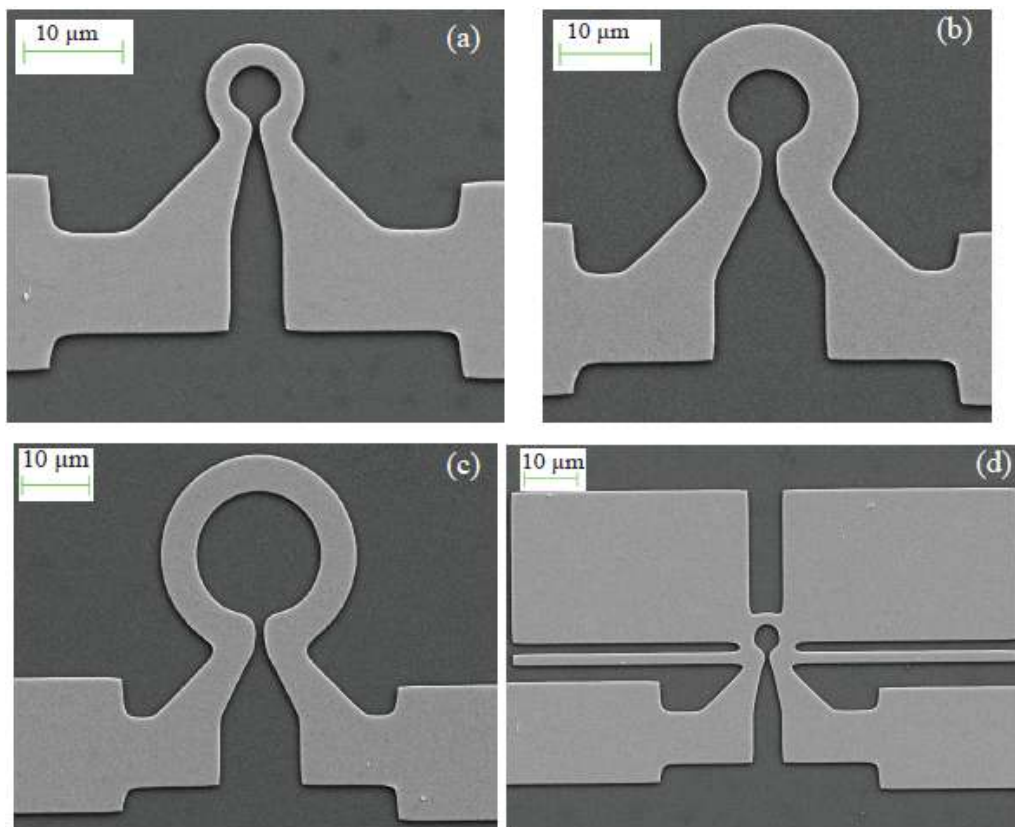

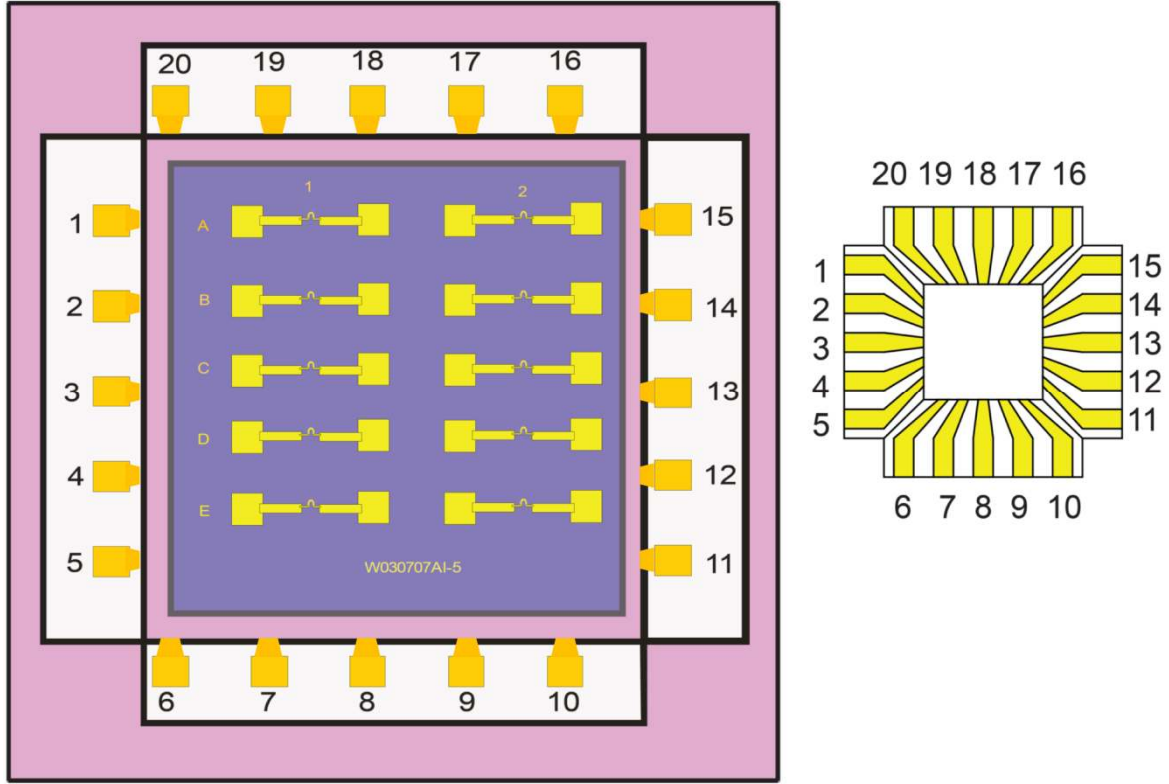FIG 3.1-4: SEM micrographs of four typical fabricated microcoil structures.

41

FIG 3.1-5 Left: The schematics of a fixed sample ensemble. The sample (blue) is glued on the sample holder (pink). The insulation plastic sheet (white) with copper pads (yellow) is glued around the sample. Right: Layout of the insulation plastic sheet. The number is defined for each bonding pad.

3.2 High frequency adaptation for samples

Motivated by fast electrical control over spin dynamics, it is required to obtain a pulsed current with a short transition time, i.e. on the order of several 100 ps. This means the sample should be adapted for high-frequency (HF) electrical operation.

To perform HF operation during experiments, all the electronic setup is with 50 ohm matching. SMA cables and SMA connectors are used to make connections between electronic instruments. The sample is terminated with a 50 ohm resistor in the cryostat. A schematic of electric connection during measurements is presented in FIG 3.2-1. A signal generator serves as a voltage source, and by using a voltage modulator with GHz bandwidth, the voltage amplitude could be driven up to Vpp = 8V within a transition time constant of a few 100 ps. The modulated voltage pulse is applied to the cryostat sample via a SMA adapter allowing RF signal transmission on a GHz scale. Two SMA transmission cables are used inside the cryostat. Each endpoint of each cable is split into the ground line and the signal line. The signal lines are directly connected, while the ground lines are connected via the 50 ohm terminator. By thermal soldering the inner side of the SMA adapter and the conducting pads on the sample, each line of cables is properly connected to achieve the electrical connections for the on-chip microcoil structure.

For the whole electrical connections described above, there are several factors which limit the HF behavior capability due to non-ideal 50 ohm matching: (i) The broken part of the two cables inside

the cryostat; (ii) Each soldering part; (iii) The bonding Au wires; (iv) The on-chip metal structures making metal-semiconductor contacts.
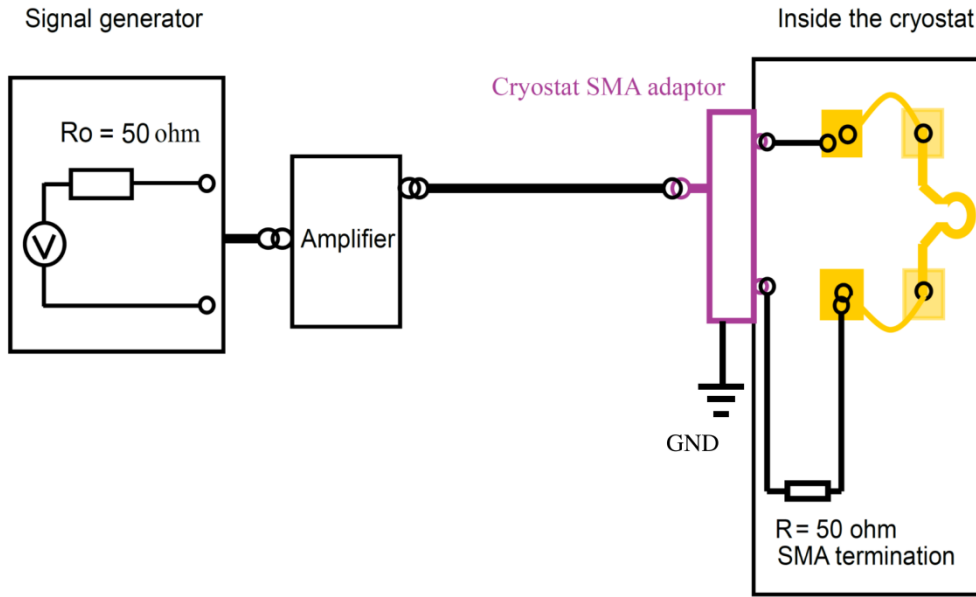

FIG 3.2-1: Schematic description of electrical connections between a signal generator and the studied sample in a cryostat.
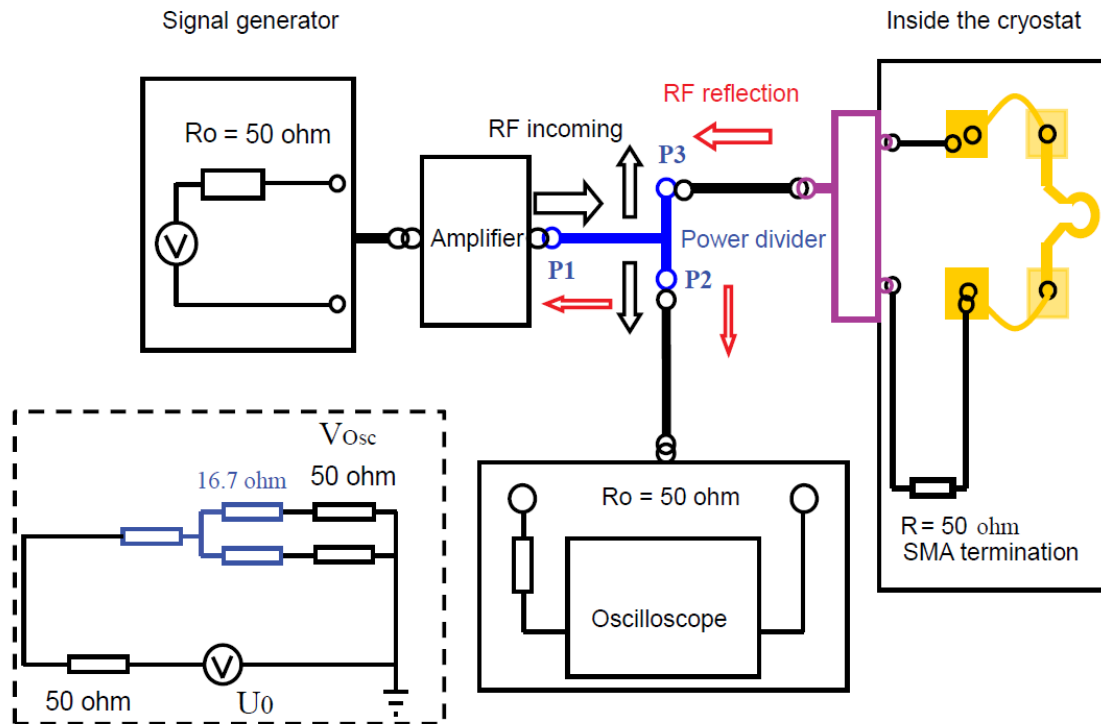

FIG 3.2-2: Schematic description of electrical connections to probe the reflection RF signals from the cryostat sample.

In order to test the HF capability, the reflection waveform from the cryostat is probed by using the scheme presented in FIG 3.2-2. Here a 6 dB power divider (MODEL 5331, Picosecond Pulse Labs) receives RF wave (black arrows) and divides it into two parts with an equal amplitude. One part

travels into the cryostat and the other into an oscilloscope with 50 ohm output resistance. The inset gives a simplified diagram of the electrical circuits. Each port of the power divider carries a resistance of 16.7 ohm (blue rectangles). Since both the signal generator and the oscilloscope have a 50 ohm matching, the only possible mismatching comes from the cryostat, i.e. the sample construction. In the case of a perfect 50 ohm matching in the cryostat, the total resistance of the load circuit is 50 ohm. Thus, the whole circuit has a 50 ohm matching. Then no reflection wave (red arrows) is expected. Otherwise, the oscilloscope is expected to detect a distorted RF wave as a superposition of the incoming RF and the reflected signal.

FIG 3.2-3 shows the probed temporal profiles of a voltage pulse by a sampling oscilloscope (Tektronix 7854) and a GHz sampling unit (Tektronix7S11 & 7T11). The used signal generator is an Agilent 81133A, which is sufficient to provide voltage pulses with a transit time less than 90 ps. These fast leading/falling edges are confirmed as seen in FIG 3.2-3(a), in which the oscilloscope is directly connected via a SMA cable with the signal generator. To estimate the wave reflection during the RF transmission[4], the electrical configuration is used as described in FIG 3.2-2. FIG 3.2-3(b) presents the waveform in the case that P3 is connected to a perfect 50 ohm termination. The electrical edge transit time is kept below 100 ps. This means the electrical circuit could afford the transmission of such a RF pulse even in case of non-ideal matching. As a comparison, P3 port is kept open for the measurement of FIG 3.2-3(c). There is a complex waveform as a result of serious mismatch in this frequency regime. For the measurement of FIG 3.2-3(d), P3 is connected with the cryostat. The detected waveform is quite similar to the one in FIG 3.2-3(a), which means the electrical properties of the cryostat are close to a perfect 50 ohm resistor on a GHz frequency scale.

Further, similar testing was performed for voltage pulses which are typically used under experimental measurements. The cryostat temperature is 4.5 K. The pulse width is 4 ns for FIG 3.2-4(a) and (b) and the repetition period is 20 ns. The similarities between FIG 3.2-4(a) and (b) confirm a rather small RF reflection from the low-temperature cryostat. For waveforms presented in FIG 3.2-4(c) and (d), the pulse width is 7 ns and the repetition period is 35 ns. The voltage modulator is used between the signal generator and the 6dB power divider. A weak reflection is present in FIG 3.2-4(d). Since the amplitude of the reflection waveform is relatively small and the transmit time is fast enough, it could be estimated that the voltage waveform applied on the sample is close to FIG 3.2-4(c). For detected waveforms from FIG 3.2-4(a) to (d), the leading/falling edge time constant is generally below 400 ps.

The generation of fast electrical pulse allows one to perform on-chip electrical spin control on a time scale of a few 100 ps. By combination of time- and polarization- resolved photoluminescence measurements, the fast spin dynamics controlled by the electrical pulse could be detected on a sub-nanosecond time scale.

---

[4] The test measurements in FIG 3.2-3 were performed in the early stage of this work. A T-junction connector *without* the three 16.7 ohm resistors was used as the power divider. This made the circuit mismatched in a whole. Therefore the testing results gave an indication of better HF operation in the case of the 6dB power divider.
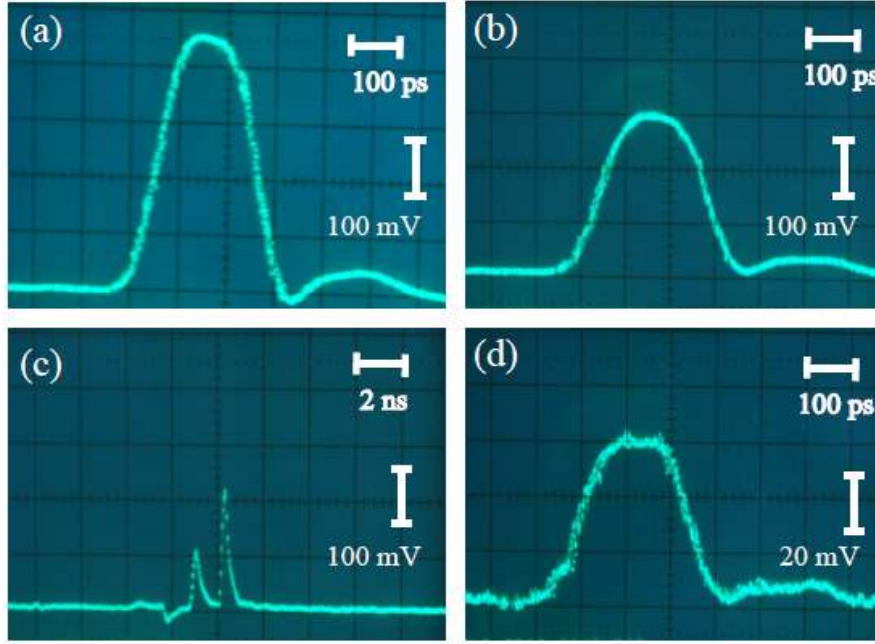
FIG 3.2-3: Probed temporal profile of a voltage pulse at room temperature. The pulse width is 200 ps. (a) The signal generator is directly connected with the oscilloscope; (b) P3 (see FIG 3.2-2) is connected with a perfect 50 ohm terminator; (c) P3 is terminated as an open circuit; (d) The electrical connections are used as FIG 3.2-2. The output voltage from the signal generator for (a) ~ (c) is 500 mV, and the output voltage for (d) is 100 mV.
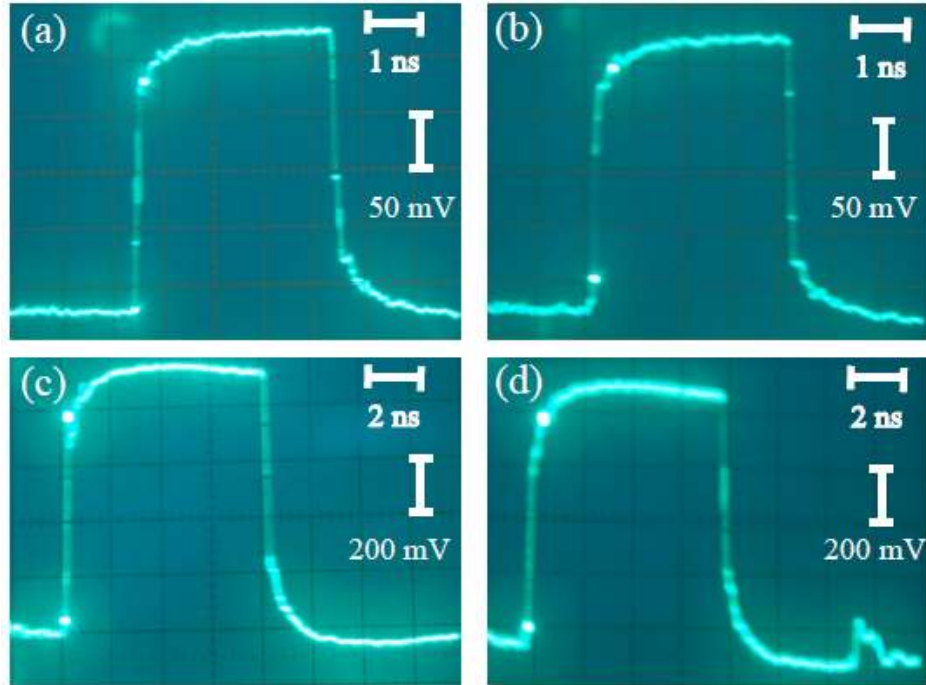

FIG 3.2-4 : Probed temporal profile of a voltage pulse at a temperature of T = 4.5 K. For (a) and (c), P3 is connected with a perfect 50 ohm terminator; for (b) and (d), the electrical connections are adopted as FIG 3.2-2. For (a) and (b), the pulse width is 4 ns and the repetition period is 20 ns. For (c) and (d), the pulse width is 7 ns and the repetition period is 35 ns; and the voltage modulator is used here. The characteristic time constants for the leading and the falling edges are less than 400 ps.

3.3   Time-resolved magneto-luminescence spectroscopy

The magnetization dynamics of Mn^{2+} ions in the $Cd_{1-x}Mn_xTe/Cd_{1-y}Mg_yTe$ quantum well system is studied in the magneto-luminescence setup. The polarization degree of photoluminescence (PL) gives a sensitive detection of the carrier spin polarization in semiconductors, e.g. via the optical Hanle effect [21]. Thanks to a spatial resolution on a micrometer length scale, the setup allows one to optically address the local spin states inside the microcoil area. Since the temporal resolution of optical detection could be down to several ten picoseconds, the local Mn^{2+} spin dynamics can be traced on a sub-nanosecond time scale.

The detected PL polarization degree is defined as

$$\rho = \frac{I^{\sigma+} - I^{\sigma-}}{I^{\sigma+} + I^{\sigma-}}, \tag{3-1}$$

where $I^{\sigma+}$ and $I^{\sigma-}$ is the PL intensity of right-circular polarization (σ^+) and left-circular polarization (σ^-), respectively. As discussed in the Section 2.3.2, the PL polarization degree is controlled by the Mn^{2+} ion magnetization and the exciton temperature. By measuring $I^{\sigma+}$ and $I^{\sigma-}$, the PL polarization degree is determined, and thus the Mn^{2+} ion spin dynamics can be evaluated.

3.3.1   Magneto-luminescence setup

A schematic illustration of the magneto-luminescence setup is given in FIG 3.3-1.
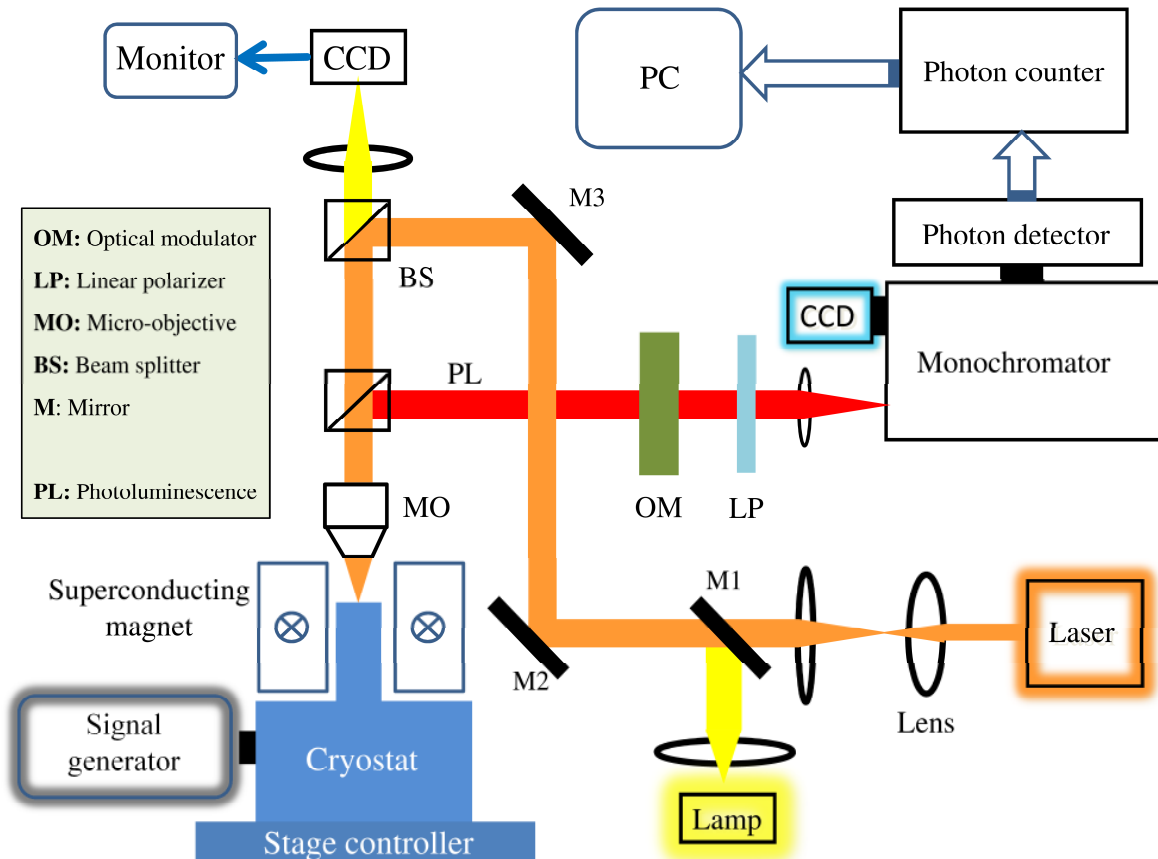

FIG 3.3-1: Schematics of the magneto-luminescence setup

- **Optical excitation**

A diode laser head with a center wavelength of 641 nm serves as the excitation source. The laser head can work under cw or pulsed operation controlled by the laser driver (PDL 800-D, PicoQuant). Alternatively a He-Ne laser with 632.8 nm wavelength (AreoTech GmbH) is used. The excitation beam is focused on the studied sample by a micro-objective with a high numerical aperture (N.A.). The used objective is either the LD-Epiplan 50× with N.A. = 0.6 (Carl Zeiss AG) or the LD EC Epiplan-Neofluar 100× with N.A. = 0.75 (Carl Zeiss AG). Approximating the incoming ray as an ideal Gaussian beam, the laser spot diameter (defined as the beam waist) under focus is [140]:

$$2\omega_0' = \frac{2\lambda \cdot F}{\pi \omega_l}, \tag{3-2}$$

where λ is the laser wavelength, F is the distance from the sample surface to the objective lens, and ω_l is the beam radius on the objective lens. Since the modern micro-objective system is an infinity optical system [141], the focal plane of the objective lens is the object plane, i.e. the sample surface here. Then here F is equal to the focal length of the objective lens. In case of the optical window full of illumination, the beam diameter is equal to the lens aperture D, i.e. $2\omega_l = D$. From the definition N.A. = $\sin(\arctan(D/2F))$, there is $\omega_l = F \cdot \tan[\arcsin(\text{N.A.})]$. The focused laser spot can be written as

$$2\omega_0' \approx \frac{2\lambda}{\pi \cdot \tan[\arcsin(N.A.)]} \tag{3-3}$$

For λ =641 nm, N.A. = 0.75, the minimal laser spot diameter $2\omega_0' \approx 360$ nm. This is the ideal case, while factors suck lacking full illumination, experimental turbulence like setup vibration and so on, limit the spot size around 1 micrometer for optical excitation.

During the experiments, the optical power is detected after M1. In order to calculate the excitation power density in the studied semiconductor layer, the optical reflectance of each optical component through the light path should be taken into account. As an approximation, the reflection coefficients of M2 and M3 are used as unity, the reflection coefficients of the beam-splitter is ~50% for each, the transmission of the micro-objective is ~90% from the datasheet, the reflectance of each side of the cryostat window is ~4% (two surfaces), and the reflection on the sample surface is ~50 %, e.g. for the studied (Cd, Mg)Te alloys, then the excitation power transmitted into the sample is $P_{exc} \approx 0.2 * P_{mea}$. Here P_{mea} is the power probed after M1. For a typically used power P_{mea} = 6 µW, the average optical excitation density can be estimated $\rho_{exc} \approx 150$ W/cm^2 for a spot size of 1 µm.

- **Sample cryostat**

The studied sample is fixed on a finger in a LHe^4 (liquid Helium ^{4}He) flow cryostat (MicrostatHiRes, Oxford Instruments). By pumping liquid Helium flow through the cryostat, the sample temperature can be cooled down to 3.5 K and varied up to 300 K by using the cryostat heater. The sample temperature is set and read by the temperature controller (ITC 530, Oxford Instruments). The cryostat is mechanically fixed on a xy-translation stage, which is driven with a micrometer resolution

by an actuator controller (ESA-C, μ-drive controller, Newport). By combing the cryostat with a superconducting magnet system (MicrostatBT, Oxford Instruments), a magnetic field ranging from -5 Tesla to +5 Tesla can be applied on the sample in Faraday geometry (optical path parallel to the magnetic field). The magnetic field is set and read by a power supply controller (IPS 120-10, Oxford Instruments). In a whole, the magneto-optical setup allows one to perform optical characterization in Faraday geometry, and it gives a spatial resolution on micrometer scale at low temperature.

To obtain the structure details and the laser spot positions, the sample is illuminated by a lamp. The sample is imaged by a CCD camera which is connected to a monitor. The excitation area within the microcoil is monitored in real time during the experiments.

- **Photoluminescence detection**

The photoluminescence is reflected from the sample through the micro-objective, guided by a 50/50 beam splitter, and focused into the monochromator (Triax 550, Horiba Jobin Yvon). There are three alternative gratings with a groove density of 600 mm^{-1}, 1200 mm^{-1} and 1800 mm^{-1}. The linear dispersion of each grating is accordingly 3.03 nm/mm, 1.55 nm/mm and 1.01 nm/mm. The dispersed PL could be either collected by a cooled CCD camera (2048×512BIVS, 26.6×6.9 mm^2, Horiba Jobin Yvon) in the front exit slit for spectral measurements, or a cooled photon-multiplied detector for counting PL photon numbers.

The collected PL wavelength range is approximated as $\Delta\lambda \approx$ (Linear dispersion) × (Exit area) by considering small diffraction angles [142]. In the case of using the 600 mm^{-1} grating, the CCD detector can cover a range of ~75 nm for the PL spectrum measurements. For the photon-counting, the spectral width is about 6 nm, if the width of the side exit slit is 2 mm. As the PL spectral width (Full width of half maximum) of studied samples is typically less than 3 nm (*e.g.*, see Chapter 4), both means of optical detecting could collect most of the PL signal.

3.3.2 Time-resolved measurements of photoluminescence polarization degree

To obtain the PL polarization degree, the photon number of σ$^+$ and σ$^-$ PL is respectively measured. The photon-counting for both kinds of polarized light is performed quasi-simultaneously compared with the setup stability. This is realized by applying a periodic PL modulation by an electro-optical modulator, which synchronizes the recording of the corresponding circularly-polarized photoluminescence. To monitor the PL polarization dynamics induced by an electrical pulse, electrical synchronization is utilized between the applied voltage sequence and the modulation signal.

- **Quasi-simultaneous measurements**

The configuration for PL polarization degree measurements is shown in FIG 3.3-2. The photoluminescence is modulated by an optical modulator: a photo-elastic modulator (PEM), liquid crystal (LC) or electro-optical modulator (EOM). After a phase retardation of π/2 or -π/2, each

circularly-polarized component of the photoluminescence is converted to a linearly-polarized signal. These two polarization directions are orthogonal.

By a $\pi/2$ phase shift, the σ^+ PL (red arrow) is converted to linearly-polarized signal with a polarization (red double-headed arrow) parallel to the following linear polarizer, while the σ^- PL (blue arrow) becomes linearly-polarized with a polarization (blue double-headed arrow) orthogonal with this polarization. As a result, the σ^+ PL passes through the linear polarizer and is recorded by the photon counter; while the σ^- PL is eliminated by the linear polarizer and cannot be counted. In case of $-\pi/2$ phase shift, the σ^- PL is counted while σ^+ PL is eliminated. The routing signal for registering σ^+ or σ^- PL intensity is synchronized with the optical modulation signal, so that the individual intensity could be transferred to two different memories.
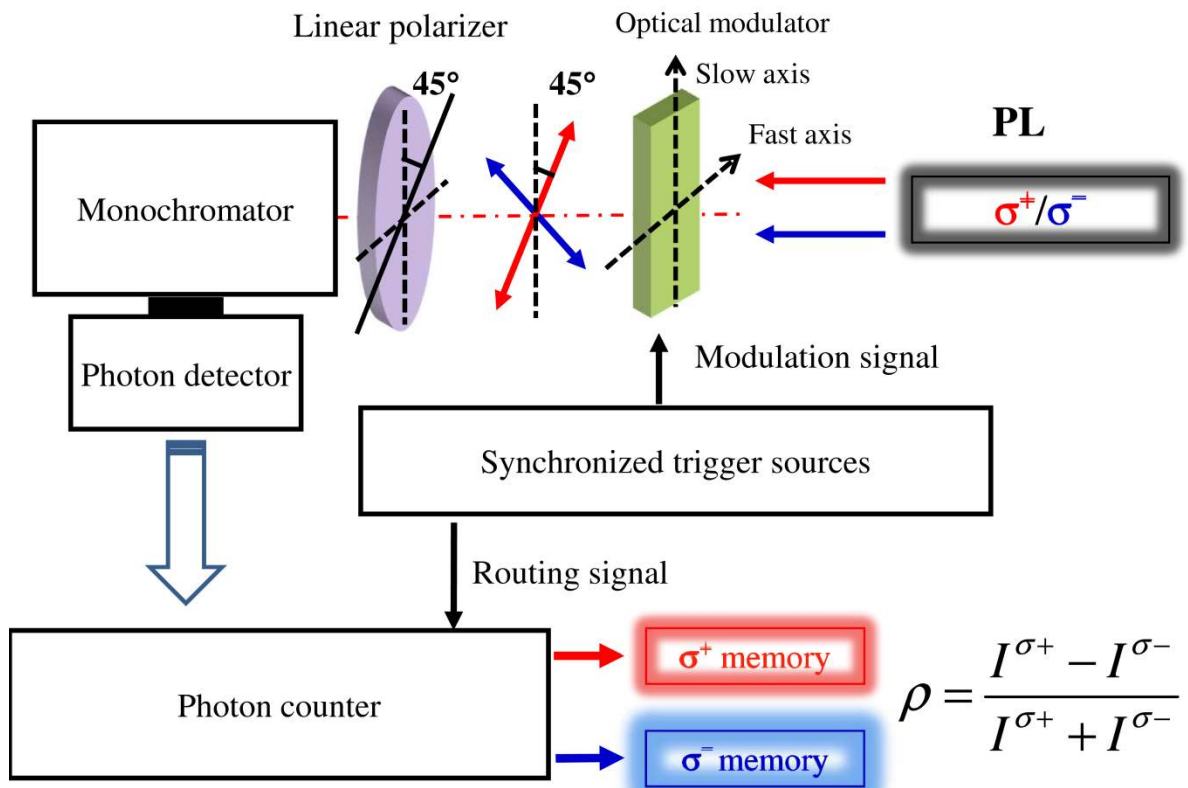

FIG 3.3-2: Schematic description of quasi-simultaneous measurements of PL polarization degree

In FIG 3.3-3, schematic descriptions of the phase modulation technique are given for recording σ^+-polarized and σ^--polarized PL intensity. In (a), the PEM makes a sinusoidal phase modulation between $\pi/2$ and $-\pi/2$. The phase shift is given by $\theta_{shift} = \pi/2 \cdot \sin(2\pi t/T)$ which is plotted in the upper panel. Here T is the modulation period. In the lower panel, the PL intensity (black: σ^+-polarized and red: σ^--polarized) after the linear polarizer is depicted (e.g. see Ref. [143]). In (b), the LC/EOM makes a squared phase modulation between $\pi/2$ and $-\pi/2$. The modulation duration is the same for two phase levels. As a result, the σ^+-/σ^--polarized PL intensity after the linear polarizer has a similar temporal profile which is depicted in the lower panel.
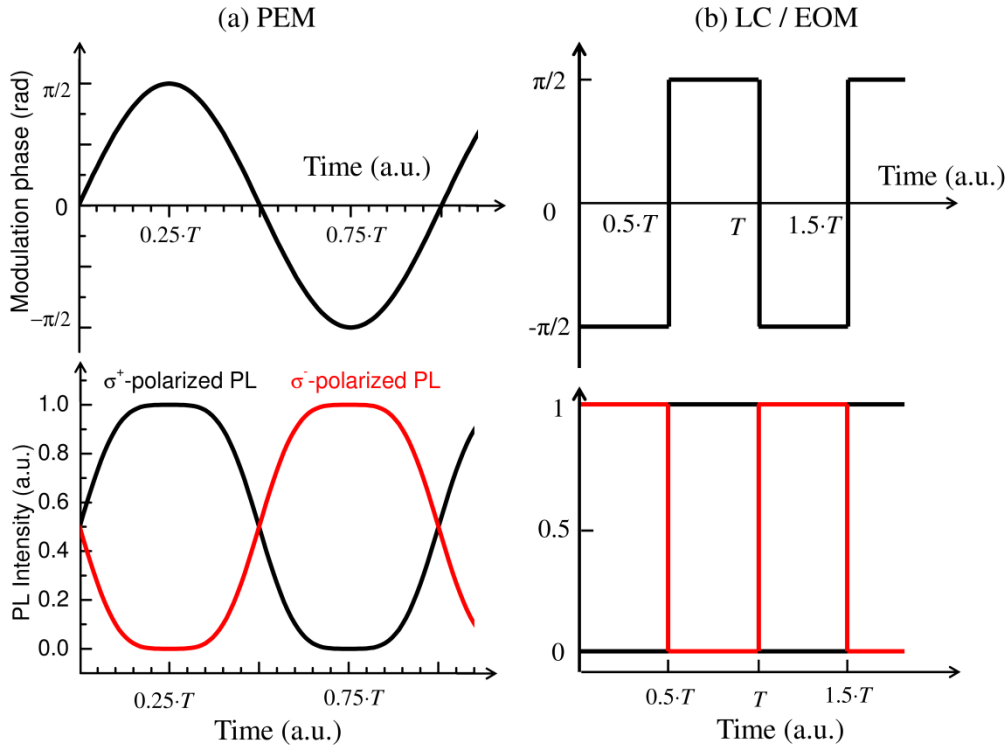
FIG 3.3-3: Schematic descriptions of the phase modulation technique for recording σ^+-polarized and σ^--polarized PL intensity. (a): PEM, after [143]; (b): LC or EOM. In each case, the upper panel represents the phase shift and the lower panels depict the PL intensity (black: σ^+-polarized, red: σ^--polarized) after the linear polarizer. The modulation period is denoted by T.

It can be seen the optical intensity modulation is periodic during experiments. If the applied time length is the same for measuring σ^+ or σ^- PL intensity, a single measurement of the PL polarization degree can be done within one modulation period. For PEM, the modulation frequency is a fixed value of 50 kHz; for LC, the used modulation frequency ranges from 0.1 Hz to 1 Hz; for EOM, the used modulation frequency ranges from 1 kHz to 10 kHz. All the used modulation periods are always above the setup stability duration. This allows one to detect the PL polarization degree in a way almost quasi-simultaneously. In order to obtain a good signal-to-noise ratio, measurements are averaged on a time scale of minutes.

A more detailed description of quasi-simultaneous polarization degree detection can be found in Ref. [143].

- **Synchronization between electrical pulse and optical detection**

To detect the PL polarization dynamics induced by an electrical pulse, the PL polarization degree is traced at a certain time delay with respect to the introduced voltage pulse sequence. Two synchronization methods are used between the electrical pulse and optical modulation.

As shown in FIG 3.3-4, the optical modulation is done by a photo-elastic modulator (PEM-90, Hinds Instruments) with a fixed modulation frequency of $f \approx 50$ kHz. There are two TTL voltage sequence outputs as triggering sources from the PEM controller. A square-wave sequence with frequency f is

used to trigger the two-channel photo-counter (SR400, Stanford Research Systems) to record the modulated PL intensity. Since there are two counting channels, the photon-counting frequency is actually with frequency $2f$. The other TTL output is used to trigger the pulse generator (HP8110A, Hewlett-Packard) with a frequency of $2f$.

The temporal window width is 100 ns (τ_{win}) for each photon-counting channel, which is adjusted to be centered at $\pi/2$ or $-\pi/2$ phase modulation (left side of FIG 3.3-4). The time interval for opening each detection window is $\tau_{inter} = 10$ µs. Therefore the time delay Δt between the electrical pulse and each photon-counting channel is the same. The time delay Δt is variable from 0 to 10 µs, which is manually controlled by the input trigger sequence and the output voltage pulse for the pulse generator.

The time resolution is limited by the detection window of 100 ns. The electrical pulse frequency is inflexible due to the fixed PEM frequency. The photon detector here is a water-cooled photomultiplier tube (R943-02, Hamamatsu). The polarization degree resolution is ~0.5%.

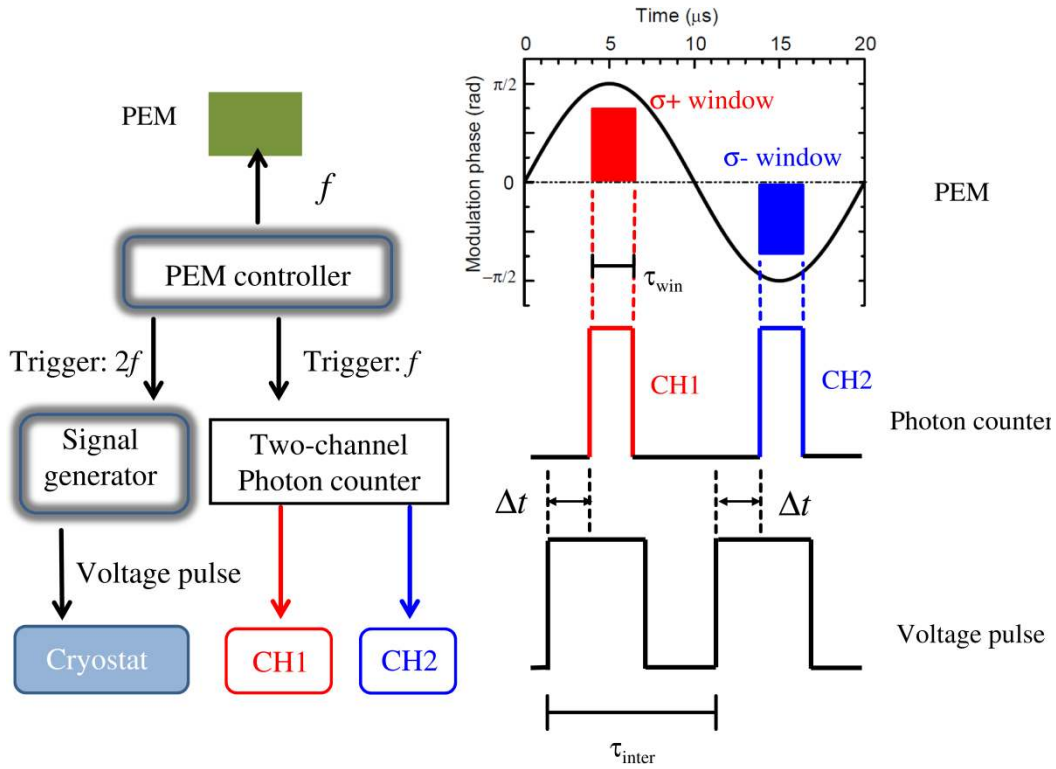FIG 3.3-4: Electronic-optical synchronization at early experiment stage. Δt is the variable time delay between the electrical pulse and the optical detection windows. PEM: Photo-elastic modulator; f = 50 kHz; CH: Channel.

To improve the time resolution and the polarization sensitivity, a time-correlated single photon counting module (TCSCP-SPC630, Becker&Hickl) with a micro channel plate (MCP-R3809-51, Hamamatsu) as the photon detector is used. The electrical connection is presented in FIG 3.3-5.

In order to make time-resolved photon counting, a TLL voltage pulse (named as CH1) provided by a pulse generator works as the "STOP" signal for the TCSPC module. The other output channel CH2 is connected to the cryostat sample to generate the on-chip magnetic field. The PL signal serves as the

"START" signal for the TCSPC system. Detailed descriptions of the TSCPC principle are given in Ref. [144]. Both output electrical sequences have a same frequency f_1, which determines the time range of the monitored PL dynamics. The TCSPC module counts the PL photons through the whole time range ($1/f_1$). The time delay is realized by a time to amplitude converter within the TCSPC unit [144]. The used f_1 value is from 500 kHz (time range of 5 μs) to 50 MHz (time range of 20 ns) during the experiments.

The optical modulation is performed by a liquid crystal (Variable retarder VIS, Meadowlark Optics) or an electro-optical modulator (LM0202 VIS KD*P, Linos), each of which is driven by a square voltage sequence. A function generator (AFG3252, Tektronix) provides the trigger sources. One output channel (CH3) provides a squared TTL wave with repetition frequency f_2 to drive the optical modulation, and the other channel (CH4) gives a synchronized TTL voltage out to the R6 bit of the TCSPC module [144]. The R6 bit works as the routing signal, which distributes two memory sections for counting the σ^+ or the σ^- PL intensity. In typical experiments, the modulation frequency is $f_2 = 0.1$ Hz for the LC and $f_2 = 1.852$ kHz for the EOM.
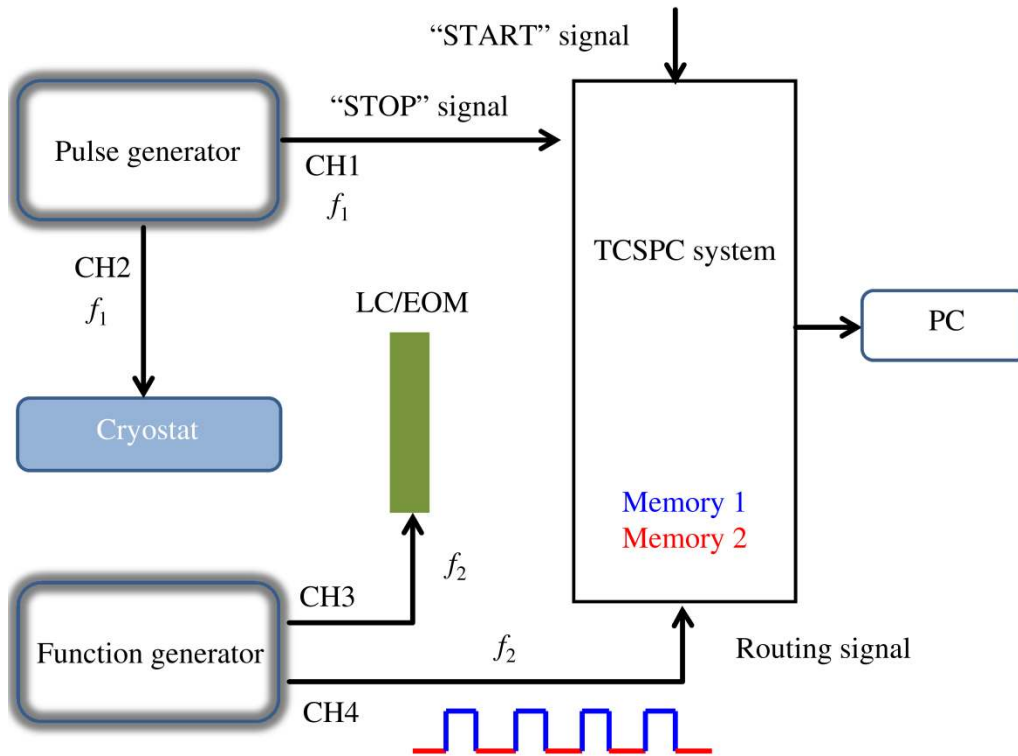

FIG 3.3-5: Electronic-optical synchronization at developed experiment stage. TCSPC: Time-correlated single photon counting; LC: Liquid crystal; EOM: Electro-optical modulator; CH: Channel.

The digital time resolution of the TCSPC system is the time duration of each counting channel which is equal to the time range over the channel number (from 64 to 4096). The real time resolution of the optical detection is limited by the photon-electron transit time of MCP, which is approximately 25 ps. Since it is not required to synchronize the applied voltage sequence (f_1 signal) on the sample to the optical modulation sequence (f_2 signal), it makes the PL dynamical detection with more flexible time

range compared with PEM-based method. Further the polarization degree resolution is improved to ~0.2%.

3.4 Time-resolved Kerr rotation technique

The studies of nuclear spin dynamics in n-GaAs is performed by the time-resolved Kerr rotation (TRKR) setup. The TRKR technique is a pump-probe optical method to detect the electron spin precession dynamics. It has been widely utilized to address ultrafast dynamic spin properties in different material systems [145-147]. This thesis concerns to the electron spin precession dynamics around a magnetic field. The monitored magnetic field is a sum of the applied static field and the dynamic nuclear field namely the Overhauser field [69]. Therefore by evaluating the electron precession Larmor frequency, the nuclear field is determined and thus the nuclear spin dynamics is addressed.

3.4.1 Magneto-optic effects

When light propagates in a medium, the polarization state can be varied by changing the medium magnetization, *e.g.* by applying an external magnetic field. The magneto-optic effects can be manifested during the transmission of the light through a magnetic medium or the reflection of the light from the medium surface. As a typical consequence, linearly-polarized light will be changed to elliptically-polarized light with a rotation of the polarization plane. A schematic picture is presented in FIG 3.4-1.

In the case of light transmission (upper part, FIG 3.4-1), the magneto-optic effect is named Faraday effect [148] in the geometry of the material magnetization M collinear to the wave vector of the light k (M // k), while it is called Voigt effect [149] or Cotton-Mouton effect [150] for $M \perp k$. In the reflection case, it appears as the magneto-optic Kerr effect [151] (lower part, FIG 3.4-1). It can be classified into three fundamental geometries by considering the relative orientation between M and the incidence plane of the light. The polar Kerr rotation applies to the case in which M is in the out-of-plane direction and parallel to the incidence plane. The longitudinal Kerr rotation lies for the case where M is in-plane and parallel to the incidence plane, while the transverse Kerr rotation dominates if M is of in-plane direction and perpendicular to the incidence plane. Since each type of Kerr effect is related to the light reflection on a surface, it can be further decomposed into the Kerr effect for the *s* polarization state and the *p* polarization state, respectively[5].

For a general case with arbitrary medium magnetization, M can be decomposed into a sum of magnetizations in fundamental directions. The total change of the light polarization state is a superposition of those magneto-optic effects. For the light propagation from a nonmagnetic medium

---

[5] In FIG 3.4-1, the *s* polarization state and the *p* polarization state are indicated. The *s* polarization state has the electric field vector perpendicular to the incidence plane, while the *p* polarization state has the electric field vector in the incidence plane.

(vacuum) to a magnetic medium, both transmission and reflection can exist on the medium boundary [152], and thus all types of magneto-optic effects should be included. For a magnetic material with a large optical absorption coefficient, *e.g.* metals or semiconductors with high-energy excitation, the transmission effects can be neglected [153, 154]. This is just the case for the studied sample within this thesis. Since the *k*-vector of the linearly polarized light during the experiments is always of a small angle to the normal of the sample surface, the polar Kerr effect is much more pronounced compared with the other two effects[154-156].

(a) Faraday effect   (b) Voigt effect /Cotton-Mouton effect

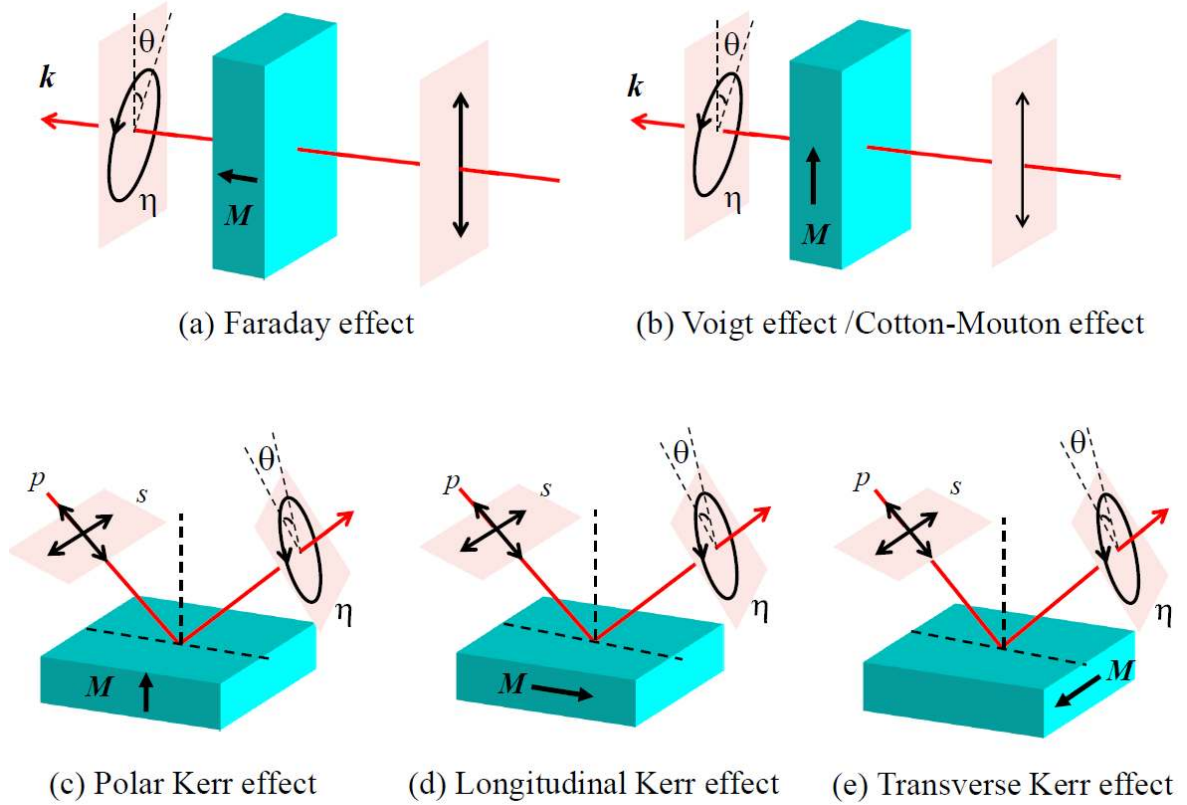(c) Polar Kerr effect   (d) Longitudinal Kerr effect   (e) Transverse Kerr effect

FIG 3.4-1: Magneto-optic effects in transmission through a magnetic medium (a-b) and reflection on the surface of a magnetic medium (c-e). For each magneto-optic effect in a fundamental geometry, the orientation is given between the medium magnetization M and the wave vector of the light or the incidence plane of the light. θ is the rotation angle and η the ellipticity of the elliptical polarization state.

The magneto-optics can be described in the context of either macroscopic dielectric theory or microscopic quantum theory [157]. The latter concerns the spin coupling between the electric field of the propagating light and the electron spin. For a spin-polarized electron with a spin vector collinear to the wave vector of the electric field in a magnetic medium, the probability of the electronic state transition is different between left-circularly polarized optical excitation and right-circularly polarized one. This causes the dependence of the refractive index on the light polarization [158-160]. Such magnetic circular dichroism is the basic origin of the magneto-optic effects. In this thesis, the macroscopic explanation based on wave propagation in dielectrics is given in the following.

- **Light propagation in a magnetized dielectric material**

The light propagation in a medium can be described by Maxwell's equations [152]. Considering the light of a plane wave with the form

$$E(r,\text{t}) = E_0 e^{i(k \cdot r - \omega t)} \tag{3-4}$$

$$H(r,\text{t}) = H_0 e^{i(k \cdot r - \omega t)} \tag{3-5}$$

with $E(r,\text{t})$ as the electric field vector and $H(r,\text{t})$ as the magnetic field vector. By using Maxwell's equations for this electromagnetic plane wave, it gives

$$\nabla \times E(r,t) + \mu_0 \mu(\omega) \frac{\partial H(r,t)}{\partial t} = \bar{0} \tag{3-6}$$

$$\nabla \times H(r,t) - \varepsilon_0 \varepsilon(\omega) \frac{\partial E(r,t)}{\partial t} = \bar{0} \tag{3-7}$$

Equations (3-6) ~ (3-7) lead to

$$\begin{aligned} k \times E - \omega \mu_0 \mu H &= \bar{0} \\ k \times H + \omega \varepsilon_0 \varepsilon E &= \bar{0} \end{aligned} \tag{3-8}$$

Here ε_0 is the vacuum electric permittivity, and μ_0 is the vacuum magnetic permeability. The permittivity tensor of the medium is represented as $\varepsilon(\omega)$, and $\mu(\omega)$ is the permeability tensor.

The H vector can be eliminated by using the formula $k \times (k \times E) = k(k \cdot E) - k^2 E$. As $k \cdot E = 0$ due to the transverse nature of the electromagnetic wave, it gives

$$-k^2 E + \varepsilon_0 \mu_0 \mu \omega^2 \varepsilon \cdot E = \bar{0} \tag{3-9}$$

As the effect of magnetic permeability in optical phenomena is generally small, it can be assumed that $\mu(\omega) = 1$ with 1 as the unit tensor. Thus, in the case of medium magnetization, $\varepsilon(\omega)$ is dominant affecting the optical properties. For simplicity, the magnetization M is considered in the z-axis direction and the medium is with cubic symmetry [161]. Then the permittivity tensor is given:

$$\varepsilon(\omega, M) = \begin{vmatrix} \varepsilon_{xx} & \varepsilon_{xy} & 0 \\ -\varepsilon_{xy} & \varepsilon_{xx} & 0 \\ 0 & 0 & \varepsilon_{zz} \end{vmatrix} \tag{3-10}$$

Each tensor component may have a complex value, i.e. $\varepsilon_{ij} = \varepsilon'_{ij} + i\varepsilon''_{ij}$, and it depends on the magnetization M. The off-diagonal components introduce the anisotropy of the permeability via the magnetization inducing the magneto-optic effects, and vanish if the medium is not magnetized.

By giving the definitions $k_0 = \omega/c_0 = \sqrt{\varepsilon_0 \mu_0}\, \omega$, where c_0 is the light velocity in vacuum and $N = k/k_0$ as the vector of the *complex* refractive index, equation (3-9) becomes

$$\begin{vmatrix} N^2 - \varepsilon_{xx} & -\varepsilon_{xy} & 0 \\ \varepsilon_{xy} & N^2 - \varepsilon_{xx} & 0 \\ 0 & 0 & N^2 - \varepsilon_{zz} \end{vmatrix} \begin{vmatrix} E_x \\ E_y \\ E_z \end{vmatrix} = 0 \tag{3-11}$$

Here the case of light propagation along z-axis direction is considered. Then $E_z = 0$, and equation (3-11) is written as

$$(N^2 - \varepsilon_{xx})E_x - \varepsilon_{xy}E_y = 0$$
$$\varepsilon_{xy}E_x + (N^2 - \varepsilon_{xx})E_y = 0$$

(3-12)

To have non-zero solutions of E_x and E_y, the following relations must be fulfilled:

$$N_\pm^2 = \varepsilon_{xx} \pm i\varepsilon_{xy}$$

(3-13)

$$\pm iE_x = E_y = e^{\pm i\pi/2}E_x$$

(3-14)

These mean there are two normal modes of light propagation in the magnetized medium, and there is a fixed phase shift of $\pm\pi/2$ between E_x and E_y in each mode. Thus the normal modes are right-circularly polarized (σ^+, items are labelled with subscript "+" in this mode) and left-circularly polarized (σ^-, items are labelled with subscript "-" in this mode). The electric displacement (or called by electric flux density) in the medium then becomes

$$D_\pm = N_\pm^2 \varepsilon_0 (E_x \mp iE_y)$$

(3-15)

To express the relation between the complex dielectric tensor and the refractive index in σ^+ and σ^- modes, some helpful definitions are given:

$$\varepsilon_{xx} = \varepsilon_{xx}' + i\varepsilon_{xx}''; \ \varepsilon_{xy} = \varepsilon_{xy}' + i\varepsilon_{xy}''$$
$$N_\pm = n_\pm + i\kappa_\pm$$
$$\Delta n = n_+ - n_-; \ n = (n_+ + n_-)/2$$
$$\Delta\kappa = \kappa_+ - \kappa_-; \ \kappa = (\kappa_+ + \kappa_-)/2$$

(3-16)

Here n is the refractive index, and κ is the extinction coefficient of the light in the medium. After some algebraic transformations, the dielectric tensor elements can be expressed in terms of the refractive indices as:

$$\varepsilon_{xx}' = n^2 - \kappa^2 + \frac{1}{4}(\Delta n^2 - \Delta\kappa^2), \ \varepsilon_{xx}'' = 2n\kappa + \frac{1}{2}\Delta n\Delta\kappa$$
$$\varepsilon_{xy}' = n\Delta\kappa + \kappa\Delta n, \ \varepsilon_{xy}'' = \kappa\Delta\kappa - n\Delta n$$

(3-17)

Similarly the difference between the refractive indices and the extinction coefficients can be described in terms of the dielectric tensor elements as:

$$\Delta n = \frac{\kappa\varepsilon_{xy}' - n\varepsilon_{xy}''}{n^2 + \kappa^2}$$
$$\Delta\kappa = \frac{n\varepsilon_{xy}' + \kappa\varepsilon_{xy}''}{n^2 + \kappa^2}$$

(3-18)

Thus, the magnetization gives rise to the anisotropy of the dielectric tensor in (3.10), which determines the two modes of light propagation in the medium. For the two modes, the refractive indices and the extinction coefficients are not degenerate like in the non-magnetized case. Then it can be expected both the light wave amplitude and the phase could be changed by different

magnitudes for the light propagation of the two modes. The non-degeneracy of σ^+ and σ^- light propagation is responsible for the interpretation of the magneto-optic effects, which are schematically demonstrated in FIG A3-2 (Section A3).

- **Magneto-optic Faraday effect**

The Faraday effect is described in FIG 3.4-1(a), which could be the dominant magneto-optic effect especially for long optical transmission scale. For simplicity, it is assumed that both the magnetization **M** and the wave vector **k** are along z-axis direction, and the light is linearly-polarized in x-axis direction. The electric field is expressed as $\boldsymbol{E} = \begin{pmatrix} E_+ \\ E_- \end{pmatrix} = \dfrac{|E_x|}{\sqrt{2}} \begin{pmatrix} 1 \\ 1 \end{pmatrix}$ in the circular system with

$|E_+| = |E_-| = \dfrac{|E_x|}{\sqrt{2}}$ (see section A3). For the light transmission in the magnetized sample of a thickness

d, the respective electric field component becomes

$$E_+ = \frac{|E_x|}{\sqrt{2}} e^{i(k_+ d - \omega t)} = \frac{|E_x|}{\sqrt{2}} e^{i(N_+ k_0 d - \omega t)} = \frac{|E_x|}{\sqrt{2}} e^{i((n_+ + i\kappa_+)k_0 d - \omega t)} = \frac{|E_x|}{\sqrt{2}} e^{-\kappa_+ k_0 d} e^{i(n_+ k_0 d - \omega t)} \qquad (3\text{-}19)$$

$$E_- = \frac{|E_x|}{\sqrt{2}} e^{i(k_- d - \omega t)} = \frac{|E_x|}{\sqrt{2}} e^{i(N_- k_0 d - \omega t)} = \frac{|E_x|}{\sqrt{2}} e^{i((n_- + i\kappa_-)k_0 d - \omega t)} = \frac{|E_x|}{\sqrt{2}} e^{-\kappa_- k_0 d} e^{i(n_- k_0 d - \omega t)} \qquad (3\text{-}20)$$

Since the complex refractive indices N_+, N_- are non-degenerate as a consequence of magnetization, the phase and the amplitude are different for σ^+ and σ^- light. The linearly polarized light changes to an elliptically polarized light after transmission through the magnetized medium [Section A3]. The Faraday rotation angle is given as following (see equation (A-2)):

$$\theta_F = \frac{1}{2}(\arg(E_-) - \arg(E_+)) = \frac{1}{2}(n_- - n_+)k_0 d = \frac{-\omega d}{2c_0}\Delta n = \frac{-\omega d}{2c_0}\frac{\kappa \varepsilon_{xy}{}' - n\varepsilon_{xy}{}''}{n^2 + \kappa^2} \qquad (3\text{-}21)$$

The ellipticity of the polarization state is

$$\eta_F = \frac{|E_-| - |E_+|}{|E_-| + |E_+|} = \frac{e^{-\kappa_- k_0 d} - e^{-\kappa_+ k_0 d}}{e^{-\kappa_- k_0 d} + e^{-\kappa_+ k_0 d}} = \frac{e^{(\kappa_+ - \kappa_-)k_0 d/2} - e^{-(\kappa_+ - \kappa_-)k_0 d/2}}{e^{(\kappa_+ - \kappa_-)k_0 d/2} + e^{-(\kappa_+ - \kappa_-)k_0 d/2}} = \tanh(\frac{\Delta\kappa\omega d}{2c_0}) = \tanh(\frac{\omega d}{2c_0}\frac{n\varepsilon_{xy}{}' + \kappa\varepsilon_{xy}{}''}{n^2 + \kappa^2})$$

$$(3\text{-}22)$$

For the two circular modes, the relative phase shift is due to the circular birefringence, while the amplitude difference is caused by magnetic circular dichroism. In case of a long optical length, i.e. a small optical absorption, which means $\kappa \ll n$, the Faraday rotation and ellipticity can be approximated as

$$\theta_F \approx \frac{\omega d}{2nc_0}\varepsilon_{xy}{}'' + O(\kappa)$$

$$\eta_F \approx \frac{\omega d}{2nc_0}\varepsilon_{xy}{}' + O(\kappa)$$

$$(3\text{-}23)$$

- **Magneto-optic Kerr effect**

As a surface reflection effect, the Kerr effect depends on the reflection coefficients with respect to s wave and p wave, which can be described by the Fresnel reflection matrix [155]:

$$\boldsymbol{R} = \begin{pmatrix} r_{pp} & r_{ps} \\ r_{sp} & r_{ss} \end{pmatrix} \tag{3-24}$$

Here r_{ij} is the magnitude ratio of the i-polarized reflected electric field to the j-polarized incident electric field. The matrix element indicates the strength of the j-polarized wave changing to an i-polarized via boundary reflection. In absence of medium magnetization, non-diagonal elements r_{ps} and r_{sp} are zero. The magnetization gives rise to non-zero r_{ps} and r_{sp}, which determine the strength of the Kerr effect.

The current focus is the polar Kerr effect as shown in FIG 3.4-1(c) with normal incidence. In this case, the s-polarization wave and p-polarization wave cannot be any longer distinguished. This results in degenerate Fresnel reflection coefficients. It only needs to consider the reflection difference between the two normal circular modes. The reflection coefficients from the vacuum to the medium are [152]:

$$r_{\pm} = \frac{N_{\pm} - 1}{N_{\pm} + 1} \tag{3-25}$$

The incident light is assumed to be linearly-polarized in x-axis direction. The electric field is expressed as $\boldsymbol{E}_i = \begin{pmatrix} E_{i+} \\ E_{i-} \end{pmatrix} = \frac{|E_x|}{\sqrt{2}} \begin{pmatrix} 1 \\ 1 \end{pmatrix}$ with $|E_{i+}| = |E_{i-}| = \frac{|E_x|}{\sqrt{2}}$ [see Section A3]. The reflection wave is

$$\boldsymbol{E}_r = \begin{pmatrix} E_{r+} \\ E_{r-} \end{pmatrix} = \frac{|E_x|}{\sqrt{2}} \begin{pmatrix} r_+ \\ r_- \end{pmatrix} = \frac{|E_x|}{\sqrt{2}} \begin{pmatrix} (N_+ - 1)/(N_+ + 1) \\ (N_- - 1)/(N_- + 1) \end{pmatrix} = \frac{|E_x|}{\sqrt{2}} \begin{pmatrix} (n_+ - 1 + i\kappa_+)/(n_+ + 1 + i\kappa_+) \\ (n_- - 1 + i\kappa_-)/(n_- + 1 + i\kappa_-) \end{pmatrix} \tag{3-26}$$

The Kerr rotation angle is given by equation (A-7):

$$\theta_K = \frac{1}{2}(\arg(E_{r-}) - \arg(E_{r+})) = \frac{1}{2}(\arg(\frac{n_- - 1 + i\kappa_-}{n_- + 1 + i\kappa_-}) - \arg(\frac{n_+ - 1 + i\kappa_+}{n_+ + 1 + i\kappa_+})) = \frac{1}{2}(\theta_{K-} - \theta_{K+}), \tag{3-27}$$

with $\theta_{K+} = \arg(\frac{n_+ - 1 + i\kappa_+}{n_+ + 1 + i\kappa_+})$ and $\theta_{K-} = \arg(\frac{n_- - 1 + i\kappa_-}{n_- + 1 + i\kappa_-})$. It further leads to

$$\tan\theta_{K+} = \frac{2\kappa_+}{n_+^2 - 1 + \kappa_+^2}$$

$$\tan\theta_{K-} = \frac{2\kappa_-}{n_-^2 - 1 + \kappa_-^2} \tag{3-28}$$

By using the trigonometric relation of $\tan(2\theta_K) = \tan(\theta_{K+} - \theta_{K-}) = \frac{\tan\theta_{K+} - \tan\theta_{K-}}{1 + \tan\theta_{K+}\tan\theta_{K-}}$ and some algebraic transformations, it can be obtained as

$$\tan(2\theta_K) = \frac{-2[(n_-^2\kappa_+ - n_+^2\kappa_-) - (\kappa_+\kappa_- + 1)(\kappa_- - \kappa_+)]}{(n_+^2 + \kappa_+^2 - 1)(n_-^2 + \kappa_-^2 - 1) + 4\kappa_+\kappa_-} \tag{3-29}$$

Using the definitions in (3.16) and relations in (3.18), and neglecting items of higher orders, i.e. $O(\Delta n \Delta \kappa)$, $O(\Delta n^2)$ and $O(\Delta \kappa^2)$ *et al.*, it could be approximated as

$$\tan(2\theta_K) \approx \frac{-2[(n^3 - 3n\kappa^2 - n)\varepsilon_{xy}' + (3n^2\kappa - \kappa^3 - \kappa)\varepsilon_{xy}'']}{(n^2 + \kappa^2)((n+1)^2 + \kappa^2)((n-1)^2 + \kappa^2)} \tag{3-30}$$

For a small rotation angle, there is $\tan(2\theta_K) \approx 2\theta_K$. Then the Kerr rotation is further approximated as

$$\theta_K \approx -\frac{(n^3 - 3n\kappa^2 - n)\varepsilon_{xy}' + (3n^2\kappa - \kappa^3 - \kappa)\varepsilon_{xy}''}{(n^2 + \kappa^2)((n+1)^2 + \kappa^2)((n-1)^2 + \kappa^2)} \tag{3-31}$$

The ellipticity is given by equation (A-8):

$$\eta_K = \frac{|E_{r-}| - |E_{r+}|}{|E_{r-}| + |E_{r+}|} = \frac{|r_-| - |r_+|}{|r_-| + |r_+|} = \frac{|r_-|^2 - |r_+|^2}{(|r_-| + |r_+|)^2} \tag{3-32}$$

By similar mathematic processing, the ellipticity due to Kerr rotation can be obtained as

$$\eta_K \approx \frac{(\kappa^3 - 3n^2\kappa + \kappa)\varepsilon_{xy}' + (n^3 - 3n\kappa^2 - n)\varepsilon_{xy}''}{(n^2 + \kappa^2)((n+1)^2 + \kappa^2)((n-1)^2 + \kappa^2)} \tag{3-33}$$

In the experiment, the optical excitation is at a wavelength of 817.6 nm. To give a qualitative estimation of the magneto-optic effect, an absorption coefficient $\alpha \sim 10^4$ cm^{-1} is assumed at low temperature by considering excitation above absorption edge [162]. The penetration depth is on the order of 1 μm, which is much less than the substrate thickness of ~500 μm. The reflection from the substrate could be neglected, and thus the Faraday effect will be ignored due to the light reflection from the sample backside [153, 154, 163]. The dielectric constants of the studied n-GaAs are adopted from [164], i.e. $n \approx 3.7$, $\kappa \approx 0.1$. By using equation (3-31), the Kerr rotation angle is calculated $|\theta_K| \approx (0.02\varepsilon_{xy}' + 0.002\varepsilon_{xy}'')$, and $\eta_K \approx (-0.002\varepsilon_{xy}' + 0.02\varepsilon_{xy}'')$ from equation (3-33). Based on experimental results in Ref. [165], the value of ε_{xy}' and ε_{xy}'' is on the order of 10^{-2}. The Kerr rotation is supposed to be as weak as a few 10^{-1} milliradians and the ellipticity hardly changes by $\eta_K \sim 10^{-4}$. The magneto-optic Kerr effect has been observed and analysed in similar semiconductor systems [153, 154, 166, 167]. The sensitive detection of such small change of the light polarization is achieved by the time-resolved Kerr rotation setup discussed in the following section.

3.4.2 Time-resolved Kerr rotation setup

A schematic illustration of the time-resolved Kerr rotation setup is given in FIG 3.4-2.

- **Pump-probe beams**

The laser beams are provided by a mode-locked Ti-Sapphire laser system (Mira 900-D, Coherent), which is optically pumped by a solid state laser of 532 nm wavelength (Verdi 6, Coherent). The

lasing is performed in picosecond-mode with a repetition rate of ∼ 76 MHz. The temporal width of the generated laser pulses is ∼2 ps, and the wavelength is adjusted to $\lambda = 817.6$ nm. The output beam is divided by a beam splitter (BS1:50/50) into two beams, i.e. the pump beam and the probe beam. The pump beam is responsible for generating electron spin polarization, while the probe beam is used to detect the electron spin polarization via measuring the Kerr rotation.
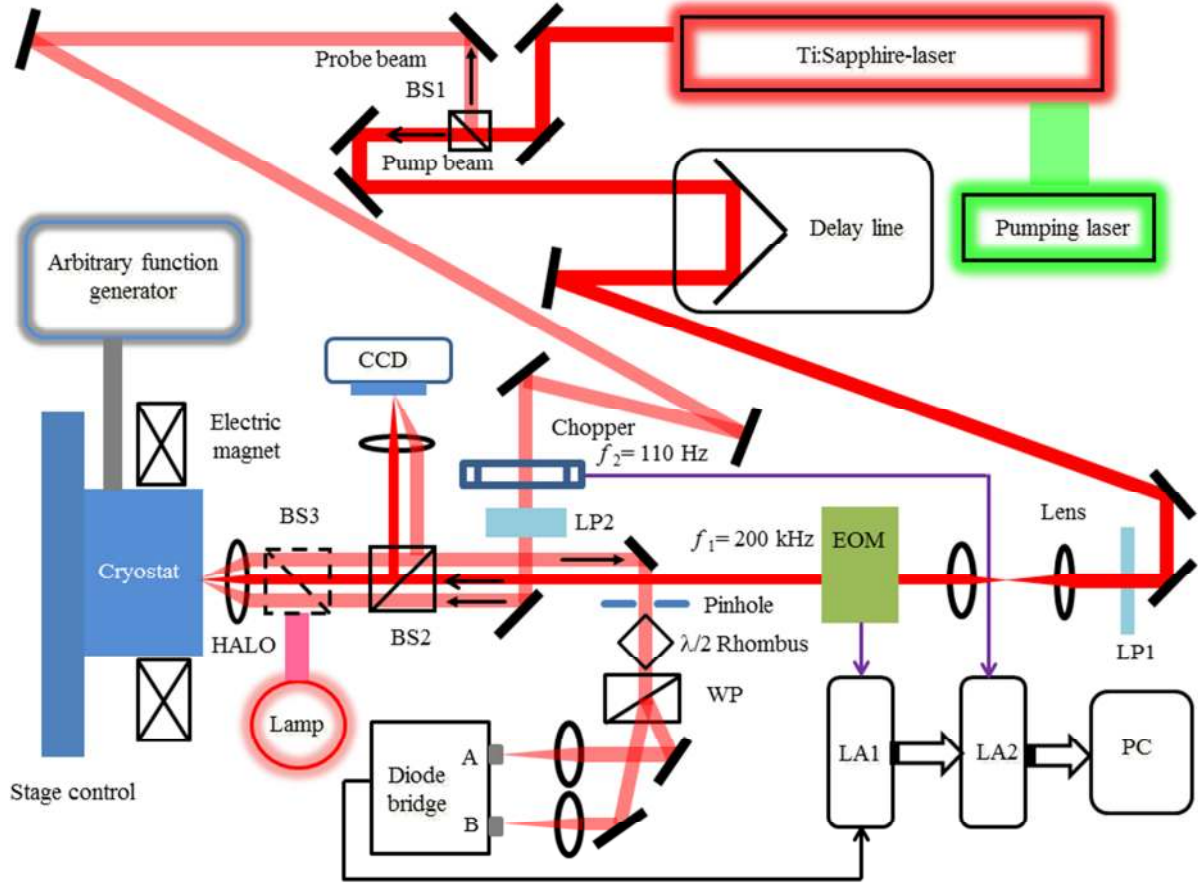

FIG 3.4-2: Schematics of the time-resolved Kerr rotation setup. For abbreviations in the figures, BS: beam splitter; LP: linear polarizer; EOM: electro-optic modulator; HALO: high-aperture laser objective; WP: Wollaston prism; LA: lock-in amplifier.

The pump beam is reflected by a retroreflector (BBR1-5, Newport Inc.), which is mounted on a motorized positioning stage with a remote controller (PS 90, OWIS). The linear polarizer (LP1) changes polarization of the pump beam parallel to the fast/slow axis of the following EOM. The lens group collimates and resizes the beam to a diameter of ∼2.5 mm at the EOM entrance window. The EOM is electrically driven by a TTL sequence from an arbitrary function generator (AFG 3252, Tektronix). The optical modulation frequency is 200 kHz for $\lambda/4$, $\lambda/2$ or $3\lambda/4$ phase retardation, which accordingly transforms the light to the polarization state of σ^+, linearly polarized and σ^-, respectively. The duty cycle is chosen as 50:50 or 80:20. To get circular-polarized light on average (within one period), one level is set to $\lambda/4$ or $3\lambda/4$ phase modulation, while the other is set to $\lambda/2$ phase modulation. To get *linearly* polarized light *on average*, the duty cycle is used as 50:50 and the

two levels are set to $\lambda/4$ and $3\lambda/4$, respectively. The beam is focused onto the sample by a high-aperture laser objective (Linos). The focal length is 50 mm, the N.A. is 0.31, and the incident clear aperture is 30.3 mm. By using Equation (3.3), the spot size is estimated around 10 μm for the pump beam.

The probe beam is guided through an optical chopper (MC1000A, Thorlabs). The beam intensity is modulated with a frequency of 110 Hz. The following linear polarizer (LP2, extinction ratio $< 10^{-6}$) makes the light highly linear-polarized. The diameter of the probe beam is around 4 mm, and focused onto the sample by the HALO. By using equation-(3-34), the spot size is estimated around 6.5 μm for the probe beam on the sample surface.

The length difference of the light path between the pump beam and the probe beam is controlled by the motor-activated stage. It functions as a time delay-line. The controlled length scale is $L = 1$ m, and doubles by considering the reflection path. It is capable to provide a time delay of $\Delta t = 2L/c0 \approx 2 \times 1$ m$/(3 \times 10^8$ m/s$) \approx 6.7$ ns, which gives an upper-limit for the pump-probe time range. The step size is 2.5 mm, which gives a temporal resolution of ~8.3 ps for the pump-probe measurements.

The incident beam positions on the HALO are shown in FIG 3.4-3. For most measurements, the power of pump beam is measured ~3 mW and the probe beam is ~ 0.6 mW in front of HALO. The excitation power ratio is always kept around 5:1 during all pump-probe measurements. Taking account into the beam size, the incidence angle is $\theta_1 \approx 18°$ for both. Then the refracted angle is $\theta_2 \approx \theta_1 /n_{GaAs} \approx 4.9°$ in the GaAs active layer (also see inset of FIG 3.4-4). For the pump beam, this tilting angle can enhance the nuclear field facilitating the experimental observations. For the probe beam, this geometry could well separate the incident and reflection beam, which carries the Kerr rotation signal for detection.
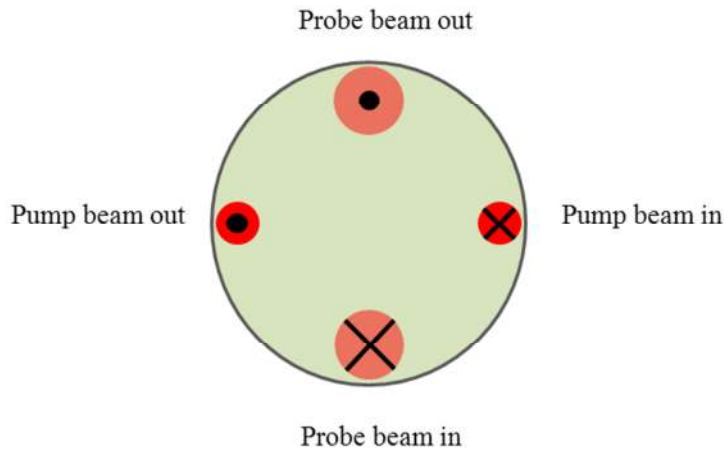

FIG 3.4-3: Incident positions of pump and probe beams on the HALO

- **Sample cryostat**

The studied sample is pasted on a sample holder in a Helium-flow microcryostat (Oxford Instruments). By pumping liquid Helium flow through the cryostat, the sample temperature can be cooled down to 2.2 K and increased up to 500 K by using the cryostat heater. The sample

temperature is set and read by the temperature controller (ITC 5305, Oxford Instruments). The cryostat is mechanically fixed on a xyz-translation stage, which is controlled manually. An electric-magnet (Magnet BE-10, Bruker) can provide a magnetic field up to 1.3 Tesla on the sample in Voigt geometry, i.e. the optical path is perpendicular to the magnetic field. The magnetic field is set and read by a power supply controller.

To obtain the structure details and the laser spot positions, the sample is illuminated by a lamp. The sample is imaged by a CCD camera which is connected to a monitor. The overlapping between the pump beam and probe beam, and the detected area within the microcoil are checked prior to starting the measurements. The beam splitter BS3 (50%:50%) is removed during measurements. The beam splitter BS2 has a ratio of 92% and 8% for transmission and reflection, respectively.

- **Detection of the Kerr rotation signal**

The reflection of the linearly polarized probe beam carries the Kerr rotation information. It propagates through a mechanical pinhole and a $\lambda/2$ phase retarder of a Rhombus prism. The Wollaston prism (WP) separates the beam into two beams with normal polarization states. Each beam is focused into one photodiode detector (A/B) within the auto-balanced photoreceiver (Nirvana 2007, New Focus). The $\lambda/2$ retarder can be rotated around its optical axes, so that the light polarization can be adjusted to arbitrary direction. In case of no electron spin polarization in the studied sample, the retarder is rotated to a fixed position, at which the light intensity of the two beams after the WP is the same. Therefore it is assured the diode bridge is balanced with $\Delta U = |U_A - U_B| = 0$ for the sample without magnetization. Then in case of non-zero electron spin polarization after circular-polarized pumping, ΔU represents the electron spin polarization during measurements.

The voltage difference ΔU is extracted by a double lock-in technique [153, 154]. The electric signal is introduced to the first lock-in amplifier (DSP 7265, EG&G Instrument) with a reference signal of $f_1 = 200$ kHz, which is synchronized with the EOM modulation. For the second lock-in amplifier (Model 5301, EG&G Princeton Applied Research), the reference signal has a frequency $f_2 = 110$ Hz given by the output TTL square wave from the mechanical chopper. This gives a detection sensitivity of less than 1 µrad for the Kerr rotation of the probe beam [153].

- **Data evaluation**

The pump-probe measurements are performed in the so-called oblique experiment geometry presented in FIG 3.4-4. The external magnetic field $\boldsymbol{B}_{ext}$ is applied in the in-plane direction, while the optical beams are incident with titling angles to the sample surface. The incident angle is indicated in the inset. After circularly polarized (σ^+/σ^-) optical pumping, the spin-polarized electron ($\boldsymbol{S}$) ensemble precesses around the magnetic field of $\boldsymbol{B}_{tot} = \boldsymbol{B}_{ext} + \boldsymbol{B}_N$ with $\boldsymbol{B}_N$ as the nuclear field. The linearly polarized probe beam is used to detect the S_x component of electron spin $\boldsymbol{S}$, mainly arising from the polar magneto-optic Kerr effect.

A typical scanning of TRKR measurements is presented in FIG 3.4-5. After optical absorption, spin polarized electron-hole pairs are generated. (i) In the first few 10 ps, the dephasing process of the

hole spin is done due to strong state mixing between heavy and light holes; meanwhile the optically generated carriers average spin polarization to the donor-bounded electrons via exchange interaction [168]. (ii) In the next several 100 ps, the total electron spin ensemble precesses around the $\boldsymbol{B}_{tot}$ with a certain extent of spin dephasing. (iii) After electron-hole recombination, the bound electrons are left and the spin relaxation process ranges from a few ns even up to 100 ns, which depends on the sample doping level and the experiment conditions. Therefore the detected signal can be expressed as

$S_x = \sum_i | S_i | e^{-t/T_{2i}^*} \cos \omega_i t$, with i for the different carrier type, ω the precession frequency, T_2^* the spin

dephasing time constant and S as the carrier spin polarization .
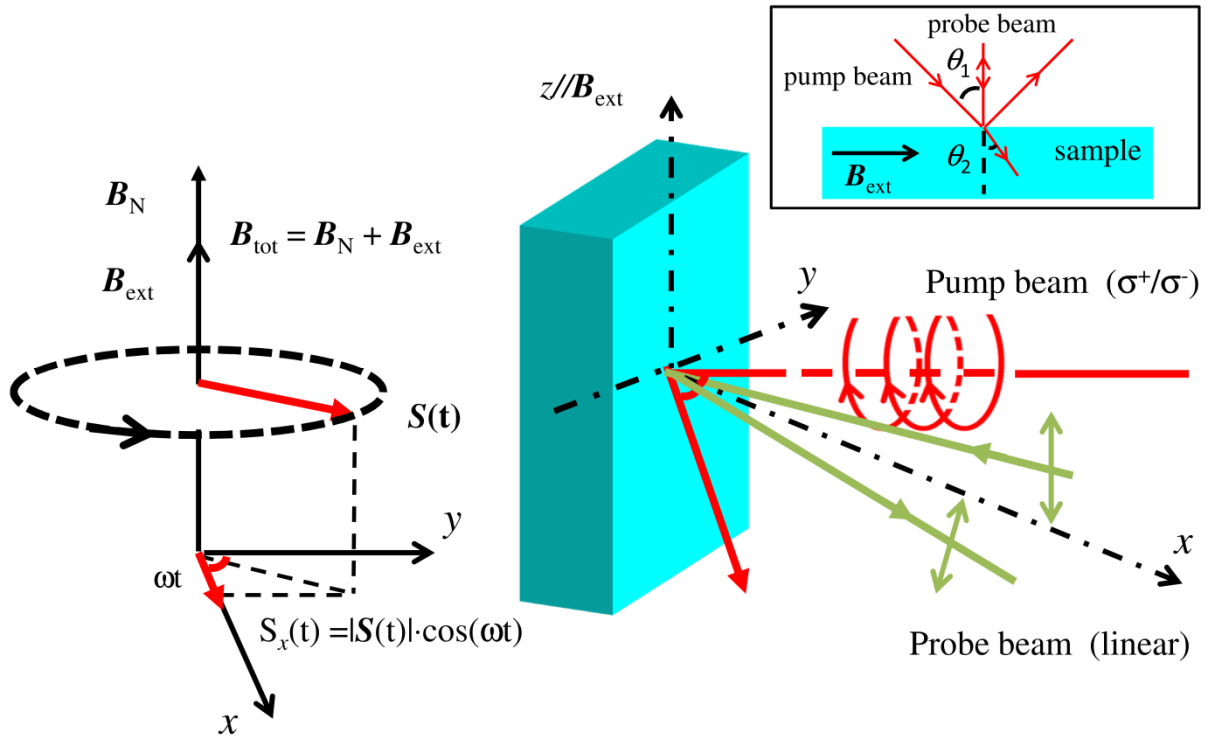
FIG 3.4-4: Pump-probe experiment geometry. After circularly polarized (σ^+/σ^-) optical pumping (red), the electron spin S precesses around the total field B_{tot}. The polar Kerr rotation is detected via the probe beam (green) with linear polarization at incidence.

Since the carrier spin dynamics is complicated within the first few 100 ps, and on the other hand the electron spin precession Larmor frequency ω_L is the focus of the data evaluation, fittings are performed according to experimental data with time delay longer than 200 ps. From $\omega_L = g\mu_B B_{tot}/\hbar = g\mu_B|\boldsymbol{B}_{ext}+\boldsymbol{B}_N|/\hbar$, the extracted ω_L represents the nuclear field. Here g is the Landé g factor, μ_B is Bohr magneton and $\hbar$ is reduced Planck constant. The red curve is fitted by the function

$$S_x(t) =| S | \cdot e^{-t/T_2^*} \cos \omega_L t + DC \tag{3-35}$$

The data-fitting is performed by 1stOpt software (7D-Soft High Technology Inc.). The quantities $|S|$, T_2^*, ω_L and DC are treated as free parameters. The Levenberg-Marquardt algorithm is adopted and

the fitting is finished with a typical correlation coefficient of 0.9999. The blue curve gives an indication of the electron spin dephasing envelope.
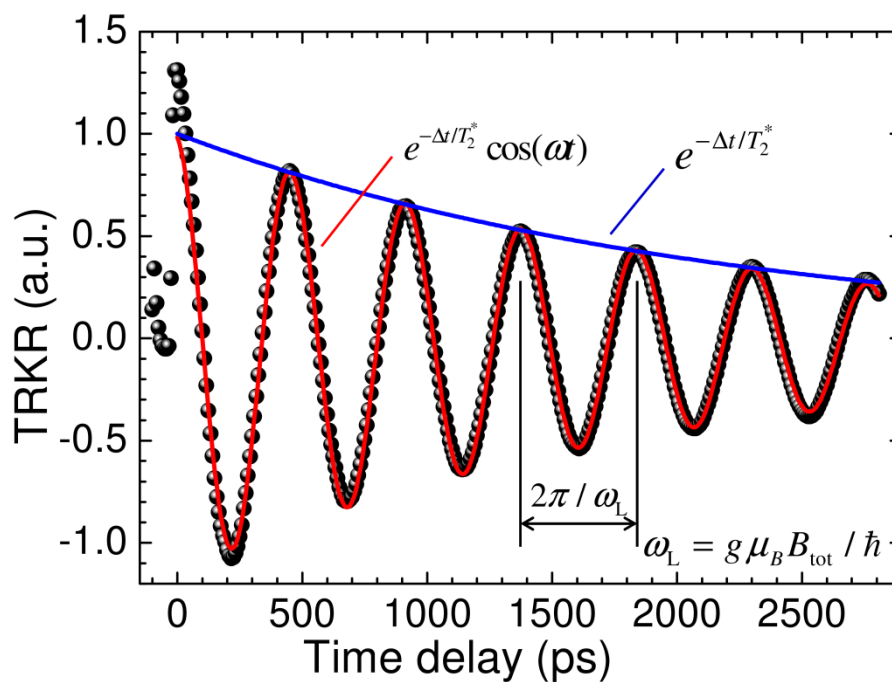

FIG 3.4-5: Fitting for TRKR experimental data. The solid balls are experimental data and the red curve is by fitting. The blue envelop indicates electron spin dephasing and the periodic oscillation is from the electron Larmor precession around the total magnetic field. For the fittings, $T_2^* = 1$ ns and $\omega_L = 13.585$ GHz.

4   LOCAL CONTROL OF SPIN POLARIZATION BY AN ON-CHIP MICROSCALE CURRENT LOOP

In this chapter, the concept of local electrical control of spin polarization is demonstrated by using the on-chip microscale current loop. In the first part, the magnetic properties of the diluted magnetic semiconductor quantum wells are characterized in a static magnetic field. The strong *sp-d* exchange interaction between the carriers and Mn ions makes the excitons have a large effective *g* factor, which is experimentally determined to be ~200 at liquid helium temperature. The photoluminescence thus shows pronounced polarization in the low field regime. In the second part, a magnetic field is generated by introducing a current through the on-chip microcoil. The switchable magnetic field allows an electrical control of the spin polarization, which is a competing result between the current-induced magnetic field raising the magnetization of Mn ions and the current-generated local heating for the demagnetization. A method is developed to extract the contribution from each mechanism. In the last part, the magnetization dynamics on a sample with a higher Mn content is found to occur on a time scale below 10 ns, so that it can function as a detector for the phonon dynamics which is on a longer time scale.

4.1   Diluted magnetic semiconductor quantum wells in a static magnetic field

The layer structures of the studied semiconductor samples are schematically given in FIG 4.1-1. Two wafers of diluted magnetic semiconductor quantum wells (DMS QWs) are investigated. The samples are grown by molecular beam epitaxy on an undoped GaAs (001) substrate with a 2.47 μm thick CdTe buffer layer. A DMS QW of $Cd_{1-x}Mn_xTe$ with a thickness of 12 nm is embedded between a 1.23 μm thick lower $Cd_{1-y}Mg_yTe$ barrier and a 70 nm $Cd_{1-y}Mg_yTe$ cap layer, both with a Mg content y = 0.30. For the DMS QW layer, the manganese concentration is x = 0.067 and x = 0.024 for Sample 1 and Sample 2, respectively.

On the left side, the energy bandgap structure for the heterostructures is given. The values are calculated using the empirical formulae given in Equation (2.45) for (Cd, Mn)Te DMS QW and Equation (2.46) for the (Cd, Mg)Te barrier. Due to the pinning of the surface acceptor states and the Fermi level of the QW layer, there is a band bending across the heterostructures, and thus the sample is *p*-doped with the hole gas. The sheet density of the hole gas is determined by monitoring the Moss-Burstein shift, the energy shift between the photoluminescence (PL) energy and the optical absorption energy [169]. The hole density is strongly dependent on the cap layer thickness [109]. Thereby this method is found valid for the Mn concentration up to x = 0.093. The hole density is found maximum for a cap layer thickness of ~25 nm. Based on the systematic studies in Ref. [109], the hole density is estimated $\sim 7 \times 10^{10}$ cm^{-2} for the studied samples with a capper layer thickness of 70 nm. The existence of the acceptor states is suggested to originate from the formation of telluride oxides, which play a role to trap electrons [170].
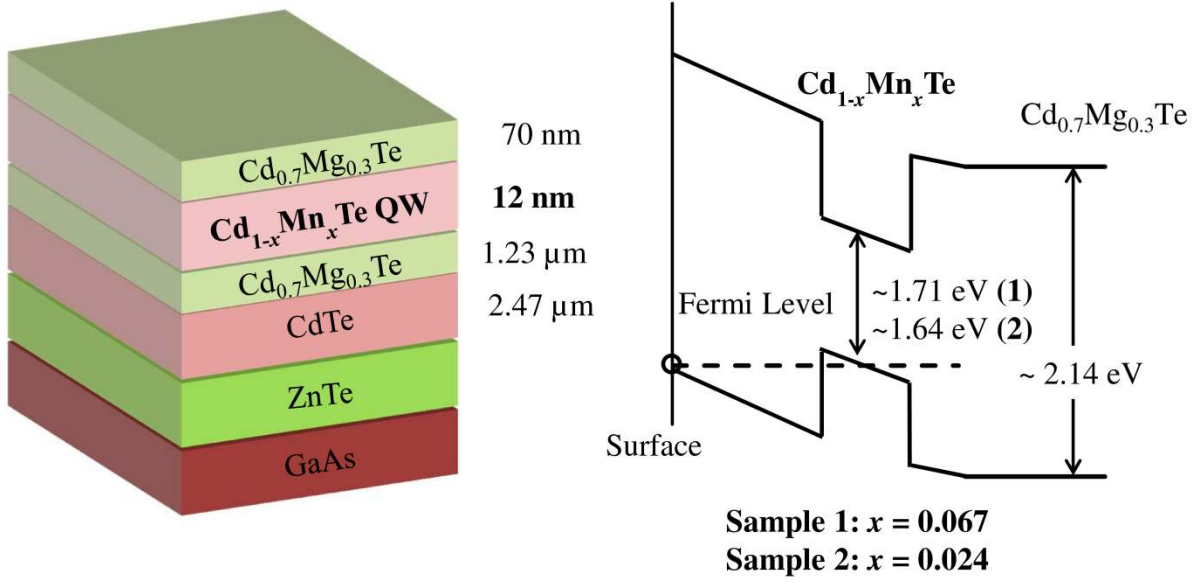
FIG 4.1-1: Left: Layer structure schematics of the studied DMS QWs. Right: the energy band structure for the heterostructure. The values of energy bandgaps are marked. The pinning of the Fermi level and the surface states gives rise to the band bending. After Ref.[169] .

4.1.1 PL spectrum studies

As theoretically demonstrated in Section 2.3.2, the giant Zeeman splitting can be manifested in the PL spectrums of a DMS structure in a magnetic field. The energy splitting is hardly dependent of the exciton type, either neutral exciton (X) or positively charged (trion, $X+$), each of which has a huge effective g factor. These results from the magnetization of Mn ions, which strongly polarize the carriers via sp-d exchange interaction.

The magnetic field dependence of the σ^+-polarized PL spectrum is presented in FIG 4.1-2 for both samples with x = 0.024 (left) and x = 0.067 (right). For each sample, both trions and neutral excitons are observed in the PL measurements. This evidences the existence of the hole gas from the surface doping. At an external field of $B_{ext} = 0$, the PL intensity is dominated by X^+ and the X is absent for the sample with x = 0.024, while both X^+ and X are present for the sample with x = 0.067. This is possibly due to the higher Mn concentration which gives a larger bandgap, so that the Fermi level is less below the valence band edge and thus, the hole density is reduced.

By increasing B_{ext}, the X intensity becomes more prominent while the X^+ intensity is reduced. This arises from increasing sp-d exchange interaction competing with the dissociation energy [125]. The exchange interaction polarizes the holes in a preferred orientation, while the trions always take two holes with antiparallel spin orientations. This dissociation energy can be estimated ~ 4 meV from the spectral distance between the X peak and the X^+ peak. This explains why the X^+ intensity is vanishing at a magnetic field of around 1 T for the sample of the higher Mn content and at around 5 T for the lower Mn content. The broader spectral width for the higher Mn content might be due to the

enhanced interface roughness (between the QW and the barrier) or alloy fluctuations [171], and the larger magnetic fluctuation [172] , which both contribute larger fluctuations of the exciton energy.
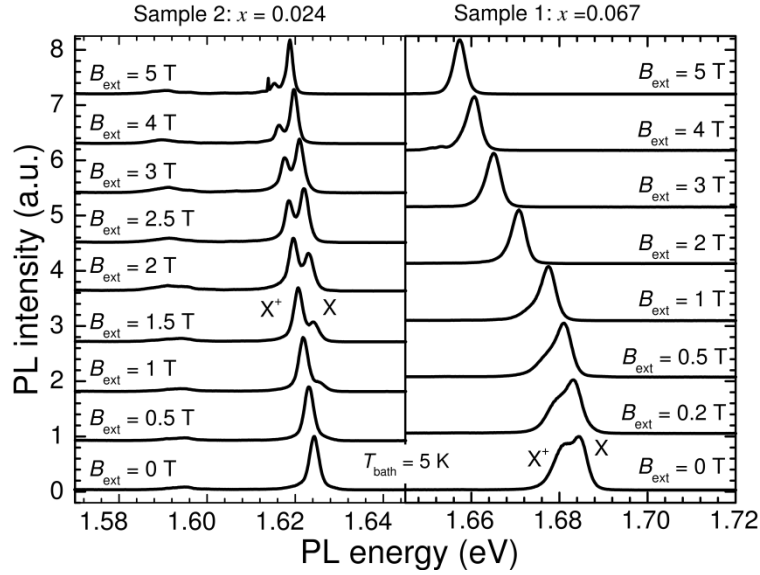

FIG 4.1-2: Magnetic field dependence of the σ^+-polarized PL spectra for the sample with x = 0.024 (left) and x= 0.067, respectively. The neutral exciton (X) and the positively charged exciton (X^+) are marked. The PL intensity is dominated by X^+ in the low field, while X is dominating in the high magnetic field regime.

As a pronounced effect, the PL spectra are both clearly red-shifted by increasing the magnetic field. The field dependence of the PL energy shift is plotted in FIG 4.1-3. Since the energy splitting for X and X^+ have a similar dependence of the magnetic field, either X or X^+ PL energy shift gives an estimation of the *sp-d* exchange interaction. The energy shift is extracted with respective to the PL energy at zero field, using the X line for x = 0.067 and X^+ line for x = 0.024 from FIG 4.1-2. Each energy shift can be nicely fitted (red lines) by the Brillouin function described in Equation (2-54) and Table 2-2. The effective Mn^{2+} ion spin is $S_{eff} \approx 1.10$ for sample 1 and $S_{eff} \approx 1.02$ for sample 2. These values are close to the theoretically predicted plotted in FIG 2.3-3. The antiferromagnetic temperature parameters are $T_0 \approx 3.9$ K and $T_0 \approx 2.6$ K. Further, the effective exciton g factor is evaluated about ~ 200 for sample 1 and ~ 60 for sample 2, which are in good agreement with calculations indicated in FIG 2.3-4 and Equation (2.78).

The PL spectra for different temperatures are shown in FIG 4.1-4. The measurements were performed for sample 1. At zero external field (a), the PL energy shift versus temperature is determined by the Varshni shift: the PL energy is red-shifted for a higher temperature [173]. As well, the X^+ intensity is clearly reduced by raising the temperature, which is a competing result between the increasing thermal kinetic energy and the diminishing dissociation energy [125]. The X^+ is highly suppressed at a temperature above 20 K. In case of a strong magnetic field $B_{ext} = 5$ T, the PL spectrum undertakes a blue-shift with increasing the temperature. This is mainly influenced by the weaker Mn ion magnetization at an elevated temperature, and thus the *sp-d* exchange interaction is

reduced giving a smaller energy splitting. The monitored energy shift is a combination of the giant Zeeman effect and the Varshni shift.
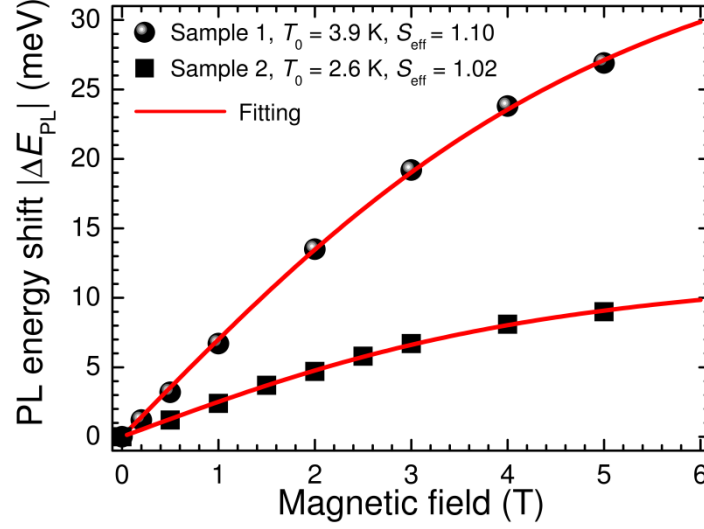

FIG 4.1-3: Magnetic field dependence of the σ^+-polarized PL energy shift. The energy shift is extracted respective to PL energy of the neutral exciton (sample 2) and the trion (sample 1) at zero magnetic field. Red lines are fittings by the Brillouin function, and the fitting parameters are indicated for each sample. $T_{bath} = 5$ K.
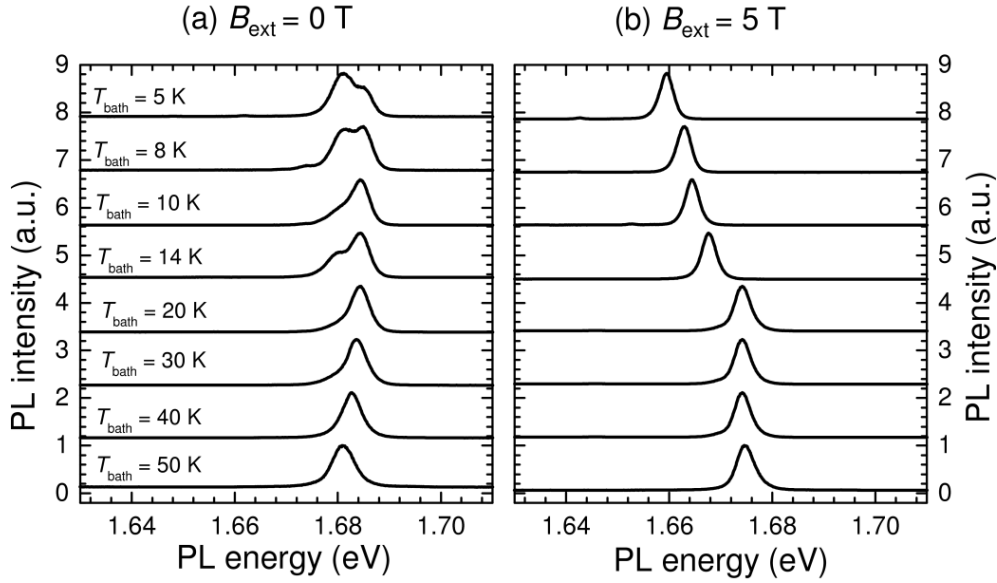

FIG 4.1-4: Temperature dependence of the PL spectra for sample x= 0.067. The Varshni shift is reflected in the case of $B_{ext} = 0$ T (a), and the energy shift in case of $B_{ext} = 5$ T (b) is controlled by both the Varshni shift and the giant Zeeman effect.

The giant Zeeman splitting ΔE_{PL}^{ex} versus temperature is plotted in FIG 4.1-5. It is obtained from FIG 4.1-4 (b) by subtracting the Varshni shift evaluated from FIG 4.1-4 (a). The energy shift is nicely fitted with the Brillouin function (red line) using the same parameters as determined in FIG 4.1-3. The Mn ion magnetization is suppressed in the high temperature regime, i.e. the *sp-d* exchange

interaction is reduced by a factor of two from $T_{bath} = 5$ K to $T_{bath} = 20$ K. The Varshni shift is depicted in the inset, and the data are fitted by

$$\Delta E_{varsh} = -\frac{aT_{bath}^2}{T_{bath} + b},$$ (4-1)

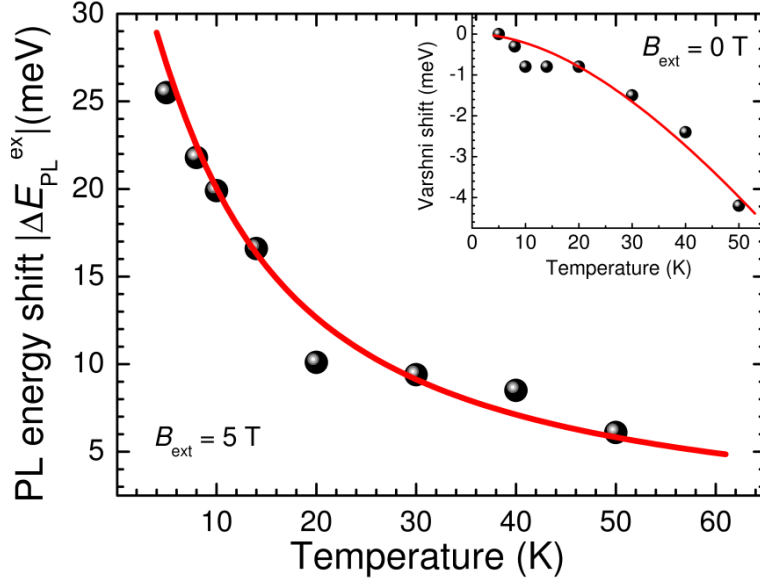in which the fitting parameters are $a = 0.24$ meV/K and $b = 100$ K, which are close to the literature data [174].

FIG 4.1-5: Temperature dependence of the PL energy shift for sample x= 0.067. The extracted energy shift is controlled by the giant Zeeman splitting at $B_{ext} = 5$ T, and it is fitted by the Brillouin function using the same parameters as FIG 4.1-3. The Varshni shift is depicted in the inset for $B_{ext} = 0$ T.

4.1.2 PL polarization studies

In addition to the PL energy shift, the PL polarization can characterize the giant Zeeman effect in the low magnetic field regime. As theoretically discussed in Section 2.3.2, the PL polarization can sensitively reflect the Mn^{2+} ion magnetization at a weak magnetic field and the exciton energy relaxation after a non-resonant excitation. The following measurements are performed in static magnetic fields, so the results of the PL polarization are characterized by the magnetization of Mn ions in an equilibrium (or quasi-equilibrium) state. These data give important references for the results after this section.

The magnetic field dependence of the PL polarization degree is presented in FIG 4.1-6. For each sample, there is a pronounced PL polarization in the low field regime, which gets saturated with a value of $\rho_s \sim 92\%$. It is less than unity due to several possible facts. First, the saturated PL polarization degree is $(1 + \tau_s/\tau_{EX})^{-1}$ according to Equation (2.74) or (2.88). The finite spin relaxation time τ_s of a few picoseconds and the exciton life τ_{EX} of 100 ps ~ 200 ps can make $\rho_s < 1$. The second factor can be simply due to the imperfect polarization optics in Section 3.3.1. The third possible

reason can be due to the fluctuation of the Mn ion, which can depolarize the exciton spins reducing the PL polarization [137]. It requires an external field up to a few Tesla to suppress the magnetization fluctuations in DMS quantum dots [175]. Nevertheless this effect seems to play little role for the studied QW structures. A critical Mn concentration in an epilayer was verified to be x = 0.07 for achieving the formation of magnetic polarons [176], and thus it is quite unlikely to obtain magnetic polarons for the sample of x = 0.024 here.

The PL polarization is more sensitive to the applied magnetic field for the sample 1 than for sample 2. This is a direct result of a larger Mn magnetization for a higher Mn concentration, while it turns out to more strongly polarize the photon-excited carriers via the *sp-d* exchange interaction. According to the saturation level of ρ_s, the experimental data can be nicely fitted by Equation (2.74) or (2.88) using T_0 and S_{eff} determined from the spectroscopic results in FIG 4.1-3. From time-resolved PL measurements, $\tau_{X,X_+} = 220$ ps is used for Sample 1 and $\tau_{X,X_+} = 160$ ps for Sample 2. The spin relaxation time is $\tau_s = 5$ ps for both fittings. A constant exciton temperature $T_{X,X_+} = T_{bath} + \Delta T_{exc}$ is assumed and a value of $\Delta T_{exc} = 8.5$ K is used for both samples. This exciton temperature being higher than the bath temperature is reasonable by considering the non-resonant excitation at 1.943 eV and an energy relaxation time which is comparable with the exciton lifetime. Here the excitation level is over 200 meV above the QW energy bandgap but ~200 meV lower than the barrier energy level. The lattice heating from the hot excitons is less than 1 K and thus it is neglected, e.g. see FIG 4.1-8.
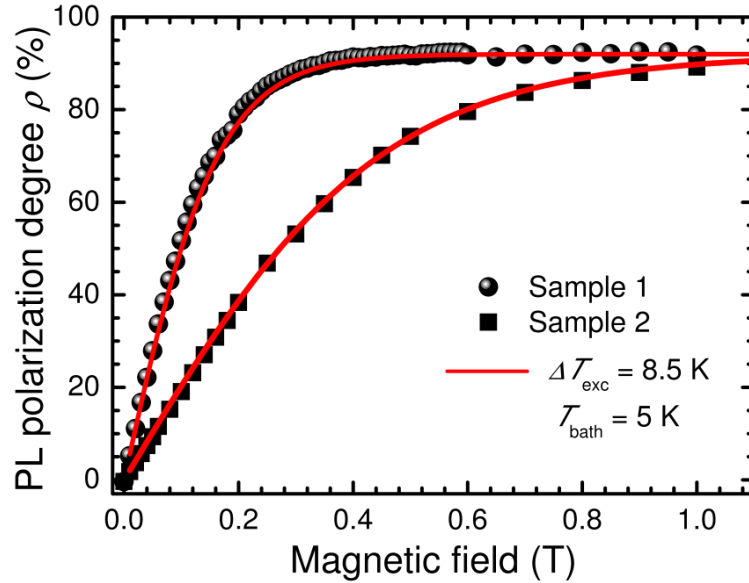

FIG 4.1-6: PL polarization degree versus a static magnetic field. The experimental data of each sample are fitted by using same parameters determined from FIG 4.1-3. The exciton temperature is used higher than the bath temperature by ΔT_{exc} for both samples. The excitation power density is ~150 W/cm^2.

FIG 4.1-7 presents the temperature dependence of the PL polarization for the two samples in an external magnetic field of $B_{ext} = 100$ mT. The PL polarization is clearly reduced by increasing the

sample temperature, and it can be resolved for a temperature difference of 1 K. These data cannot be well fitted anymore using determined parameters above, since the exciton lifetime, the spin relaxation and kinetic relaxation time all depend on temperature. These data serve as references for determining the Mn^{2+} ion spin heating for the experimental results discussed later.

The power dependence of the PL polarization is given in FIG 4.1-8 for the two samples. The magnetic field is $B_{ext} = 100$ mT, and the bath temperature is $T_{bath} = 5$ K. Generally the polarization is reduced by increasing the optical excitation power. The excess kinetic energy of the photon-excited carriers can be transferred to the pre-existing holes and efficiently transferred to the Mn ions. Meanwhile the carriers can dissipate kinetics to the lattice system which can heat the Mn ions by spin-lattice relaxation [42, 63]. The coupling between the Mn ions, carriers and the lattice system is presented in Section 5.1.2, e.g. see FIG 5.1-1. There is an appreciable heating of Mn ions for the power larger than 10 μW (corresponding a power density of $\rho_{exc} \sim 250$ W/cm^2, see Section 3.3.1). To evaluate the density of the optically generated carriers, the optical absorption coefficient is used as $\alpha_{CdTe} \approx 2 \times 10^4$ cm^{-1} [177], and the exciton lifetime is used as $\tau_{EX} \approx 200$ ps. The photon-generated carrier density is given as $n_{opt} \sim \rho_{exc} \cdot \tau_{EX} \cdot [1- \exp(-L_z \cdot \alpha_{CdTe})] \approx 4 \times 10^9$ cm^{-2}. Here the thickness of the QW is denoted as $L_z = 12$ nm. To note, the hole density from surface doping is $\sim 7 \times 10^{10}$ cm^{-2}. Therefore pronounced heating could be generated even by a relatively small amount of hot carriers compared with the carriers from surface doping.
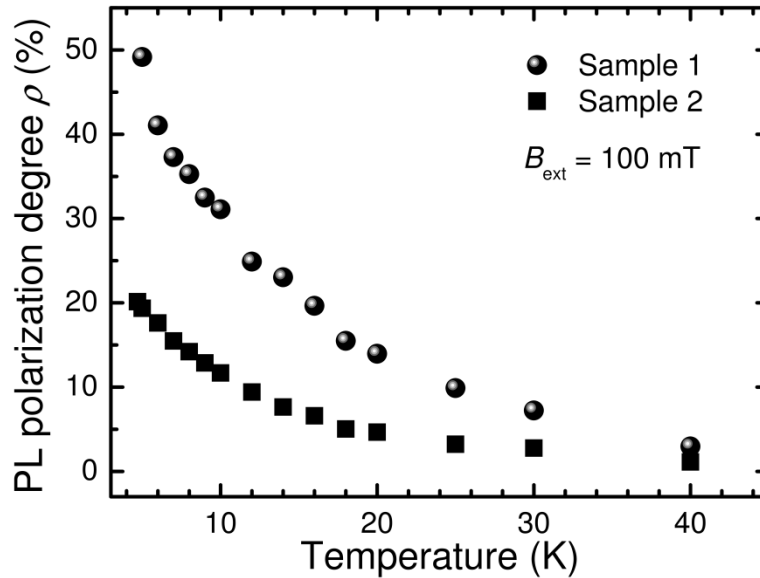

FIG 4.1-7: Temperature dependence of the PL polarization degree in a magnetic field of $B_{ext} = 100$ mT. The excitation power density is ~150 W/cm^2.

By comparing the power dependence of the PL polarization and the temperature dependence in FIG 4.1-7, it can be seen that the Mn heating is larger for the sample of a lower Mn content than the higher one by using the same excitation power. For an excitation power of 200 μW, the Mn heating is ~5 K in case of x = 0.023 and less than 2 K for x = 0.067. This can be understood by considering a

faster spin-lattice relaxation process in sample 1, in which the Mn ions can couple more strongly with the lattice system [178]. As a result, the Mn heating is more contributed from the heated lattice system, which holds a much larger thermal capacity and thus the Mn ions are less efficiently heated by hot carriers for the sample with x = 0.067.
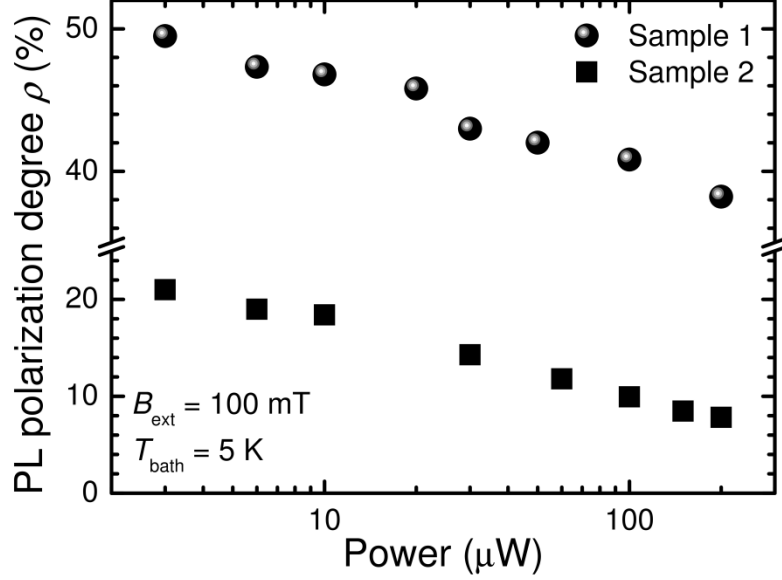

FIG 4.1-8: Power dependence of the PL polarization degree in a magnetic field of B_{ext} = 100 mT and a bath temperature of T_{bath} = 5 K. The excitation power density is ~150 W/cm^2.

4.2   Local control of spin polarization by an on-chip current loop

To obtain local spin manipulation is one key topic towards the applications of spin-based electronic devices [20]. By applying an electric field, the carrier concentration can be controlled to modulate the carrier-Mn ion exchange interaction in a DMS QW [26], the electron-electron exchange interaction can be varied by adjusting the overlapping of the electronic wavefunction in a double quantum dot system [34], the electron wavefunction can be dragged to tune the value of the Lande g factor in a heterostructure [179], or the spin-orbit coupling can be directly controlled [35]. The optical methods have been demonstrated to manipulate the electron spins in an ultrafast regime based on optical Stark effect [36] and the inverse Faraday effect [180]. These effects could be treated like the generation of an *effective* magnetic field for the carrier spins.

The straightforward method is to use a magnetic field. Such an on-chip magnetic field can stem from a micro/nano-ferromagnet (FM) on top of the semiconductor [28-31, 62], which allows one to define a locally varying landscape of spin states in the semiconductor. It was even suggested to trap carriers with a defined spin states on a nanometer scale [181]. However, the ability to vary the magnetization of the micro/nanostructured FMs in order to gain external control over the local spin polarization is quite limited. One possibility is to employ short, intense laser pulses under an applied external magnetic field [182, 183] or even in zero field by using polarized optical excitation [180]. Another alternative is the current-induced magnetic field from a sub-millimeter coil which has been utilized

to electrically manipulate spin states of Mn^{2+} ions for studying the magnetization dynamics in DMS QWs [33, 56].Here a microscale coil is used to achieve the local spin control in a DMS QW. The PL results presented in this section are obtained by using the experiment scheme in FIG 3.3-4.

A schematic description of the concept is given in FIG 4.2-1.By introducing a current through the microcoil, a magnetic field B_I is generated in the coil center dominant in the out-of-plane direction. The Mn ions are magnetized, and via *sp-d* exchange interaction, the carriers are highly spin-polarized. Since the exciton spin relaxation process is much faster than the exciton recombination rate, i.e. $\tau_s <<$ τ_{EX}, the excitons experience a giant Zeeman effect during the lifetime, and thus the PL emission is expected to be circularly polarized. In order to maximize the giant Zeeman splitting or the exciton spin polarization, a large effective *g* factor is required. Therefore the studied sample is chosen to be Sample 1 with the Mn content of x = 0.067, and the PL polarization degree (under cw excitation) is expected to be pronounced in presence of a few mT magnetic field as shown in FIG 4.1-6.
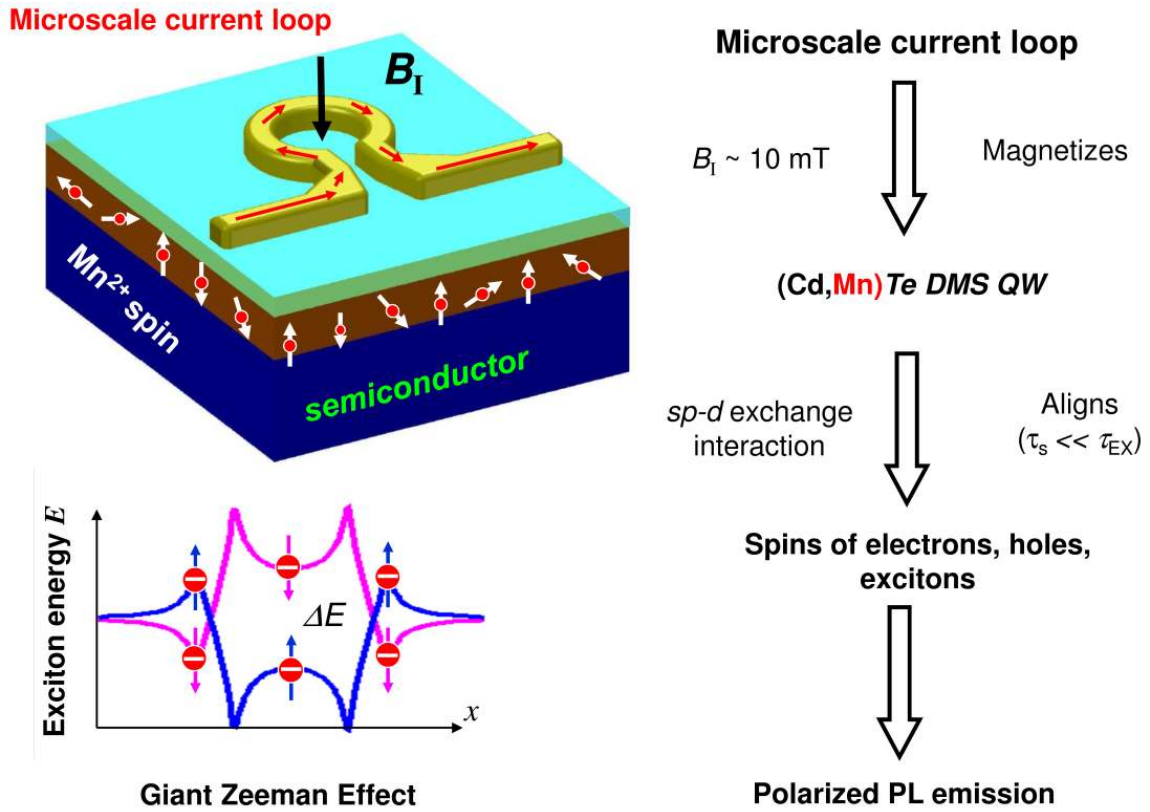

FIG 4.2-1: Schematic description of the local spin control by a microscale current loop in a DMS QW

FIG 4.2-2(a) shows an optical micrograph of the A2 structure with an inner radius of 2.8 μm and coil width of 2 μm. In FIG 4.2-2(c), the spin polarization degree $\rho = (I^{\sigma^+} - I^{\sigma^-})/(I^{\sigma^+} + I^{\sigma^-})$ in the coil center (black), with I^{σ^+}, I^{σ^-} being the intensities of σ^+ and σ^- polarized light, respectively, is depicted versus the DC current amplitude at $T_{bath} = 4.2$ K. By increasing the current amplitude, a pronounced spin polarization is obtained, and the spin polarization changes its sign when inversing the current direction, as expected. At large current amplitudes, ρ reaches a maximum of ~ ±3% as a consequence

of the current-generated heat, which introduces thermal disorder into the Mn^{2+} and carrier spin systems aligned by the current-induced field. FIG 4.2-2(b) shows a scanning electron micrograph of the C2 structure with an inner radius of 2.4 μm, a coil width of 3 μm, and several metal pads around the coil, a layout which is used from Ref. [139]. In general, the spin polarization (red) in the C2 center shows a similar relation to the current amplitude as in A2, but for $I > \sim 60$ mA, ρ(C2) is obviously larger than ρ(A2). This verifies that the design of the C2 coil allows for an efficient dissipation of the current-generated heat resulting in higher Mn^{2+} and carrier spin polarizations.
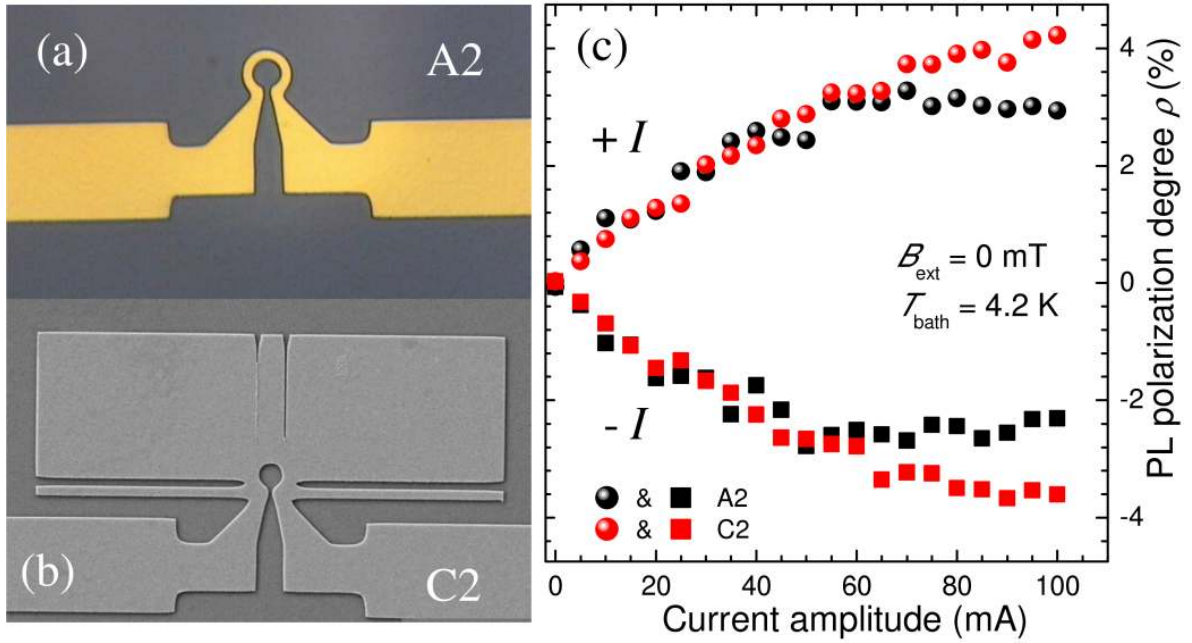

FIG 4.2-2: (a) Optical micrograph of the A2 structure. (b) Scanning electron micrograph of the C2 structure. (c) Circular PL polarization ρ versus the amplitude I of a DC current for A2 (black) and C2 (red) structures at $T_{bath} = 4.2$ K.

In order to further enhance the spin polarization by suppressing heat generation, current pulses are used in the C2 coil. The electrical pulse width is ~ 400 ns and a time window of 100 ns of the photon counter was chosen with a delay of $\Delta t = 170$ ns with respect to the rising edge of the pulse (see inset of FIG 4.2-3, left). As presented in FIG 4.2-3 (left), the PL polarization ρ increases linearly with the current amplitude for $I < \sim 60$ mA and reaches gradually a maximum of ± 8.5 % at $I = \pm 300$ mA. On the right side, the measured relation between spin polarization ρ and an external magnetic field is plotted for different temperatures. As can be seen in the figure, ρ increases linearly with B_{ext} in the low field limit. Thus, one expects a linear relation of $\rho(I)$ for small currents, where heat generation can be neglected (dashed line in the left plott). For $I > \sim 60$ mA the polarization ρ deviates from the linear relation with I, which is attributed to a distinct contribution of heating at large currents.

In order to quantitatively separate the two contributions which determine the spin polarization, namely the current-induced magnetic field B_I, which aligns the Mn^{2+} spins and the current-generated heat, which increases the spin temperature of the Mn^{2+} ions $T_{Mn,}$ and thus the disorder of the Mn^{2+} spins, measurements are performed to determine the spin polarization induced by a pulsed current at an external magnetic field of $B_{ext} = 100$ mT.

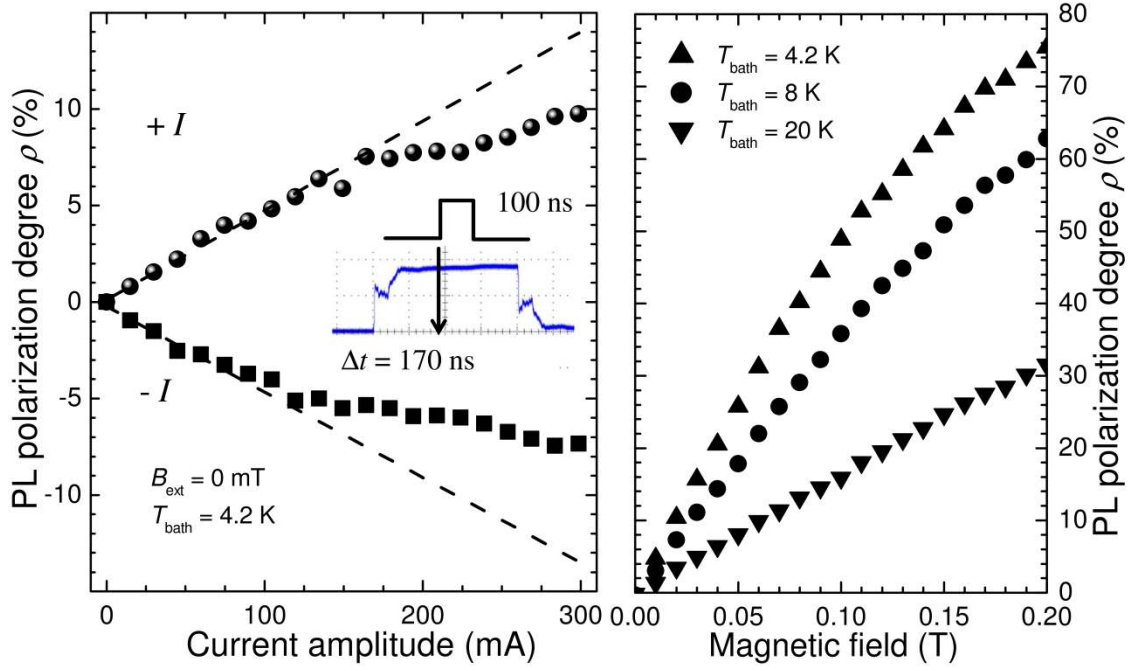FIG 4.2-3: Left: PL polarization degree ρ versus the amplitude of a pulsed current I at T_{bath} = 4.2 K. The dashed lines indicate the linear $\rho(I)$ relation at small currents. The inset depicts the temporal shape of the current pulse (blue) and the temporal shape as well as the time delay Δt of the observation window (black). Right: The PL polarization ρ is plotted versus B_{ext} for T_{bath} = 4.2 K, 8 K, and 20 K, respectively.

From Equation (2.80), it can be seen that the PL polarization is proportional to the total field and the bath temperature, i.e. $\rho \sim B_{tot} \cdot T_{Mn}^{-1} \cdot T_{EX}^{-1}$, in the low magnetic field regime. Here T_{Mn} is the Mn ion spin temperature with and T_{EX} is the average exciton temperature. Since the Mn ion magnetization is on the saturation level at a time delay of Δt = 170 ns and the magnetization process is shorter than the observation window of 100 ns (see Section 4.3), the Mn ion spin temperature can be approximated as an average value T_{Mn}. It can be used as $T_{Mn} = T_{Mn0} + \Delta T_{Mn}$, where T_{Mn0} is the Mn ion spin temperature without heating and ΔT_{Mn} is Mn ion spin heating from the current. Similarly, the exciton temperature can be written as $T_{EX} = T_{EX0} + \Delta T_{EX}$, where T_{EX0} is the exciton temperature without heating and ΔT_{EX} is exciton heating from the current. The heating of both subsystems is due to the elevated lattice temperature $T_{Latt} = T_{bath} + \Delta T_{Latt}$, then it can be treated the heating of the three subsystems is equal, i.e. $\Delta T_{Mn} = \Delta T_{EX} = \Delta T_{Latt}$. It is obtained

$$\rho_{\pm} \sim \left(B_{ext} \pm B_{I} \right) \cdot (T_{Mn0} + \Delta T_{Latt})^{-1} \cdot (T_{EX0} + \Delta T_{Latt})^{-1} \tag{4-2}$$

Here ρ_+ is the PL polarization measured at $B_{ext} + B_I$, and ρ_- is obtained at $B_{ext} - B_I$.

Fig. 4.2-4(a) shows the spin polarization ρ_+ and ρ_- versus the current amplitude, respectively. As the induced magnetic field depends on the current direction, while the generated heat does not, $\rho_{av} = (\rho_+ + \rho_-)/2$ directly indicates the local heating at B_{ext} = 100 mT by using Equation (4-2). The average PL polarization ρ_{av} is plotted as left axis in FIG 4.2-4(b). By comparing $\rho_{av}(I)$ with the temperature dependence of ρ at B_{ext} = 100 mT (FIG 4.1-7), the change of the Mn^{2+} spin temperature $\Delta T_{Mn}(I)$ with

the current I can be directly extracted at the time delay of $\Delta t = 170$ ns (see right axis). The heating is growing with increasing the current amplitude. For $I = 300$ mA, a heating of the Mn^{2+} spin system is up to about 6 K in the coil center.
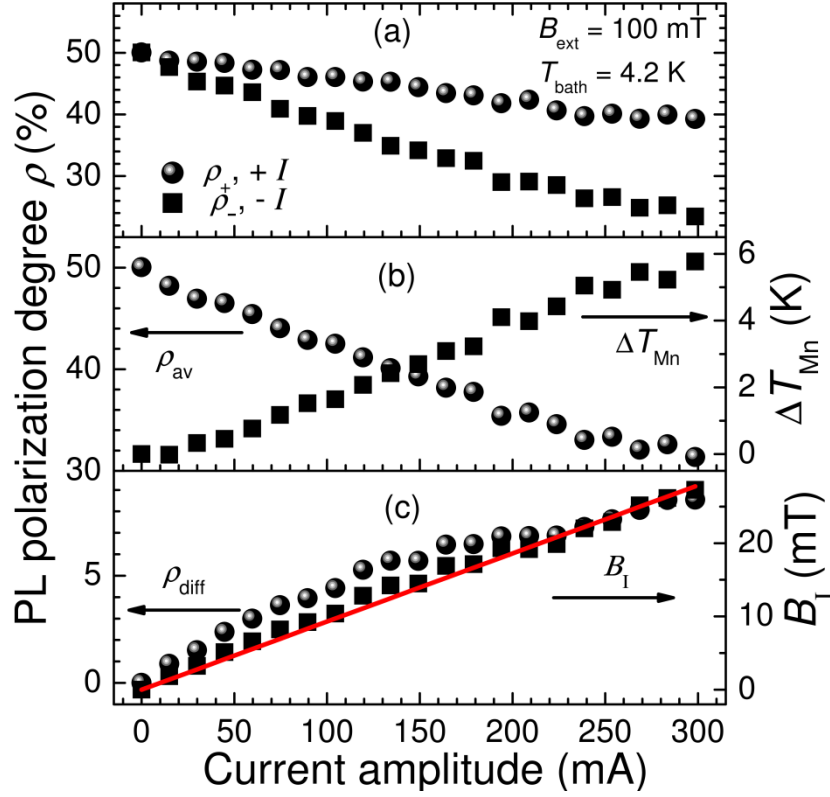

FIG 4.2-4: (a) PL polarization degree ρ versus the amplitude of a pulsed current with positive $(+I)$ and negative $(-I)$ sign at $T_{bath} = 4.2$ K and $B_{ext} = 100$ mT. (b) ρ_{av} (left axis) and the extracted change of Mn^{2+} spin temperature, ΔT_{Mn} (right axis), versus current amplitude.(c) The extracted current induced magnetic field B_I versus current amplitude I. The red line is a linear fitting.

By considering the linear relation between ρ and B for weak fields, the slope of $\rho(B)$ at a given temperature can be approximated as $\Delta\rho/\Delta B(I) \approx \rho_{av}(I)/B_{ext}$. Thus the induced magnetic field can be written as $B(I) \approx \rho_{diff}(I)/(\Delta\rho/\Delta B(I)) \approx \rho_{diff}(I)/\rho_{av}(I)*100$ mT, where $\rho_{diff}(I)$ is the half of the spin polarization difference between $\rho_+(I)$ and $\rho_-(I)$, i.e. $\rho_{diff}(I) = 0.5 \cdot [\rho_+(I) - \rho_-(I)]$, plotted as the left axis in FIG 4.2-4(c). In the right axis, the evaluated current induced magnetic field B_I is shown to depend linearly on the current amplitude I, i.e. $B_I = 0.093$ mT/mA*I, which is fitted by the red line.

As presented in FIG 4.2-5, the lateral distribution of the current-induced carrier spin polarization $\rho(x)$ is monitored by using a spatial scanning with a micrometer resolution across the micro-coil structure. The studied B2 structure has an inner radius 4.7 μm and a coil width of 4.9 μm (inset). Because the Au coil is opaque, only the spin polarization on the uncovered part of the DMS can be optically addressed. A negative pulse with $I = -300$ mA is introduced, and a maximum of $\rho \approx -6$ % is obtained in the coil center, decreasing in the vicinity of the Au coil. Outside the coil a small positive

value of ρ, vanishing on a 10 µm scale, is found, which indicates the expected sign reversal of the current induced magnetic field B_I there.
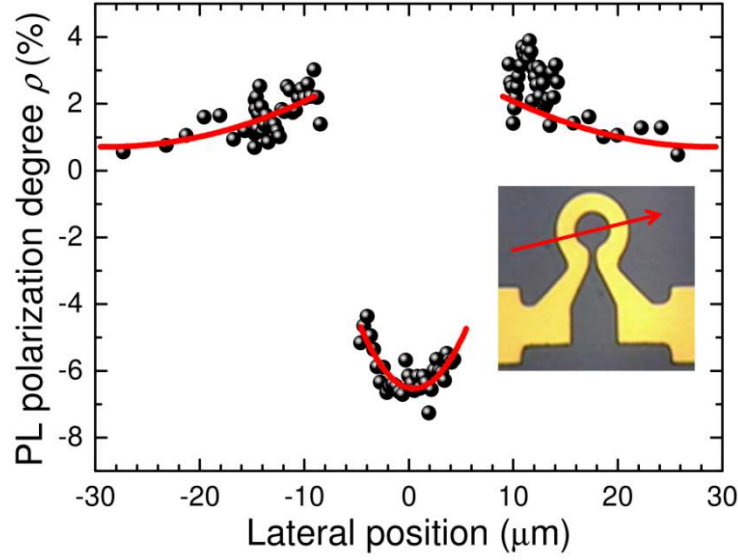

FIG 4.2-5: Spatially resolved PL polarization degree $\rho(x)$ across the B2 coil (see inset, the red arrow indicates the scan path). The current amplitude is -300 mA and $T_{bath} = 5$ K, and the solid lines serve as a guide to the eye.
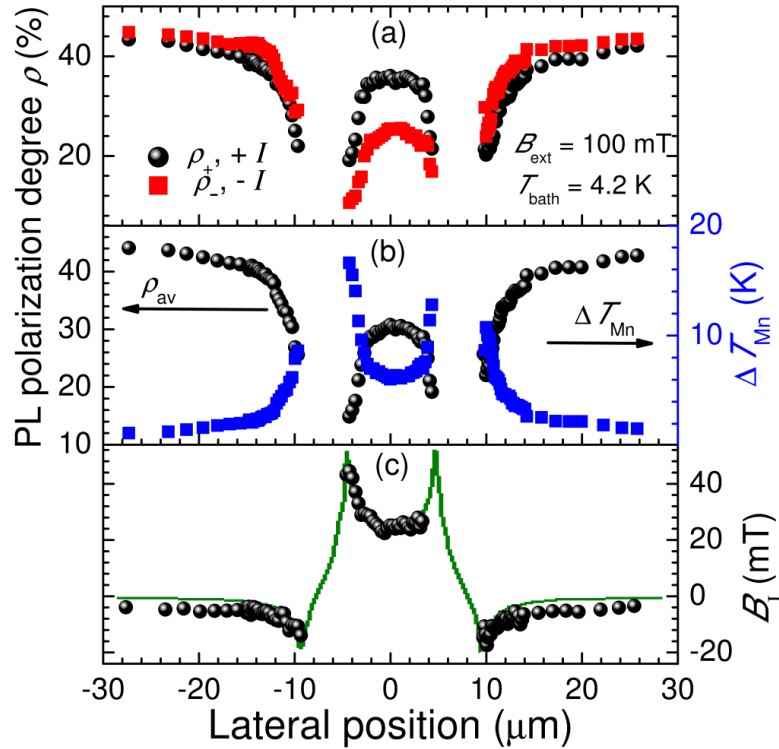

FIG 4.2-6: (a) Spatially resolved polarization degree across B2 with positive ($+I$) and negative ($-I$) sign in an external magnetic field of $B_{ext} = 100$ mT, a temperature $T_{bath} = 4.2$ K and $I = 300$ mA. (b) Spatially resolved average polarization degree $\rho_{av}(x)$ (left axis) and local variation of the Mn^{2+} spin heating $\Delta T_{Mn}(x)$ (right axis). (c) Spatial distribution of the extracted current induced magnetic field B_I and the theoretically calculated one (green curve).

To quantitatively separate the two contributions which determine the spatial distribution of $\rho(x)$, namely the current induced magnetic field $B_I(x)$ and the local Mn ion spin heating $\Delta T_{Mn}(x)$, the same treatment is applied as above based on Equation (4-2).

The spatial dependence of the PL polarization is plotted in FIG 4.2-6(a). Similarly, the PL polarization at a given lateral position x is represented as $\rho_+(x)$ for the positive current and $\rho_-(x)$ for the negative one. An average PL polarization is given by $\rho_{av}(x) = 0.5\cdot[\rho_+(x) + \rho_-(x)]$ which is purely determined by the local heating at a certain magnetic field of $B_{ext} = 100$ mT. In FIG 4.2-6(b), the $\rho_{av}(x)$ is presented in the left axis, and the spatial dependence of the local heating $\Delta T_{Mn}(x)$ is extracted by comparing $\rho_{av}(x)$ and $\rho(T_{bath})$ in FIG 4.1-7. As expected, the strongest heating is observed in the direct vicinity of the metal coil. FIG 4.2-6(c) gives the current-induced magnetic field distribution $B_I(x) = \rho_{diff}(x)/(\Delta\rho/\Delta B(x))$ with $\rho_{diff}(x) = 0.5\cdot[\rho_+(x) - \rho_-(x)]$. The experimentally determined values nicely agree with the theoretically calculated field distribution from Biot-Savart's law, as illustrated by the green curve.

4.3 Mn ion spin heating by pulsed current-generated phonons

As discussed in the previous section, the on-chip current loop can function as a phonon generator to heat the Mn ion spin system. The giant Zeeman effect can sensitively probe the Mn ion magnetization which is affected by the Mn ion spin temperature, so that the DMS layer can work as a detector for the dynamics of the nonequilibrium phonons [184-187]. Thereby, the nonequilibrium phonons are generated by heating a thin metal film deposited on the sample. The generated phonons are typically in the sub-THz frequency regime, and thus gain a ballistic transport length scale above 1 mm [185, 186]. It is suggested that the Mn ions of the DMS layer are resonantly heated by the spin-phonon coupling. As the Mn^{2+} ion has a zero orbital spin, the coupling between one single Mn ion and the phonon system is quite weak. Rather the Mn ion spin-phonon coupling is much more effective between one phonon and a pair of Mn ions, which is mediated by the Dzyaloshinski-Moriya exchange interaction [58, 188]. Therefore the dynamics of the phonons can be probed by monitoring the transient PL spectral shift. The detected phonon energy is equal to the Zeeman energy splitting of the Mn ions in presence of an external field, and thus the phonon frequency spectrum can be figured out by tuning the magnetic field magnitude.

In Ref. [185, 186], the Mn content was chosen $x_{Mn} \geq 0.07$, so that the Mn ion spin-lattice relaxation (SLR) process is below 100 ns [55-57]. The time resolution is limited by the SLR process which is much faster compared with the phonon decay on the order of 1 μs at a bath temperature of ~2 K. The phonon decay is expected faster at elevated temperatures [189, 190]. In the low Mn content regime, i.e. $x_{Mn} \leq 0.03$, the phonon decay is much faster than the SLR process which is above 10 μs. Thus the SLR process can be probed with a time resolution limited by the phonon lifetime [64, 65, 188]. Nonequilibrium phonons can also be generated by non-resonant laser excitation, and the x_{Mn} dependence of the SLR process has been quite systematically studied in Ref. [120, 191, 192].

The SLR rate is strongly depends on the sample temperature. For a rough estimation, the following relation is given from Ref. [58]

$$\tau_{SLR}^{-1} \propto (3 + e^{24.4/T_{bath}})^{-1} \cdot (e^{24.4/T_{bath}} - 1)^{-1} \tag{4-3}$$

Here it is assumed the SLR rate mainly controlled by the Mn ion pairs, which becomes more with increasing the Mn concentration. If the temperature is elevated by a factor of two, the SLR time constant can be shortened by two orders of magnitude

Similar to the reported technique, the nonequilibrium phonons are here generated by an electrical pulse. The used microcoil has an aperture of 8.5 μm and a width of 5.6 μm, similar to the structure shown in the inset of FIG 4.2-5. The studied sample has a Mn content of x_{Mn} = 0.067 (Sample 1) and the bath temperature is generally 5 K or above. For a sample with x_{Mn} = 0.05, it has been determined $\tau_{SLR} \approx$ 100 ns at a temperature of 4.7 K [57]. By considering the fact that the SLR is becoming fast with increasing the Mn content [55] and the strong temperature dependence, the SLR time in the studied is expected much less than 100 ns. From Ref. [193], it has been indicated the phonon decay time has been estimated ~400 ns in a same sample. Therefore the PL polarization measurements here allow one to monitor the phonon dynamics with a time resolution limited by the SLR time in the sample with x_{Mn} = 0.067, in a field of 100 mT. The PL results presented in this section are obtained by using the experimental scheme in FIG 3.3-5.

First, in order to determine the SLR time in the studied sample, the PL polarization measurements are performed with a constant sample temperature. In this way, the PL polarization dynamics directly represents the SLR dynamics. This can be realized by choosing an electrical pulse with a repetition period less than the phonon lifetime. In FIG 4.3-1, the PL measurements are measured in an external field of B_{ext} = 100 mT. The electrical pulse repetition period τ_{rep} = 120 ns is chosen, and the pulse width τ_{pul} = 40 ns. The electrical transit time is 2 ns. In this case, a dynamic equilibrium is established between the phonon generation and the phonon decay, so that the DMS layer experiences a quasi-thermal equilibrium. Within the repetition period, the lattice temperature and the Mn ion spin temperature is a constant value. The σ⁺-polarized PL intensity (black) and σ⁻-polarized PL intensity (red) are respectively recorded by the modulation technique based on the TCSPC system (Section 3.3.2), and the PL polarization (blue) is evaluated according to the definition in Equation (3-1). The PL polarization dynamics directly reflects the magnetization of the Mn ions as $T_{Mn} \approx T_{Latt} \approx T_{EX}$ throughout the repetition period, and it is only affected by the pulsed magnetic field.

As expected, the positive current can induce a positive contribution of the spin polarization presented in (a) and (c), and the negative current reduces the spin polarization in (b) and (d). The onset and decay of spin polarization is generally below 5 ns. This much faster rate is not surprising by considering the lattice temperature. In case of I = 100 mA, the PL polarization level is ~32% caused only by the static external field. The lattice temperature is estimated about 10 K by comparing it with the reference results in FIG 4.1-7. In case of I = 200 mA, the PL polarization level is further reduced to ~20%, which corresponds to a lattice temperature of 16 K. This agrees well with the

theoretical discussion above. The short SLR process allows the phonon dynamics to be monitored with a time resolution of a few nanoseconds.
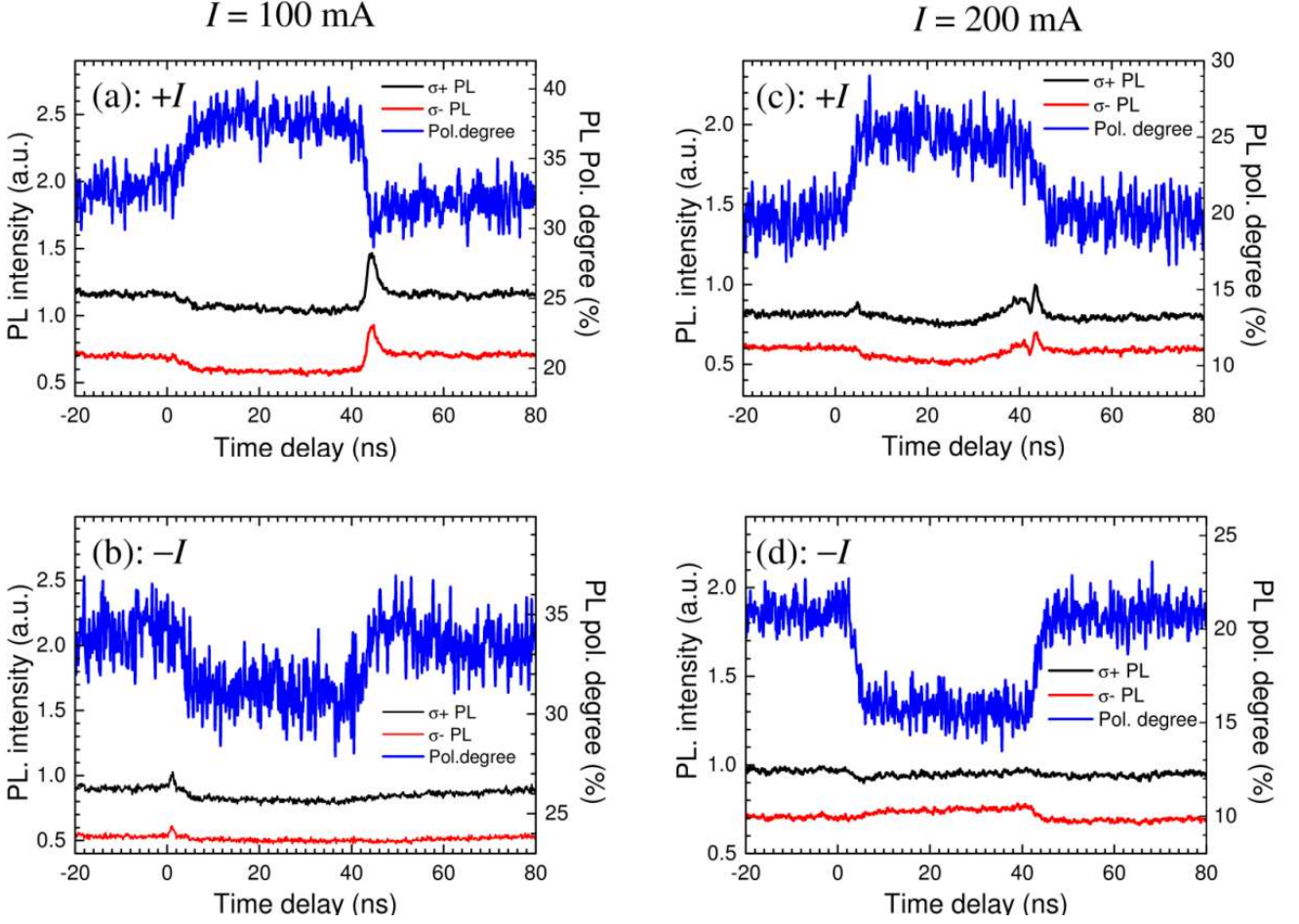

FIG 4.3-1: Time-resolved PL polarization degree induced by an electrical pulse. The generated phonons are in a quasi-thermal equilibrium state since the pulse repetition period is shorter than the phonon lifetime. The external field is B_{ext} = 100 mT. The time delay is with respect to the leading edge of the electrical pulse. The pulse width is 40 ns and the repetition period is 120 ns. The electrical transmit time is 2 ns. (a): a positive current is introduced I = 100 mA; (b): a negative current is introduced I = -100 mA; (c) I = 200 mA; (d) I = -200 mA. The PL polarization (blue) is calculated from the detected σ^+-polarized PL intensity (black) and the σ^--polarized PL intensity (red). For the presented results, x_{Mn} = 0.067.

To generate nonequilibrium phonons, a longer repetition period of τ_{rep} = 2 μs is used for measurements depicted in FIG 4.3-2. In this case, as the phonon lifetime is shorter than the repetition period, the quasi-thermal equilibrium cannot be established throughout one electrical period. As a result, the current-generated phonons undertake a nonequilibrium generations process as well a nonequilibrium decay process. The lattice system obtains a dynamical temperature and the Mn ion spin system follows the dynamics via the fast SLR process. For the left panel (a ~ c), the pulse width is τ_{pul} = 400 ns. In (a), the time-resolved PL polarization degree induced by the current pulse is depicted for a positive current I = 100 mA (black) and the negative current I = -100 mA (red). In the time delay Δt of the first few nanoseconds, there is fast spin polarization formation which again confirms the fast SLR process. Afterwards the spin polarization is suppressed for both currents due

80

to the accumulation of the current-generated phonons. The dynamic PL polarization at a time delay of Δt is represented as $\rho_+(\Delta t)$ for the positive current and $\rho_-(\Delta t)$ for the negative current. The average dynamical polarization, which is defined as $\rho_{av}(\Delta t) = 0.5 \cdot (\rho_+(\Delta t) + \rho_-(\Delta t))$, is plotted in the left axis of (b). By applying a same argument as in FIG 4.2-4 and FIG 4.2-6, the $\rho_{av}(\Delta t)$ directly reflects the Mn ion spin heating, but with a time resolution down to a few nanoseconds. The Mn ion spin heating is plotted in the right axis (blue). As expected the heating is maximum at the end of the current pulse. Both the growth process and the decay process of the Mn spin heating can be exponentially fitted with a time constant of 200 ns, which is just the phonon lifetime $\tau_{phonon} = 200$ ns. The dynamical magnetic field is evaluated as $B(\Delta t) \approx \rho_{diff}(\Delta t)/\rho_{av}(\Delta t)*100$ mT, and it is plotted in (c). The amplitude of the magnetic field pulse is ~9 mT, which agrees quite well with the value determined for $I = 100$ mA in FIG 4.2-4.
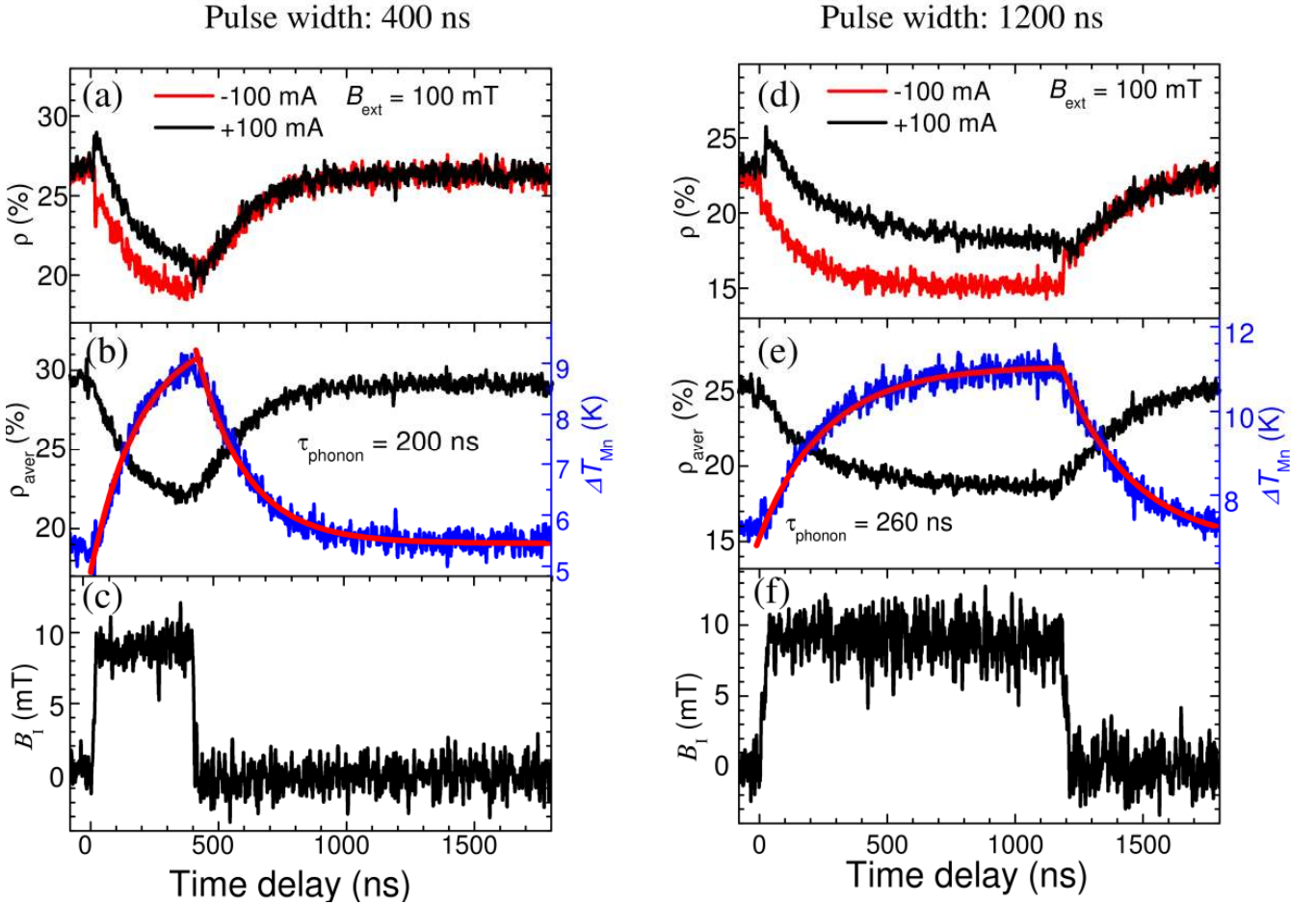

FIG 4.3-2: Time-resolved PL polarization degree induced by an electric pulse. The generated phonons are in a nonequilibrium state since the pulse repetition period is longer than the phonon lifetime. The external field is $B_{ext} = 100$ mT. The current amplitude is 100 mA. The time delay is with respect to the leading edge of the electrical pulse. The repetition period is 2 µs. The pulse width is 400 ns for (a) ~ (c), and it is 1200 ns for (d) ~ (f). The electrical transmit time is 2 ns. (a) and (d): Time-resolved polarization degree for the positive current(black) and negative (red). (b) and (e): Time-resolved average PL polarization (red, left axis) and extracted Mn ion spin heating (blue, right axis). The phonon dynamics are fitted by the red lines. (c) and (f): Evaluated magnetic field pulses. For the presented results, $x_{Mn} = 0.067$.

81

In the right panel (d ~ f), experiment results are presented for a longer pulse width $\tau_{pul} = 1200$ ns. The time-resolved PL polarization for the positive pulsed current and the negative one is plotted in (d), respectively. The averaged $\rho_{av}(\Delta t)$ and the extracted Mn ion spin heating are given in (e). By an exponential fitting, the phonon lifetime is determined as $\tau_{phonon} = 260$ ns. The evaluated magnetic field is shown in (f). The field amplitude is ~9 mT, in a nice agreement with the amplitude in (c).

5 SUB-NS MAGNETIZATION DYNAMICS IN DILUTED MAGNETIC SEMICONDUCTOR QUANTUM WELLS

In this chapter, the magnetization dynamics down to zero magnetic field is addressed in diluted magnetic semiconductor quantum wells. In the first part, the interaction of Mn ions with the local environment is introduced and the magnetic properties affected by carriers are discussed. These two factors can strongly determine the Mn ion magnetization dynamics in the regime of a low magnetic field. Next the experimental results of the magnetization dynamics are presented showing a pronounced dependence on the external magnetic field. This is due to the interplay between the local anisotropic spin interactions of Mn ions and the Zeeman interaction with the external field. The numerical simulations based on the Lindblad master equation are performed and the theoretical calculations coincide well with the experiment results.

5.1 Interactions on Mn ions

For a localized Mn ion carrying a magnetic moment in a solid system, the Mn ion interacts with the local crystal environment [108]. These include the hyperfine interaction between the five $3d^5$ electrons and the nuclei of the Mn ion, and the spin coupling with the cubic crystal field or any electrical field, e.g. caused by strain in semiconductor quantum structures. In the presence of carriers, the single Mn ion has *s-d* exchange interaction with electrons and *p-d* exchange interaction with holes. One Mn ion can also interact with the neighbouring Mn ions via *d-d* exchange interaction [44, 107]. These mechanisms can affect the magnetization dynamics of the Mn ions [56, 63-65, 178, 191, 192].

5.1.1 Local spin environment

For a paramagnetic center, e.g. a Mn ion, the local magnetic interaction can be assessed by the electron paramagnetic resonance (EPR) technique. The corresponding Mn ion spin Hamiltonian is written as [194-196]

$$\hat{H} = \hat{H}_z + \hat{H}_{hf} + \hat{H}_{cub} + \sum \hat{H}_{strain} + \hat{H}_{elec}, \text{with}$$

$$\hat{H}_z = g_{Mn}\mu_B \boldsymbol{B}_{ext} \cdot \hat{\boldsymbol{S}},$$

$$\hat{H}_{hf} = A\hat{\boldsymbol{I}} \cdot \hat{\boldsymbol{S}}, \tag{5-1}$$

$$\hat{H}_{cub} = \frac{a}{6}\left[\hat{S}_x^4 + \hat{S}_y^4 + \hat{S}_z^4 - \frac{S(S+1)(3S^2+3S+1)}{5}\right],$$

$$\hat{H}_{strain} = D_s\left[\hat{S}_z^2 - \frac{S(S+1)}{3}\right] + E_s\left[\hat{S}_x^2 - \hat{S}_y^2\right]$$

Here $\hat{S}$ and $\hat{I}$ are the electron spin and nuclear spin of the Mn ion, respectively. $\boldsymbol{B}_{ext}$ denotes the applied external magnetic which defines the direction of the spin component S_z. The first item is the Zeeman energy with the Mn g factor of $g_{Mn} \approx 2.01$ [108]. The second item H_{hf} is the hyperfine interaction with a hyperfine coupling constant $A \approx 0.68$ μeV [56]. The spin coupling with the cubic crystal field is given in the third item with $a \approx 0.32$ μeV [56]. The fourth item is the Mn ion spin coupling with a total strain-induced electrical field. In the studied (Cd, Mn)Te/Cd$_{0.7}$Mg$_{0.3}$Te DMS QW, the uniaxial strain along the growth direction (z-axis) is around $\delta_{zz} = -0.003$ by considering the mismatch of the crystal lattice constants [44, 103]. The coefficients can be deduced $D_s \approx 0.62$ μeV and $E_s = 0$ for strain applied in [001] direction [103, 195, 197, 198]. In case of a strain in [110] or [111] direction, both coefficients are non-zero. This could happen by local fluctuations and dislocations. In Ref. [56], a strain of $\delta_{xy} = 0.004$ is suggested for the (Cd,Mn)Te QWs, and thus it can be calculated $D_s \approx -0.41$ μeV and $E_s = 1.12$ μeV [103, 195, 197, 198]. The last term $\hat{H}_{elec}$ describes the spin coupling with the electrical field, which can be present due to the pinning of the surface state and the Fermi level in the studied samples [169] or due to the applied voltage on the metal structures. The complex formalism is given in Ref.[196]. Since the magnitude of the electric field is on the order of 10^7 V/m, H_{elec} is estimated to be around a few neV, and thus it can be neglected compared with the other terms.

The Zeeman energy splitting between Mn ion spin sublevels is around 1 μeV for a magnetic field of 10 mT. This indicates that the anisotropic spin interactions, i.e. H_{hf}, H_{cub} and H_{strain}, can compete with the Zeeman interaction in the low field regime [56], and they are expected to highly modify the magnetization dynamics, which is dominated by the spin-lattice relaxation (SLR) process in the strong field regime [42, 184].

5.1.2 Magnetic properties affected by carriers

In a DMS system, the existing carriers can affect the magnetic properties of the Mn ions in two folds. For the magnetization dynamics, the SLR process can be accelerated by introducing carriers which bypass the relatively slow spin-phonon coupling [42, 184]. For the static property, the carriers can enhance the magnetic susceptibility, and provide an additional effective magnetic field experienced by the Mn ions [49, 52].

In FIG 5.1-1, a schematic description is given for the relaxation channels between different energy reservoirs in a DMS system in the presence of carriers. There are three sub systems, the Mn ion spin system, the lattice system and the carriers. The Mn ions can couple with the lattice system via spin-phonon coupling, namely the SLR process, which is in a time range from a few nanoseconds to milliseconds depending on the Mn content and the temperature [42, 55, 56, 58, 184, 192]. As an additional relaxation channel, the carriers, i.e. electrons and holes, can make spin transitions of the Mn ions via a spin-flip scattering process [63, 64]. In addition, the carriers strongly couple with lattice system via a kinetic relaxation process which is typically on a time scale of 100 ps or even less

[117]. As a result, the carriers can provide an indirect channel to transfer the energy of the Mn ion spin system to the lattice system. In DMS QW structures, the SLR process has been experimentally demonstrated to be accelerated by tuning the density of the two-dimension (2D) electron gas [64] or the hole gas [65].
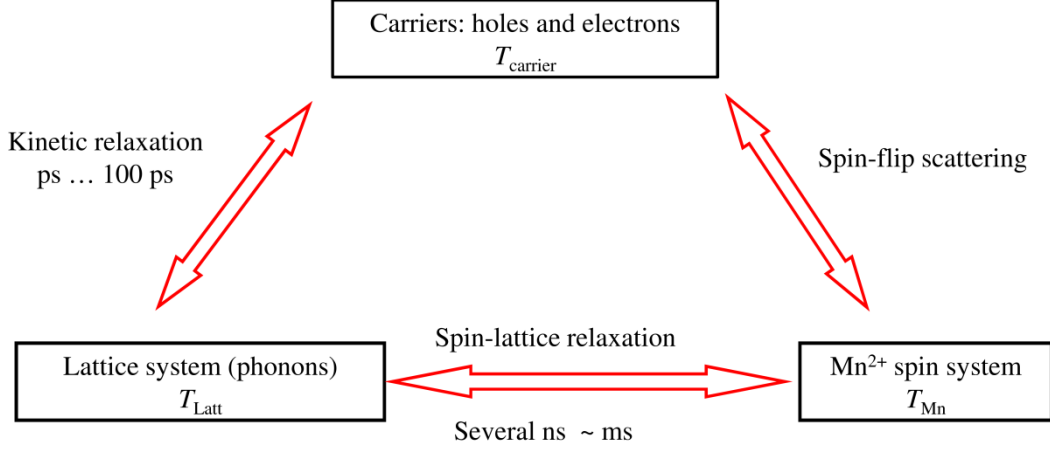

FIG 5.1-1: The schematic description of different energy reservoirs and their relaxation channels in a DMS system in presence of carriers

For the spin-flip scattering process between the carriers and the Mn ions, the relaxation rate is mainly determined by the carrier density and the external field. In a spin-flip event, the Mn ion is put to a lower energetic spin level and the carrier is changed to a higher energetic spin level, so that the energy is conserved. Generally the scattering rate is larger for a degenerate carrier gas compared with the non-degenerate one. This is due to two facts: (i) the strong *sp-d* exchange interaction makes the Zeeman energy splitting between carrier spin sublevels much larger than that for the Mn ion spin; (ii) the carrier spin transition probability is expected to be higher if different spin states are occupied near the Fermi level. In other words, the acceleration of the SLR process is enhanced by increasing the 2D carrier density, and the acceleration becomes saturated if the Fermi level is much larger than the Zeeman energy splitting.

In Ref. [63], a saturation density of a 2D electron gas is theoretically estimated as $n_e \approx 1 \times 10^{11} \text{cm}^2$ in the low field regime for a Mn content $x = 0.01$. Below this concentration, the SLR rate can be faster by a factor of five or so if the electron density is increased higher by one order of magnitude. The effect is expected to be even stronger for the 2D hole gas, since the hole gas holds a larger effective mass leading to a larger density of states (DOS) and holes couple with the Mn ions by a stronger *p-d* exchange interaction. This has been experimentally confirmed in Ref. [65]. The in-plane effective mass of the heavy hole is about 2.5 times of the electron mass, i.e. $m_{\text{hh-in}} \approx 0.25 \cdot m_0$ and $m_{\text{e-in}} \approx 0.1 \cdot m_0$ [116]. The *p-d* exchange interaction is about four times as strong as the *s-d* exchange interaction. By considering these factors, the saturation density of the 2D hole gas can be expected to be larger by one order of magnitude or so than the 2D electron gas. In the studied sample, the hole density is $n_h \approx$

7×10^{10} cm^2, which is likely below the complete degenerate condition in the low field regime, i.e. B_{ext} = 100 mT.

As a second prominent effect, the magnetic susceptibility of the Mn ions can be enhanced due to free carriers in a DMS system. This is basically due to carrier-mediated ferromagnetic coupling compensating the antiferromagnetic exchange interaction between Mn ion spins [49]. Once the former overcomes the latter, the Mn ions are changed from the paramagnetic phase to the ferromagnetic phase. This can happen by lowering the temperature or increasing the carrier concentration, so that the magnetic susceptibility can be highly enhanced forming the spontaneous magnetization of the Mn ions [48]. Again, since the *p-d* exchange interaction is stronger than the *s-d* exchange interaction and because of the larger DOS, *p*-type doping (holes) are typically used to achieve the ferromagnetism in DMS systems. The carrier-controlled ferromagnetism was first found in III-V [51] and later II-VI DMS systems [52]. The carrier density can be adjusted by modulation doping [52, 199], and by optical/electrical injection or depletion [26, 48, 200]. The Curie temperature has been theoretically predicted for different DMS materials [50]. In the studied (Cd, Mn)Te DMS structures, the Curie temperature was experimentally found to be below 4 K in case of *p*-type doping [48, 201].

As the sample temperature in current measurements was above 5 K, i.e. higher than the Curie temperature, the magnetic susceptibility is considered in the paramagnetic phase. In Section 2.3.2, the Mn ion magnetization for an undoped DMS system has been described by the mean field approximation (e.g. see Equation (2-53)). By considering the approximation valid in the low field regime given in Equation (2-53), the magnetization is rewritten as

$$M_0 = M(B_{\text{ext}}, T_{\text{bath}}) = \frac{35 g_{\text{Mn}}{}^2 \mu_{\text{B}}{}^2 N_0 x_{\text{eff}}}{12 k_{\text{B}}} \frac{B_{\text{ext}}}{T_{\text{bath}} + T_0} = \frac{C B_{\text{ext}}}{T_{\text{bath}} + T_0} \tag{5-2}$$

The constant C is the Currie constant with $C = \dfrac{35 g_{\text{Mn}}{}^2 \mu_{\text{B}}{}^2 N_0 x_{\text{eff}}}{12 k_{\text{B}}}$. According to the definition, the magnetic susceptibility in absence of carriers is denoted as

$$\chi_0 = \frac{\partial M}{\partial B_{\text{ext}}} = \frac{C}{T_{\text{bath}} + T_0} \tag{5-3}$$

From the theory proposed in Ref. [49], the carriers (e.g. holes) in a DMS QW can introduce an effective magnetic field B^* seen by the Mn ions which is a function of B_{ext}, and this field is given by

$$B^*(B_{\text{ext}}) = \frac{|\beta|}{2 g_{\text{Mn}} \mu_{\text{B}}} \frac{n_\downarrow - n_\uparrow}{L_{\text{w}}} = \frac{|N_0 \beta|}{2 g_{\text{Mn}} \mu_{\text{B}}} \frac{n_\downarrow - n_\uparrow}{N_0 L_{\text{w}}}, \tag{5-4}$$

in which n↑ is the hole density for m_{j} = +3/2 and n↓ is the hole density for m_{j} = -3/2, respectively. Here only the heavy holes are considered for the studied QW structures, and the QW width is L_{w}. The enhanced magnetic susceptibility is given

$$\chi_c = \frac{\partial M(B_{ext} + B^*(B_{ext}), T_{bath})}{\partial B_{ext}} = \frac{C}{T_{bath} + T_0}\left(1 + \frac{B^*(B_{ext})}{B_{ext}}\right) \tag{5-5}$$

Therefore the enhanced magnitude of the magnetic susceptibility is

$$\eta_\chi = \frac{\chi_c}{\chi_0} - 1 = \frac{B^*(B_{ext})}{B_{ext}} \tag{5-6}$$

The energy diagram of the hole spin sublevel is given is FIG 5.1-2, in which the energy axis is reversed. In absence of an external field, the spin states are degenerate, i.e. $n_\downarrow = n_\uparrow$. Once an external field B_{ext} is applied, there is a giant Zeeman splitting Δ_{hh} between spin-up state and spin-down state. The Fermi energy level is given by E_F, which is here defined respective to the valence band bottom. According to the Fermi-Dirac distribution, the hole density is given

$$n_\downarrow = \int_{-\frac{1}{2}\Delta_{hh}}^{\infty} D_h \frac{dE}{e^{(E-E_F)/k_B T_{bath}} + 1}$$
$$n_\uparrow = \int_{+\frac{1}{2}\Delta_{hh}}^{\infty} D_h \frac{dE}{e^{(E-E_F)/k_B T_{bath}} + 1} \tag{5-7}$$

Here the heavy hole DOS is D_h, and k_B is the Boltzmann constant. For a 2D hole gas, the value of D_h is assumed constant as $D_h = \frac{m_{hh-in}}{2\pi\hbar^2}$. In the studied (Cd, Mn)Te DMS QW, the calculation gives $D_h \approx$ 5×10^{10}cm^{-2}·meV^{-1} by using $m_{hh-in} \approx 0.25 \cdot m_0$. After making the integration, the following relations are found

$$\Delta n_h = n_\downarrow - n_\uparrow = D_h \Delta_{hh} + D_h k_B T_{bath} \ln\frac{1 + e^{-(0.5\cdot\Delta_{hh} + E_F)/k_B T_{bath}}}{1 + e^{(0.5\cdot\Delta_{hh} - E_F)/k_B T_{bath}}}$$
$$n_h = n_\downarrow + n_\uparrow = 2D_h E_F + D_h k_B T_{bath} \ln\left(1 + e^{-(0.5\cdot\Delta_{hh} + E_F)/k_B T_{bath}}\right)\left(1 + e^{(0.5\cdot\Delta_{hh} - E_F)/k_B T_{bath}}\right) \tag{5-8}$$

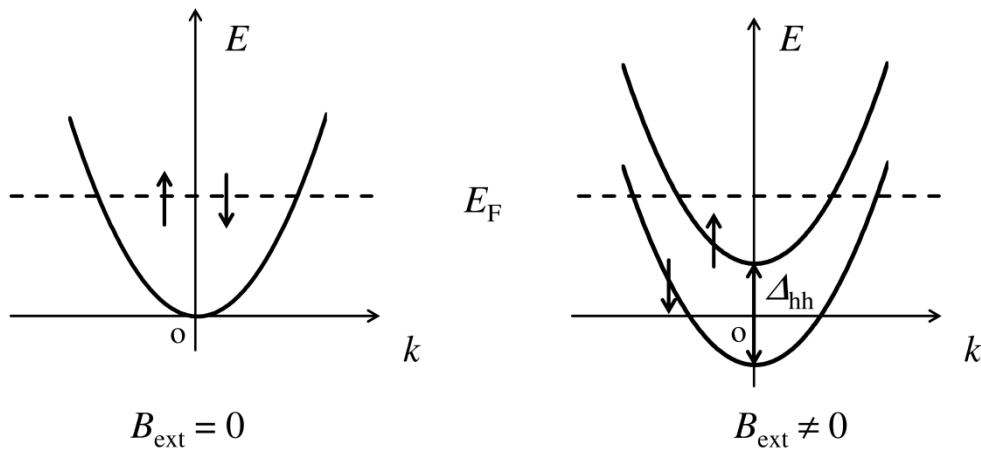The Fermi level can be determined by using the second relation, if n_h is known.

FIG 5.1-2: Energy levels of heavy hole spin states. The energy axis is reversed. (a) The external field is $B_{ext} = 0$, the energy values of two spin states are degenerate; (b) The degeneracy is lifted for $B_{ext} \neq 0$ with an energy splitting Δ_{hh}.

In FIG 5.1-3, the hole density dependence of the Fermi level is depicted on the left-axis. It is almost independent on the magnetic field in the low field regime by judging the overlapping between B_{ext} = 0 mT (black line) and B_{ext} = 100 mT (blue line). The energy splitting $\Delta_{hh} \approx 0.5$ meV is used for B_{ext} = 100 mT, which is estimated for sample 1 with x_{Mn} = 0.067 at T_{bath} = 10 K (see FIG 4.1-5). The surface doping density is $n_h \approx 7 \times 10^{10}$ cm^{-2} indicated by the dashed line, and it could be seen the Fermi level is quite close to the zero level.
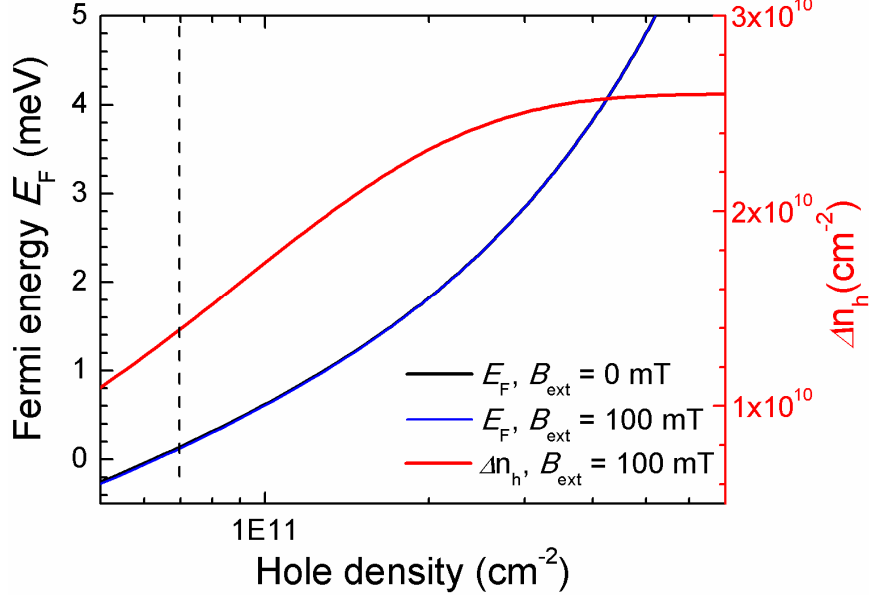

FIG 5.1-3: The heavy hole density dependence of the Fermi energy (left-axis) and the density of the spin-polarized holes (right-axis). For the numerical calculations, the temperature is used as T = 10 K, and the energy splitting between the heavy hole spin levels is used as Δ_{hh} = 0.5 meV at an external field of B_{ext} = 100 mT. The dashed vertical line indicates the hole density for the studied sample, i.e. $n_h \approx 7 \times 10^{10}$ cm^{-2}.

Based on the calculated Fermi energy levels, the density dependence of the spin-polarized holes Δn_h is plotted on the right-axis. For a hole density $n_h < \sim 3 \times 10^{11}$ cm^{-2}, the value of Δn_h is steadily growing by increasing the total density n_h, while it becomes saturated and n_h-independent for higher hole densities. This is due to the much higher Fermi energy level as compared with the thermal energy and the energy splitting, so that only lower energy states can contribute to Δn_h. This agrees well with the conclusion in Ref. [49]: the effective field B^* is independent on the carrier density in case $E_F \gg k_B T_{bath}$ for a perfect 2D hole gas system.

For $n_h \approx 7 \times 10^{10}$ cm^{-2}, it can be obtained $\Delta n_h \approx 1.4 \times 10^{10}$ cm^{-2}. This indicates a hole spin polarization of 20%, which gives a reasonable agreement with the measured PL spin polarization of ~ 30 % at ~ 10 K, e.g. see FIG 4.1-7. To note, the PL polarization is determined by the excitonic Zeeman splitting, which is larger than the hole Zeeman splitting by a factor of 1.25. For $n_h > 3 \times 10^{11}$ cm^{-2}, the saturated level is obtained with $\Delta n_h \approx 2.6 \times 10^{10}$ cm^{-2}.

From the calculated value of Δn_h, the effective field can be estimated by using Equation (5-4). The used parameters are: L_w = 12 nm, N_0 = 1.46 $\times 10^{22}$ cm^{-3}, $|N_0\beta|$ = 0.88 eV and g_{Mn} = 2.01. It is

obtained $B^* \approx 2.2 \times 10^{-10} \cdot \Delta n_h \cdot$ (mT·cm^2). In case of $n_h \approx 7 \times 10^{10}$ cm^{-2}, which corresponds to $\Delta n_h \approx 1.4 \times 10^{10}$ cm^{-2}, $B^* \approx 3$ mT is obtained. In case of $n_h > 3 \times 10^{11}$ cm^{-2}, which corresponds to $\Delta n_h \approx 2.6 \times 10^{10}$ cm^{-2}, $B^* \approx 5.7$ mT is obtained. This effective field gives a small enhancement for the magnetic susceptibility, by a few percents if one considers $\eta_\chi = B^* / B_{ext}$. By modulating the hole concentration for the studied DMS QW, a maximum change of the effective field is $\Delta B^* \approx \pm 3$ mT. In addition, the hole-hole interaction should be taken into account in the regime of the large carrier density. This results in an enhancement of the Pauli susceptibility of the carriers, and then a further enhancement of the magnetic susceptibility is expected for the Mn ions. This enhancement was found to be a factor of two or so for a *p*-doped (Cd,Mn)Te DMS system [53]. This effect can make the effective field larger than the calculated ΔB^* by a factor of two or so, i.e. $\Delta B^* \approx \pm 6$ mT in the experiment conditions.

5.2   Sub-ns magnetization dynamics in DMS QWs

To study the magnetization dynamics of magnetic centers is of fundamental interest in physics. In a DMS system, Mn ions can serve as paramagnetic centers due to the isoelectric property of the Mn ion with absence of the orbit spin. The magnetization dynamics of the Mn ions describes the relaxation process of the Mn ion spins to a new equilibrium state. This can also provide basic information for the quest how fast the Mn ion spin system can be controlled [20, 41].

Quite generally, the magnetization dynamics of Mn ions is investigated in presence of a strong magnetic field, i.e. a few Tesla. In order to investigate the SLR process which dominates the longitudinal spin relaxation process, the Mn ion spin system is driven out of equilibrium by an external disturbance, i.e. direct heating the Mn ion system via nonequilibrium phonons [57, 184, 188, 191] or indirect heating via optically generated nonequilibrium hot carriers [42, 192, 202, 203]. The SLR process of Mn ions has been investigated by detecting the magnetization-induced electrical signal [57, 204], and optically monitoring the dynamical recovery of the giant Zeeman shift of the PL spectrum [42, 184]. The SLR rate indicates how fast the dynamical equilibrium can be established between the Mn ion system and the lattice system. Concerning the transverse relaxation process, namely the spin-spin interaction of the Mn ions, it describes how fast a spin system loses its coherence. This can be either deduced from the resonance linewidth in EPR experiments [108] or obtained from the spin dephasing time in time-resolved magneto-optic Faraday [60, 205] or Kerr rotation measurements [61, 62].   At liquid helium temperature, the SLR time ranges from 100 ns to milliseconds strongly depending on the Mn content, while the spin-spin interaction time is typically on the order of a few 100 ps [55].

In order to accelerate the SLR process, carriers are introduced to provide an extra channel bypassing the relatively slow spin-phonon coupling [63], e.g. see FIG 5.1-1. Experimental results demonstrate an acceleration of a factor of two to four by increasing the carrier density by one order of magnitude [64, 65, 206]. Another alternative is to use a superlattice, in which the Mn contents are different for

the neighbouring layers. The SLR rate for the layer with the lower Mn content can be increased via spin-diffusion from the layer with the higher Mn content which has a faster SLR process [59]. Nevertheless, it seems not possible to shift the SLR time towards the sub-ns time scale in presence of a strong magnetic field. In absence of an external field, recent studies performed by Goryca et al. reveal a nanosecond magnetization dynamics of the Mn ions in dilute (Cd, Mn)Te QWs [33, 56, 207] and QDs [208, 209].

In FIG 5.2-1, the magnetic field dependence of the PL polarization dynamics induced by a pulsed field is presented for sample 1 (x_{Mn} = 0.067). The experimentally measured σ^+-polarized PL (red) and σ^--polarized PL intensity (blue) are plotted in the lower part of each sub-figure and the PL polarization (black) is evaluated according to Equation (3-1) at each time delay. Since the electrical repetition period, i.e. 35 ns for (a) ~ (c) and 50 ns for (d) ~ (f), is much shorter than the phonon lifetime as determined in Section 4.3, the detected PL polarization dynamics is a direct representation of the magnetization dynamics of the Mn ions. The PL intensity is slightly enhanced by nonequilibrium carriers at two edges of the electrical pulse. Because the lifetime of these electrically generated transient carriers is ~200 ps, their effect on the Mn ion magnetization dynamics is negelected after their vanishing.

Results in (a) ~ (c) depict the field dependence of the Mn ion magnetization dynamics induced by a pulsed current through the microcoil presented in the left figure, top. The magnetization dynamics is found to be 0.9 ns from fitting (magenta line) in the absence of an applied static field. Once an external field is applied of B_{ext} = 50 mT, the onset of the spin formation process is clearly slowed down to ~1.8 ns. By increasing the static field to 100 mT, the magnetization dynamics is further slowed down to ~2.1 ns, which agrees well the PL polarization dynamics observed in Section 4.3. Here the bath temperature is estimated ~11 K by comparing the PL polarization degree after the spin decay process with the characteristic results in FIG 4.1-7.

In (d) ~ (f), the field dependence of the magnetization dynamics is depicted for a microcoil presented in the right figure, top. The inner aperture is smaller and the metals pads are expected to provide efficient heat dissipation. At zero external field, the magnetization dynamics induced by the pulsed field can be well exponentially fitted with the same time constant 0.9 ns as used in (a). In the presence of a static field B_{ext} = 50 mT, the spin formation process is slowed down to ~1.6 ns, which is similar to (b). By increasing the static field to 100 mT, the spin formation is still well fitted by a time constant of 1.6 ns.

For sample 2 with x_{Mn} = 0.024, the field dependence of the magnetization dynamics is shown in FIG 5.2-2. The used microcoil is same as the left top in FIG 5.2-1. In figure (a), the pulse repetition period is 35 ns, then the magnetization dynamics can be directly determined from the PL polarization dynamics. Here the PL polarization difference ρ_{diff} (see Section 4.2) is plotted to improve the signal to noise ratio. In the absence of a static field, the magnetization dynamics is found ~ 1 ns, which is quite close to the dynamics for the sample 1 in case of B_{ext} = 0 mT. No pronounced spin formation is observed if an external field of 100 mT is applied.
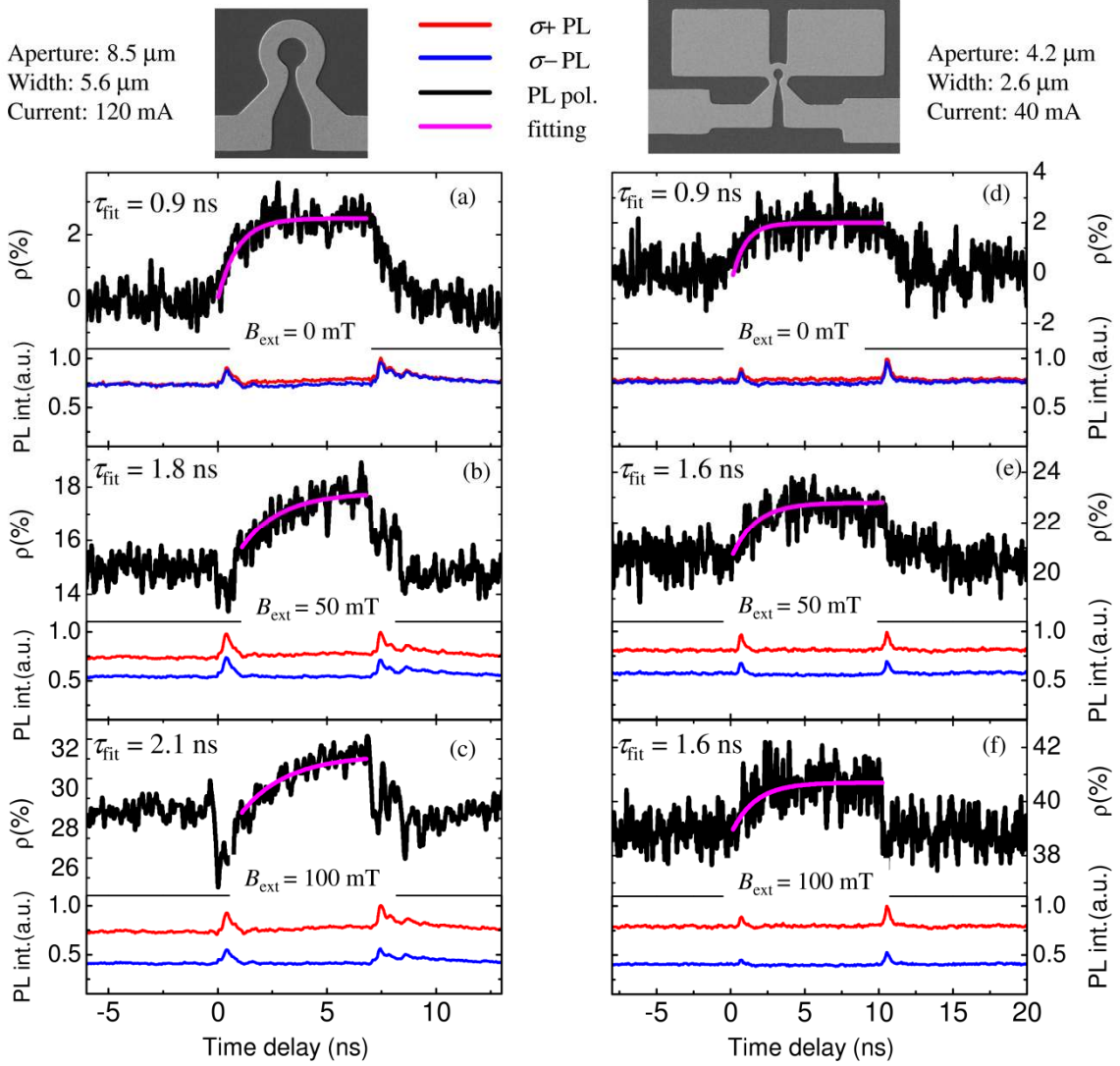
FIG 5.2-1: Magnetic field dependence of the PL polarization formation process for sample 1 with x_{Mn} = 0.067. The time-resolved PL polarization (black) is evaluated from the experimentally measured σ^+-polarized PL (red) and σ^--polarized PL intensity (blue). In each case, the magnitude of the magnetic field is indicated and the formation process is exponentially fitted (magenta) with the given constant. (a) ~ (c): induced by a pulsed current through the microcoil on the left side. The current amplitude is 120 mA, the pulse width is 7 ns and the repetion period is 35 ns. (d) ~ (f): induced by a pulsed current through the microcoil on the right side. The current amplitude is 40 mA, the pulse width is 10 ns and the repetion period is 50 ns. The time delay is relative to the leading edge of the electrical pulse.

In figure (b), a longer electrical pulse is used, i.e. τ_{pul} = 400 ns and the repetition period is 2 μs. The magnetization is still controlled by a fast dynamic process at zero external field, i.e. the data are fitted by a time constant of 3 ns. In the presence of B_{ext} = 100 mT, the spin formation is observed on a much longer time scale. The magnetization dynamics, spin formation or spin decay, is composed of a fast process and a clearly slower process. Each dynamical process can be well fitted bi-exponentially by a short time constant of 3 ns and a longer time constant of 100 ns. This agrees well with the reported results in Ref. [33, 56, 207, 208].
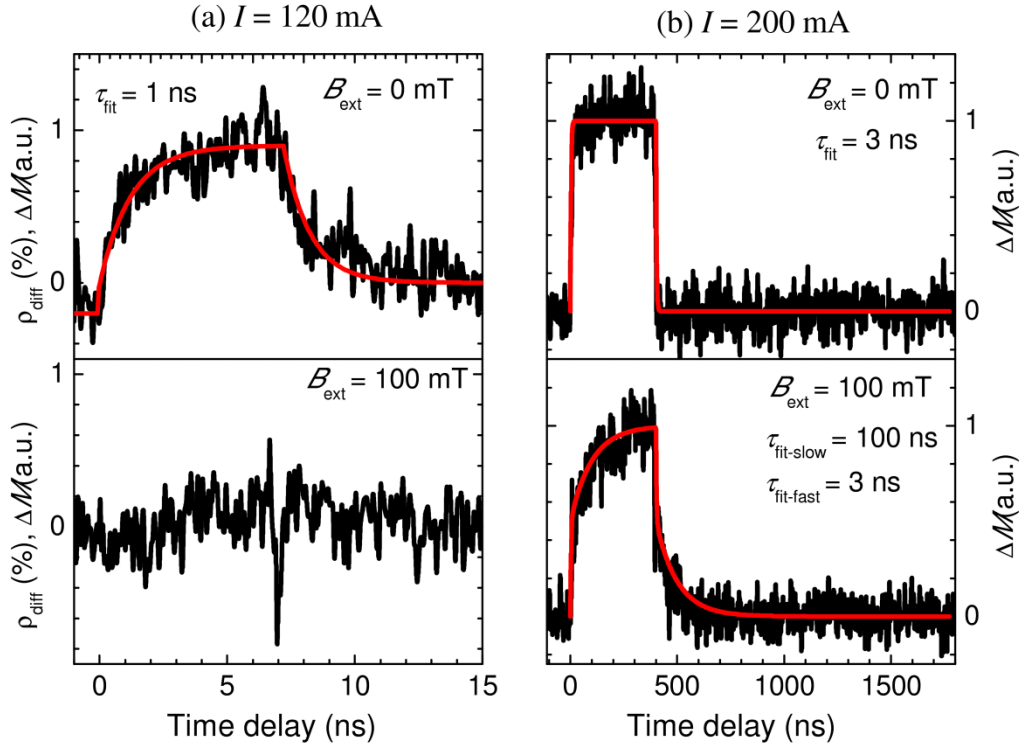
FIG 5.2-2: Magnetic field dependence of the PL polarization dynamics for sample 2 with x_{Mn} = 0.024. In each case, the magnitude of the magnetic field is indicated . (a): The current amplitude is 120 mA, the pulse width is 7 ns and the repetition period is 35 ns. (b): The current amplitude is 200 mA, the pulse width is 400 ns and the repetition period is 2 µs. The time delay is given with respect to the leading edge of the electrical pulse. The pronounded magnetization dynamics is mono-exponentially fitted by the given time constant at B_{ext} = 0 and bi-exponentially fitted by the given constants at B_{ext} = 100 mT.

By varying the pulse width τ_{pul} and the current amplitude I, the magnetization dynamics is further analyzed in the case of B_{ext} = 100 mT. The experimental data are summarized in Table 5-1. As a quite general rule, each magnetization dynamics (formation or decay) is composed of a slow component and a fast component. The fast process has a time constant between 3 ns and 10 ns, while the slow one ranges from 100 ns to 200 ns. The amplitude of each component is comparable, and the ratio between two component amplitudes is the same for the formation and the decay process for a specific pulsed current. The slow component is comparable to the SLR time for this sample at the bath temperature which is between 8 K and 15 K according to Equation (4-3) and the experimental data in Ref.[202].

In the absence of a static field, the magnetization dynamics is always fast on a time scale of a few nanoseconds (< 5 ns, see Table 5-2). It seems that these fast components are independent on the static field and the current parameters within the experimental errors.

In case of the longer pulse width, the presented magnetization dynamics is obtained by using the relation $\Delta M(\Delta t) \propto \rho_{diff}(\Delta t) / \rho_{av}(\Delta t)$, in which Δt is the time delay. As indicated in Equation (4-2), $\rho_{av}(\Delta t)$ reflects the magnetization dynamics controlled by the dynamical Mn ion spin temperature T_{Mn} (but at a constant magnetic field) and the exciton temperature T_{EX}, i.e. $\rho_{av}(\Delta t) \propto M(B_{ext}, T_{Mn},$

$\Delta t)\cdot T_{\mathrm{EX}}^{-1}$. Due to fast carrier-lattice relaxation time, the exciton temperature can be regarded to be the same as the lattice temperature. The Mn ion spin temperature is convolution of the dynamical temperature and the SLR relaxation process [188]. For the quantity $\rho_{\mathrm{diff}}(\Delta t)$, it could be regarded a result of the spin response to the pulsed field B_{I}, the magnetization dynamics affected by the Mn ion spin heating and the exciton temperature, i.e. $\rho_{\mathrm{diff}}(\Delta t) \propto M(B_{\mathrm{I}}, T_{\mathrm{Mn}}, \Delta t)\cdot T_{\mathrm{EX}}^{-1}$. In the low field regime, the quality $\rho_{\mathrm{diff}}(\Delta t) / \rho_{\mathrm{av}}(\Delta t)$ reflects the magnetization dynamics induced by the pulsed field $B_{\mathrm{I}}(\Delta t)$. This should allow one to give a rough estimation of the magnetization dynamics.

τ_{pul} / I ⟍ Slow / fast	Amplitude, formation	Time constants, formation	Amplitude, decay	Time constants, decay
400 ns / 100 mA	0.6 / 0.4	100 ns / 5 ns	0.6 / 0.4	150 ns / 5 ns
400 ns/ 200 mA	0.5 / 0.5	100 ns / 3 ns	0.5 / 0.5	100 ns / 3 ns
1200 ns / 100 mA	0.8 / 0.2	120 ns / 5 ns	0.8 / 0.2	100 ns / 5 ns
1200 ns / 200 mA	0.5 / 0.5	200 ns / 10 ns	0.5 / 0.5	150 ns / 10 ns

Table 5-1: Fitted parameters of the magnetization dynamics induced by different pulsed currents for sample 2 ($x_{\mathrm{Mn}} = 0.024$) at $B_{\mathrm{ext}} = 100$ mT. Both the formation process and the decay process are analysed. Each dynamical process is biexponentially fitted by a fast and slow component and the normalized amplitude of each amplitude is indicated.

From the experimental results presented above for sample 1 and sample 2, it can be concluded, (i) the magnetization dynamics is independent of the Mn content in the absence of a static magnetic field; (ii) the magnetization dynamics is clearly slowed down by applying an external field. A summary of the observed magnetization dynamics is given in Table 5-2 for the studied two samples.

B_{ext} (mT) ⟍ Dynamics (ns)	Sample 1, x = 0.067	Sample 2, x = 0.024	
		fast	slow
0	0.9	< 5 ns	none
50	1.7 ± 0.1	-	-
100	1.85 ± 0.25	6.5 ± 3.5	150 ± 50

Table 5-2: Summary of the observed magnetization dynamics for two samples.

In order to understand the field dependence of the pulsed field-induced magnetization dynamics, the Hamiltonian of one Mn ion is considered as described by Equation (5-1). Both the electron spin states $|S>$ and the nuclear spin states $|I>$ of the Mn ion are taken into account, and the z-component is defined parallel to the direction of the external magnetic field. The state is denoted as $|S_i, I_j>$ for the electron spin of S_i and the nuclear spin of I_j. There are totally 36 states which are orthogonal with each other by considering $S = 5/2$ and $I = 5/2$. Based on the Mn ion spin Hamiltonian by using the parameters given in Section 5.1.1., the energy levels of the eigenstates are plotted in FIG 5.2-3. Each eigenstate is a linear sum of different states of $|S_i, I_j>$.

For small values of the magnetic field as shown in (b), there are strong state anticrossings. They origin from the anisotropic spin interactions including the hyperfine interaction and the spin coupling with the crystal field as well the strain-induced electric field. The anticrossings indicate adiabatic state transitions which bypass the energy transfer between the spin system and the phonon system via SLR process. Therefore the state transition process controlling the magnetization dynamics can be treated as a series of Landau-Zener processes by sweeping the magnetic field [56] in the absence of a static field. For the larger magnetic field, e.g. 100 mT in (a), it can be seen that most eigenstates are energetically separated. In this case, the magnetization dynamics induced by a pulsed field is expected to be dominant by the spin-lattice relaxation.
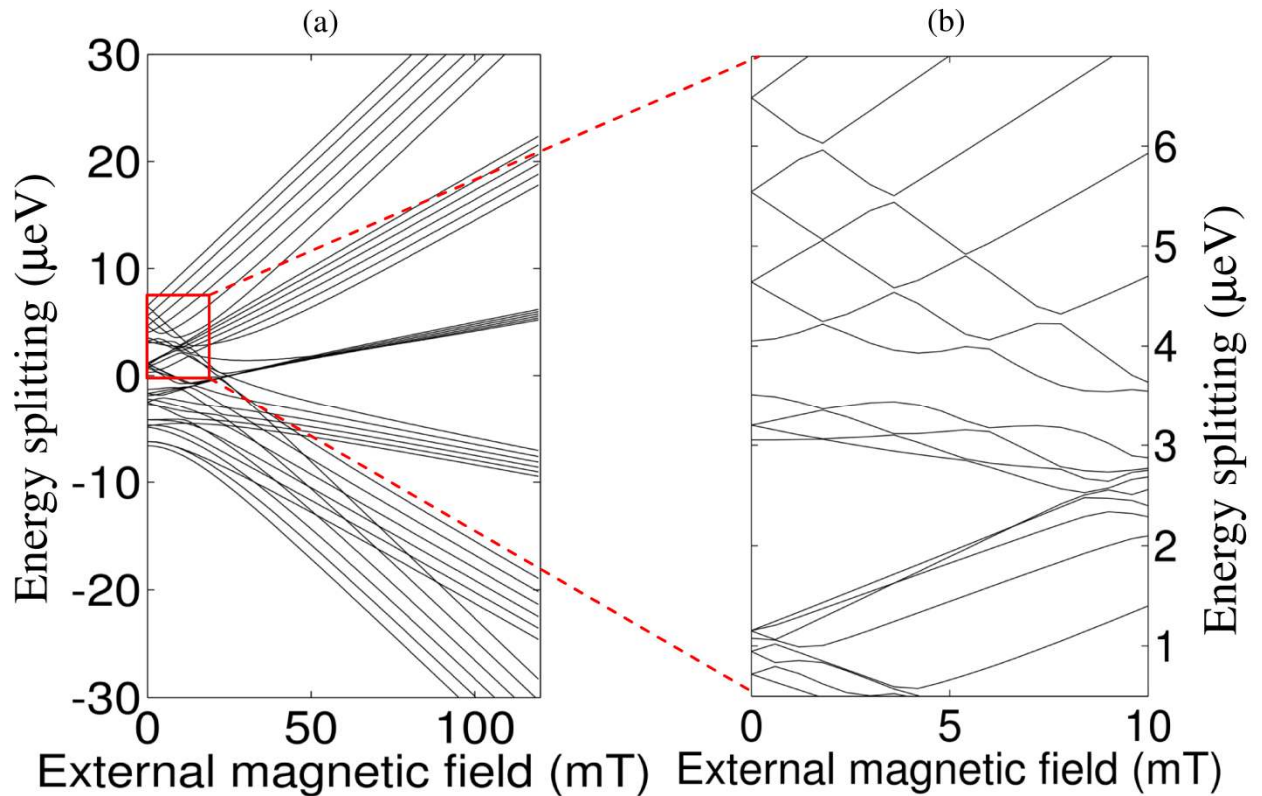

FIG 5.2-3: Numerically calculated energy levels of eigenstates by taking account into the hyperfine interaction, mismatch-induced strain and the crystal field. Each eigenstate is composed of the electron spin states and the nuclear spin states of one Mn ion. The right figure is selected area of the left figure.

The spin dynamics of one Mn ion induced by a pulsed field is numerically simulated by solving the Lindblad-type master equation [210]:

$$\frac{d\rho}{dt} = \frac{1}{i\hbar}\left[\hat{H}, \rho\right] + \left(2\hat{L}\rho\hat{L}^{\dagger} - \left\{\hat{L}^{\dagger}\hat{L}, \rho\right\}\right) \tag{5-9}$$

Here $\hat{H}$ spin Hamiltonian in Equation (5-1), ρ is the spin density matrix for the eigenstates determined in FIG 5.2-3, and $\hat{L}$ the Lindblad operator. The Lindblad operator can be simplified as $\hat{L} = \hat{L}_1 + \hat{L}_2 + \hat{L}_3$, with $\hat{L}_1 = \Gamma_1\hat{\sigma}_+$, $\hat{L}_2 = \Gamma_2\hat{\sigma}_-$, and $\hat{L}_3 = \Gamma_3\hat{\sigma}_z$. The terms of $\hat{L}_1$ and $\hat{L}_2$ describe the spin-lattice relaxation process and the constants Γ_1 and Γ_2 are determined by the SLR rate and the Zeeman energy splitting between the subbands. Only the Mn ion SLR is considered while neglecting the nuclear SLR process. The constant values are given by $\Gamma_1^{-1} = \tau_{SLR}$ and $\Gamma_2^{-1} = \Gamma_1^{-1} \cdot \exp(-\Delta E/k_B T_{bath})$, where ΔE is the energy splitting between the subbands. The term L_3 describes the spin-spin relaxation process and Γ_3 is the spin-spin relaxation rate. $\hat{\sigma}_+$, $\hat{\sigma}_-$ and $\hat{\sigma}_z$ are the Pauli matrices.

The simulation results are presented in FIG 5.2-4 for sample 1 ($x_{Mn} = 0.067$). According to the experimental conditions, the used parameters are: the bath temperature is 10 K, the magnitude of the pulsed field is 9 mT, and the SLR time is 3 ns and the spin-spin interaction is used as 500 ps [55]. It can be seen, the simulation results are in a qualitative agreement with the experiment results presented in FIG 5.2-1: the magnetization dynamics is fast on a sub-ns time scale in the absence of a static field. A slow component with much smaller amplitude is also indicated. The dynamics is clearly slowed down by increasing the external field. In (a) where the in-plane strain is considered absent, the pulsed field induced magnetization dynamics is almost indistinguishable for $B_{ext} = 50$ mT and $B_{ext} = 100$ mT, which is similar with the experimental observations. In Ref. [56], a strain of $\delta_{xy} = 0.004$ is introduced due to local fluctuations or dislocations. The simulation results are presented in (b) incorporating this effect. As a result the magnetization dynamics is further accelerated in case of $B_{ext} = 0$ mT and the slow component disappears. The magnetization dynamics becomes distinguishable between $B_{ext} = 50$ mT and $B_{ext} = 100$ mT and the SLR process is more dominant for a higher magnetic field. Definitely the strain in the [110] direction can accelerate the magnetization dynamics due to the anisotropic interactions with the Mn ion spins. This might explain why the dynamics is observed relatively faster for the microcoil with a smaller aperture, as demonstrated in FIG 5.2-1. The bath temperature is estimated ~7 K for FIG 5.2-1(f), and the bath temperature is estimated ~11 K for FIG 5.2-1(c). Thus the SLR process is supposed to be longer in FIG 5.2-1(f). This contrary indicates the faster spin dynamics in FIG 5.2-1(f) might origin from the microcoil geometry, e.g. it could be expected the strain in the DMS layer is larger for this microcoil due to a smaller aperture size. Such an acceleration of the magnetization dynamics was also found in a (Cd, Mn)Te QD system with a stronger strain compared with a QW system [209].
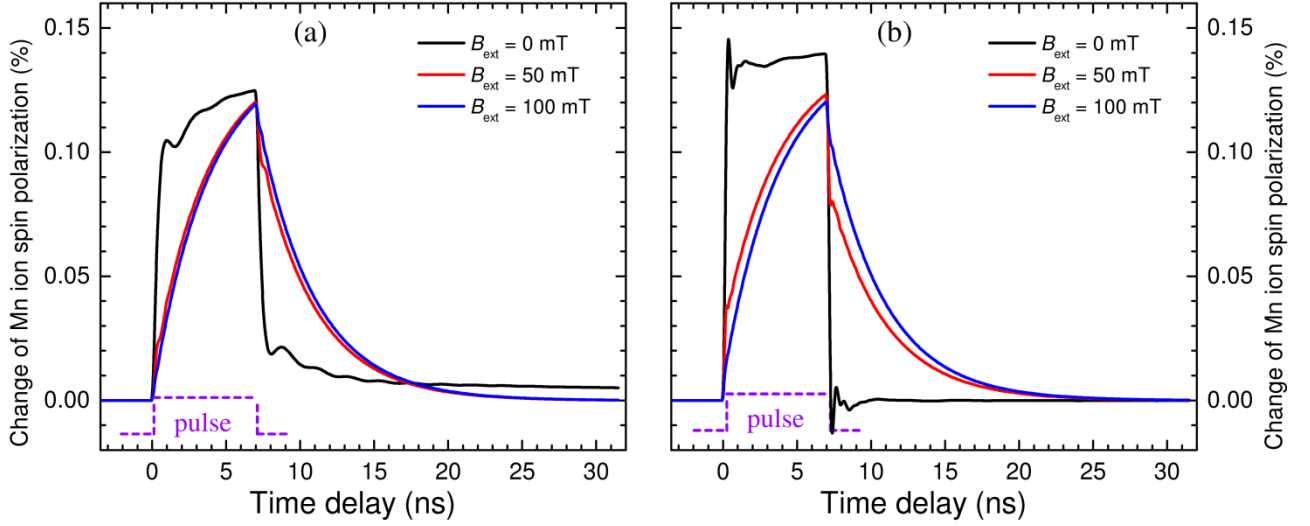
FIG 5.2-4: Numerically calculated magnetic field dependence of one Mn ion spin dynamics induced by a pulsed magnetic field for sample 1 ($x_{Mn} = 0.067$). For the simulations, the magnitude of the pulsed field (magenta dashed line) is 9 mT, the pulse width is 7 ns, the bath temperature is 10 K, a SLR time of 3ns and spin-spin time of 500 ps are used. The magnitude of the external field is indicated by a specific color. (a): strain $\delta_{xy} = 0$; (b) $\delta_{xy} = 0.004$.

A similar simulation is performed for sample 2 ($x_{Mn} = 0.024$). The numerical calculations are given in FIG 5.2-5. The used parameters are: the bath temperature is 10 K, the magnitude of the pulsed field is 9 mT, and the SLR time is 150 ns and the spin-spin interaction is approximated as 500 ps. At zero external field, the magnetization dynamics almost instantaneously follows the pulsed field. This agrees nicely with the experimental result: the magnetization dynamics is independent of the Mn content in case of $B_{ext} = 0$ mT. In case of an external field, the magnetization dynamics contains a fast component and a slow component. The amplitude of the slow component is growing by increasing the magnetic field while the amplitude of the fast component is going down. This field dependence of each component amplitude coincides well with the experimentally extracted data in Ref. [33, 207]. As a prominent effect found experimentally, the external field greatly slows the magnetization dynamics which trends to the SLR process

It has to be mentioned that the simulation is performed for one Mn ion isolated from surrounding ones. Thereby, the d-d exchange interaction from the neighbouring Mn ions is not taken into account. Since the d-d exchange interaction is anisotropic, a further acceleration is expected for a DMS sample with a higher Mn content. In addition, the magnetization saturation level is expected to be reduced due to anti-ferromagnetic coupling between the Mn ion pairs. The exchange interaction between the Mn ion and the existing holes is also not included. One can expect that the carriers can slow down the magnetization dynamics induced by a pulsed field in the absence of a static field, and the carriers can accelerate the dynamical process in the presence of a moderate magnetic field [56, 208].
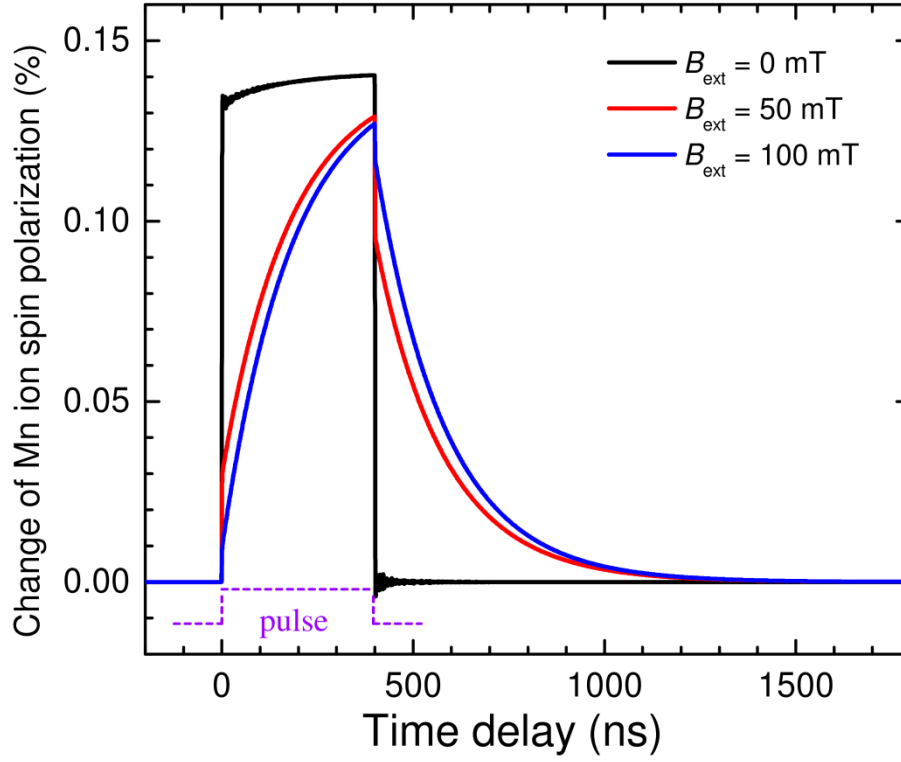
FIG 5.2-5: Numerically calculated magnetic field dependence of one Mn ion spin dynamics induced by a pulsed magnetic field for sample 2 ($x_{Mn} = 0.024$). For the simulations, the magnitude of the pulsed field (magenta dashed line) is 9 mT, the pusle width is 400 ns, the bath temperature is 10 K, a SLR time of 3ns and spin-spin time of 500 ps are used. The magnitude of the external field is indicated by a specific color. The strain $\delta_{xy} = 0.004$.

6   LOCAL MANIPULATION OF NUCLEAR SPINS IN A

SEMICONDUCTOR

This chapter deals with the nuclear spin polarization and coherent nuclear spin manipulation in an n-GaAs sample. At first a theoretical background is discussed regarding the electron-nucleus hyperfine coupling which controls the dynamic nuclear polarization and the nuclear spin relaxation in a semiconductor. Experimentally the dynamic nuclear field is optically addressed by the time-resolved Kerr rotation technique. By means of optically generating spin-polarized electrons, the nuclear field is built up on a typical time scale of minutes. The dependence of the nuclear field properties is studied by varying the experimental conditions. By utilizing an on-chip microcoil fabricated atop the semiconductor sample and introducing a radio frequency current through the microcoil to produce a resonance magnetic field, optically detected nuclear magnetic resonance is demonstrated on a length scale of a few micrometers. Further, the Rabi oscillation of ^{75}As nuclear spins is observed with an effective dephasing time of ~200 μs.

6.1   Dynamic nuclear polarization in a semiconductor

Since the nuclear magnetic moment is rather small, the nuclear spin polarization is quite small in thermal equilibrium state. To enhance the nuclear spin polarization, it was proposed and predicted theoretically to be achieved by making use of non-equilibrium electrons in metals by the pioneering work in Ref. [69]. Thereby, the basic idea is to polarize the nuclei via the Fermi contact hyperfine interaction, since the non-equilibrium electrons can flip the nuclear spins in a preferred orientation [211]. The enhancement factor is proportional to the deviation of the electron spin polarization out of the electron spin in thermal equilibrium state. It was also proposed to drive the electron spin states from the thermal equilibrium by applying electron spin resonance excitation with a saturating radio frequency (RF) magnetic field. This phenomenon is known as Overhauser effect and the generated effective nuclear field is named Overhauser field.

Actually the fundamental requirement to cause the Overhauser effect is to generate an average electron spin ($<S>$) different from the electron spin (S_0) under thermal equilibrium. The difference of $|<S> - S_0|$ determines the strength of the Overhauser field. There are more general methods to achieve a nonzero $|<S> - S_0|$, while the RF resonance excitation is not a necessary condition.

Two pioneering experiments demonstrating the Overhauser effect in semiconductors are introduced here. In an experiment performed in an InSb semiconductor sample [71], the nuclei were found to get polarized by injecting hot electrons from a DC current under an external magnetic field. Later, optical pumping was also found to be able to highly polarize the nuclear spins in a high-purity Si sample [70]. The required condition can be fulfilled by controlling the polarization of the excitation light by considering the optical selection rules [21]. For a semiconductor with a finite electron spin

polarization at thermal equilibrium state, e.g. under a strong external field, the optically generated electrons can be set to non-polarized by linear optical pumping for enhancing the nuclear spin polarization. In the case of negligible electron spin polarization, e.g. under a week external field, the optically generated electrons can be spin-polarized by circular optical pumping for generating an enhanced nuclear spin polarization. In both two experiments, the nuclear polarization processes were observed to occur on a time scale of hours. Recent studies indicate the requirement can be met either by spin-polarized electron injection [79, 212-216], or by fabricating ferromagnetic layers/structures to imprint the nuclear field [217]. The nuclear spin polarization is enhanced by several orders of magnitudes than the thermal equilibrium value by using the Overhauser effect. This has been widely used to facilitate studies of nuclear spin properties in various semiconductor systems [21, 72, 73].
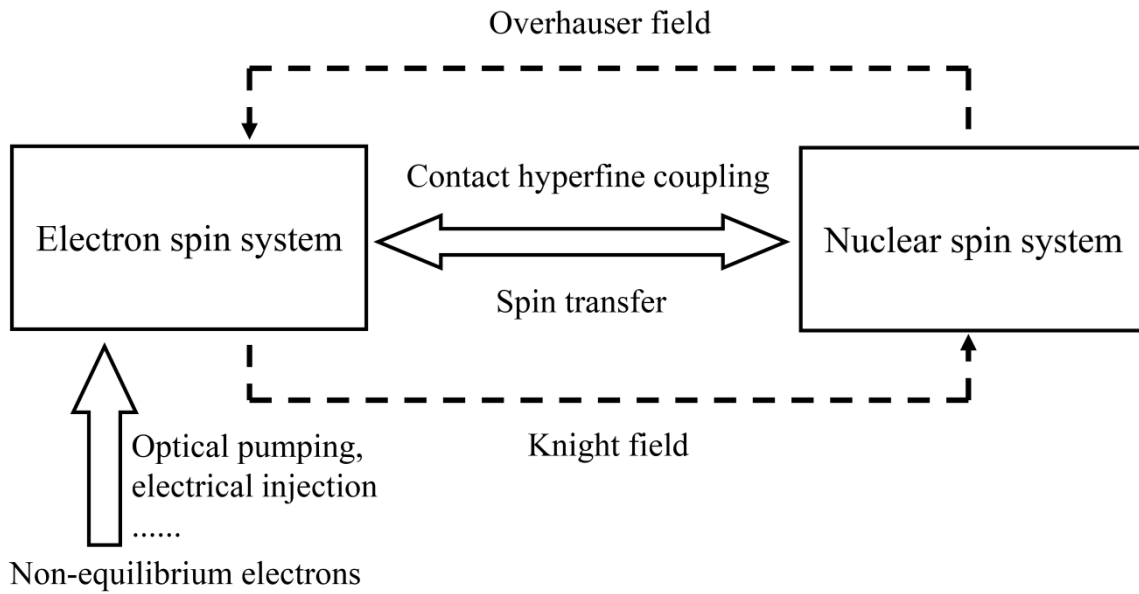

FIG 6.1-1: Electron-nucleus coupling by contact hyperfine interaction

The process of generating nuclear polarization is presented in FIG 6-1-1. Non-equilibrium electrons are injected in the semiconductor either by means of optical pumping or electrical injection etc. This nonequilibrium electron source aims to continuously transfer the excess non-equilibrium spin $|<S>-S_0|$ to the nuclear spin system via contact hyperfine interaction, so that the nuclear spins get polarize, the so called dynamic nuclear polarization (DNP) process. In the dynamic equilibrium state, the electrons see an effective nuclear field, the Overhauser field, and the nuclei see an effective electronic field named as Knight field. The enhanced nuclear magnetization is probed either by conventional nuclear magnetic resonance (NMR) spectrometer by monitoring the free-induction decay signals [72], or detected from optical methods, e.g. Hanle effect [21].

In III-V semiconductors, the hyperfine interaction constant A_{hf} is on the order of 100 μeV (Table 6-1). The coupling can generate an effective nuclear field up to a magnitude of several Tesla, which has been observed in bulk semiconductors [21, 72, 77, 78, 84, 94, 213-215, 217-226], quantum wells [79,

89, 90, 212, 227-233] and quantum dots [34, 73, 81, 216, 234-238]. The pronounced Overhauser field has been manifested in different spin-related phenomenon in the semiconductor electronic system. For electron spin resonance experiments, the resonance spectrum is broadened and shifted due to the Overhauser shift which depends on the electron spin states [219, 220, 224]. In photo-/electro-luminescence experiments, the Hanle curve shape of luminescence polarization is changed as a result of the additional nuclear field [21, 78, 212, 213], or the photoluminescence spectrum is energetically shifted [81, 216, 234, 236]. In electron-transport measurements, the magnetoresistance is either varied as the nuclear field is large enough to tune the Laudau filling level [230-233], or it is modified due to the non-uniform generation of the nuclear field [214, 215]. In a double quantum dot system, the leakage current is modulated by the nuclear polarization which can determine the electron energy splitting between two neighbouring dots [34, 235]. In time-resolved Faraday/Kerr rotation measurements, the dynamical change of the electron Larmor frequency is observed which is ascribed to the DNP formation along the external magnetic field [89, 94, 220-223].

In II-VI semiconductors, the electron-nucleus hyperfine coupling is much weaker as presented in Table 6-1. Nevertheless, the Overhauser effect has been also experimentally confirmed in optical pumping NMR measurements [239-242]. In addition, the change of the electron Larmor frequency resulting from the Overhauser field has been also detected by means of time-resolved Faraday technique [83]. Further in a CdSe/ZnSe quantum dot system which is intrinsically n-doped, the DNP formation is observed as a non-equilibrium process in the absence of a magnetic field. An external field can strongly quench this electron-nucleus coupling [73, 80, 82, 243, 244]. The observed nuclear field generally has a magnitude of a few mT or so. This might be one reason why nuclear spin studies are not so widely performed in II-VI systems up to date.

	Isotope	Nuclear spin number	Isotope abundance	A_{hf} (μeV)
GaAs, InAs,	^{69}Ga	3/2	60%	~ 100
	^{71}Ga	3/2	40%	
	^{75}As	3/2	100%	
	^{113}In	3/2	4.3%	
	^{115}In	3/2	95.7%	
CdSe	^{77}Se	1/2	7.6%	~ -10
	^{111}Cd	1/2	12.8%	
	^{113}Cd	1/2	12.2%	
Si,	^{29}Si	1/2	4.7%	~ 0.2
C	^{13}C	1/2	1.1%	~ 1

Table 6-1: Parameters of electron-nucleus hyperfine interaction for several typical isotope species in semiconductors (data after Ref. [73], Ref.[245] and Ref.[246])

In materials of the IV group, e.g. Si and C, the isotope with nuclear spins is strongly diluted. This means one electron can couple with a much smaller amount of nuclear spins. In these materials, the DNP formation is typically achieved by electrical injection [246] or optically pumping local defects [247]. In the carbon nanotubes, the ^{13}C nuclear spins has been found to be crucial for the electron spin transport [246]. The hyperfine interaction is regarded to be less critical for the electron spin transport in Si-based device [248], and Si actually has been used as a clean host system for nuclear spins [249] .

In semiconductors, mostly the observed Overhauser effect origins from the Fermi-contact hyperfine interaction coupling between the electron spin and the nuclear spin. A short discussion from a theoretical aspect is given in the following section.

6.2   Electron-nucleus hyperfine coupling

In a semiconductor, there could be four types of hyperfine interaction: electron-nucleus contact coupling, hole-nucleus contact coupling electron-nucleus dipole-dipole coupling and hole-nucleus dipole-dipole coupling [66, 72, 245, 250].   In the contact hyperfine interaction, the nuclear spins interact with the carrier spins at the nuclei. An electron in the conduction band, which has s-like symmetry, can strongly couple with the nuclear spins. For a hole, which has p-like symmetry, the contact hyperfine coupling vanishes at the nuclei locations. The situation is opposite for the dipole-dipole hyperfine interaction, which arises from the interaction between the nuclear spins and the carrier orbital spins. As a result of the different wavefunction symmetry, the electron-nucleus dipole coupling is negligible compared with the hole-nucleus dipole coupling. In GaAs, hole-nucleus dipole hyperfine interaction is estimated ~ -10 μeV, which is weaker by one order of magnitude than the electron-nucleus contact hyperfine interaction [245]. Generally the carrier-nuclear spin coupling is dominated by the electron-nucleus contact hyperfine interaction in a n-doped GaAs system.

For an electron in the conduction band, the Hamiltonian of the contact hyperfine interaction at a nucleus site is given as [66]

$$\hat{H}_{\text{hf}} = \frac{4\mu_0}{3}\mu_B g_n \mu_N \hat{\boldsymbol{I}}(\boldsymbol{R}_I)\cdot\hat{S}\cdot\rho_e(\boldsymbol{R}_I) = \frac{4\mu_0}{3}\mu_B g_n \mu_N \hat{\boldsymbol{I}}(\boldsymbol{R}_I)\cdot\hat{S}\cdot\delta(\boldsymbol{R}_I)\cdot\left|\psi(\boldsymbol{R}_I)\right|^2, \qquad (6\text{-}1)$$

where μ_0 is the vacuum permeability, μ_B is the Bohr magneton, g_n is the nuclear g factor, μ_N is the nuclear magneton, $\hat{\boldsymbol{I}}(\boldsymbol{R}_I)$ is the nuclear spin operator at the nucleus site $\boldsymbol{R}_I$, $\hat{S}$ is the electron spin operator, and $\rho_e(\boldsymbol{R}_I)$ is the electron density given by the electron wavefunction. From Bloch theorem, the wavefunction is treated as a product of the electron density function $\delta(R)$ and an envelope function $\psi(R)$. At the nuclei position $\boldsymbol{R}_I$, the electron density constant $d(\boldsymbol{R}_I)$ is defined by

$d\left(\boldsymbol{R}_I\right) \ = \ \delta(\boldsymbol{R}_I) = -\frac{1}{2}\nabla(\frac{1}{r^2})\bigg|_{r\to 0}$, and it is normalized in the volume of a Wigner-Seitz cell. The value

of the wavefunction envelope at $\boldsymbol{R}_I$ is given by $\psi(\boldsymbol{R}_I)$ which is normalized over the whole space as $\int_R |\psi(\boldsymbol{R})|^2 d^3\boldsymbol{R} = 1$. If the electron wavefunction is limited inside a Wigner-Seitz cell, the contact hyperfine interaction becomes the case of coupling between an inner-shell electron and the nucleus [66].

For GaAs, it has been determined d (^{69}Ga) = d (^{71}Ga) $\approx 5.8\times10^{31}$ m^{-3}, d (^{75}As) $\approx 9.8\times10^{31}$ m^{-3} [77, 251]. The hyperfine coupling constant A_{hf} is defined as $A_{hf} = \dfrac{4\mu_0}{3}\mu_B g_n \mu_N d(\boldsymbol{R}_I)$. In GaAs, the contact hyperfine constant is calculated: $A_{hf}(^{69}$Ga$) \approx 35.6$ μeV, $A_{hf}(^{71}$Ga$) \approx 45.3$ μeV, and $A_{hf}(^{75}$As$) \approx$ 43.0 μeV. In a Wigner-Seitz cell the total hyperfine coupling constant $A_{hf}(GaAs) \approx \sum_\alpha \chi^\alpha A_{hf}(\alpha) \approx$ 0.6* $A_{hf}(^{69}$Ga$)$ + 0.4* $A_{hf}(^{71}$Ga$)$ + $A_{hf}(^{75}$As$) \approx 82.5$ μeV. Hereby the isotope abundance χ^α is taken into account, and $\chi^{69Ga} \approx 60\%$, $\chi^{71Ga} \approx 40\%$, $\chi^{75As} = 100\%$.

For one nucleus site Equation (6-1) is rewritten as

$$\hat{H}_{hf} = A_{hf} |\phi(\boldsymbol{R}_I)|^2 \hat{\boldsymbol{I}}\cdot\hat{\boldsymbol{S}} \tag{6-2}$$

In the Ising form it is given as

$$\hat{H}_{hf} = A_{hf} |\phi(\boldsymbol{R}_I)|^2 [\hat{I}_z\hat{S}_z + \frac{1}{2}(\hat{I}_+\hat{S}_- + \hat{I}_-\hat{S}_+)] \tag{6-3}$$

Here the Ladder operators are defined as $\hat{I}_+ = \hat{I}_x + i\hat{I}_y$, $\hat{I}_- = \hat{I}_x - i\hat{I}_y$, $\hat{S}_+ = \hat{S}_x + i\hat{S}_y$ and $\hat{S}_+ = \hat{S}_x - i\hat{S}_y$.

From Equation (6-3) it can directly be seen that, the non-equilibrium electrons flip the nuclear spins continuously from electron spin injection, so that the nuclei get spin-polarized to give the Overhauser field.

6.2.1 Overhauser field and Knight field

Since the electron wavefunction covers a large range of nuclear sites, the contact hyperfine interaction experienced by one electron is governed by :

$$\hat{H}_{hf} = A_{hf}\hat{\boldsymbol{S}}\cdot\sum_{\boldsymbol{R}_I} |\psi(\boldsymbol{R}_I)|^2 \hat{\boldsymbol{I}}(\boldsymbol{R}_I) = A_{hf}\hat{\boldsymbol{S}}\cdot\hat{\boldsymbol{I}}_{av}, \tag{6-4}$$

where $\hat{\boldsymbol{I}}_{av}$ is the average nuclear spin over the whole nucleus sites. There is an effective nuclear field seen by the electron. As there are three nuclear species in GaAs, the nuclear field contribution from isotope α is written as

$$\boldsymbol{B}_N(\alpha) = \frac{H_{hf}}{g_e\mu_B S} = \frac{4\mu_0}{3g_e}g_n\mu_N d(\alpha) < \boldsymbol{I}_{av}{}^\alpha >, \tag{6-5}$$

where g_e is the electron Landé g factor and $\boldsymbol{I}_{av}{}^\alpha$ is the average nuclear spin for α isotope species. For the case of spatially uniform nuclear spin polarization, this effective field is independent on the electronic state, either free electron state or localized state in a semiconductor.

In GaAs it is found $g_e \approx -0.44$. For a complete nuclear spin polarization with $\langle \boldsymbol{I}_{av}^{\alpha} \rangle = 3/2$, the nuclear field contribution from each isotope is: $b_N(^{69}\text{Ga}) = -1.37$ T, $b_N(^{71}\text{Ga}) = -1.17$ T, and $b_N(^{69}\text{Ga}) = -2.76$ T.

From Equation (6-5), it can be seen that the giant effective nuclear field is basically due to the large electron density (indicated by $d(\alpha)$) at the nucleus sites. If the electron wavefunction is homogeneously smeared instead of highly concentrated at nucleus sites, the effective nuclear field is estimated to be on the order of 0.1 mT which is likely a dipole-dipole spin interaction.

On the other hand, the nuclei can see an effective magnetic field, namely the Knight field, from the electron. Since one electron can couple with many nuclei, the contact hyperfine interaction is shared by all the involved nuclei. From Equation (6-2), the effective electronic field seen by the nucleus at $\boldsymbol{R}_I$ is

$$\boldsymbol{B}_e(\boldsymbol{R}_I) = -\frac{A|\phi(\boldsymbol{R}_I)|^2 \boldsymbol{I} \cdot \boldsymbol{S}}{g_n \mu_N I} v_{cell} = -\frac{4\mu_0 \mu_B d(\boldsymbol{R}_I)}{3}|\phi(\boldsymbol{R}_I)|^2 v_{cell} \boldsymbol{S} \tag{6-6}$$

Here v_{cell} is the volume of Wigner-Seitz with $v_{cell} \approx 4.5\times10^{-29}$ m^{-3} [103]. It can be seen, the electronic magnetic field depends on the envelope function, and is independent on the nuclear spin. If there is more than one electron seen by one nucleus, the effective field is a sum of each electron i, i.e.

$$\boldsymbol{B}_e(\boldsymbol{R}_I) = \sum_i \boldsymbol{B}_{ei}(\boldsymbol{R}_I) = -\sum_i \frac{4\mu_0 \mu_B d(\boldsymbol{R}_I)}{3}|\phi_i(\boldsymbol{R}_I)|^2 v_{cell} \boldsymbol{S}_i \tag{6-7}$$

For free electronic states in a semiconductor, the Knight field can be quite weak. In an InSb sample with an electron density of 10^{15} cm^{-3}, the Knight field magnitude was evaluated ~0.1 mT with full electron spin polarization [252]. It can be expected the magnitude is larger for localized electrons. In a Si-doped GaAs sample, if one considers a donor-bound electron with a wavefunction envelope

$$\phi(\boldsymbol{R}) = \left(\frac{1}{\pi a_B^3}\right)^{1/2} e^{-R/a_B}, \text{with} \int |\phi(\boldsymbol{R})| d^3\boldsymbol{R} = 1 \tag{6-8}$$

Here R is the distance relative to the donor, a_B is the Bohr radius for the shallow donor, and typically $a_B \approx 10$ nm is used in bulk GaAs [77]. Put the Equation (6-8) into Equation (6-6), one obtains

$$\boldsymbol{B}_e(\boldsymbol{R}_I) = -\frac{4\mu_0 \mu_B d(\boldsymbol{R}_I)}{3\pi a_B^3} v_{cell} e^{-2R/a_B} \Gamma_t \boldsymbol{S} = B_e(0) e^{-R/a_B} \Gamma_t \boldsymbol{S},$$

$$\text{with } B_e(0) = -\frac{4\mu_0 \mu_B d(\boldsymbol{R}_I)}{3\pi a_B^3} v_{cell} \tag{6-9}$$

Here $B_e(0)$ is the Knight field at the donor site, and Γ_t is the time fraction of the donor occupied by the electron. Γ_t has a value between zero and unity, and Γ_t is determined by thermal activation, hopping to neighbouring donor sites and carrier recombination. The field amplitude for each nuclear species is calculated: $B_e(0, ^{69}\text{Ga}) = B_e(0, ^{71}\text{Ga}) \approx -12.9$ mT, and $B_e(0, ^{75}\text{As}) = -21.8$ mT. Further, within the range of the Bohr radius, the average Knight field can be given as

$$\langle \boldsymbol{B}_e \rangle = \frac{1}{a_B} \int_0^{a_B} B_e(0) e^{-2R/a_B} \Gamma_t S dr = \sum_\alpha \chi^\alpha B_e(0,\alpha) S \left(\frac{1}{a_B} \int_0^{a_B} e^{-2R/a_B} dr \right) \approx 0.32 \sum_\alpha \chi^\alpha B_e(0,\alpha) \Gamma_t S \quad (6\text{-}10)$$

By considering the isotope abundance, the averaged Knight field amplitude is $\langle \boldsymbol{B}_e \rangle \approx -17.35 \cdot \Gamma_t S$ mT. For $S = \pm 1/2$, the maximal average amplitude is $|\langle \boldsymbol{B}_e \rangle| \approx (8.7 \cdot \Gamma_t)$ mT. In order to get a large Knight field, the factor Γ_t is critical, which means a long occupation of the electron at the donor.

The experimental observed value is typically smaller. A reported value is $|\langle \boldsymbol{B}_e \rangle| \approx 0.09$ mT in a compensated p-type GaAs [77], and $|\langle \boldsymbol{B}_e \rangle| \approx 0.6$ mT in a single electron-charged GaAs quantum dot [81]. Both experiments indicate a quite inhomogeneous distribution of the Knight field.

6.2.2 Nuclear spin polarization in a semiconductor

In a semiconductor, the nuclear spins can relax via several channels. The fluctuating hyperfine interaction described in (6-1) aims to polarize the nuclear spins, while the other mechanisms could depolarize the non-equilibrium nuclear spins. The latter include nuclear dipole-dipole interaction, nuclear exchange interaction, thermal relaxation, and local ion-induced quadrupolar interaction etc. [66, 77, 79, 253] . Here the focus is on the contact hyperfine interaction inducing nuclear spin polarization.

Explicitly the nuclear spins relax via the spin flip-flop process indicated in Equation (6-3). For simplicity, the high-temperature approximation is generally used. For nuclear spin studies, high-temperature approximation is valid due to the small thermal equilibrium spin polarization at helium temperature [66]. This means the Zeeman energy splitting of electron and nuclear spins is much smaller than the thermal energy, i.e. $|g_n \mu_n B I|$ and $|g_e \mu_B B S| << k_B T_{bath}$.

Here T_{bath} is the lattice temperature and k_B is the Boltzmann constant. For conduction electrons in the regime of Fermi-Dirac statistics, e.g. in highly-doped metallic n-GaAs, where electrons are degenerate as in metals, the nuclear spin relaxation rate in the case of $I = 1/2$ is given by [66]

$$T_{\text{hf-pol}}^{-1} = \frac{1}{2\hbar} \mu_0^2 \mu_B^2 g_n^2 \mu_N^2 v_{cell}^2 |d(\boldsymbol{R}_I)|^2 n_e^2 \frac{T}{k_B T_F^2}, \quad (6\text{-}11)$$

in which T_F is the Fermi temperature, n_e is the electron concentration. The Fermi temperature can be estimated based on the free electron gas model [250]. For a metallic n-GaAs of $n_e = 10^{18} \text{cm}^{-3}$, the above equation gives $T_{\text{hf-pol}}(^{75}\text{As}) \approx 9 \times 10^3$ seconds for $T = 5$ K and $T_F = 1000$ K.

Similarly for conduction electrons in the regime of Boltzmann statistics, e.g. in intrinsic GaAs with non-degenerate electronic states, the nuclear spin relaxation rate in the case of $I = 1/2$ is given [66]

$$T_{\text{hf-pol}}^{-1} = \frac{16}{9\hbar^4} \mu_0^2 \mu_B^2 g_n^2 \mu_N^2 n_e v_{cell}^2 |d(\boldsymbol{R}_I)|^2 \left(\frac{m_{\text{eff}}^3 k_B T}{2\pi^3} \right)^{\frac{1}{2}}, \quad (6\text{-}12)$$

where m_{eff} is effective electron mass. As an estimation for GaAs with $n_e = 10^{15}$ cm^{-3}, the above equation gives $T_{\text{hf-pol}}(^{75}\text{As}) \approx 5 \times 10^4$ seconds using $T = 5$ K and $m_{\text{eff}} = 0.067 m_0$.

For electrons localized around donors described in Equation (6-8), the nuclear spin relaxation rate is calculated to be [21, 218]

$$T_{\text{hf-pol}}^{-1} = \frac{8}{9\pi^2} \frac{\mu_0^2 \mu_B^2 g_n^2 \mu_N^2 v_{\text{cell}}^2 |d(\mathbf{R}_I)|^2}{\hbar^2 a_B^6} \Gamma_t \tau_e e^{-4R/a_B} , \tag{6-13}$$

where τ_e is the electron correlation time. By using $\Gamma_t = 1$, $\tau_e = 10^{-11}$ s [225], it is estimated at the donor site $T_{\text{hf-pol}}$ (^{75}As, 0) ≈ 0.17 seconds, and $T_{\text{hf-pol}}$ (^{75}As, a_B) ≈ 9.6 seconds at a distance away of the Bohr radius. Compared with the nuclear spin relaxation from the free electrons, the relaxation rate is obviously much faster for the localized electronic states. This is basically due to much stronger contact hyperfine interaction in the localized regime.

In the case of localized electrons, the nuclear spins beyond the Bohr radius regime, get relaxed (spin-polarized) via the nuclear spin diffusion process [225]. The diffusion rate is given

$$\tau_{\text{diff}}^{-1}(\alpha) = D_n(\alpha) / R^2 \tag{6-14}$$

where $D_n(\alpha)$ is the nuclear spin diffusion constant of nuclear species α on the order of 10^{-13} cm^2/s, and R is the distance to the donor site for rough estimation. For a semi-insulating GaAs sample with a small n-doping and electrons are mainly localized states, e.g. $n_e = 10^{15}$ cm^{-3}, the distance between neighbouring donors is $a_{\text{DD}} \approx 100$ nm $\approx 10a_B$. From Equation (6-14), then the nuclear spin diffusion time is $\tau_{\text{diff}} \approx D_n^{-1} \cdot (a_{\text{DD}}/2)^2 \approx 250$ seconds. Nuclear spin diffusion on a similar time scale has been experimentally observed in bulk GaAs samples alike [72, 225, 226].

For a n-GaAs with a doping level close to the metal-insulator-transition regime, e.g. $n_e \sim 10^{16}$ cm^{-3}, the detected nuclear spin relaxation time ranges from several 10^2 seconds [94, 221] to about 10^3 seconds [250]. This could not be explained with satisfactory either by the theory for free electrons or by the nuclear spin diffusion model for localized electrons. It is quite likely the nuclear spin polarization in this regime originates from the co-existing of two electronic states comprising both delocalized electrons and localized electrons [163, 254-256]. In addition, the localized electrons can couple via spin-spin exchange interaction which is antiferromagnetic. The spin exchange interaction makes a flip-flop process for two coupling electrons with a rather short electron correlation time on the order of 10^{-11} s, and thus results in a fluctuating field seen by the nuclear spins. This additional fluctuating field is able to accelerate the nuclear polarization process. Up to date, the mechanism origins responsible for contact hyperfine interaction in bulk GaAs is still under discussion. A more complex model is required including factors such like electronic states [257] and optical absorption [258].

In general, the nuclear spin polarization process is slowed down by applying an external field [66, 82, 243, 259]. As presented in FIG 6-2-1, the contact hyperfine interaction makes a simultaneous flip-flop process for the electron spin and the nuclear spin. For an easy description, the electron is has a negative effective g factor and the nucleus has a positive one with $I = 1/2$. Here the z-axis is defined to be the direction of the external magnetic field. The electron spin is $S_z = -1/2$, and thus it occupies

the lower energy state by assuming an external field parallel to the z axis. Due to hyperfine interaction, the electron spin is changed to $S_z = 1/2$ (i.e. a higher energy level), while the nuclear spin state is changed from $I = 1/2$ to $I = -1/2$. Each spin flip process is related to energy change, which is provided by absorption or emission of phonons in the crystal. For the electron, the energy change is $\Delta E_e = g_e \mu_B |\boldsymbol{B}_{ext} + \boldsymbol{B}_N| \Delta S_z = g_e \mu_B |\boldsymbol{B}_{ext} + \boldsymbol{B}_N|$, and for the nuclear spin the energy change is $\Delta E_n = g_n \mu_n |\boldsymbol{B}_{ext} + \boldsymbol{B}_e| \Delta I_z = -g_n \mu_n |\boldsymbol{B}_{ext} + \boldsymbol{B}_e|$. The total energy exhausted in this process is

$$\Delta E = \Delta E_e + \Delta E_n = g_e \mu_B \mid \boldsymbol{B}_{ext} + \boldsymbol{B}_N \mid + g_n \mu_n \mid \boldsymbol{B}_{ext} + \boldsymbol{B}_e \mid \qquad (6\text{-}15)$$

As $g_e < 0$ and $g_n > 0$, this spin flip-flop process requires an energy amount; the reverse process transfers the same amount of energy from the spin system to the lattice reservoir. The argument is similar for arbitrary signs of g_e and g_n. As μ_n is much smaller than μ_B ($\mu_B \approx 1800\mu_n$), Equation (6-15) is usually approximated as

$$\Delta E \approx \Delta E_e = g_e \mu_B \mid \boldsymbol{B}_{ext} + \boldsymbol{B}_N \mid \qquad (6\text{-}16)$$
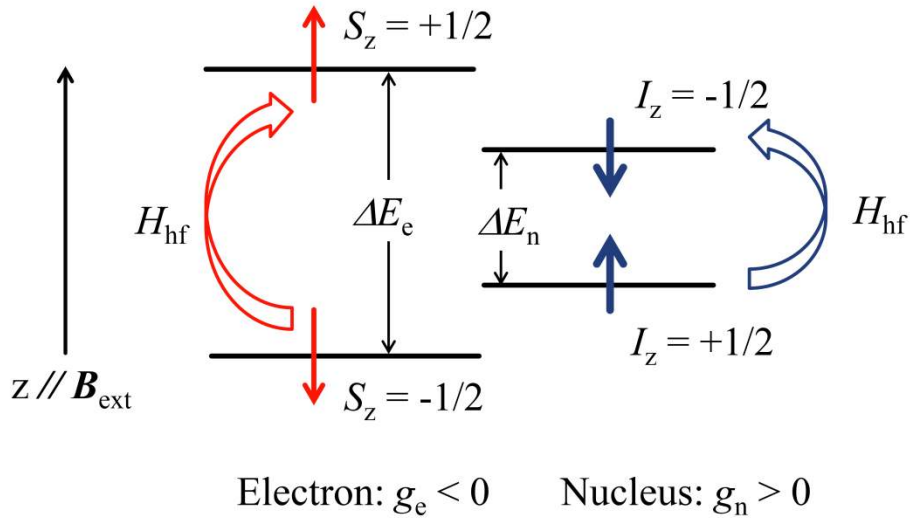

FIG 6.2-1: Electron-nuclear spin flip-flop process mediated by contact hyperfine interaction. The external field lifts up the degeneracy for different spin states. The energy splitting between the electron spin states (ΔE_e) is not equal to the energy splitting between the nuclear spin states (ΔE_n).

From a statistical aspect, the hyperfine interaction fluctuation is weakened by the Zeeman energy caused by the applied external field, and thus the relaxation is slowed down. The spin relaxation rate for nuclear species α is modified by multiplying a factor given by [66, 76, 216, 225]

$$T_{\text{hf-pol}}^{-1}(B_{ext}, \alpha) = T_{\text{hf-pol}}^{-1}(0, \alpha) \frac{1}{1 + \tau_e^2 (\Delta E / \hbar)^2} \approx T_{\text{hf-pol}}^{-1}(0, \alpha) \frac{1}{1 + (\omega_e \tau_e)^2}, \text{with } \omega_e = \Delta E_e / \hbar, \quad (6\text{-}17)$$

where ω_e is electron precession frequency around the total field, and the expression $T_{\text{hf-pol}}^{-1}(0, \alpha)$ denotes the relaxation rate calculated from Equation (6-11) ~ (6-13).

6.2.3 Dynamic nuclear polarization

As a consequence of fluctuating contact hyperfine interaction, the nuclear spins of α isotope get spin-polarized with an equilibrium state [66, 218, 224]

$$\langle \boldsymbol{I}_{\text{hf}}(\alpha) \rangle = \boldsymbol{I}_0(\alpha) + f_{1\alpha} \frac{4 I_\alpha (I_\alpha + 1)}{3} (\langle \boldsymbol{S} \rangle - \boldsymbol{S}_0) \tag{6-18}$$

Here $\boldsymbol{I}_0(\alpha)$ and $\boldsymbol{S}_0$ is the mean nuclear spin and electron spin in the thermal equilibrium state, respectively. $<S>$ is the average electron spin during the lifetime. The coefficient $f_{1\alpha}$ is called the nuclear spin leakage factor defined as

$$f_{1\alpha} = \frac{T_{hf-pol}^{-1}(\alpha)}{T_{hf-pol}^{-1}(\alpha) + T_{irhf-dep}^{-1}(\alpha)}, \tag{6-19}$$

where $T_{\text{irhf-dep}}^{-1}(\alpha)$ is the nuclear spin depolarization rate of isotope α due to any other relaxation channel except the contact hyperfine interaction. It can be different for different nuclear species. Therefore the nuclear polarization rate of Equation (6-17) is modified by taking into account the leakage factor,

$$T_{\text{hf-pol}}'^{-1}(B_{\text{ext}}, \alpha) = T_{\text{hf-pol}}^{-1}(B_{\text{ext}}, \alpha) + T_{\text{irhf-dep}}^{-1}(B_{\text{ext}}, \alpha) = f_{1\alpha}^{-1} T_{\text{hf-pol}}^{-1}(B_{\text{ext}}, \alpha) \tag{6-20}$$

Since $\boldsymbol{I}_0(\alpha)$ is too small to be noticeable, Equation (6-18) is simplified as

$$\langle \boldsymbol{I}_{\text{hf}}(\alpha) \rangle \approx \frac{4 I_\alpha (I_\alpha + 1) f_{1\alpha}}{3} (\langle \boldsymbol{S} \rangle - \boldsymbol{S}_0) \tag{6-21}$$

While polarizing nuclear spins, the contact hyperfine interaction in addition partly depolarizes the nuclear spins assisted by nuclear spin-spin interaction. The nuclear spin depolarization is driven by nuclear dipole-dipole interaction and nuclear spin exchange interaction [77]. The precession around the dynamical effective electronic field can also depolarize nuclear spins [79, 234]. This depolarization rate is

$$T_{\text{hf-dep}}^{-1}(B_{\text{ext}}, \alpha) = \frac{\xi B_L^2}{\left| \boldsymbol{B}_{\text{ext}} + \boldsymbol{B}_e \right|^2} T_{\text{hf-pol}}'^{-1}(B_{\text{ext}}, \alpha), \tag{6-22}$$

Here it is approximated the electronic field is the same for each nuclear isotope. The expression for an arbitrary case is given in Ref. [77].

In Equation (6-22), $\boldsymbol{B}_e$ is the Knight field. The nuclear dipole field B_L is typically on the order of 0.1 mT, and ξ is a factor charactering the depolarizing rate. If the nuclear spin-spin interaction is solely given by the dipole-dipole interaction, ξ is equal to $\sqrt{3}$. While normally ξ has small value in bulk GaAs, it becomes quite large (up to 10^4) if the hyperfine interaction is subject to a large electron spin anisotropic interaction which can strongly depolarizes the electron spins, e.g. electron-hole exchange interaction in quantum dots [234] or anisotropic electron spin interaction in semiconductor-ferromagnet hybrid structures [79, 217].

The rate equation for the dynamical nuclear polarization (DNP) process incorporating the nuclear polarization and depolarization process is written as [79]

$$\frac{d\langle \boldsymbol{I}(\alpha)\rangle}{dt} = -\frac{\langle \boldsymbol{I}(\alpha)\rangle - \langle \boldsymbol{I}_{\mathrm{hf}}(\alpha)\rangle}{T'_{\mathrm{hf\text{-}pol}}(B_{\mathrm{ext}},\alpha)} - \frac{\langle \boldsymbol{I}(\alpha)\rangle}{T_{\mathrm{hf\text{-}dep}}(B_{\mathrm{ext}},\alpha)} \tag{6-23}$$

In steady state with $\dfrac{d\langle \boldsymbol{I}(\alpha)\rangle}{dt} = 0$, and by considering Equation (6-22), the nuclear spin of isotope

species α is given

$$\langle \boldsymbol{I}_s(\alpha)\rangle = \frac{4I_\alpha(I_\alpha+1)}{3} f_{1\alpha} \frac{(\boldsymbol{B}_{\mathrm{ext}}+\boldsymbol{B}_e)\cdot(\langle \boldsymbol{S}\rangle - \boldsymbol{S}_0)}{|\boldsymbol{B}_{\mathrm{ext}}+\boldsymbol{B}_e|^2 + \xi B_L^2}(\boldsymbol{B}_{\mathrm{ext}}+\boldsymbol{B}_e) \tag{6-24}$$

To keep in mind, the nuclear spin direction is along the field ($\boldsymbol{B}_{\mathrm{ext}} + \boldsymbol{B}_e$) seen by nuclei [77, 81]. The rate of the nuclear dynamic polarization from the rate equation of (6-23) is given as

$$T_{\mathrm{DNP}}{}^{-1}(B_{\mathrm{ext}},\alpha) = T'_{\mathrm{hf\text{-}pol}}{}^{-1}(B_{\mathrm{ext}},\alpha) + T_{\mathrm{hf\text{-}dep}}{}^{-1}(B_{\mathrm{ext}},\alpha) = \left(1 + \frac{\xi B_L^2}{|\boldsymbol{B}_{\mathrm{ext}}+\boldsymbol{B}_e|^2}\right) T'_{\mathrm{hf\text{-}pol}}{}^{-1}(B_{\mathrm{ext}},\alpha) \tag{6-25}$$

The total Overhauser field seen by an electron is the sum over three isotope species in GaAs

$$\boldsymbol{B}_N = \sum_\alpha \boldsymbol{B}_N(\alpha) = \sum_\alpha b_N(\alpha)\frac{\langle \boldsymbol{I}_s(\alpha)\rangle}{I_\alpha} = \sum_\alpha \frac{4(I_\alpha+1)f_{1\alpha}b_N(\alpha)}{3}\frac{(\boldsymbol{B}_{\mathrm{ext}}+\boldsymbol{B}_e)\cdot(\langle \boldsymbol{S}\rangle - \boldsymbol{S}_0)}{|\boldsymbol{B}_{\mathrm{ext}}+\boldsymbol{B}_e|^2 + \xi B_L^2}(\boldsymbol{B}_{\mathrm{ext}}+\boldsymbol{B}_e) \tag{6-26}$$

This indicates that, it has always to be ensured $|\boldsymbol{B}_{\mathrm{ext}} + \boldsymbol{B}_e|^2 \gg \xi B_L^2$ to obtain an appreciable nuclear field. In bulk materials, the Knight field $|\boldsymbol{B}_e|^2$ is typically smaller than the field ξB_L^2, an external field on the order of 1 mT is required to suppress the nuclear spin-spin fluctuations. In some quantum structures with high values of ξ, stronger external fields up to a few 100 mT are needed to generate observable DNP [79, 234]. Recently, it is demonstrated that the Knight field is strong enough to get an observable DNP process in single-electron charged quantum dots in the absence of an external field [80-82], which is due to the strong spatial confinement and relatively the weak nuclear depolarization.

According to Ref. [66], one can define a nuclear spin temperature from Equation (6.24) [21, 77, 218]

$$T_{\mathrm{NS}} = \frac{g_n \mu_N}{4k_{\mathrm{B}}}\frac{|\boldsymbol{B}_{\mathrm{ext}}+\boldsymbol{B}_e|^2 + \xi B_L^2}{(\boldsymbol{B}_{\mathrm{ext}}+\boldsymbol{B}_e)\cdot(\langle \boldsymbol{S}\rangle - \boldsymbol{S}_0)} \tag{6-27}$$

This spin temperature can be positive or negative depending on the electron spin. As a typical estimation, for $|\boldsymbol{B}_{\mathrm{ext}} + \boldsymbol{B}_e| \sim 0.1$ T and neglecting ξB_L^2, ($\langle S\rangle - S_0$) $\sim$ ($\langle S_z\rangle - S_{z0}$) ~ 0.1 and $g_n \sim 1$ [77], $T_{\mathrm{NS}} \sim 10^{-4}$ K is obtained. This is far below the sample temperature ($T = 5$ K for most experiments). This is the reason why "nuclear spin cooling" is often used for the nuclear spin polarization by Overhauser effect.

In bulk GaAs I_α is equal to 3/2 for each isotope, and for experiments presented in this work it is generally satisfied $|\boldsymbol{B}_e| \ll |\boldsymbol{B}_{\mathrm{ext}}|$ as well $|\xi B_L^2| \ll |\boldsymbol{B}_{\mathrm{ext}}|^2$. This means the nuclear field is along the external field (z-axis direction) $|\langle I_s(\alpha)\rangle| \approx \langle I_z(\alpha)\rangle$, and so is the electron spin as $|\langle S\rangle - S_0\rangle \approx (\langle S_z\rangle - S_{z0})$. Thus only the z-component spin is considered. Equations (6.25) ~ (6.27) become

$$B_N \approx \frac{10}{3} \sum_{\alpha} b_N(\alpha) f_{1\alpha} (\langle S_z \rangle - S_{z0})$$

$$T_{\mathrm{DNP}}^{-1}(B_{\mathrm{ext}}, \alpha) \approx T_{\mathrm{hf\text{-}pol}}'^{-1}(B_{\mathrm{ext}}, \alpha) \approx \frac{f_{1\alpha}^{-1} T_{\mathrm{hf\text{-}pol}}^{-1}(0, \alpha)}{1 + \tau_e^2 (g_e \mu_B \,|\, \boldsymbol{B}_{\mathrm{ext}} + \boldsymbol{B}_N \,|\, / \hbar)^2} \qquad (6\text{-}28)$$

$$T_{\mathrm{NS}} = \frac{g_n \mu_N}{4 k_B} \frac{|B_{ext}|^2 + \xi B_L^2}{(B_{ext}) \cdot (\langle S_z \rangle - S_{z0})}$$

For localized electronic states, either donor-bound or confined in a quantum dot, the nuclear field from DNP process is spatially inhomogeneous. The nuclear spin diffusion discussed above should be considered for the dynamic equilibrium process, which is governed by

$$\frac{d \langle I_z(\alpha) \rangle}{dt} = -\frac{\langle I_z(\alpha) \rangle - \langle I_{z,s}(\alpha) \rangle}{T_{DNP}(B_{\mathrm{ext}}, \alpha)} - \frac{\langle I_z(\alpha) \rangle}{\tau_{\mathrm{diff}}(\alpha)} \qquad (6\text{-}29)$$

To note, the DNP rate is a variable value during the nuclear spin dynamics, as it is controlled by the dynamic total field of $\boldsymbol{B}_{\mathrm{tot}} = (\boldsymbol{B}_{\mathrm{ext}} + \boldsymbol{B}_N)$. For instance, in case of $\boldsymbol{B}_N$ parallel to $\boldsymbol{B}_{\mathrm{ext}}$, the DNP process is slowed down, while in case of $\boldsymbol{B}_N$ anti-parallel to $\boldsymbol{B}_{\mathrm{ext}}$, the nuclear polarization is faster. Especially once the Overhauser field compensates the external field, the total field is zero and the DNP formation process is highly accelerated, i.e. see Equation (6-17). The nuclear spin diffusion with a fixed rate works as a depolarization source here. The dynamic relationship between $T_{\mathrm{DNP}}^{-1}(\boldsymbol{B}_{\mathrm{ext}}, \alpha)$ and $\tau_{\mathrm{diff}}^{-1}(\alpha)$ limits the nuclear field amplitude in the steady state. This means the dynamic nuclear spin polarization depends on the nuclear spin history as a non-Markovian process. In recent studies performed in quantum dots, this property is observed as a bistability phenomenon of the nuclear spin polarization. The steady Overhauser field has a hysteretic character if one controls the nuclear field, via scanning the external field [76], the optical excitation power [236] or the injected electron spin polarization [75].

6.3 Optically pumping dynamic nuclear polarization in n-GaAs

To control the nuclear field, it is critical to control the deviation of the electron spin from the equilibrium state, i.e. the quantity ($\langle S_z \rangle$ - S_{z0}) in Equation (6-28). It can be varied by changing the injected electron spin, the temperature, optical excitation power and so on. The electron spin after optical pumping is [72, 219]

$$\langle S_z \rangle = \frac{S_{z\text{-inj}}}{1 + \tau_e / \tau_s} + \frac{S_{z0}}{1 + \tau_s / \tau_e}, \text{ with } S_{z0} = \frac{1}{2} \tanh(\frac{g_e \mu_B B_{\mathrm{ext}}}{2 k_B T}), \qquad (6\text{-}30)$$

where $S_{z\text{-inj}}$ is the injected electron spin according to the optical selection rules, τ_e is the electron lifetime, τ_s is the electron spin lifetime, and S_{z0} is the electron spin in the thermal equilibrium by taking Boltzmann distribution. The critical factor which determines the Overhauser field is

$$\left\langle S_{\text{z}} \right\rangle - S_{\text{z0}} = \frac{S_{\text{z-inj}} - S_{\text{z0}}}{1 + \tau_{\text{e}} / \tau_{\text{s}}} \qquad (6\text{-}31)$$

It can be seen that, the nuclear field is proportional to the factor ($S_{\text{z-inj}}$ - S_{z0}), where $S_{\text{z-inj}}$ is directly determined by the polarization of the optical pumping. Based on the optical selection rules in bulk GaAs [21], the right-circularly polarized (σ^+, with helicity "+1") excitation gives $S_{\text{z-inj}}$ up to -0.25; the left-circularly polarized (σ^-, with helicity "-1") excitation gives $S_{\text{z-inj}}$ up to +0.25; and linearly polarized excitation makes $S_{\text{z-inj}}$ equal to zero. As demonstrated in earlier time, either circularly or linearly polarized pumping can generate the Overhauser effect in the presence of an external magnetic field [70]. Also as a consequence of a finite S_{z0}, the nuclear field has been observed with different magnitudes between σ^+- and σ^-- polarized excitation in a large external field [260].

The measurements were performed on a Si-doped GaAs sample, grown with molecular beam epitaxy on a GaAs (100) substrate. The active layer has a thickness of 2 µm, an electron density of 5×10^{16} cm^{-3}, and a mobility of $\mu = 4115$ cm^2/Vs at room temperature. The active region is sandwiched by an undoped GaAs layer of 50 nm below and a Si-doped GaAs layer above. The latter one is gradually doped up to an electron density of 5×10^{18} cm^{-3} within 15 nm and followed by another 15 nm thick GaAs layer with a constant doping level of 5×10^{18} cm^{-3}. This avoids band bending effects within the active layer due to surface depletion and ensures that the nuclear spins probed experience a macroscopic homogeneous electrical environment.

The dynamic nuclear field is investigated by the time-resolved Kerr rotation (TRKR) technique. The electron spin polarization is generated from optical pumping, and it is transferred to the doping electrons via fast exchange interaction [168]. The doping electrons are here regarded dominant for the DNP formation. The experiment geometry is described in Section 3.4.2.

FIG 6.3-1 presents the continuous TRKR scanning under linearly polarized optical excitation. To note, experimentally the polarization of the pump beam is achieved by the light polarization *on average*, e.g. see Section 3.4.2 .The monitored electron precession is not remarkably dependent on the lab time, as there is no indication of clear phase shift of the TRKR data.

In the case of circularly poalrized excitation, for σ^+- polarized excitation as presented in FIG 6.3-2 and for σ^-- polarized excitation as presented in FIG 6.3-3, there is a clear dynamic phase shift on the time scale of minutes (indicated by dashed lines). For σ^+- (σ^--) polarized excitation, the phase shift is clearly observed, which is a result of an increment (decrement) of the electron Larmor precession frequency. This indicates an increment (decrement) of the total field seen by the electrons and thus makes a faster (slower) electron spin precession. The total field $\boldsymbol{B}_{\text{tot}}$ is a sum of the applied external field $\boldsymbol{B}_{\text{ext}}$ and the dynamic nuclear field $\boldsymbol{B}_{\text{N}}$ as a result of the Overhauser effect, i.e. $\boldsymbol{B}_{\text{tot}} = \boldsymbol{B}_{\text{ext}} + \boldsymbol{B}_{\text{N}}$. Therefore for the current experiment conditions of $|\boldsymbol{B}_{\text{ext}}| = 374$ mT and $T = 5$ K, (i) the nuclear field is negligible under linearly-polarized excitation; (ii) the nuclear field is parallel to the external field under σ^+-polarized excitation; (iii) the nuclear field is anti-parallel to the external field under

σ⁻-polarized excitation. This can be understood by considering the relation between the electron spin in equilibrium and the electron spin by circular-polarized optical injection.
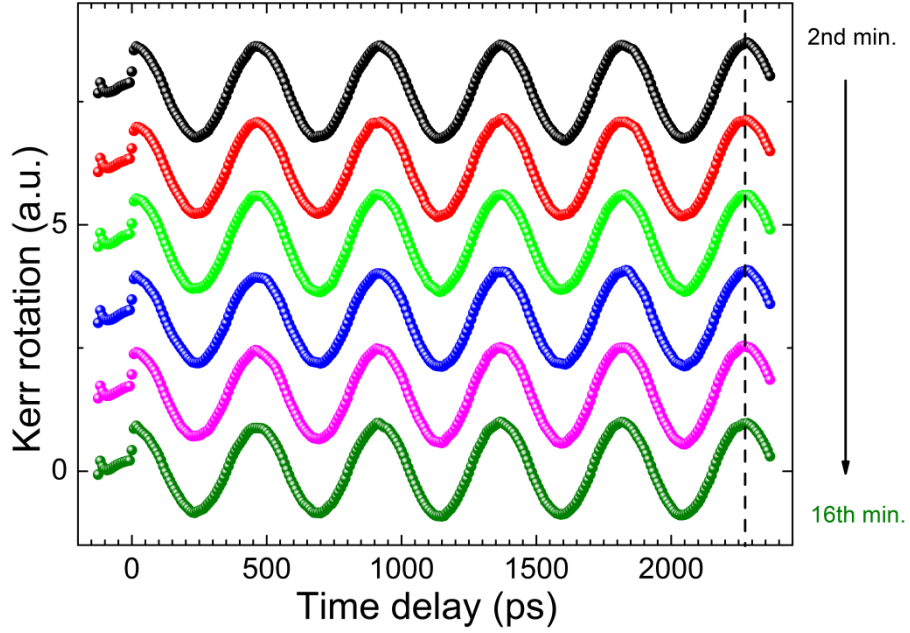

FIG 6.3-1: Continuous scanning of TRKR measurements under linearly polarized optical excitation. Each TRKR scan takes ~ 2 minutes. The lab time is indicated on the right side. The dashed line indicates negligible phase shift of the electron spin precession. The external magnetic field is 374 mT, and the cryostat temperature is 5 K.
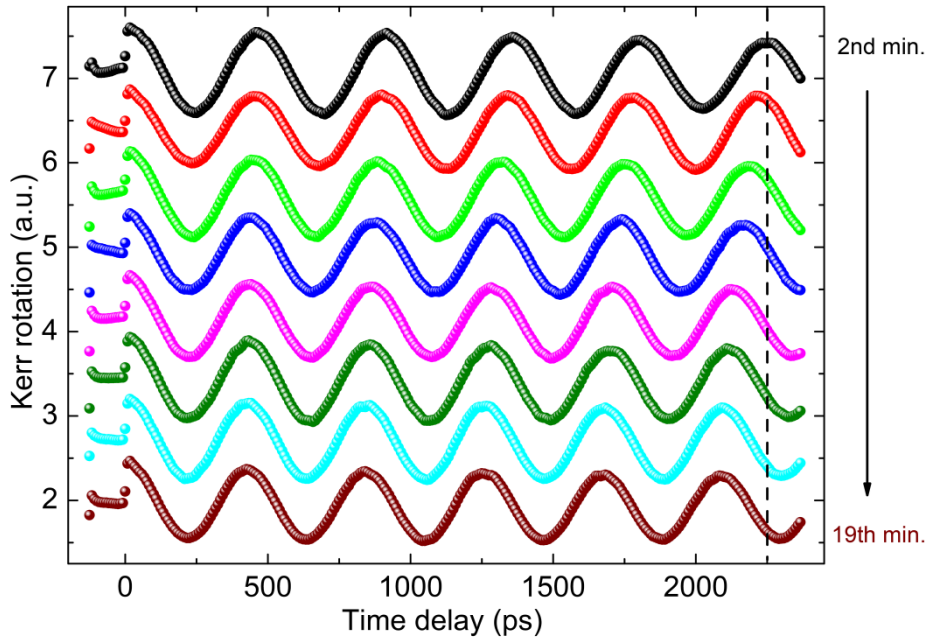

FIG 6.3-2: Continuous scanning of TRKR measurements under σ⁺-polarized optical excitation. The lab time is indicated on the right side. The dashed line indicates a phase shift of the electron spin precession resulting from the nuclear field parallel to the external field. The external magnetic field is 374 mT, and the cryostat temperature is 8 K.
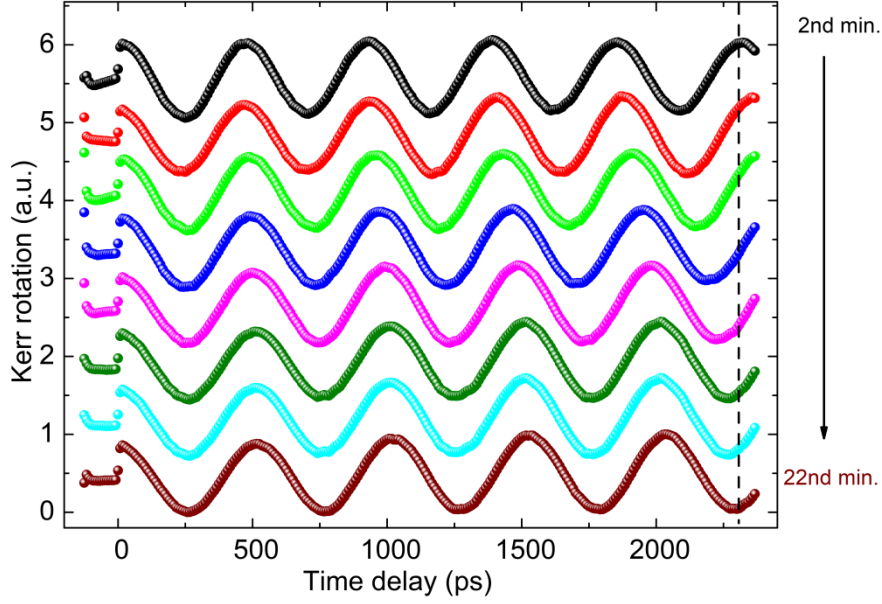
FIG 6.3-3: Continuous scanning of TRKR measurements under σ^--polarized optical excitation. The lab time is indicated on the right side. The dashed line indicates a phase shift of the electron spin precession resulting from the nuclear field anti-parallel to the external field. The external magnetic field is 374 mT, and the cryostat temperature is 10 K.

Since the n-GaAs sample is doped with a concentration of 5×10^{16} cm^{-3}, i.e. above the metal-insulator-transition level, the electrons are neither completely localized nor completely free as in metals. Here the electron spin polarization is estimated for the upper limit and the lower limit. The effective electron g factor $g_e \approx -0.42$ is used based on recent work [163, 255, 256]. In case of completely localized electronic states, the electron temperature equal to the cryostat temperature of ~4 K, the spin electron is obtained as $S_{z0} \sim -0.0065$ by using a Boltzmann statistics. In case of completely free electrons, the Fermi temperature is estimated around 85 K by using the free electron gas model [250], the electron spin is as low as ~ -0.0003. Thus for linearly polarized excitation, S_{z0} is expected to be between ~ -0.0003 and -0.0065 while $S_{inj} = 0$.

For circularly polarized excitation (σ^+ or σ^-), an electron spin of $|S_{inj}| = 0.25$ is expected by considering the optical selection rules in n-GaAs [21]. In addition, in our experiment the pump beam was modulated between linear polarization and σ^+ (or σ^-) - polarization with a duty cycle of 50 %. This results in a maximum circular-optically generated electron spin of $|S_{inj}(max)| = 0.125$. Only the z-component $S_{z\text{-}inj}$ is responsible for dynamical nuclear spin polarization. Considering the experimental geometry presented by FIG 3.4-4 (Section 3.4.2): the incident angle of the pump beam $\theta_1 \sim 18°$ (and thus the refractive $\theta_2 \sim 4.9°$ in the GaAs active layer using $n_{GaAs} \approx 3.7$ and following Snell's law), it is obtained $|S_{z\text{-}inj}(max)| \cdot \sin(\theta_2) \sim 0.01$, i.e. clearly larger than the expected spin in case of linear polarized excitation. So it is reasonable to observe a clear phase shift of electron spin precession for circular optical pumping, while it is negligible for linear excitation.

By neglecting the equilibrium S_{z0}, the nuclear field direction is only determined by the sign of $S_{z\text{-}inj}$ using Equation (6-28). The σ^+-polarized excitation generates a negative $S_{z\text{-}inj}$, aligning the nuclear spins anti-parallel to the external field, so that the electrons see an Overhauser field parallel to $\boldsymbol{B}_{ext}$

(note, b_N is negative). In contrast, the σ^--polarized excitation generates a positive $S_{\text{z-inj}}$, aligning the nuclear spins parallel to the external field, and thus the electrons see an Overhauser field anti-parallel to $\boldsymbol{B}_{\text{ext}}$. This gives a qualitative explanation of the dynamic phase shift presented in FIG 6.3-2 and FIG 6.3-3.

6.3.1 Dependence of DNP on optical helicity

The magnitude of the nuclear field is directly determined by the injected electron spin. The excitation optical helicity controls the injected electron spin. To more conveniently study the nuclear spin dynamics, the electron precession Larmor frequency ω_L is extracted from the TRKR measurements. It is defined as

$$\omega_L\left(t\right) = g_e\mu_B\boldsymbol{B}_{\text{tot}} / \hbar = g_e\mu_B\left(\boldsymbol{B}_{\text{ext}} + \boldsymbol{B}_N\left(t\right)\right)/\hbar , \qquad (6\text{-}32)$$

and thus $\omega_L(t)$ can directly represent the dynamic nuclear field $\boldsymbol{B}_N(t)$. The method to evaluate the Larmor frequency is given in Section 3.4.2.

As presented in FIG 6.3-4, the polarization of the optical pumping is systematically varied over time and the characteristic electron Larmor frequency ω_L (upper panel) is extracted from each TRKR scan. Under linearly polarized optical excitation, no observable change of $\omega_L = 13.9$ GHz is obtained indicating a negligible nuclear field. After switching to σ^+ - polarized excitation with a duty cycle of $D_\tau = 20\%$, an increase of ω_L up to ~14.5 GHz is found. This indicates an Overhauser field parallel to the external field with a magnitude of $B_N \sim +15$ mT (lower panel) by using Equation (6.32). After DNP saturation, the optical excitation is switched to σ^-- polarized with the same duty cycle. As expected, ω_L is reduced down to ~13.3 GHz, indicating that the nuclear filed now is anti-parallel to the external field resulting in $B_{\text{tot}} = B_{\text{ext}} - B_N$. Again, B_N is found to be ~ -15 mT. To further enhance the Overhauser field magnitude, we increased the duty cycle of the polarized optical pumping to 50%, which is expected to result in an increase of the average electron spin polarization and thus in an increase of the achieved Overhauser field. After switching to σ^+ excitation with $D_\tau = 50\%$, the nuclear field reverses its sign and increases up to about +35 mT, which results in $\omega_L \sim 15.2$ GHz. An anti-parallel B_N with similar amplitude is observed for σ^- excitation with $D_\tau = 50\%$. In case of $D_\tau = 80\%$, the amplitude of the Overhauser field is further enhanced to $B_N \sim 50$ mT. Finally, switching back to linear polarized excitation, the nuclear field vanishes to zero.

As discussed in Equation (6.28), B_{ext} is much larger than the Knight field and much larger than the nuclear depolarization field $(|\xi B_L^2|)^{1/2}$ under the experimental conditions. Thus for theoretically estimating the expected Overhauser field, a simplified form can be used by combining Equations (6-28) and (6-31)

$$\left|\boldsymbol{B}_N\right| = \frac{10}{3}\cdot\left|b_N\right|\cdot\frac{\left|S_{\text{inj}}\right|\cdot\sin(\theta_2)}{1+\tau_e / \tau_s}\cdot f_1\cdot\rho_e \qquad (6\text{-}33)$$

Here ρ_e is the polarization degree of the optical excitation, and the average leakage factor f_1 is used for three nuclear species. From the TRKR results from FIG 6.3-1 to FIG 6.3-3, the electron spin

dephasing time is approximated as $T_2^* \approx 10$ ns, which is used as the spin relaxation time $\tau_s = T_2^*$ in n-GaAs in the regime of low magnetic field and temperature [8]. Since there are existing electrons from doping, it is assumed the electron life time is just the laser excitation period $\tau_e \approx 13$ ns. By using $|S_{inj}| = 0.25$ for a complete σ^+ - or σ^- - excitation, $\theta_2 \approx 4.9°$, the expected Overhauser field is $\sim(160 \cdot f_l \cdot \rho_e)$ mT. Considering the duty cycle of polarized excitation, D_τ, and comparing the measured magnitude of the Overhauser field B_N with the calculated value, the leakage factor here is estimated ~ 0.5, which is a reasonable value at low temperature [79].
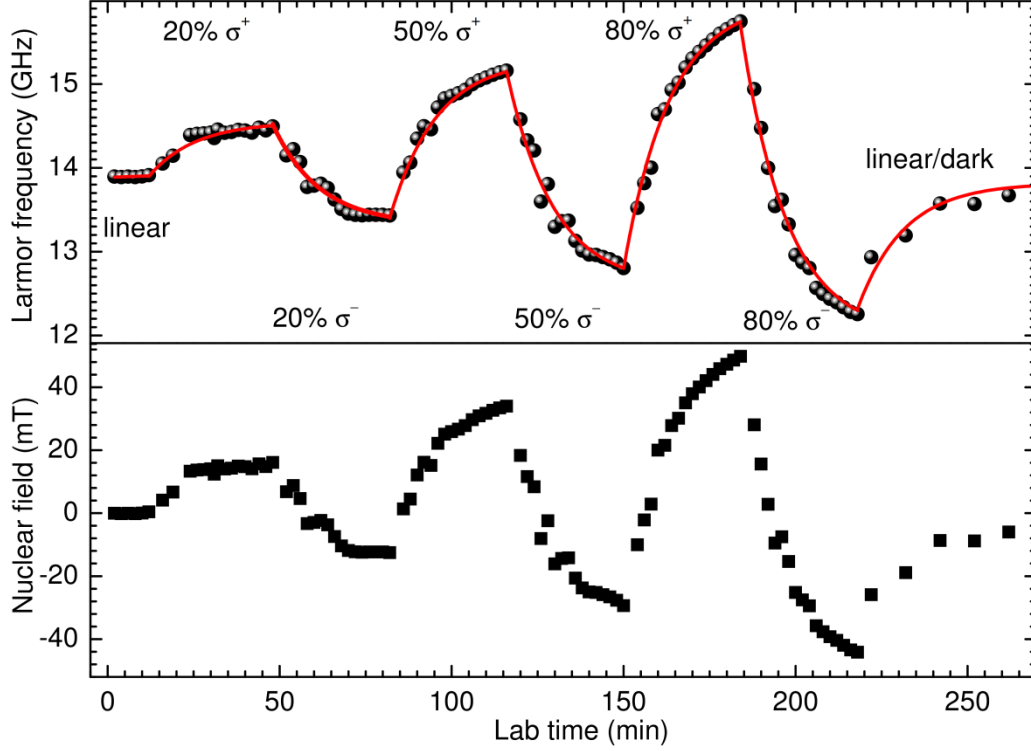
FIG 6.3-4: upper panel: Electron Larmor precession frequency versus laboratory time. Duty cycle and helicity of the pump beam, which were varied with time, are indicated. The transient change in the Larmor frequency due to DNP is mono-exponentially fitted with a time constant of 13.5 min (line). Lower panel: The corresponding dynamic nuclear field for the upper panel. The external magnetic field is 374 mT, and the cryostat temperature is 5 K.

Concerning to the nuclear spin dynamics, as indicated in FIG 6.3-4, the DNP process can be fitted quite well with a time constant of 13.5 min (red lines). Within the experimental error, this time constant is found to be hardly dependent on duty cycle and optical helicity. The observed DNP formation time is faster by one order of magnitude than the calculated value from Equation (6-11) assuming free electronic states, and is slower by orders of magnitude than the calculated value from Equation (6-13) assuming localized electronic states. Comparable values have been found in similar GaAs systems [94, 250], while the origin to explain the discrepancy from the theory is still under discussion [72].

6.3.2   Power dependence

In FIG 6.3-5, TRKR measurements are presented by varying the excitation power under linearly polarized optical pumping. The presented data are normalized by scaling the detected signals with multiplying the indicated coefficients. The amplitude of the Kerr rotation at zero time-delay, is enhanced with increasing the excitation power. This is due to more spin-polarized electrons from optical pumping, e.g. see Section 3.4.2. On the other hand the probe beam also takes higher optical intensity to generate larger photon-voltage for the diode-bridge detector.

As a more prominent dependence on the power, the electron dephasing time is clearly reduced for stronger optical excitation. The detected spin dynamics is a sum of the two electronic systems, delocalized and localized electrons [254]. The excitation level here is 1.5176 eV, and the energy of the donor-bounded electron is ~1.513 eV. See Ref. [103]. Since the excitation energy is above the energy level of the localized electron, higher excitation density can generate more delocalized electrons coexisting with the localized electrons. The delocalized electrons typically carry excess energy, which makes relatively faster spin dephasing compared with the localized electrons. As a result, the spin dephasing is manifested by a shorter time due to the increasing population of delocalized electrons over localized from higher optical excitation. The delocalized electrons take an effective g factor with a smaller absolute value (to note $g_e < 0$) as compared for localized ones [163], and thus there is clear phase shift by changing the excitation density. The relative phase shift is indicated by the dashed line, and the corresponding Larmor frequency is given in FIG 6.3-6 (red).
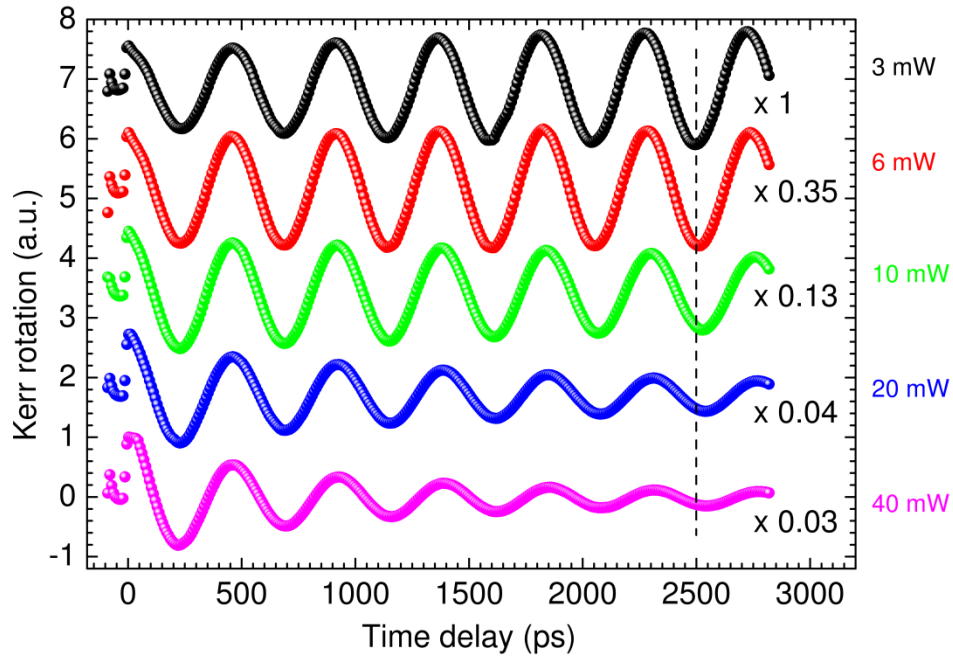
FIG 6.3-5: Power dependence of TRKR measurements under linearly polarized optical excitation. The power of the pump beam is given on the right side. The power ratio of the pump beam to the probe beam is always kept as 5:1, and only the pump power value is indicated. The presented data are scaled from the detected signals by the indicated coefficients. The dashed line indicates a phase shift of the electron spin precession resulting from the change of the electron g factor. The external magnetic field is 374 mT, and the cryostat temperature is 5 K.

The power dependence of the Larmor frequency ω_L is also given in FIG 6.3-6 for σ^+-polarized (black) and σ^--polarized (blue) optical excitation. Clearly the Larmor frequency is decreased (increased) for σ^+- polarized (σ^-- polarized) excitation, which means a reduction of the nuclear field with increasing excitation power. Based on the three groups of ω_L determined in FIG 6.3-6 and Equation (6-32), the power dependence of nuclear field is extracted and presented in FIG 6.3-7 (left axis).
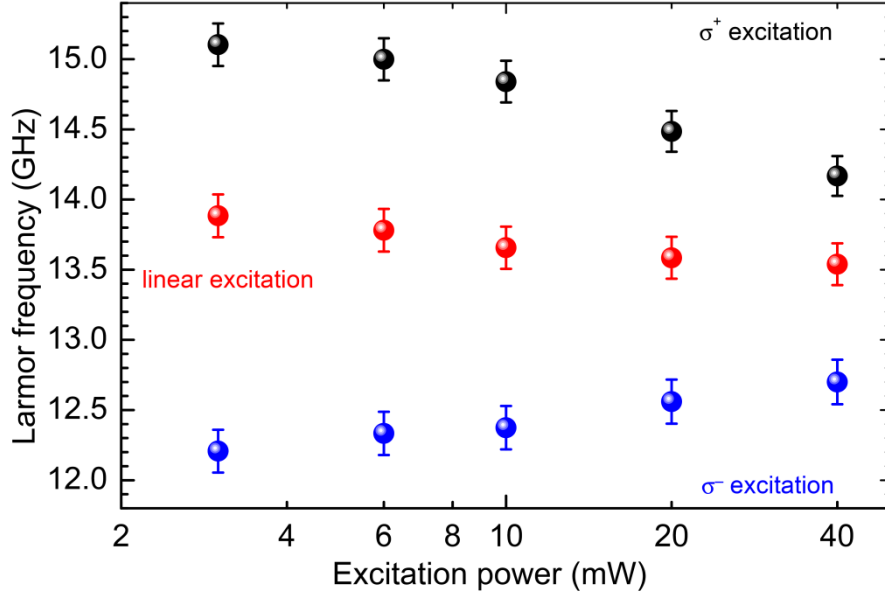
FIG 6.3-6: Power dependence of the Larmor frequency under linearly polarized (red), σ^+-polarized (black) and σ^--polarized (blue) optical excitation. The external magnetic field is 374 mT, and the cryostat temperature is 5 K.
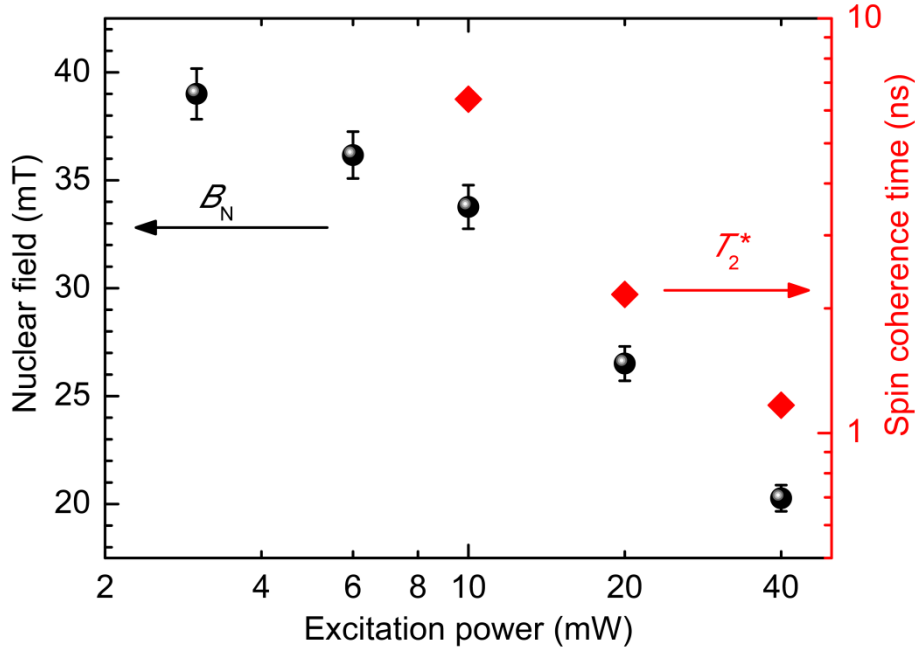
FIG 6.3-7: Power dependence of the nuclear field (left axis) and the electron dephasing time (right axis). The external magnetic field is 374 mT, and the cryostat temperature is 5 K. The nuclear field is averaged for σ^+-polarized and σ^--polarized cases.

The nuclear field magnitude is decreasing by increasing the excitation power. The nuclear field is reduced from ~40 mT to ~20 mT by increasing the power from 3 mW to 40 mW. This is in contrary with reported dependence of the nuclear field on excitation power [90, 154]. This might be due to much weaker excitation there, e.g. the optical power density is ~ 40 W/cm^2 as an upper excitation in Ref. [90] while the value is ~3000 W/cm^2 as a lower excitation within the current work. For a large density of optically generated carriers, the electron spin-spin interaction, e.g. via electron-electron scattering and exchange coupling, becomes stronger, which can accelerate the electron spin dephasing progress and thus shortens the spin relaxation time [93]. The spin lifetime is assumed equal to the dephasing time as mentioned above, and the power dependence is given in the right axis of FIG 6.3-7. Generally the spin lifetime is decreased from ~ 10 ns down to ~1 ns while the power is increased. By considering Equation (6-31), the shorter spin lifetime gives smaller average electron spin, which indicates weaker hyperfine interaction between the electrons and nuclei. In addition, the anti-ferromagnetic electron spin-spin interaction can depolarize the nuclear spins, and this mechanism is enhanced by increasing the electron population. Then it is expected the generated nuclear field is getting smaller.

6.3.3 Temperature dependence

In FIG 6.3-8, TRKR measurements are presented for varying the cryostat temperature under linearly polarized optical pumping. The Kerr rotation is significantly smaller for higher temperature, which causes the energy bandgap narrowing [103]. Since the excitation energy is kept constant (as 1.5176 eV) which gives more excess kinetics for optically generated carries for smaller energy bandgap, the spin injection becomes less efficient at a higher temperature. In addition, since the detected Kerr rotation signal is from electrons above the Fermi level, then the electron population is much less as compared with the electron population in case of resonant excitation, which happens at a temperature of ~5 K in current studies.

The temperature dependence of the injected electron spin is extracted in FIG 6.3-8 (right axis). According to $g_e \approx g_0 + 6.3 \cdot E_k \text{(eV)}$ [163, 261], where g_0 is the g factor at resonant excitation and E_k is the energy above the conduction band, the electron g factor changes to a smaller absolute value. This is due to the fact that g_0 becomes absolutely smaller and E_k becomes relatively larger as a result of the bandgap shrinkage when the temperature is increased. This is reflected by the clear phase shift of the electron spin precession, and it is indicated by the dashed line in FIG. 6.3-8. Nevertheless, the spin dephasing time is of little dependence on the temperature, in good agreement with previous studies [163].

The Larmor frequency sequence for different temperatures is presented in FIG 6.3-9. For a cryostat temperature, the Larmor frequency is determined for both σ$^+$- (for each dynamical rising process) and σ$^-$- (for each dynamical lowering process) polarized excitation and the DNP process is also

monitored. Based on these systematic data, the temperature dependence of the nuclear field and the DNP formation rate are extracted.

The steady nuclear field is estimated by using the electron g factor determined from FIG 6.3-8 and the Larmor frequency values under σ^+- and σ^--polarized excitation from FIG 6.3-9. The temperature dependence is presented in FIG 6.3-10 (left axis). A nuclear field of ~ 40 mT is obtained in the temperature regime below 10 K. For the higher temperature range, the nuclear field is strongly suppressed and almost vanishes at 50 K. This can be ascribed to two origins: (i) More delocalized electrons are generated at higher temperature. The delocalized electron has a longer DNP time compared with the localized electrons, so the nuclear spin polarization rate is reduced. In addition, the nuclear spin depolarization rate is enhanced due to the more prominent role by the thermal relaxation at higher temperatures. Therefore the nuclear field after DNP saturation is reduced by considering a smaller leakage factor from Equation (6-19). (ii) The spin injection efficiency is greatly diminished in case of excitation highly above the bandgap energy. The temperature dependence of injected electron spin is presented in the right axis of FIG 6.3-10. The extracted spin value is estimated from the peak-peak amplitude value at zero time delay for each TRKR measurement, and normalized by the maximum. The injected electron spin is clearly reduced by increasing the temperature, and thus the hyperfine coupling strength becomes less. To note, the trend is quite close to the nuclear field dependence on the temperature.
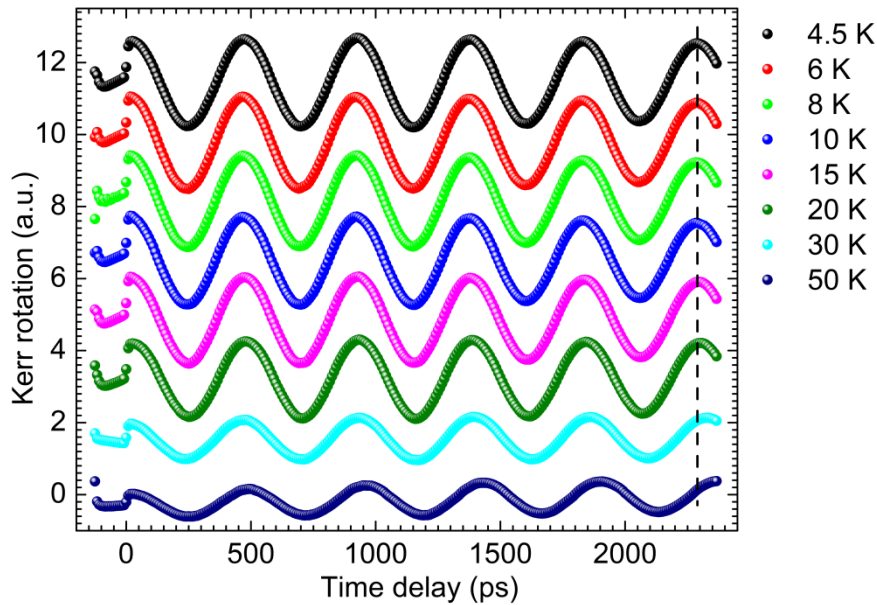
FIG 6.3-8: Temperature dependence of TRKR measurements under linearly polarized optical excitation. The temperature is given on the right side. The dashed line indicates a phase shift of the electron spin precession. The external magnetic field is 374 mT.

The temperature dependence of the DNP formation rate is presented in FIG 6.3-11. In the low temperature regime less than 10 K, the DNP formation time is independent on the temperature change and is kept constantly ~ 10 minutes, while the rate increases almost linearly with the

temperature (indicated by the dashed line) beyond 10 K. For the free electrons considered in Equation (6-11), the hyperfine interaction rate has a linear relation with the temperature. Other relaxation channels depolarizing nuclear spins, such as thermal relaxation including nuclear spin-lattice relaxation and quadrupolar relaxation, come into consideration at higher temperature. The thermal relaxation rate is expected to have a linear relation with the lattice temperature below the Debye temperature [66] which is ~344 K in GaAs [103]. Thus it is expected the total DNP rate is proportional to the temperature in case of free electrons. This is in a qualitative agreement with the presented data
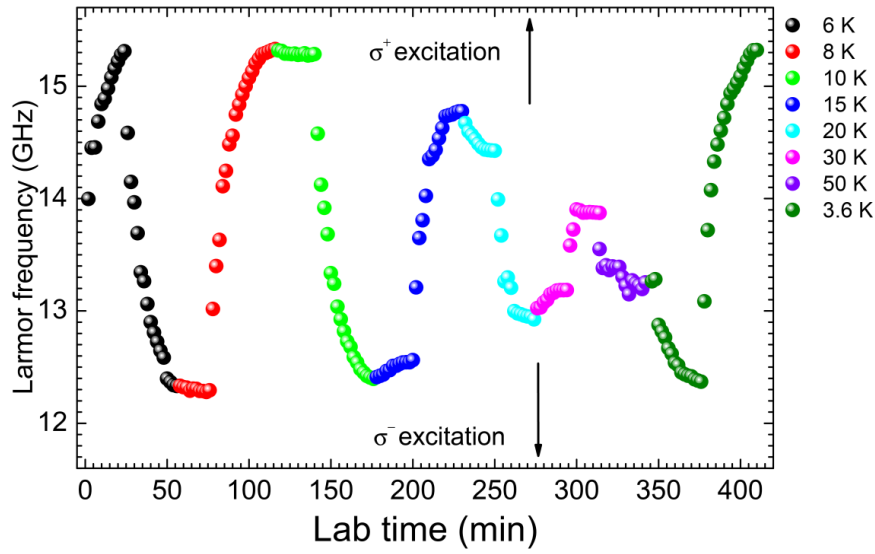
FIG 6.3-9: Electron Larmor precession frequency versus laboratory time. The optical polarization is indicated by arrows. The cryostat temperature, which was varied with time, is indicated by a specific color. The external magnetic field is 374 mT.
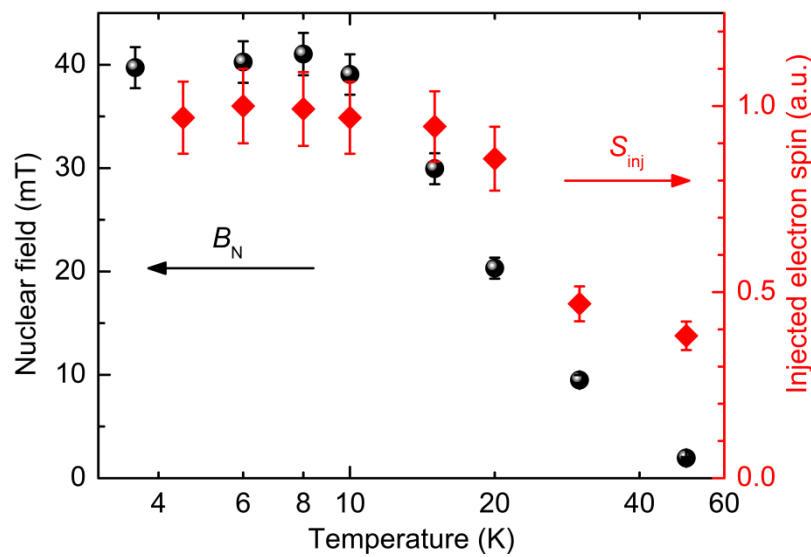
FIG 6.3-10: Temperature dependence of the nuclear field (left axis) and the injected electron spin (right axis). The latter is extracted by the peak-peak amplitude value at zero time delay for each TRKR measurement, and normalized by the maximum. The external magnetic field is 374 mT.
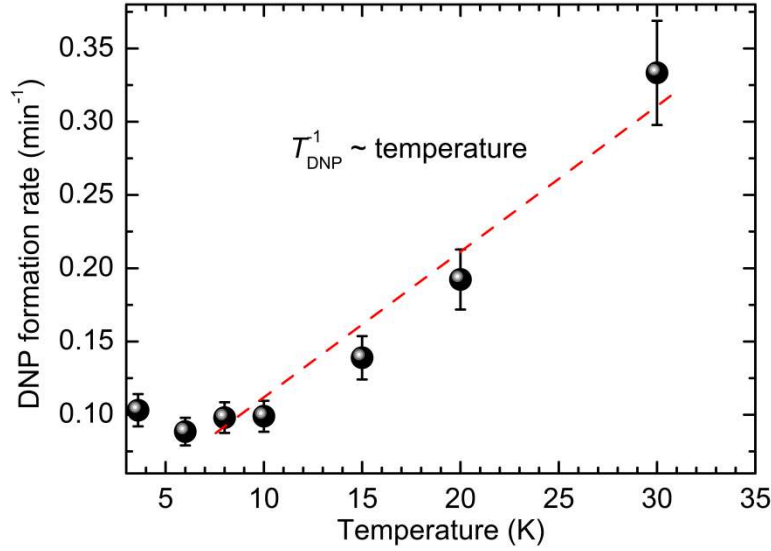
FIG 6.3-11: Temperature dependence of the DNP rate. The dashed line is a guide for eyes. The external magnetic field is 374 mT.

6.4 Optically detected nuclear magnetic resonance using an on-chip microcoil

To obtain manipulation of nuclear spins in semiconductors is of fundamental interest for the emerging field of quantum information processing. On one side, nuclear spin states can represent quantum bits [67, 262]; on the other side, the electron-nucleus coupling is an ultimate factor limiting electron spin lifetime in quantum structures [80, 237, 238]. In addition, nuclear spins can affect the electron spin transport [213-215], and further nuclear spins can lock the electron spin states under resonant electrical or optical excitations [263-265]. It is thus required to attain a powerful and spatially selective approach for nuclear spin manipulation, *e.g.* based on nuclear magnetic resonance (NMR). It has been shown for different III-V semiconductors that optically [21, 77, 84, 85, 88-92, 94, 266] or electrically injected spin-polarized electrons [79, 86, 87] strongly enhance nuclear spin polarization via hyperfine interaction in comparison with conventional NMR. Different experimental methods have been developed to optically or electrically detect the NMR, *e.g.* highly sensitive detection of nuclear spin polarization from free induction decay signals [72], luminescence depolarization due to the Hanle effect [21, 77, 79, 84, 85], electrical resistance variance in the quantum Hall effect regime [86, 87], the effective nuclear field B_N (namely the Overhauser field) induced PL spectrum shift [88] or the electron spin precession dynamics, the latter probed by time-resolved magneto-optical Faraday/Kerr rotation [89-93].

Quite often, the RF field needed for NMR is produced from a Helmholtz coil with a typical power consumption of ~ 100 W or so [89]. Other approaches include all-optical NMR making use of the Knight field from optically generated spin-polarized electrons [90, 94], or an in-built micro-stripe which has been hitherto used in the ultralow temperature regime of ~50 mK [86]. In contrast, an on-chip micro-coil can generate pulsed magnetic fields up to several 10 mT in the GHz regime with power consumption down to several 10 mW [193, 267].

6.4.1 Magnetic resonance in two passages

For considerations of the nuclear magnetization under resonance conditions, the analysis is typically performed in a rotating frame [66, 168, 268]. In the following only the nuclear species α_1 is considered close to magnetic resonance while the others α_i ($i \neq 1$) are far from resonance and thus not affected by the RF field.

In FIG 6.4-1 (a), the rotating frame is chosen to have an angular velocity $\boldsymbol{\omega}_r$ parallel to $\boldsymbol{B}_{\text{ext}}$. The RF magnetic field $\boldsymbol{B}_{\text{RF}}$ is assumed to oscillate perpendicular to the external field B_{ext}. In the lab frame,

the RF field is $\boldsymbol{B}_{\text{RF}} = \boldsymbol{x}B_{\text{RF}}\cos(\omega_{\text{RF}}t) = B_1\left(\left[\boldsymbol{x}\cos(\omega_{\text{RF}}t)+\boldsymbol{y}\sin(\omega_{\text{RF}}t)\right]+\left[\boldsymbol{x}\cos(\omega_{\text{RF}}t)-\boldsymbol{y}\sin(\omega_{\text{RF}}t)\right]\right)$

with $B_1 = B_{\text{RF}}/2$. Here $\boldsymbol{x}$ and $\boldsymbol{y}$ are the unit vectors for each direction axis. It is set $|\boldsymbol{\omega}_r| = |\omega_{\text{RF}}|$. Then the RF field can be treated as a sum of two rotating magnetic fields with the opposite angular velocity directions, i.e. $\boldsymbol{\omega}_r$ and $-\boldsymbol{\omega}_r$. Generally the latter component is ignored for analysis since it is away from the resonance condition and $B_{\text{ext}} \gg B_1$ [66, 268]. Therefore the RF field is simply $\boldsymbol{x}B_1$ in the rotating frame. The longitudinal field seen by the nuclear spins is $\Delta\boldsymbol{B} = \boldsymbol{B}_{\text{ext}} - \boldsymbol{\omega}_r / 2\pi\gamma_{\alpha 1}$, where $\gamma_{\alpha 1}$ is the gyromagnetic ratio for the isotope species α_1. In the rotating frame, the effective field seen by the nuclear spins is

$$B_{\text{eff}} = \left(|B_1|^2 + |\Delta B|^2\right)^{1/2}, \quad \text{with } \Phi = \arctan\left(\frac{B_1}{\Delta B}\right) \tag{6-34}$$
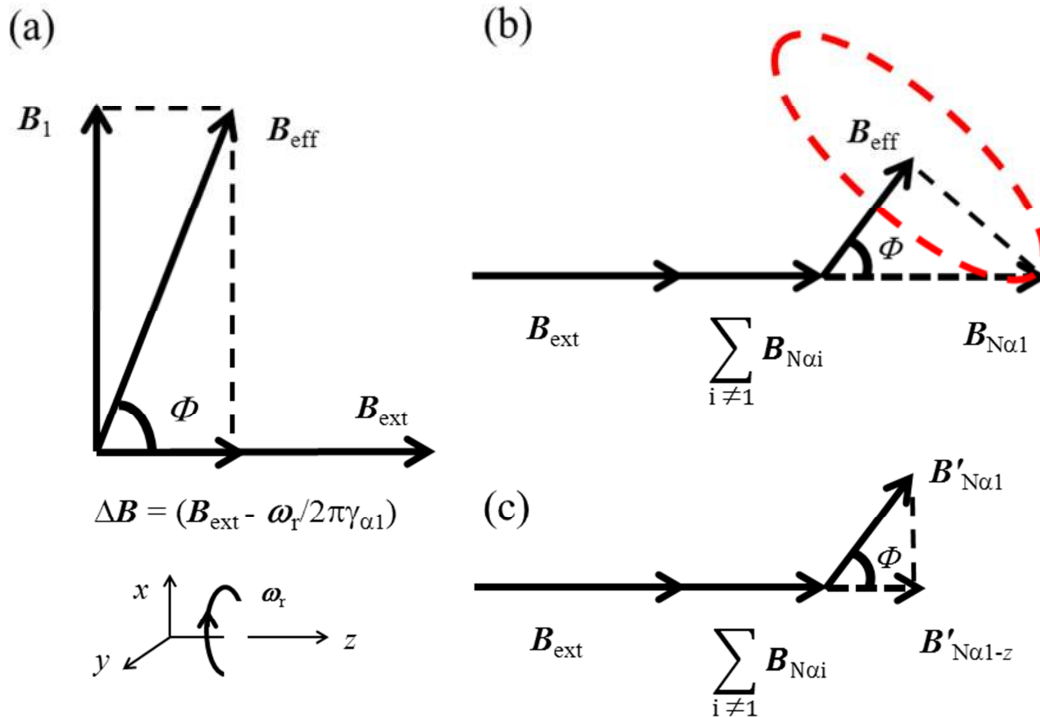

FIG 6.4-1: Nuclear field affected by a RF magnetic field. (a) The effective field seen by the nuclear species α_1 in the rotating frame. (b) Nuclear field evolution the short time regime. The dashed red line indicates the precession vector of the nuclear field $\boldsymbol{B}_{\text{N}\alpha 1}$ in the rotating frame. (c) Steady nuclear filed in the long time regime. The z-component $\boldsymbol{B}'_{\text{N}\alpha 1\text{-}z}$ is the stationary Overhauser field in the lab frame.

In the short time regime, on the time scale shorter than the nuclear spin-spin interaction which is on the order of 100 µs in GaAs [168], the nuclear magnetization precesses around the effective field once the RF field is applied. The dynamic nuclear field $B_{N\alpha1}$ is indicated by the dashed line in FIG 6.4-1 (b). The NMR spectral width measured in this regime is a reflection of the local nuclear spin interaction, such as nuclear spin exchange interaction, dipole-dipole interaction, quadrupolar interaction etc. [66, 72, 268]. In the resonance case of $\Delta B = 0$ or $\omega_{RF} = 2\pi\gamma_{\alpha1}B_{ext}$, the nuclear spins precess around the RF field B_1 in the rotating frame, and manifest as nutation in the lab frame. The phenomenon is known as Rabi oscillations, with the Rabi frequency of $f^{Rabi}_{\alpha1} = \gamma_{\alpha1}B_1 = 1/2\gamma_{\alpha1}\cdot B_{RF}$ and an effective nuclear spin dephasing time T_2^{Rabi}.

In FIG 6.4-1(c), the long time regime is presented. The nuclear filed approaches equilibrium at a new stationary level under RF excitation. This happens on a longer time scale, and it is approximated as the DNP formation time. The nuclear spins experience hyperfine relaxation process in the presence of the RF field. In the rotating frame, the new nuclear field $B_{N\alpha1}{}'$ is collinear with the effective field $\boldsymbol{B}_{eff}$, and it is still along the external field $\boldsymbol{B}_{ext}$ by considering the transverse average component in the lab frame. The magnitude could be written as

$$B'_{N\alpha1\text{-}z} = B_{N\alpha1}\cos^2(\Phi) \tag{6-35}$$

It can be seen, the measured NMR spectrum in this regime is related to the magnitude of the RF field. The NMR spectral width is a convolution of half of the RF field and the local nuclear spin interaction determined by NMR in the fast passage.

The total magnetic field seen by the electron is the sum of the external field, the nuclear field not affected by the RF excitation, and the dynamic field of the isotope changed by the RF field, i.e. $\boldsymbol{B}_{tot}(t) = \boldsymbol{B}_{ext} + \sum_{i\neq1}\boldsymbol{B}_{N\alpha i} + \boldsymbol{B}_{N\alpha1}(t)$ as described in FIG 6.4-1(b) and (c). By monitoring the dynamic electron Larmor frequency, the nuclear spin dynamics can be extracted under NMR conditions.

6.4.2 Optically detected NMR in n-GaAs

The studied sample is the same as described in Section 6.3, and the cryostat temperature is set as 5 K in this section. The NMR experiment geometry is schematically given in FIG 6.4-2(a). The nuclear field is generated collinear with the external field by using the optical oblique geometry described in Section 3.4.2. To induce magnetic resonance, an on-chip microcoil is patterned on the semiconductor. The microcoil used in the experiments has an inner diameter of 19 µm and a width of 6 µm as shown FIG 6.2-2(b). By introducing a RF current through the microcoil, an oscillating magnetic field is generated inside the coil with a component perpendicular to the external field, and thus NMR geometry is fulfilled as presented in FIG 6.4-1. The electrical resistance of the microcoil is negligible at low temperatures compared to the 50 ohm terminal resistor. As the microcoil is connected between ground and the 50 ohm resistor, the electric potential of the metal stripes is too low to produce a significant electric field in the studied GaAs active layer by the microcoil.
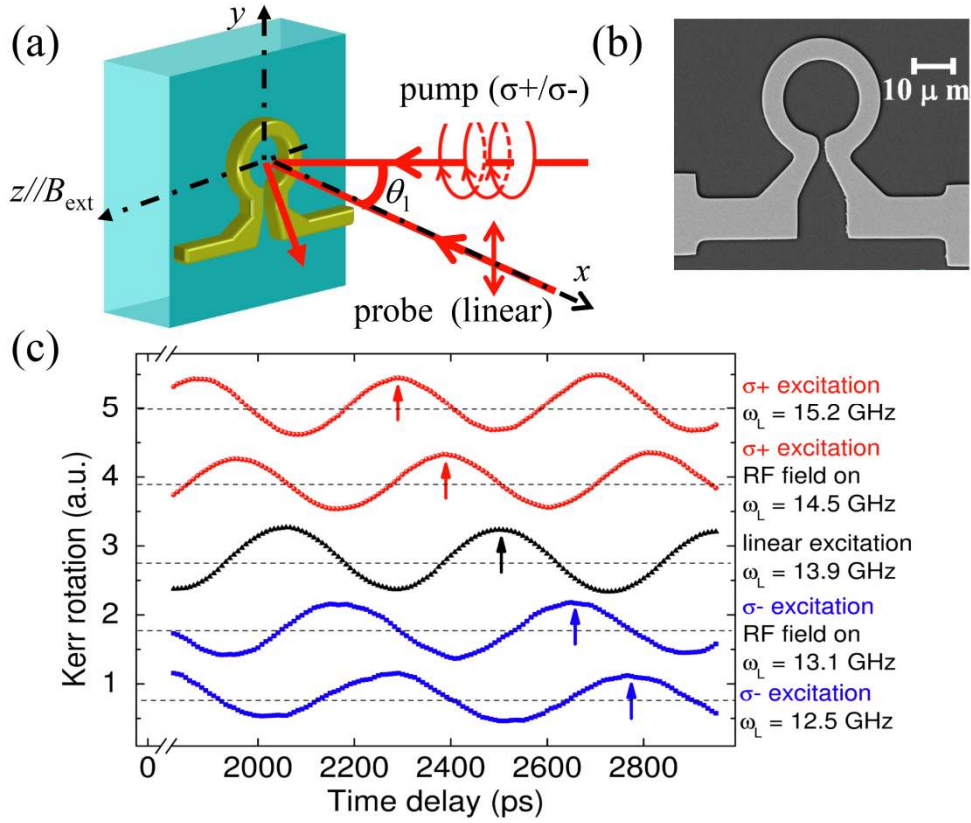
FIG 6.4-2: (a) Experimental geometry for the TRKR measurements and NMR conditions; (b) Scanning electron micrograph of the microcoil structure; (c) TRKR signal obtained for linear polarized optical excitation, σ^+-polarized excitation and σ^--polarized excitation. For the two latter cases, data obtained with and without RF excitation at resonance conditions for the ^{75}As isotope are compared. The arrows indicate the phase shift with respect to zero time delay, which is the consequence of the different Larmor frequency in each case.

In FIG 6.4-2(c), it can be seen that for σ^+-polarized pumping, the Larmor frequency ω_L increases from 13.9 GHz to 15.2 GHz, which indicates the nuclear field $\boldsymbol{B}_N$ is parallel to $\boldsymbol{B}_{ext}$. The situation is just opposite σ^--polarized excitation is used for the pump beam: The Overhauser field $\boldsymbol{B}_N$ should now be anti-parallel to $\boldsymbol{B}_{ext}$, and the Larmor frequency is reduced to 12.5 GHz. These results are similar to what is discussed in Section 6.3.

By introducing a RF current through the microcoil with frequency 2.72 MHz, which is expected to be the resonance frequency for ^{75}As at $B_{ext} = 374$ mT, a distinct change of the Larmor frequency can be seen in the TRKR data: In case of σ^+ (σ^-) – polarized pumping, the Larmor frequency drops (increases) to a value of $\omega_L = 14.5$ GHz (13.1 GHz), indicating a significant depolarization of the nuclear spins. The Larmor frequency does not reach the value measured for linearly polarized pumping as only the ^{75}As nuclear spins are depolarized by NMR, while the nuclei of the other isotopes (^{69}Ga, ^{71}Ga) are not noticeably affected. To note, the depolarization level is almost same for both polarizations, i.e. $|\Delta\omega_L| = 0.7$ GHz for σ^+-polarized excitation and $|\Delta\omega_L| = 0.6$ GHz for σ^--polarized excitation. This means the nuclear field amplitude is actually independent on the optical

excitation helicity. This gives further evidence that the equilibrium electron spin is negligible compared with the optically injected electron spin, and thus the nuclear field at linear excitation can be ignored (e.g. see discussions in the beginning part of Section 6.3.1).

To obtain the ^{75}As NMR spectrum, TRKR measurements are performed for different frequency values as presented in FIG 6.4-3. The DNP formation was ensured to be on the saturation level prior to switching on the RF field. For each RF frequency, the RF excitation is always on during the measurements and the TRKR scanning was performed for ten times, which totally take around 10 min. Since the DNP formation time has been found ~10 minutes for three isotope species in Section 6.3.1, it is expected the DNP formation of each isotope is shorter than the total TRKR scanning time. Therefore the NMR condition here is in the long time regime. For the measurements, the current amplitude through the microcoil was set to 30 mA. For the RF frequency of 2.72 MHz, there is a maximum phase shift indicating the strongest nuclear spin depolarization at (close to) the resonance center. The phase shift becomes smaller as the RF frequency is away the center frequency.
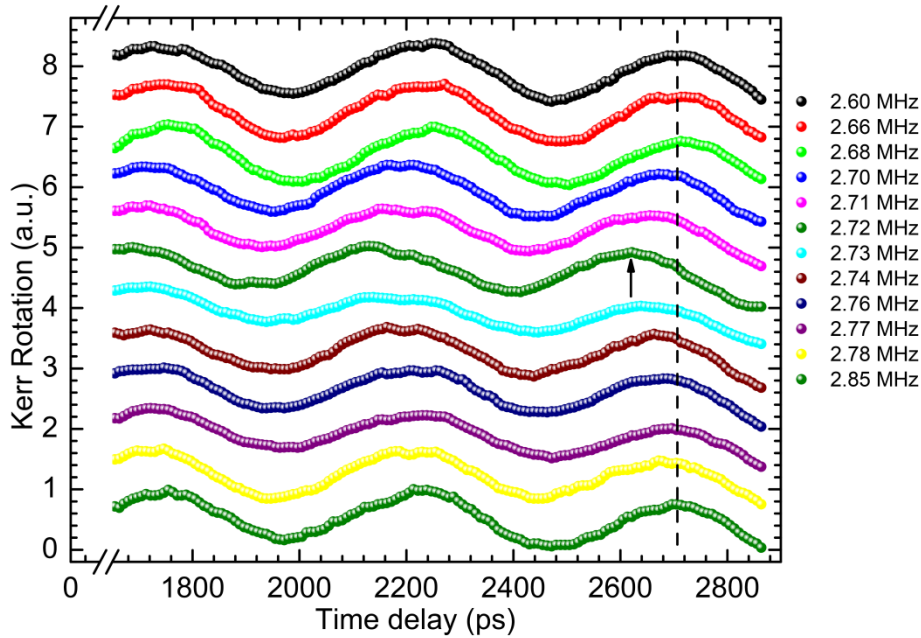
FIG 6.4-3: TRKR measurements under RF excitation for different frequency values. The frequency is given on the right side. The arrow indicates a maximum phase shift for the ^{75}As resonance at 2.72 MHz. The optical pumping is σ^--polarized and the external magnetic field is 374 mT.

The NMR spectra are given in terms of extracted Larmor frequency values, which are plotted in FIG 6.4-4(a) for both σ^+-polarized and σ^--polarized optical excitation. The NMR features of all three species of isotopes are observed by sweeping the RF frequency. The center frequency of each NMR peak follows well the relation of $f_\alpha = \gamma_\alpha B_{ext}$, where γ_α is the nuclear gyromagnetic ratio for the isotope α (α : ^{69}Ga, ^{71}Ga and ^{75}As). The NMR spectral linewidth is between 20 kHz and 40 kHz and thus much larger than expected due to the dipole-dipole broadening in bulk GaAs [269], which suggests resonance saturation conditions [66] as well as a contribution from the RF field in the long time regime.

At the center frequency of each NMR spectrum, the change of ω_L corresponds to a reduction of the total Overhauser field B_N by $B_{N\alpha}$ for each isotope species α. The sum of $B_{N\alpha}$ for all three isotope species is comparable to the total Overhauser field B_N. This indicates complete spin depolarization of the specific isotope for each NMR resonance. Interestingly, the measured ratio $B_{N\alpha}/B_N$ does not agree with the theoretically calculated value: $B_N{}^{71}{}_{Ga}$ is expected to be less than $B_N{}^{69}{}_{Ga}$ in pure GaAs crystals from Ref. [77], in obvious contradiction to the measured data. As $B_{N\alpha} \sim f_{l\alpha} \cdot b_{n\alpha}$ with $b_{n\alpha}$ being the calculated nuclear field (see Section 6.2-3) for complete spin polarization, we attribute this to a nuclear spin leakage factor $f_{l\alpha}$, which is varying for different isotope species. The spin leakage factor $f_{l\alpha}$ is defined in Equation (6-19) written as $f_{l\alpha} = (1+\tau_{\text{hf-pol}}(\alpha)/\tau_{\text{irhf-dep}}(\alpha))^{-1}$, where $\tau_{\text{hf-pol}}(\alpha)$ is the nuclear spin polarization time and $\tau_{\text{irhf-dep}}(\alpha)$ the depolarization time constant, which competes with the DNP process via any nuclear spin relaxation channels. Isotope specific values of $\tau_{\text{hf-pol}}(\alpha)/\tau_{\text{irhf-dep}}(\alpha)$ can arise in case of nuclear spin relaxation via quadrupolar interaction, whereas nuclear spin relaxation by thermal vibrations can be neglected at 5 K [250]. It is thus suggested that the ionized donors in our n-GaAs layer induce an electrical field gradient. This is statistically varying, e.g., due to trapping, hopping or recombination of electrons, and interacts with the nuclear quadrupole moment thus causing nuclear spin relaxation [253, 270]. This apparently results in a larger leakage factor for the ^{71}Ga as compared to the ^{69}Ga isotope, in agreement with earlier results [270]. Considering the theory given in Ref. [77], it can be extracted from the experimental data that the leakage factor relation between the isotopes is $f_l{}^{75}{}_{As}:f_l{}^{69}{}_{Ga}:f_l{}^{71}{}_{Ga} \approx 20:16:25$.
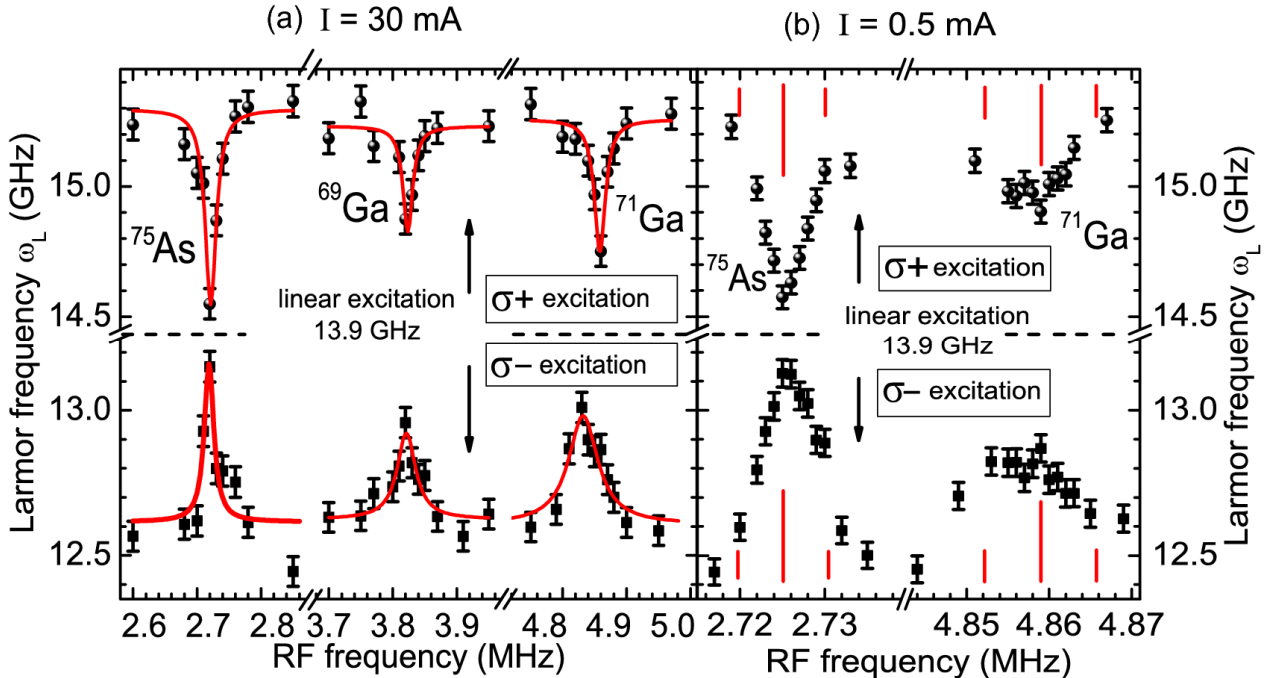

FIG 6.4-4: (a) Optically detected NMR of ^{75}As, ^{69}Ga and ^{71}Ga after σ^+- (balls) and σ^-- (squares) polarized excitation. B_{ext} is 374 mT and the current amplitude $I = 30$ mA. Red lines are a guide to the eye. (b) NMR of ^{75}As and ^{71}Ga at $I = 0.5$ mA. Vertical lines indicate the expected spectral splitting due to the local quadrupolar field.

A further hint of the impact of quadrupolar interaction generated most likely by ionized donors is presented in FIG 6.4-4(b). By decreasing the current amplitude to 0.5 mA, the NMR linewidth of ^{75}As and ^{71}Ga is reduced to ~10 kHz, and no clear Knight shift is observed for σ^+ and σ^- excitation. Apparently, the line shape of the NMR resonances is changed now. In case of a donor-induced local quadrupolar field [85, 270], a resonance broadening or even the occurrence of distinct satellites are expected, depending on the linewidth caused by the nuclear dipole field [269]. By using the values summarized in Ref. [253] with the Bohr radius of $a_B \approx 10$ nm, a quadrupolar field B_{NQ} is ~ 0.3 mT is obtained for ^{71}Ga, while a value of ~ 0.4 mT is found for $B_{NQ}(^{75}$As). The expected splittings of the NMR resonances are included in FIG 6.4-2(b) as vertical lines. In spite of our limited signal to noise ratio, it is concluded that the broadening of the NMR resonances for low RF fields might be attributed to the local quadrupolar effects. From the literature [87, 270], a smaller magnitude of the resonance satellites is expected for the ^{75}As species as compared to the ^{71}Ga one, in qualitative agreement with the presented data.

To address the coherent dynamics of nuclear spins, Rabi oscillation measurements were performed for the ^{75}As nuclei, as shown in FIG 6.4-5. In this kind of experiments, a RF pulse triggers a coherent absorption-emission cycle between nuclear spin states of the ^{75}As nuclei, which are energetically separated due to the external magnetic field [66]. Thus, the nuclear magnetization direction can be controlled by the RF pulse width under resonance conditions. In this case, the NMR is in the short time regime. To suppress the current-generated RF field inhomogeneity [193], a pinhole was used for probing the spin dynamics within a range of less than 5 µm in the center of the microcoil. The applied RF pulse sequence has a frequency of 2.72 MHz and a current amplitude of 30 mA.
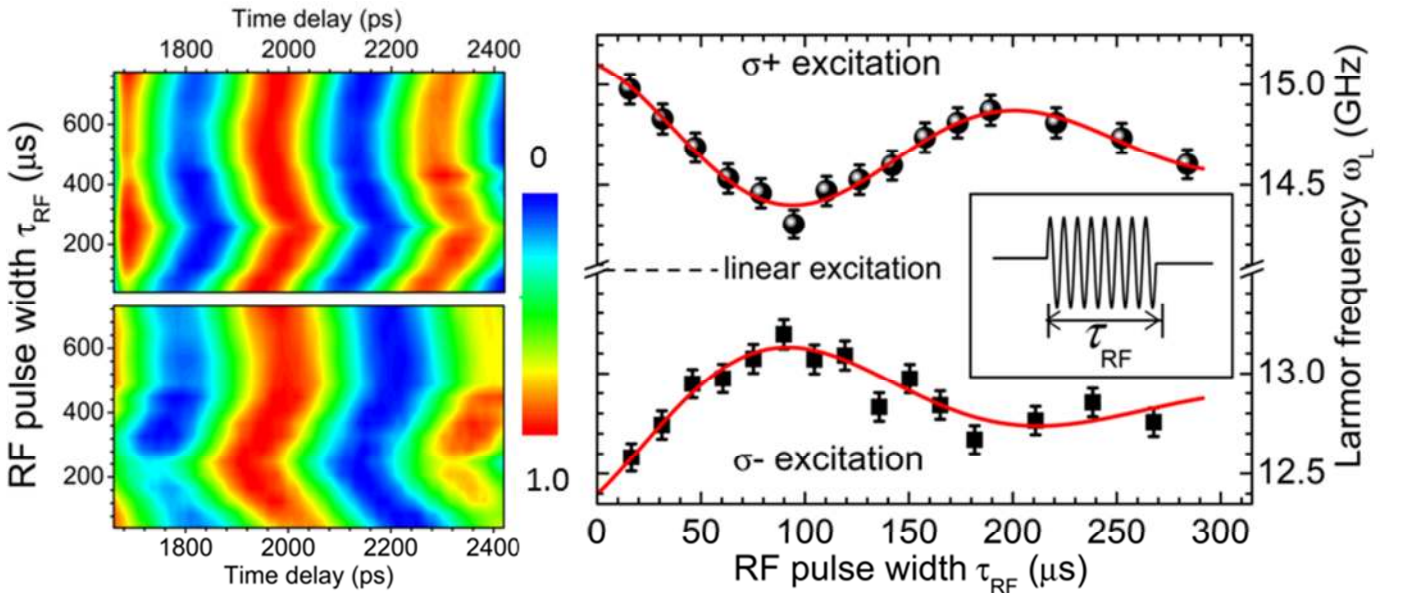
FIG 6.4-5: (a) 2D plot of the TRKR data for ^{75}As Rabi oscillations. The upper panel is obtained with σ^+-polarized excitation and the lower panel is obtained with σ^--polarized excitation. The RF current amplitude is 30 mA at a frequency of 2.72 MHz. (b) Extracted Larmor frequency vs RF pulse width. The extracted ω_L data are fitted by damped cosine functions (lines). The RF pulse is indicated in the inset.

As presented in FIG 6.4-5(a), the TRKR data are plotted versus the RF pulse width τ_{RF}, which is given in the vertical axis. Pronounced phase oscillations of the Kerr rotation signal can be seen by varying τ_{RF}, under both σ^+-polarized excitation and σ^--polarized excitation. FIG 6.4-5(b) presents the extracted Larmor frequency for each τ_{RF}. By fitting the data with damped cosine functions, it can be determined that the ^{75}As nuclear magnetization coherently nutates with a Rabi frequency of f_{Rabi}^{75As} ~ 4 kHz. Clearly by a π pulse (~ 100 μs) control, the nuclear magnetization is reversed. By using the relation of $f^{Rabi}_{75As} = 1/2\gamma_{75As} \cdot B_{RF}$, B_{RF} is estimated to be ~ 1.2 mT. The effective dephasing time T_2^{Rabi} is estimated ~ 200 μs, which is close to the literature value for GaAs in the adiabatic regime [89].

7   DYNAMIC NUCLEAR SPIN RESONANCE IN A SEMICONDUCTOR

The chapter addresses dynamic nuclear magnetic resonance in n-GaAs, mainly with respect to the observed optically forbidden magnetic resonance absorption. The local nuclear spin interaction is introduced regarding the nuclear magnetic moment and the nuclear quadrupole moment. The multi-spin magnetic resonance is explained according to the local nuclear spin perturbations, and the multi-photon absorption due to the tilted RF excitation is discussed. A two-level model is given for the measured nuclear spin dynamics, describing the interplay between the dynamic nuclear polarization via hyperfine interaction and nuclear spin depolarization due to magnetic resonance absorption. Comparing the characteristic nuclear spin relaxation rate obtained in experiment with master equation simulations, the underlying nuclear spin depolarization mechanism for each resonance is identified.

7.1   Local nuclear spin environment

Nuclear magnetic resonance (NMR) represents a technique widely utilized to address nuclei in various materials, e.g. in order to analyze the local nuclear spin environment [66]. Recent progress in quantum information processing requires an in depth understanding of nuclear spins [43, 262], particularly in semiconductor quantum structures, where the nuclear properties are varying on a mesoscopic length scale. The local quadrupolar interaction is found so strong that the concept of the nuclear spin temperature cannot be valid [95-97]. In addition, the Knight field is demonstrated non-uniform as a consequence of the inhomogeneous electron wavefunction in a quantum dot [98]. The ability of dynamic nuclear spin polarization via hyperfine interaction with spin polarized electrons greatly facilitates access to the nuclear spins in semiconductors via NMR experiments [21, 72]. These results give insight *e.g.* into the dipole-dipole (DD) interaction strength [89, 99] or the impact of the nuclear quadrupole (NQ) interaction under a local electrical field from atomic distortion [21, 100, 271], doping (defects) [85] or strain [87, 272]. Such local perturbations can cause a mixing of nuclear spin states and thus induce optically-forbidden [79, 99, 100], non-fundamental magnetic resonances by radio frequency (RF) absorption.

Usually, the properties of the nuclear spins are extracted from either spectral features of the NMR signal, like spectral broadening and spectral shift, or spin-echo type of experiments. In this way, the nuclear spin information is typically analyzed as a result of the total local nuclear spin interaction, e.g. including both DD and NQ interaction. Since the optically forbidden NMR originates from the local perturbations, the nuclear spin resonance has a characteristic transition rate determined by the perturbation strength. Therefore new insights on the local nuclear spin interaction in semiconductors

are expected by investigating the transient nuclear spin dynamics under non-fundamental resonance conditions.

For the local nuclear spin environment in solids, the nuclear dipole-dipole magnetic coupling and the nuclear quadrupole interaction are considered in the following.

7.1.1 Dipole-dipole interaction

The interaction of two magnetic moments is known as dipole-dipole coupling. Two neighbouring nuclei can interact with each other via nuclear spin dipole-dipole coupling. In FIG 7.1-1, the relative space relationship is given for two nuclei, nucleus 1 and nucleus 2 in both rectangular coordinates and spherical coordinates. The nuclear spin of nucleus 1 is I_1 and is I_2 for nucleus 2. The nuclear magnetic moment for two nuclei are respectively given as

$$\begin{aligned} \boldsymbol{\mu}_1 &= \gamma_{n1} h \boldsymbol{I}_1, \\ \boldsymbol{\mu}_2 &= \gamma_{n2} h \boldsymbol{I}_2 \end{aligned}, \tag{7-1}$$

where h is the Planck constant ($h = 2\pi\hbar$), and γ_{n1}, γ_{n2} is the gyromagnetic ratio for nucleus 1 and nucleus 2, respectively. The dipole-dipole coupling between the two nuclei is

$$\hat{H}_{DD-12} = \frac{\mu_0}{4\pi}\left(\frac{\hat{\boldsymbol{\mu}}_1 \cdot \hat{\boldsymbol{\mu}}_2}{r^3} - \frac{3\left(\hat{\boldsymbol{\mu}}_1 \cdot \hat{\boldsymbol{r}}\right)\left(\hat{\boldsymbol{\mu}}_2 \cdot \hat{\boldsymbol{r}}\right)}{r^5} \right), \tag{7-2}$$

where r is the radius vector from $\boldsymbol{\mu}_1$ and $\boldsymbol{\mu}_2$, and μ_0 is the vacuum permeability.
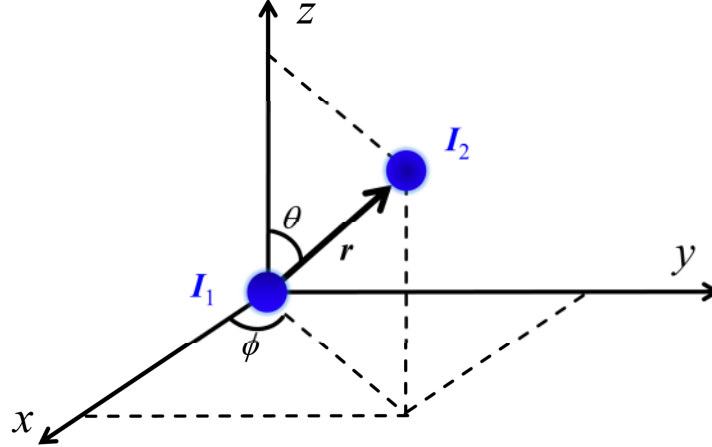
FIG 7.1-1: Coordinate representation for two nuclei, nucleus 1 and nucleus 2. The coordinate of nucleus 2 (with nuclear spin I_2) is given relative to nucleus 1 (with nuclear spin I_1) at the origin. The relationship between rectangular coordinates x, y, z and spherical coordinates r, θ, ϕ is indicated.

Using spherical representatives, the dipole-dipole Hamiltonian above can be rewritten as [66, 268]

$$H_{DD-12} = \frac{\mu_0}{4\pi}\frac{\gamma_{n1}\gamma_{n2}h^2}{r^3}\left(A + B + C + D + E + F\right), \tag{7-3}$$

in which each item is expressed in terms of the raising and lowering operator as

$$A = \hat{I}_{1z}\hat{I}_{2z}\left(1 - 3\cos^2\theta\right)$$

$$B = -\frac{1}{4}\left(\hat{I}_{1+}\hat{I}_{2-} + \hat{I}_{1-}\hat{I}_{2+}\right)\left(1 - 3\cos^2\theta\right)$$

$$C = -\frac{3}{2}\left(\hat{I}_{1+}\hat{I}_{2z} + \hat{I}_{1z}\hat{I}_{2+}\right)\sin\theta\cos\theta e^{-i\phi}$$

$$D = -\frac{3}{2}\left(\hat{I}_{1-}\hat{I}_{2z} + \hat{I}_{1z}\hat{I}_{2-}\right)\sin\theta\cos\theta e^{i\phi} \tag{7-4}$$

$$E = -\frac{3}{4}\hat{I}_{1+}\hat{I}_{2+}\sin^2\theta e^{-i2\phi}$$

$$F = -\frac{3}{4}\hat{I}_{1-}\hat{I}_{2-}\sin^2\theta e^{i2\phi}$$

Here the nuclear spin eigenstates are defined in the z-axis direction, i.e. parallel to the external field $\boldsymbol{B}_{\text{ext}}$. The first item (A) directly contributes to the nuclear spin energy level, while the left (B ~ F) items can perturb the eigenstates so that the nuclear spins are mixed. These elements are responsible for optically-forbidden NMR, which break the selection rules for spin state transitions.

The strength of the dipole-dipole coupling is estimated to be on the order of $\frac{\mu_0}{4\pi}\frac{\gamma_{n1}\gamma_{n2}h^2}{r^3}$. For the

nucleus 2, it can see an effective dipole field $B_{DD} \approx \frac{\mu_0}{4\pi}\frac{\gamma_{n1}h}{r^3}$ from nucleus 1. For one nucleus ^{75}As

located in a GaAs crystal, the nearest neighbour nucleus is one ^{69}Ga or ^{71}Ga nucleus. The atomic distance is $r \approx 0.433 \cdot a_{\text{Latt}}$ (see Section 2.1), where a_{Latt} is GaAs lattice constant with $a_{\text{Latt}} \approx 0.56$ nm. Then the dipole field from one nucleus is $B_{\text{DD}} \approx 0.05$ mT. In the presence of an external magnetic field B_{ext}, one nuclear spin performs nuclear precession with a certain Larmor frequency. Since the precession frequency is not same for unlike nuclear spins, the effective dipole field is random, which allows flipping the nuclear spins. It thus can be treated as a fluctuating local field. In the NMR spectrum, it is manifested as a linewidth broadening of the RF resonance absorption [66].

In principle, one nucleus interacts with all nuclei in the crystal by dipole-dipole coupling. The DD Hamiltonian is a sum of all over the nuclei

$$\hat{H}_{DD} = \sum_{i \neq j}\hat{H}_{DD-ij} \tag{7-5}$$

The DD interaction is proportional to r^{-3}, so that the magnitude of the effective dipole field vanishes quite fast for nuclei far away. Typically the nearest neighbour nuclei and the nuclei next to the nearest neighbour are accounted in Equation (7.5).

7.1.2   Quadrupole interaction

As one nucleus carries a certain charge, it can interact with an electrical field. If the nuclear charges have a non-spherical distribution, the nucleus undergoes a quadrupole interaction [268, 273].

Here the consideration is for a nucleus of atomic number N, and total electrical charge Ne is distributed over the nuclear volume with a charge density $\rho(x, y, z)$. The nucleus center is set as the

origin position $(0, 0, 0)$. The electrical potential is given by $V(x, y, z)$ which is determined by all charges other than those of the nucleus under considerations. The electrostatic energy for the nuclear charges can be expressed as

$$H_N = \int \rho(x, y, z) V(x, y, z) dxdydz \tag{7-6}$$

By using the Taylor expansion for the potential $V(x, y, z)$ relative to the nuclear center, one obtains

$$H_N = \int \rho(x, y, z) dxdydz \left\{ V_0 + \sum_j \left(\frac{\partial V}{\partial x_j} \right)_0 x_j + \frac{1}{2} \sum_{j,k} \left(\frac{\partial^2 V}{\partial x_j \partial x_k} \right)_0 x_j x_k + \cdots \right\} \tag{7-7}$$

Here the notation is used as $x_1 = x$, $x_2 = y$, $x_3 = z$. The subscript "0" indicates the derivatives are evaluated at the origin and thus it can be taken outside the integral. Then the electrostatic energy can be represented as

$$H_N = NeV_0 + \sum_j P_j \left(\frac{\partial V}{\partial x_j} \right)_0 + \frac{1}{2} \sum_{j,k} Q_{jk}' \left(\frac{\partial^2 V}{\partial x_j \partial x_k} \right)_0 + \cdots, \tag{7-8}$$

where $\int \rho(x, y, z) dxdydz = Ne$, and the two definitions are given

$$\begin{aligned} P_j &= \int \rho(x, y, z) x_j dxdydz \\ Q_{jk}' &= \int \rho(x, y, z) x_j x_k dxdydz \end{aligned}, \tag{7-9}$$

in which P_j is known as the electric dipole moment and Q_{jk}' is known as the electric quadrupole moment tensor.

In Equation (7-8), the first expansion is spin-independent, and thus it is out of interest here. The second expansion is demonstrated to vanish due to the odd parity of the nuclear charges. The third expansion is the focus here, namely the quadrupole interaction between the nucleus and the electric field. The neglected fourth expansion known as electric octupole term vanishes and the higher orders are neglected due to much less contribution compared with the quadrupole interaction [273]. For the spin-related terms in the electrostatic energy, the nuclear quadrupole interaction is dominant, and the nuclear quadrupole Hamiltonian is obtained as

$$\hat{H}_{NQ} = \frac{1}{2} \sum_{j,k} \hat{Q}_{jk}' V_{jk}, \quad \text{with } V_{jk} = \left(\frac{\partial^2 V}{\partial x_j \partial x_k} \right)_0 \tag{7-10}$$

Since the electric field is given as $E_k = -\dfrac{\partial V}{\partial x_k}$, the term V_{jk} is just the negative derivative of the

electric field by using $V_{jk} = \left(\dfrac{\partial^2 V}{\partial x_j \partial x_k} \right)_0 = -\dfrac{\partial}{\partial x_j} \left(-\dfrac{\partial V}{\partial x_k} \right) = -\dfrac{\partial E_k}{\partial x_j}$. The quadrupole energy is actually

given by the interaction between the nuclear quadrupole moment and the electric field gradient. As convention for simplicity, a new quadrupole moment tensor is defined as

$$Q_{jk} = 3Q_{jk}{}' - \delta_{jk} \sum_{i=1}^{3} Q_{ii}{}', \tag{7-11}$$

where $\delta_{jk} = 1$ for $j = k$ and $\delta_{jk} = 0$ otherwise. The nuclear quadrupole Hamiltonian in Equation (7.11) becomes

$$H_{NQ} = \frac{1}{6} \sum_{j,k} \hat{Q}_{jk} V_{jk} + \frac{1}{2} (\sum_{i=1}^{3} \hat{Q}_{ii}{}') (\sum_{j=1}^{3} V_{jj}) \tag{7-12}$$

The discussions above are valid for an arbitrary coordinate system xyz. Now the nuclear spin effect is introduced. The nuclear spin eigenstate is defined as the nuclear spin component along the z-axis direction parallel with the external magnetic field B_{ext} which energetically separates the nuclear spin sublevels.

From a semiclassical point of view, the external charges giving the electric field gradient interact only with the temporal average of the nuclear charge distribution. Because the nuclear charges precess rapidly around the direction of the nuclear spin, the nuclear charge distribution is symmetric to the z-axis, and thus it can be expected $Q_{jk} = 0$ in case of $j \neq k$, and $Q_{11} = Q_{22}$. On the other hand, it is satisfied $Q_{11} + Q_{22} + Q_{33} = 0$ by checking Equation (7-11), so one obtains $Q_{11} = Q_{22} = -1/2Q_{33}$. Hence all quadrupole components in Equation (7-12) can be expressed in terms of Q_{33} which is referred to the nuclear spin axis.

Consider a nucleus with a nuclear spin I_z, the quadrupole moment Q based on Equation (7-9) and (7-11) is defined as [273]

$$\begin{aligned} eQ &= <\varphi_{Iz} | Q_{33} | \varphi_{Iz} > \\ &= \int \rho_{Iz}(x, y, z)(3z^2 - r^2)dxdydz \end{aligned} \tag{7-13}$$

Here φ_{Iz} is the nuclear wave function $\rho_{Iz}(x, y, z)$ is the charge density distribution for the nuclear spin state I_z, and $r^2 = x^2 + y^2 + z^2$. As convention, the nuclear quadrupole moment is denoted in units of the proton charge e, and it is with a form of eQ as appeared in literature. If $\rho_{Iz}(x, y, z)$ is spherically symmetric, the nuclear quadrupole moment is proportional to $(3z^2 - r^2)$ which is equal to zero by volume integration. This is the case for nuclear spin $I = 0$ or $I = 1/2$. For the nuclear spin number $I \geq 1$, the nuclear charge has an asymmetric distribution. The eQ is positive for an elongated charge distribution, and negative for a flattened distribution. The nuclear radius r_n is typically on the order of $10^{-15} \sim 10^{-14}$ m, and the nuclear quadrupole moment is estimated $10^{-30} \sim 10^{-28}$ m^2 [268, 273]. In general, it is larger for heavier nuclei than lighter ones.

By careful quantum-mechanical treatments, the nuclear quadrupole Hamiltonian in Equation (7-12) can be given as [273]

$$\hat{H}_{NQ} = \frac{eQ}{6I(2I-1)} \sum_{j,k} \left(\frac{3}{2} \left(\hat{I}_j \hat{I}_k + \hat{I}_k \hat{I}_j \right) - \delta_{jk} \hat{I}^2 \right) V_{jk} \tag{7-14}$$

A more detailed expression is given Ref. [253]

$$\hat{H}_{\mathrm{NQ}}(\boldsymbol{R}) = \frac{eQ}{4I(2I-1)} \{ V_{zz}(\boldsymbol{R}) \left[3\hat{I}_z^2 - I(I+1) \right]$$

$$+ V_{xz}(\boldsymbol{R}) \left[\hat{I}_z \left(\hat{I}_+ + \hat{I}_- \right) + \left(\hat{I}_+ + \hat{I}_- \right) \hat{I}_z \right] - iV_{yz}(\boldsymbol{R}) [\hat{I}_z \left(\hat{I}_+ - \hat{I}_- \right) + \left(\hat{I}_+ - \hat{I}_- \right) \hat{I}_z] \quad (7\text{-}15)$$

$$+ \frac{1}{2} \left[V_{xx}(\boldsymbol{R}) - V_{yy}(\boldsymbol{R}) \right] \left[\hat{I}_+^2 + \hat{I}_-^2 \right] - iV_{xy} \left[\hat{I}_+^2 - \hat{I}_-^2 \right] \}$$

Here the space vector $\boldsymbol{R}$ refers to the general position for one nucleus. Clearly, there is NQ-induced energy splittings between different nuclear spins in case of non-zero $V_{zz}(\boldsymbol{R})$.

In a perfect crystal with cubic symmetry, the electric field gradient vanishes at the nucleus site. An appreciable V_{jk} can appear once the crystal symmetry is broken. For crystals lacking inversion symmetry center, e.g. GaAs, the quadrupole interaction can become non-zero by introducing local atomic distortion [100, 271], applying a huge external electrical field [274, 275] or generating strain in the crystal [87, 272, 276, 277].

FIG 7.1-2 gives the configuration of the electric field $\boldsymbol{E}$ and the magnetic field $\boldsymbol{B}_{\mathrm{ext}}$. The crystal axes lie in the new coordinate system $X'Y'Z'$, in which the electrical field is given as $\boldsymbol{E} = (E_{X'}, E_{Y'}, E_{Y'})$ by the component on each axis direction. The angle between $\boldsymbol{E}$ and the Z'-axis is θ, and is φ between X' and the EZ'-plane. As defined already, the magnetic field lies in the z-axis direction in the xyz coordinate system. Similarly, θ' and φ' are the angles between $\boldsymbol{B}_{\mathrm{ext}}$ and the Z'-axis and between X' and the zZ'-plane, respectively. Then the tensor of the electric field gradient in the xyz coordinate system can be represented by the electric field components in $X'Y'Z'$-coordinates as [253, 278]

$$\begin{pmatrix} V_{xx} \\ V_{yy} \\ V_{zz} \\ V_{yz} \\ V_{xz} \\ V_{xy} \end{pmatrix} = \begin{pmatrix} -\sin 2\theta' \sin\varphi' & -\sin 2\theta' \cos\varphi' & \cos^2\theta' \sin 2\varphi' \\ 0 & 0 & -\sin 2\varphi' \\ \sin 2\theta' \sin\varphi' & \sin 2\theta' \cos\varphi' & \sin^2\theta' \sin 2\varphi' \\ \cos\theta' \cos\varphi' & -\cos\theta' \sin\varphi' & \sin\theta' \cos 2\varphi' \\ \cos 2\theta' \sin\varphi' & \cos 2\theta' \cos\varphi' & \frac{1}{2}\sin 2\theta' \sin 2\varphi' \\ -\sin\theta' \cos\varphi' & \sin\theta' \sin\varphi' & \cos\theta' \cos 2\varphi' \end{pmatrix} \begin{pmatrix} E_{X'} \\ E_{Y'} \\ E_{Z'} \end{pmatrix} R_{14}, \quad (7\text{-}16)$$

in which R_{14} is the antishielding factor given in Ref. [253, 278].

Therefore the nuclear quadrupole Hamiltonian can be analytically estimated by Equation (7.15) and (7.16). For a simple case of the magnetic field parallel with the crystal axis, $\boldsymbol{B}_{\mathrm{ext}} // Z'$-axis, which means $\theta' = 0$ and $\varphi' = 90°$, the non-zero components of V_{jk} are

$$\begin{cases} V_{xy} = -R_{14}E_z = -R_{14}E\cos\theta \\ V_{yz} = -R_{14}E_y = -R_{14}E\sin\theta\sin\varphi \\ V_{xz} = R_{14}E\sin\theta\cos\varphi \end{cases} \quad (7\text{-}17)$$

It can be seen that the NQ-induced energy levels are degenerate for different nuclear spins. But still the nuclear spin eigenstates are mixed by the NQ perturbations. This spin state mixture can give rise to the non-fundamental NMR in case of resonant RF excitation, which is similar to the arguments for DD coupling in Section 7.1-1.

In the NMR experiments performed in Section 6.4, the external magnetic field is applied in the in-plane direction, while the accurate direction with respect to the crystal axis is uncertain. As a result, the component V_{zz} can contribute an additional energy, to modify the nuclear spin energy levels in presence of B_{ext}.

The nuclear spins magnetically interact with the external field as nuclear Zeeman interaction well-known as

$$H_Z = -g_n \mu_N \boldsymbol{I} \cdot \boldsymbol{B}_{ext}, \tag{7-18}$$

where g_n is the nuclear g factor and μ_N is the nuclear magneton
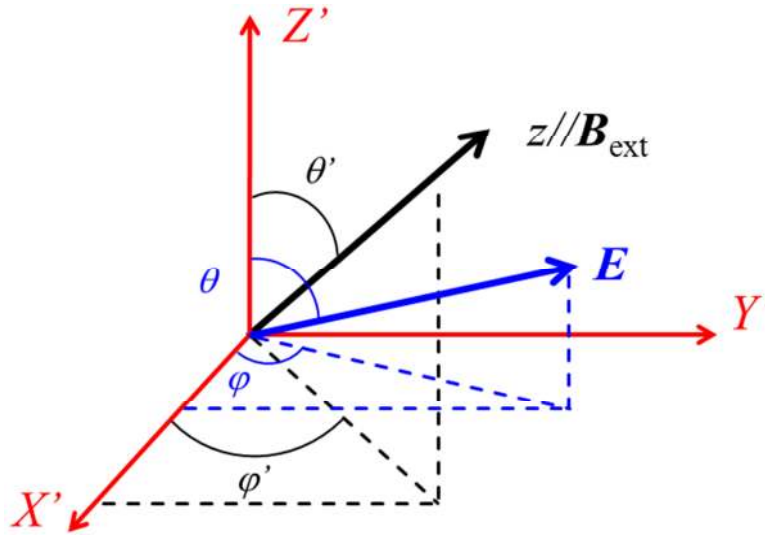
FIG 7.1-2: Geometry of the electric field and the magnetic field configuration. The crystal axes lie in the *X'Y'Z'* coordinate system, and the magnetic field is parallel to the z-axis direction in the *xyz* coordinate system (*x*- and *y*-axis are in the *X'Y'* plane, not depicted).   The angular positions of the external field $\boldsymbol{B}_{ext}$ and the electrical field $\boldsymbol{E}$ are indicated in the *X'Y'Z'* coordinate system.

Compared with H_Z, the NQ interaction is rather weak, and thus H_{NQ} is considered only by first-order perturbation. For a system with nuclear spin of $I = 3/2$ (e.g. GaAs), the effect of the NQ interaction on the NMR spectrum is schematically presented in FIG 7.1-3. In the absence of the NQ perturbation, the energy splitting is the same between nuclear spin states of $\Delta I = 1$. Thus there is only one center frequency $f = \Delta E/h = g_n \mu_N B_{ext}/h$ for resonance absorption. In the presence of nuclear quadrupole interaction, the nuclear spin energy levels are non-uniformly shifted, but with a same amount defined as $3A_Q$. The energy splitting can be thus changed by $6A_Q$. The sign of the energy shift can be judged from the first term of Equation (7-15), and it gives $A_Q = 1/12 \cdot eQV_{zz}$ by performing calculations. As a result, the NMR spectrum is split into three resonance centers, the original one and two satellites. The latter are shifted to frequencies of $(f \pm \Delta f)$, in which $\Delta f = 6A_Q/ h$.

By expanding the expression in Equation (7-16), it can be obtained

$$V_{zz} = R_{14}(\sin 2\theta' \sin \varphi' E_{X'} + \sin 2\theta' \cos \varphi' E_{Y'} + \sin^2 \theta' \sin 2\varphi' E_{Z'})$$
$$= R_{14}|\boldsymbol{E}|(\sin 2\theta' \sin \varphi' \sin \theta \cos \varphi + \sin 2\theta' \cos \varphi' \sin \theta \sin \varphi + \sin^2 \theta' \sin 2\varphi' \cos \theta) \tag{7-19}$$

In order to make a rough estimation, the magnitude is approximated as

$$V_{zz} \approx \sqrt{<V_{zz}^{\ 2}>} = \frac{\sqrt{3}}{4} R_{14}|\boldsymbol{E}| \approx 0.43 \cdot R_{14}E \text{ , with} \tag{7-20}$$

$$<V_{zz}^{\ 2}> = \frac{(R_{14}|\boldsymbol{E}|)^2 \int_0^{2\pi} (\sin 2\theta' \sin \varphi' \sin \theta \cos \varphi + \sin 2\theta' \cos \varphi' \sin \theta \sin \varphi + \sin^2 \theta' \sin 2\varphi' \cos \theta)^2 \, d\theta' d\varphi' d\theta d\varphi}{\int_0^{2\pi} d\theta' d\varphi' d\theta d\varphi}$$
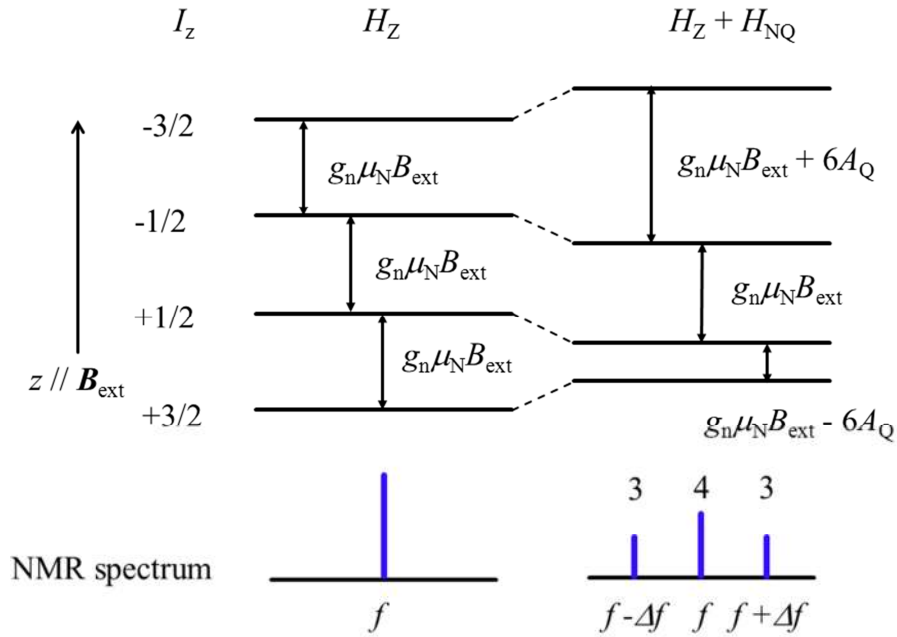
FIG 7.1-3: Quadrupole splitting of the NMR for nuclear spin $I = 3/2$. Top: spin energy sublevels. Bottom: NMR spectrum. Only center frequencies are indicated. The NQ-induced energy splitting gives the NMR satellites. The number indicates the expected relative resonance strength for each satellite.

In the studied n-GaAs sample, the ionized donors can generate local electrical fields. As a rough estimation, the electrical field is considered at a distance of the Bohr radius ($|\boldsymbol{R}| = a_B \approx 10$ nm) from the donor. The electrical field $|\boldsymbol{E}| \approx \dfrac{|e|}{4\pi\varepsilon\varepsilon_0} \cdot \dfrac{1}{a_B^2} \approx 1.1 \times 10^6$ V/m, in which $|e|$ is the ionized donor charge, ε_0 is the vacuum permittivity, and ε is the dielectric constant of GaAs. In order to calculate the NQ splitting of ^{75}As as an example, parameters summarized in Ref.[253] are used: $Q(^{75}\text{As}) = 0.314*10^{-28}$ m^2, $R_{14}(^{75}\text{As}) = 3.2*10^{12}$ m^{-1}. The quadrupole interaction for each nuclear spin state is $|H_{NQ}| = 3A_Q(^{75}\text{As}) = 1/4 \cdot eQ(^{75}\text{As})V_{zz} \approx 1/4 \cdot 0.43 \cdot eQR_{14}|\boldsymbol{E}| \approx 1.9 \times 10^{-30}$ J. The frequency shift in NMR is expected as $\Delta f(^{75}\text{As}) = 6A_Q(^{75}\text{As})/h \approx 5.7$ kHz. This energy splitting can be treated like an effective quadrupole field defined as $|B_{NQ}(^{75}\text{As})| = |H_{NQ}|/g_n\mu_N \approx 0.39$ mT. By similar calculations, for the other two nuclear species, one obtains $\Delta f(^{69}\text{Ga}) \approx 5.7$ kHz, $\Delta f(^{71}\text{Ga}) \approx 6.8$ kHz, $|B_{NQ}(^{69}\text{Ga})| \approx 0.28$ mT and

$|B_{NQ}(^{71}Ga)| \approx 0.26$ mT. The calculation results are in qualitative agreement with the experiment results presented in FIG 6.4-4 (Section 6.4).

7.2   Dynamic nuclear spin resonance in n-GaAs

The experimental configuration has been presented in FIG 6.4-2: the direction of the external field $\boldsymbol{B}_{ext}$ is defined as the z-axis direction, and the microcoil is patterned on top of the semiconductor surface. The generated on-chip RF field $\boldsymbol{B}_{RF}$ is in the x-z plane. In this case, the nuclear spin Hamiltonian is written as

$$H = H_z + H_{RF} = -g_n\mu_N \boldsymbol{I} \cdot (\boldsymbol{B}_{ext} + \boldsymbol{B}_{RF})$$
$$= -g_n\mu_N \left[I_z(B_{ext} + B_{RF-long}\cos(\omega_{RF}t)) - \frac{(I_+ + I_-)}{2}B_{RF-tran}\cos\omega_{RF}t \right] \tag{7-21}$$

Here $\boldsymbol{I}$ is the nuclear spin, and H_{RF} is the Hamiltonian contributed from the RF field. The longitudinal component of the RF field (collinear with $\boldsymbol{B}_{ext}$) is $B_{RF-long}$ and $B_{RF-tran}$ is the transverse component (perpendicular to $\boldsymbol{B}_{ext}$). The transverse part of H_{RF} contains the raising and lowering operators, and thus it can flip the nuclear spins. In the condition of resonant RF excitation, i.e. $\omega_{RF} = 2\pi\gamma_n B_{ext}$, fundament NMR is induced. The selection rule is $\Delta I_z = 1$ for nuclear spin state transitions in case of fundamental NMR. This is what observed in FIG 6.4-4 (Section 6.4).
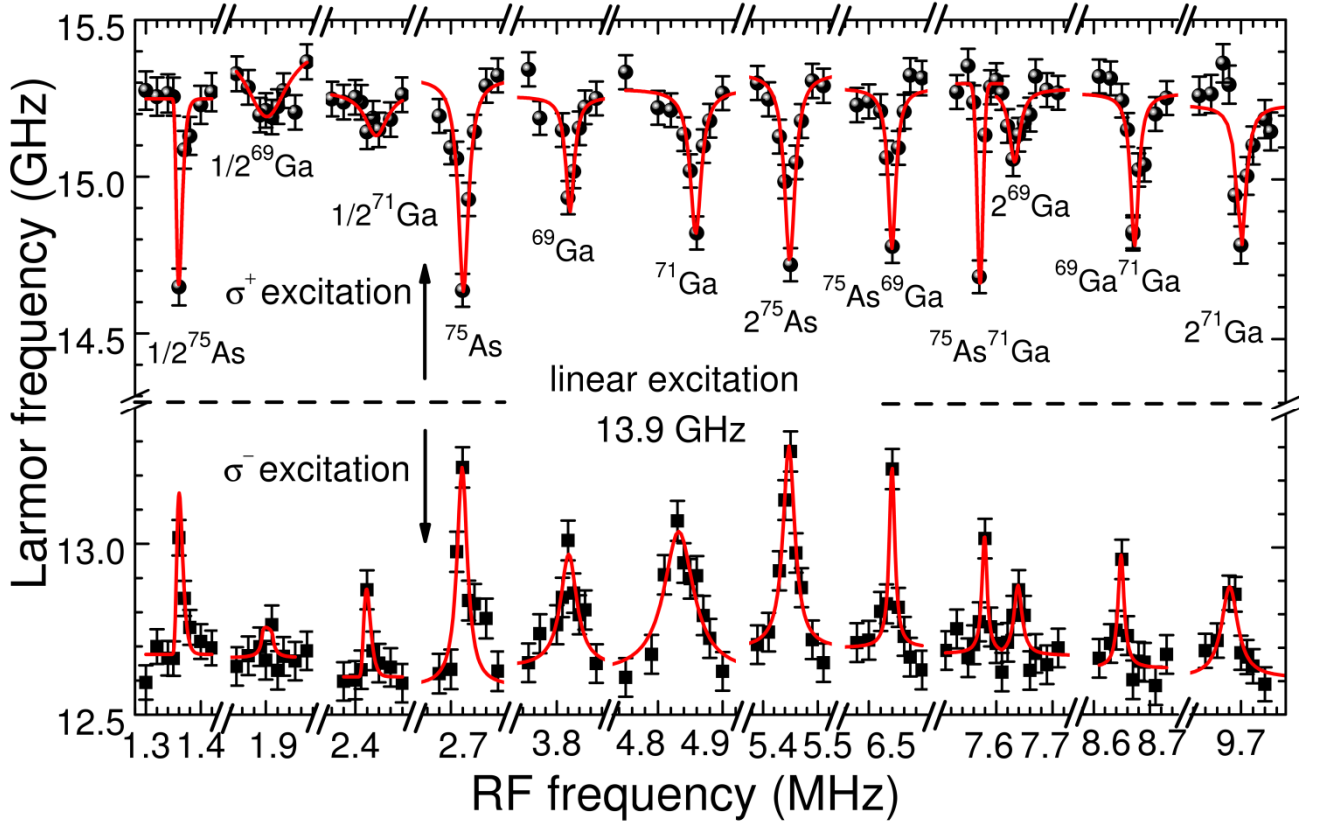
FIG 7.2-1: Optically detected NMR under σ^+ - polarized optical excitation (balls) and σ^- - polarized optical excitation (squares). The horizontal dashed line indicates the Larmor frequency measured under linear polarized excitation.

By varying the frequency of the RF field, nuclear spin depolarization is observed at different resonance frequency positions. The Larmor frequency ω_L is clearly reduced (enhanced) for σ^+ (σ^-) optical excitation. The observed NMR results are presented in FIG.7.2-1. They can be classified as four types: (1) fundamental NMR at frequencies of $f_\alpha = \gamma_\alpha B_{\text{ext}}$ [21, 72, 77, 79, 85, 87, 89, 98, 99, 222, 272], where γ_α is the nuclear gyromagnetic ratio of isotope species α; (2) two-spin NMR involving one isotope species at $2f_\alpha$ [79, 85, 99] ; (3) two-spin NMR involving different species of isotopes at $(f_{\alpha1} + f_{\alpha2})$ [79]; (4) half-harmonic NMR at $1/2f_\alpha$ [79, 100, 271, 279].

In order to understand the occurrence of the non-fundamental NMR, the total nuclear spin Hamiltonian is written as:

$$\hat{H} = \hat{H}_{\text{Z}} + \hat{H}_{\text{hf}} + \hat{H}_{\text{RF}} + \hat{H}_{\text{DD}} + \hat{H}_{\text{NQ}} \qquad (7\text{-}22)$$

The first two terms refer to the Zeeman energy and the hyperfine interaction, respectively. H_{RF} is the perturbation arising from the RF magnetic field, H_{DD} is related to the dipole-dipole interaction, and H_{NQ} represents the nuclear quadrupole interaction.

7.2.1 Non-fundamental NMR from local perturbations

The non-fundamental magnetic resonance, i.e. two-spin or two-photon resonance, breaks the selection rule. Basically it originates from local perturbations, either crystal properties or experiment geometry.

- **Two-spin nuclear magnetic resonance**

The two-spin NMR indicates the nuclear spin state transition of $\Delta I_z = 2$ by absorbing the energy of one RF quanta.   This can be explained by considering the nuclear spin environment, concerning to DD interaction and NQ interaction. From Equations (7-4) and (7-15), there are off-diagonal elements in either H_{DD} or H_{NQ}, so that the orthogonality is broken for the nuclear spin eigenstates defined along the external field. The extent of the state mixture is determined by perturbation strength with respect to the Zeeman energy splitting [99], i.e. $(H_{\text{DD}}/\Delta H_z)^2 \sim B_{\text{ext}}^{-2}$ and $(H_{\text{NQ}}/\Delta H_z)^2 \sim B_{\text{ext}}^{-2}$. Here ΔH_z is the Zeeman energy splitting between nuclear spin states which can be coupled by the local perturbations. In H_{DD} given in Equation (7-4), the terms C and D contain the first order of I_+ or I_-, and thus they mix spin states with $\Delta I_z = 1$ for two neighbouring nuclei. The terms of E and F contain the second order of I_+ or I_-, and thus they mix spin states with $\Delta I_z = 2$. Similarly H_{NQ} can induce state mixture between nuclear spins with $\Delta I_z = 1$ and $\Delta I_z = 2$ according to Equation (7-15), but only for one nucleus.

In FIG 7.2-2, a schematic explanation is given for the two-spin NMR either due to H_{DD} or H_{NQ}. In (a), the DD interaction couples nucleus 1 and nucleus 2. The nuclear spin states are I_{1z} and I_{2z}, respectively, and it is denoted as $|I_{1z}, I_{2z}\rangle$. By considering the C or D term in H_{DD}, there can be spin state mixture between $|I_{1z}, I_{2z}\rangle$ and $|I_{1z} - 1, I_{2z}\rangle$ (lower-right channel), $|I_{1z}, I_{2z}\rangle$ and $|I_{1z}, I_{2z} - 1\rangle$ (lower-left channel), $|I_{1z} - 1, I_{2z}\rangle$ and $|I_{1z} - 1, I_{2z} - 1\rangle$ (upper-right channel), or $|I_{1z}, I_{2z} - 1\rangle$ and $|I_{1z} - 1, I_{2z} - 1\rangle$ (upper-left channel). The mixture channel is indicated by the dashed double arrow. In

absence of RF excitation, such spin state mixture is in a dynamical equilibrium. As can be seen from Equation (7-21), the transverse component of H_{RF} contains the first order of I_+ or I_-, there could be spin flips of $\Delta I_z = 2$ according to the C or D term in H_{DD}. If the RF excitation has a frequency $f_{RF} = (\gamma_{n1} + \gamma_{n2}) B_{ext} = (f_{\alpha 1} + f_{\alpha 2})$, the two-spin NMR is induced. A similar argument is applied for H_{NQ} to generate two-spin NMR as shown in FIG 7.2-2 (b).

For the DD interaction, spin coupling can be between neighboring nuclei of either the same isotope species or between two different kinds of isotopes, which allows H_{DD} to induce NMR at $2f_\alpha$ and at $(f_{\alpha 1} + f_{\alpha 2})$, respectively. The nuclear quadrupole interaction only involves one nucleus (for each isotope species in GaAs the quadrupole moment is non-zero), H_{NQ} can consequently induce the $2f_\alpha$ resonance.
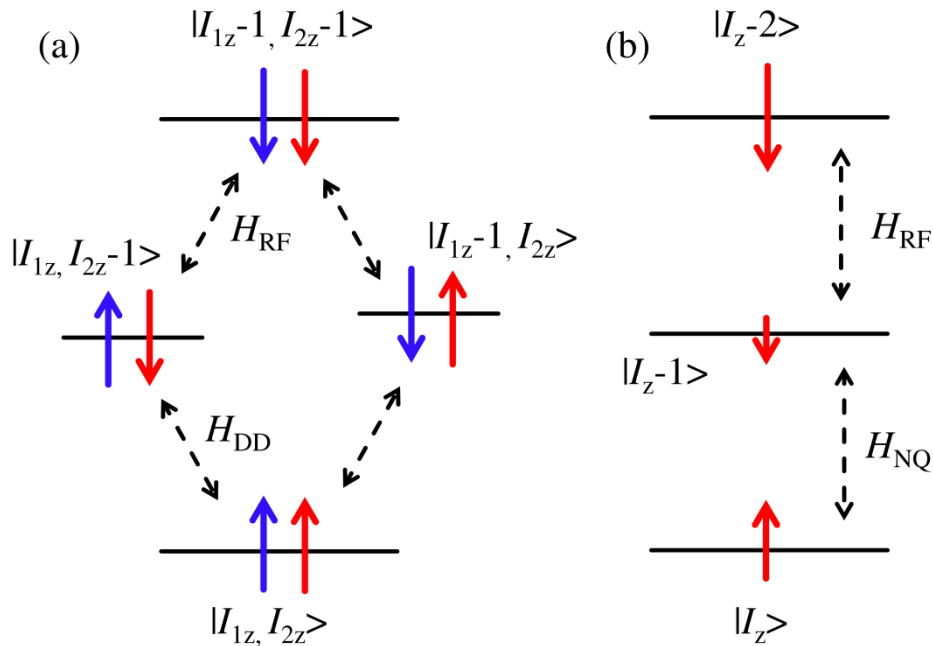
FIG 7.2-2: (a) Two-spin magnetic resonance perturbed by dipole-dipole interaction which mixes the nuclear spin states of neighbouring nuclei, 1 and 2. The isotope species of nucleus 1 and nucleus 2 can be the same or different. (b) Two-spin magnetic resonance perturbed by nuclear quadrupole interaction, which mixes the spin states for one nucleus.

- **Two-photon nuclear magnetic resonance**

The half-harmonic resonance at $1/2f_\alpha$ suggests two-quanta RF absorption for spin transitions of $\Delta I = 1$, which stems from the oscillating RF field oblique to the nuclear field [280]. This geometry can happen in case of either strong nuclear quadrupole interaction with the crystal field if the applied RF field is perpendicular to $\boldsymbol{B}_{ext}$ [21, 100, 271], or the applied RF field is intentionally oblique to $\boldsymbol{B}_{ext}$ [279]. As the quadrupole field around donors is on the order of 0.1 mT [222] (also see Section 7.1-2), which is quite small compared with $B_{ext} = 374$ mT, this hardly changes the parallelism of $\boldsymbol{B}_N$ and $\boldsymbol{B}_{ext}$. However, the transverse field component $B_{RF-tran}$ varies within the microcoil center and can achieve values on the order of 1 mT in the metal vicinity while the longitudinal field component $B_{RF-long}$ is

slightly spatially dependent (see Section 3.1). This results in B_N being oblique to the total RF field. Therefore this spatially inhomogeneous RF field from the on-chip microcoil is ascribed to be responsible for the $1/2f_\alpha$ NMR.

FIG 7.2-3 presents the oblique configuration of B_{ext} and B_{RF}. The left side gives the tilted RF field with $B_{RF\text{-}long} = z \cdot B_{RF\text{-}long} \cdot \cos(\omega_{RF}t)$ and $B_{RF\text{-}tran} = x \cdot B_{RF\text{-}tran} \cdot \cos(\omega_{RF}t)$, where x and z denote the unit vector for x-axis and z-axis direction, respectively. The tilting angle is defined as $\phi = \arctan(B_{RF\text{-}tran}/B_{RF\text{-}long})$.
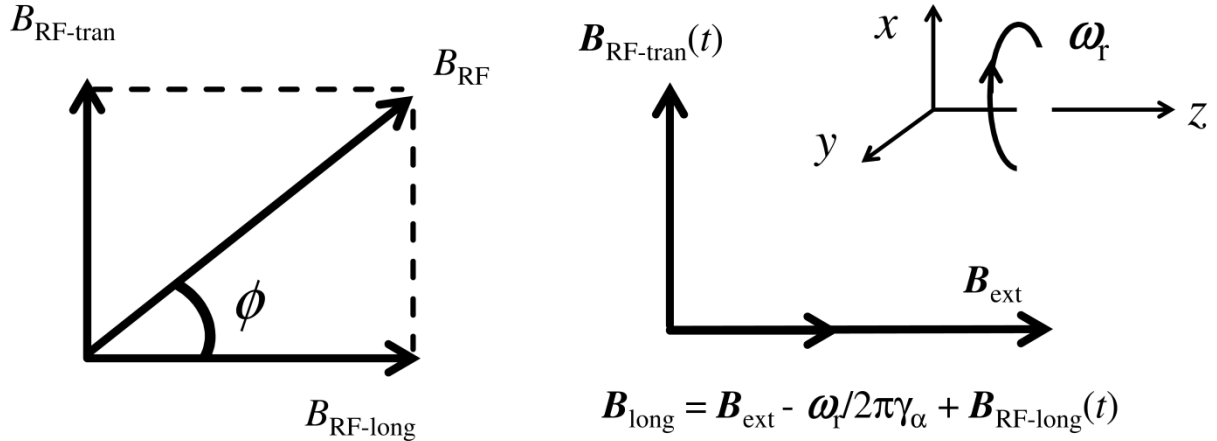
FIG 7.2-3: Configurations of the external magnetic field and the RF field for generating two-photon NMR. Left: the RF field is tilted with respect to the external field; Right: magnetic field in a rotating frame with an angular velocity of ω_r.

Similar to the treatment in FIG 6.4-1 (Section 6.4), a rotating frame with angular velocity of ω_r is used here, as presented on the right side. The total longitudinal magnetic field becomes $B_{long} = (B_{ext} - \omega_r/2\pi\gamma_\alpha + B_{RF\text{-}long} \cdot \cos(\omega_{RF}t))$ and the transverse magnetic field is $B_{tran} = 1/2 \cdot B_{RF\text{-}tran} \cdot (x \cdot \cos((\omega_{RF} - \omega_r)t) + y \cdot \sin((\omega_{RF} - \omega_r)t))$. Now the angular velocity is chosen to be [279]

$$\omega_r = \omega_{RF} + 2\pi\gamma_\alpha B_{RF\text{-}long} \cdot \cos\omega_{RF}t \tag{7-23}$$

Then in the rotating frame, the longitudinal field is

$$B_{long} = B_{ext} - \omega_{RF}/2\pi\gamma_\alpha , \tag{7-24}$$

and the transverse field becomes

$$B_{tran} = \frac{B_{RF\text{-}tran}}{2} \cdot \left[x \cdot \cos(\frac{2\pi\gamma_\alpha B_{RF\text{-}long}}{\omega_{RF}} \sin(\omega_{RF}t)) - y \cdot \sin(\frac{2\pi\gamma_\alpha B_{RF\text{-}long}}{\omega_{RF}} \sin(\omega_{RF}t)) \right], \tag{7-25}$$

in which the phase is obtained by integral for the angular speed on time

$$\int_0^t [\omega_{RF} - \omega_r(\tau)]d\tau = \int_0^t \left[-2\pi\gamma_\alpha B_{RF\text{-}long} \cdot \cos\omega_{RF}\tau \right]d\tau = \frac{-2\pi\gamma_\alpha B_{RF\text{-}long}}{\omega_{RF}} \sin\omega_{RF}t \tag{7-26}$$

By using the Taylor expansion for sine and cosine functions and keeping the first order of $B_{RF\text{-}long}$, the transverse field is approximated as

$$B_{\text{tran}} = -\mathbf{y} \cdot \frac{2\pi\gamma_\alpha B_{\text{RF-long}} B_{\text{RF-tran}}}{2\omega_{\text{RF}}} \cdot \sin(\omega_{\text{RF}} t) \tag{7-27}$$

By comparing Equation (7.24) and Equation (7.27), it can be seen that the magnetic resonance condition in the rotating frame is: $\omega_{\text{RF}} = 2\pi\gamma_\alpha B_{\text{long}}$. It turns out $f_{\text{RF}} = 1/2 \cdot \gamma_\alpha B_{\text{ext}} = 1/2\ f_\alpha$, which is just the half of the fundamental resonance frequency. Further, the magnitude of the resonance field is

$$\left| B_{\text{tran}} \right| = \frac{B_{\text{RF-long}} B_{\text{RF-tran}}}{2B_{\text{ext}}} = \frac{B_{\text{RF}}^2 \sin\phi \cos\phi}{2B_{\text{ext}}} \tag{7-28}$$

This indicates the resonance strength is reduced by increasing the external field, with a similar dependence on B_{ext} as two-spin resonance. In case of a RF field perpendicular to the external field ($\phi = 90°$) or RF field parallel to the external field ($\phi = 0$), no two-photon NMR is expected. Since the transverse field generated by the microcoil can vary greatly from the center to the metal vicinity, the resonance strength can be expected to differ much at different areas inside the microcoil. This might explain the non-uniform resonance level for the measured $1/2 f_\alpha$ NMR in FIG 7.2-1.

7.2.2 Nuclear spin dynamics under non-fundamental magnetic resonance

Two typical TRKR data sets obtained under RF resonance conditions are presented in FIG 7.2-4(a). The arrows mark the time when the RF field was switched on. In case of the fundamental ^{75}As NMR (upper panel), there is an abrupt change of the Kerr rotation signal after switching on the RF field, while for the ^{71}Ga^{75}As resonance (lower panel), the TRKR signal changes on a time scale of minutes. The variation of the Larmor frequency ω_L with lab time after switching on the RF field is plotted for a few selected resonances in FIG 7.2-4(b). Each curve can be roughly fitted by a mono-exponential decay with a nuclear spin relaxation (NSR) time constant $\tau_{\text{NSR}}(\exp)$ as summarized in Table 7-1. For the fundamental resonances, $\tau_{\text{NSR}}(\exp)$ is much shorter than 1 min and limited by the experiment setup, i.e. the time needed for recording one TRKR curve. In case of the $2f_\alpha$ and the $1/2f_\alpha$ resonances, $\tau_{\text{NSR}}(\exp)$ is on the order of 1 min, while for the $(f_{\alpha1} + f_{\alpha2})$ resonances, time constants between 2.4 min and 4.2 min are extracted from the data.

It has to be noted that the nuclei are always exposed to polarized optical excitation and thus experience DNP formation during the measurements. Thus, the nuclear spin dynamics can be described by a two-level model as shown in FIG 7.2-5. The nuclear spin polarization with a rate τ_{pol}^{-1} caused by the hyperfine interaction H_{hf} competes with the depolarization due to RF absorption with a rate τ_{dep}^{-1}. The rate equation for the dynamic Overhauser field is

$$\frac{dB_N}{dt} = \frac{B_{N0} - B_N}{\tau_{\text{pol}}} - \frac{B_N}{\tau_{\text{dep}}} \tag{7-29}$$

Here, B_{N0} is the Overhauser field in case of DNP saturation. By solving the equation above, the nuclear spin relaxation rate and the reduction of the Overhauser field ΔB_N at resonance conditions are obtained as

$$\tau_{NSR}^{-1} = (\tau_{pol}^{-1} + \tau_{dep}^{-1})$$
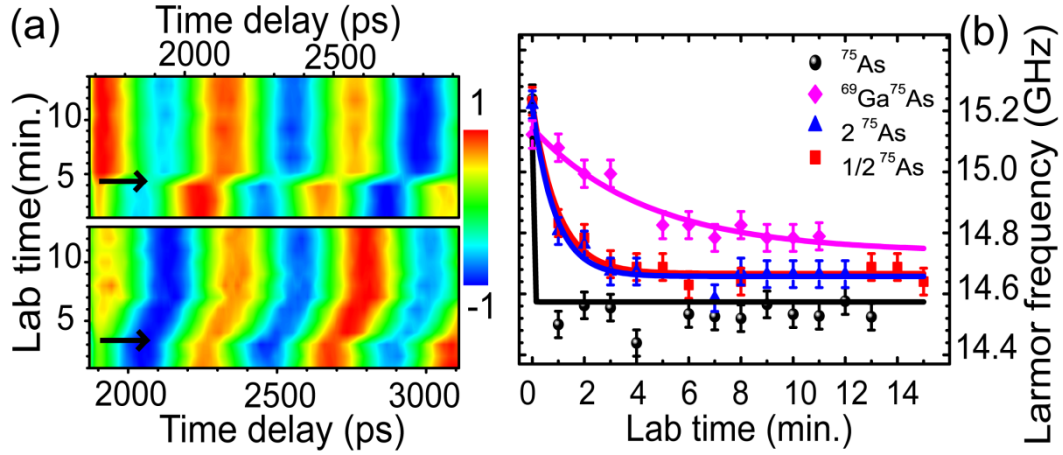$$\Delta B_N = B_{N0} / (1 + \tau_{dep} / \tau_{pol}) \tag{7-30}$$

FIG 7.2-4: (a) 2D plot of the Kerr rotation data. The color code describes the amplitude of the Kerr signal and the arrows indicate the lab time, where the RF field is switched on. The data for the upper plot are obtained at the [75]As NMR, while the lower plot represents the data recorded for the [71]Ga[75]As NMR. (b) Larmor frequency versus lab time for different resonances (symbols). The solid lines are mono-exponential fits.

NMR time (min.)	τ_{NSR} (exp.)	τ_{pol}	τ_{dep}		
			D-D	NQ	B_{tran}
[69]Ga[75]As	4.2	6.6	6.0	-	-
[71]Ga[75]As	2.7	7.8	5.6	-	-
[69]Ga[71]Ga	2.4	4.4	3.6	-	-
2 [75]As	0.8	5.0	19	0.05[1.2]	-
2 [71]Ga	1.0	2.8	7.2	0.03[0.4]	-
1/2 [75]As	1.1	5.0	-	-	1.3
1/2 [71]Ga	0.9	2.8	-	-	0.5
[75]As	<< 1	5.0	<< 1		

Table 7-1: Experimentally obtained time constant of the nuclear spin relaxation τ_{NSR}(exp), based on the average values measured for σ^+ - and σ^- - excitation (second column).   In the third column, the nuclear polarization time τ_{pol} is listed as extracted from the data presented in FIG 7.2-6. The last column summarizes the depolarization time constant τ_{dep} as obtained from the numerical simulations.

In order to determine the polarization time τ_{pol}, TRKR measurements with defined RF switching sequences were performed as shown in FIG 7.2-6. By using σ^+ - polarized optical pumping without an applied RF field, the DNP formation results in an increase of the Overhauser field with a characteristic time constant of $\tau_{pol,exp} = 9.4$ min. After saturation, the RF field is switched on with a frequency resonant to the [75]As isotope and the [75]As nuclear spins are depolarized instantaneously, i.e.

below the time scale of our experiment. Afterwards, the RF field is again switched off and the ^{75}As nuclei get polarized with a time constant of 4.6 min. This difference in the time constants is related to the fact that the first DNP process involves all three species of isotopes, while the latter one is only controlled by the DNP of the ^{75}As nuclei.

According to Ref. [250], one obtains for the DNP formation time for the isotope species α the relation $\tau_{\text{pol-}\alpha} \sim f_{\text{l-}\alpha} \cdot \chi_\alpha (\gamma_\alpha P_{\text{f-}\alpha})^{-2}$, where $f_{\text{l-}\alpha}$ is the nuclear spin leakage factor, χ_α is the isotope abundance, and $P_{\text{f-}\alpha}$ is electron probability density at the nucleus normalized by the unit cell volume [66, 250]. In Section 6.2, the leakage factor relation is calculated as $f_{l\text{-}75\text{As}}:f_{l\text{-}69\text{Ga}}:f_{l\text{-}71\text{Ga}} \approx 20:16:25$. Using the assumption $\tau_{\text{pol}} = \Sigma \tau_{\text{pol-}\alpha}$, the value $\tau_{\text{pol-}\alpha}$ for each isotope species α can be estimated. From $\tau_{\text{pol,exp}} = 9.4$ min, $\tau_{\text{pol-}75\text{As}} = 5.0$ min is extracted, which fairly well agrees with the experimental value of 4.6 min. Similar experiments have been performed for the ^{71}Ga isotope, where $\tau_{\text{pol-}71\text{Ga}} = 2.77$ min is measured, in good agreement with the calculated value of 2.8 min. In Table 1, the extracted polarization time for each NMR is listed. Hereby, we assume $\tau_{\text{pol}} = (\tau_{\text{pol-}\alpha 1} + \tau_{\text{pol-}\alpha 2})$ for the $(f^{\alpha 1} + f^{\alpha 2})$ resonances [281].
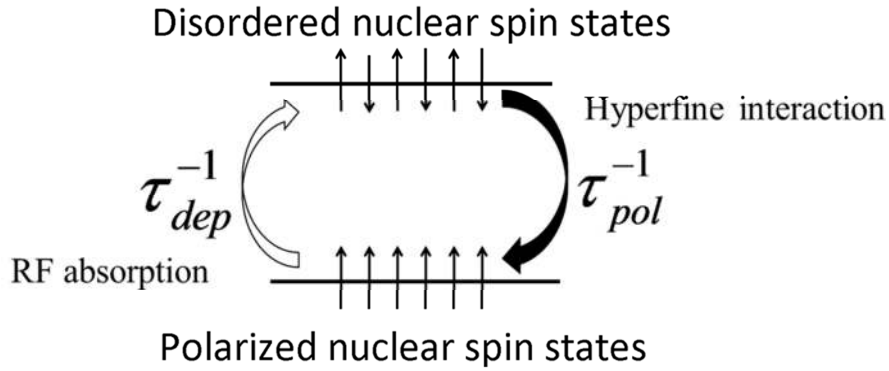
FIG 7.2-5: Two-level scheme used for describing the nuclear spin dynamics.
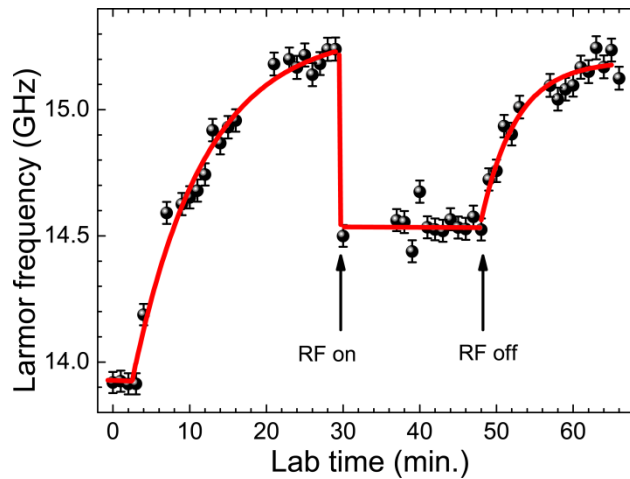
FIG 7.2-6: Larmor frequency ω_L versus lab time for a well-defined RF switching sequence. The RF excitation is to induce ^{75}As NMR. Lines are guide to eyes. The first DNP formation process before switching on RF excitation concerns all the nuclear species, and the second DNP formation process after switching off RF excitation is only due to ^{75}As nuclear spins.

In order to determine the depolarization time τ_{dep} we consider the different depolarization mechanisms for each NMR. The temporal evolution of nuclear spin states can be described by the Lindblad master equation [210]:

$$\frac{d\rho}{dt} = \frac{1}{i\hbar}[H,\rho] + \left(2L\rho L^{\dagger} - \{L^{\dagger}L, \rho\}\right) \tag{7-31}$$

Here $H = H_z + H_{RF} + H_{DD} + H_{NQ}$ is the nuclear spin Hamiltonian, ρ is the nuclear spin density matrix, and L the Lindblad operator. As the nuclear spin relaxation via thermal vibrations is negligible in the low temperature regime used here [250], the Lindblad operator can be simplified as $L = \Gamma\sigma_z$, where Γ is a constant determining the nuclear spin-spin relaxation rate and σ_z is the Pauli matrix.

To simulate the NMR-induced nuclear spin depolarization process, the following steps are performed: (i) The initial nuclear spin polarization degree is set to unity; (ii) In a first approximation, a nuclear spin-spin relaxation time of $T_2 = 100$ μs is taken for all three isotope species using the measured Rabi coherence time T_2^{Rabi} of the ^{75}As isotope (assuming $T_2^{Rabi} \approx 2*T_2$ [66, 89]) . (iii) The relaxation rate Γ is defined as the nuclear spin-spin relaxation rate relative to the instantaneous total magnetic field [282]. (iv) For the calculations of the NQ-induced NMR, the quadrupole field magnitude is taken as 0.4 mT for the ^{75}As and 0.3 mT for the ^{71}Ga isotope, respectively, from previous calculations (Section 7.1-2). For the calculations of the $1/2f_{\alpha}$ NMR, a transverse field of $B_{RF-tran} = 0.15$ mT as a calculated averaged value inside the microcoil is used.

Under these assumptions, the nuclear spin depolarization dynamics is numerically calculated from the master equation. To note, there is a uniform nuclear spin depolarization by RF excitation even there is no perturbation and the RF field is non-resonant. As an instance presented in FIG 7.2-7(a), the nuclear spin depolarization dynamics (red dots) is calculated for NQ-induced $2f_{75As}$ NMR only with RF excitation. By setting the NQ interaction equal to zero, there is still a nuclear spin depolarization process (blue dots), which can depolarize the ^{75}As nuclear spins completely. The experimental dependence of the Larmor frequency on RF excitation frequency is given in FIG 7.2-7 (b), there is no noticeable nuclear spin depolarization ranging from 0.5 MHz to 20 MHz for both σ^{+}- and σ^{-}- polarized optical excitation. This discrepancy between theoretical simulation and experiments is yet not clear. For a qualitative understanding, the used data (black line) are based on the calculated dynamics (red dots) under RF excitation and NQ interaction by excluding (dividing) the background nuclear spin dynamics (blue dots). Such a processing is applied for all the nuclear field depolarization processes.

Finally, the total dynamic nuclear field experienced by the precessing electrons is determined by weighting the nuclear field amplitude of each isotope with the respective isotope spin polarization. The calculated temporal evolution of the nuclear field is presented in FIG 7.2-8. From the numerical calculations, the characteristic decay time constants are extracted and listed in Table 7-1.

There are several interesting features that need to be discussed here. First, nuclear spin depolarization at the fundamental resonance is on the order of 100 μs, determined by the nuclear spin-spin relaxation time. Second, for the non-fundamental NMR, the nuclear spin depolarization occurs on a quite long time scale of minutes, in good agreement with the experimental findings. Hereby, the

DD-induced spin depolarization is generally much slower than the spin depolarization caused by the transverse field component $B_{RF-tran}$ and the NQ interaction, respectively. This is basically due to its much smaller perturbation strength, which is on the order of 0.01 mT or less in GaAs [99]. From the calculated data, the local NQ perturbation is identified as the dominant factor limiting the depolarization of the observed $2f_\alpha$ NMR. Note that the NQ field mainly depolarizes the nuclear spins located in the vicinity of the donors. Thus, a finite spin diffusion time τ_{diff} has to be considered for getting the total depolarization time [225]. The values given in squared brackets in Table 7-1 indicate the expected spin diffusion time by taking into account the average distance between neighboring donors in the studied sample. The DD interaction strength is enhanced for the $(f_{\alpha 1} + f_{\alpha 2})$ resonances due to shorter inter-nucleus distance, generating a faster spin depolarization as compared to the DD-induced depolarization of the $2f_\alpha$ NMR. For the $1/2f_\alpha$ NMR, the nuclear spin depolarization time is calculated based on the average value of $B_{RF-tran}$ inside the microcoil.
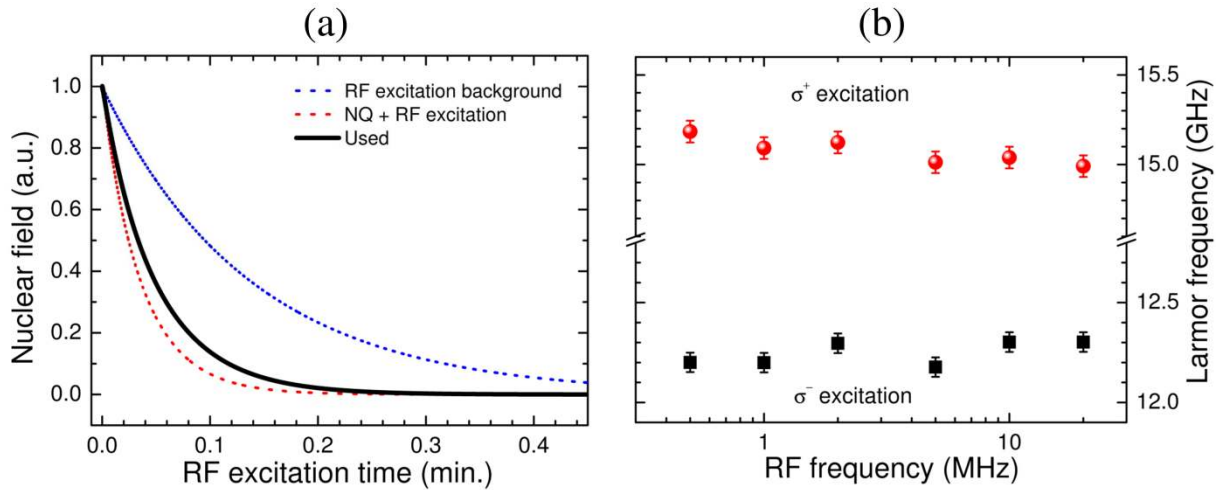
FIG 7.2-7: (a) Simulated ^{75}As nuclear field depolarization dynamics for NQ-induced $2f_{75As}$ NMR. The red dots are subject to both RF excitation and NQ interaction, while the blue dots indicate nuclear spin depolarization in absence of NQ interaction. The used nuclear field depolarization data (used) are based on the red ones by dividing the blue ones. (b) Larmor frequency dependence of RF field frequency for both σ^+- (balls) and σ^-- (squares) polarized optical excitation.

A quite good agreement between theory and experiment is obtained allowing an identification of the dominant depolarization mechanism for each NMR resonance observed in the experiment. In order to further proof the validity of the results, the change of the Larmor frequency, i.e. the Overhauser field, at NMR conditions is measured as a function of the RF field amplitude.

In FIG 7.2-9, the change of ω_L is plotted versus the square of the RF field. One should keep in mind that the nuclear spin polarization rate is only determined by the hyperfine interaction, while the spin depolarization rate strongly depends on the RF excitation power. For the ^{75}As resonance, the amplitude of nuclear spin depolarization is found to be constant over the whole RF power regime measured. This is due to the fact that independent on the RF power, the relation $\tau_{dep} \ll \tau_{pol}$ holds [66]. In contrast, in case of the non-fundamental resonances, the change of the nuclear field strongly

depends on the RF power. The nuclear spin depolarization is suppressed if the RF field amplitude is on the order of 0.01 mT or below. In this regime, τ_{dep} becomes much larger than τ_{pol} and ΔB_N becomes negligible.
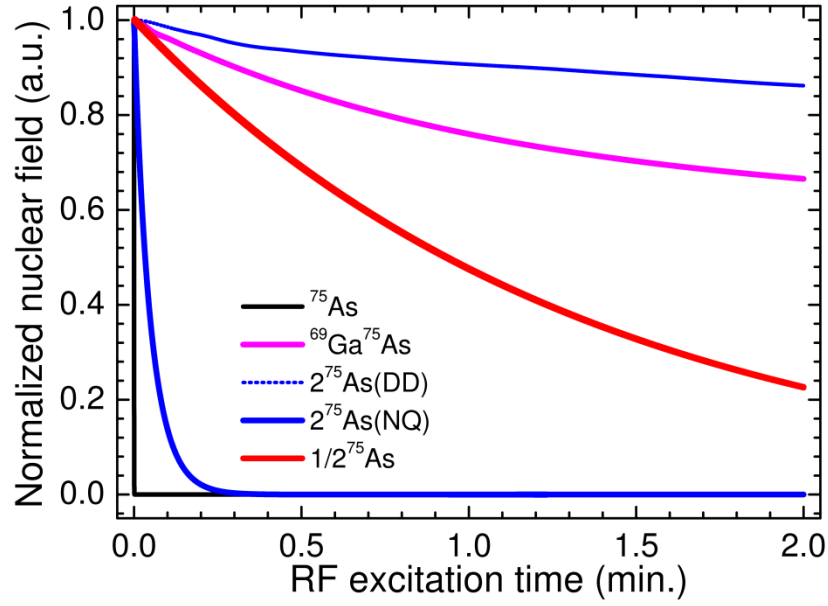
FIG 7.2-8: Numerically calculated temporal variation of the nuclear field assuming nuclear spin depolarization purely due to magnetic resonance absorption.
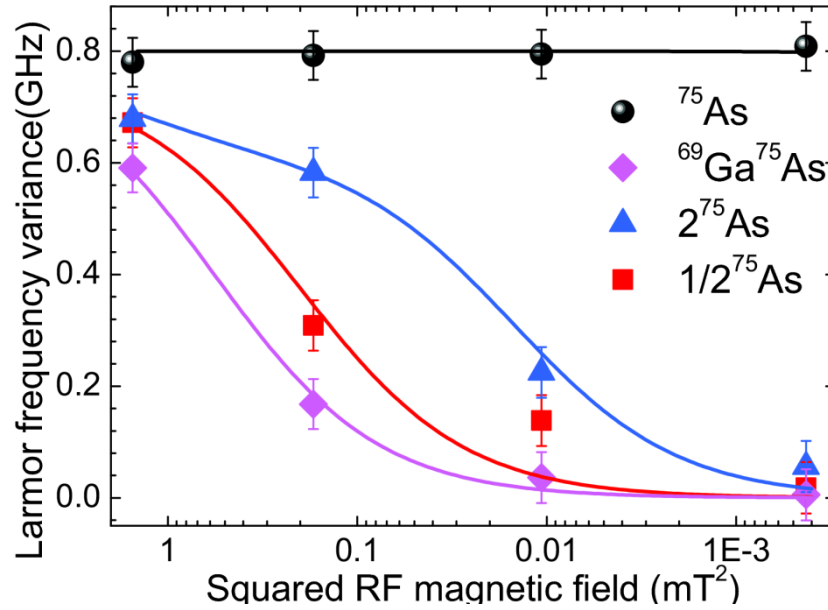

FIG 7.2-9: Larmor frequency variation under NMR conditions versus the squared RF magnetic field. Lines are guide to the eyes.

APPENDICES

A1 Standard processes for cleaning samples

1. Make sure the sample is fixed facing downwards in the tweezer, and keep it in the boiling **Choroform** solvent for 2 minutes;

2. Dry the sample by blowing Nitrogen (do not put the sample too close to the Nitrogen, a distance of about 10 cm is preferred);

3. Bring the sample into boiling **Aceton** solvent, and keep it inside for 2 minutes;

4. Keep the sample in the beaker, and make the ultrasonic pool work with a power level of 3 ~ 4 under 80 °C. Bring the beaker into the ultrasonic pool for 2 minutes;

5. Put the sample directly into boiling **Ethanol** solvent immediately, and keep it inside for 2 minutes;

6. Mount the sample on the spin-coating machine (CPS20, SEMITEC). Run the spin-coating by Programm NO.1, during which flush the sample by **Isopropanol**.

7. Dry the sample by blowing Nitrogen.

A2 Two-step EBL protocol

Material system □ GaAs   □ ZnSe   √ CdTe

Sample wafer number: W030707AI

Contact: Yuansen Chen

Technology steps	**√Signature**

► | **Sample cutting** (if required)

Size: <u>4.2 × 4.7 mm</u>

Notes:

► | **Cleaning**: A3-a protocol
- Chloroform   √
- Aceton   √
- Ethanol √

► | **First mask coating (Positive resist for bonding pads)**   **√Signature**

Thickness	PMMA
1200 nm	7% @3000 rpm

√ Baking (2 min under 160° C on Hot plate)

Notes:

► | **EBL Exposure**   **√Signature**

GDSII: omega-updated-2.csf ;

Position list:W030707AI-5.pls ;

Notes: **Exposure Protocol**

Date / Time	Mar. 16, 2009
Resist	PMMA 7%
High Voltage	20 kV
Working Distance	5 mm
Magnification	25 ×
Layout File	W030707AI-5
Structure / Layer	0
Working Area	400 (µm)
Positionlist	W030707AI-5.PLS
Writefield Size	350 × 350 µm²
Beam Current	1.304 nA
Area Step Size	0.0244 µm
Area Dwell Time	0.00109 ms
Area Dose	300 µC/cm²
Area Settling Time	5.0 ms

147

► **Development**

√ PMMA: 80 seconds, **Developer AR 600-56;**

80 seconds, **Isopropanol**

Notes:

► **Metal depostion**   √**Signature**

☐   Sputter-Coater   √   Evaporation

Coating layer(s):

Material	Thickness	Rate	Coating	Tooling factor
Cr	15 nm	~0.1 nm/s	e-beam	1.6
Pd	50 nm	~0.2 nm/s	thermal	1.8
Au	300 nm	~0.3nm/s	thermal	1.0

Notes:

► **Lift-Off**

√ *Pyrrolidon*   80 °C,   70 min;

Ultrasonic source level: _____2_____;

Time duration: _____10_____Seconds.

Notes:

► **Structure characterization**   √**Signature**

File folder of SEM pictures :

► **Second mask coating   (Positive resist for microstructures)**   √**Signature**

Thickness	PMMA
1200 nm	7% @3000 rpm

√ Baking (2 min under 160° C on the Hot plate)

Notes:

► **EBL Exposure**   **√Signature**

GDSII: omega-updated-2.csf

Position list: W030707AI-5.pls

Notes: **Exposure Protocol**

Date / Time	Mar. 18, 2009
Resist	PMMA 7%
High Voltage	20 kV
Working Distance	5 mm
Magnification	500 ×
Layout File	W030707AI-5
Structure / Layer	0
Working Area	100 (µm)
Positionlist	W030707AI-5.PLS
Writefield Size	100 × 100 µm²
Beam Current	0.013 nA
Area Step Size	0.0031 µm
Area Dwell Time	0.0003 ms
Area Dose	300 µC/cm²
Area Settling Time	5.0 ms

► **Development**

√ PMMA: 70 seconds. **Developer solvent: AR 600-56,**

                70 seconds. **Isopropanol**

Notes:

► **Metal depostion**   **√Signature**

    □   **Sputter-Coater**   **√ Evaporation**

Coating layer(s):

Material	Thickness	Rate	Coating	Tooling factor
Au	360 nm	0.2 nm / s	thermal	1.0

Notes:

► **Lift-Off**

√ Pyrrolidon   80 °C,   35 min;

Ultrasonic source level: 1   ;

Time duration: 30 Seconds.

Notes:

► **Structure characterization**   **√Signature**

File folder of SEM pictures :

A3 Representations of light polarization

The considered light wave propagates along the z-axis direction, and the electric field is written as $E = E_0 e^{i(kr-\omega t)}$, where E_0 is the complex amplitude, k is the wave vector and ω is the frequency. Due to the transverse nature of the electromagnetic wave, $E_z = 0$. By using the Jones vector, the light wave with an arbitrary polarization state can be represented as[152]:

$$\begin{pmatrix} E_x \\ E_y \end{pmatrix} = E_A \begin{pmatrix} \cos\varphi \\ e^{i\theta}\sin\varphi \end{pmatrix} \tag{A-1}$$

Here, E_x and E_y are the decomposed components of the complex amplitude of E_0 in x- and y-axis direction, respectively. $E_A = \sqrt{|E_x|^2 + |E_y|^2}$, $\varphi = \arctan(|E_y|/|E_x|)$, and θ is the relative phase between E_x and E_y. For simplicity, it is assumed $E_x = |E_x| \cdot \mathrm{Re}\{e^{i(kz-\omega t)}\}$, $E_y = |E_y| \cdot \mathrm{Re}\{e^{i(\theta+kz-\omega t)}\}$ and $|E_x| \geq |E_y|$ with $0 \leq \varphi \leq \pi/4$. The dependence on space and time has been omitted, since they are common to all expressions in the following.

The equation (A-1) represents:

(i): A linearly polarized light in the condition of $\theta = m \cdot \pi$ with m as an integer. The polarization direction is of an angle $\phi = \theta + (-1)^m \cdot \varphi$.

(ii): A circularly polarized light in the condition of $\varphi = \pi/4$ and $\theta = (m+1/2) \cdot \pi$. As a typical case, the light is right-circularly polarized for $\theta = \pi/2$ and left-circularly polarized for $\theta = -\pi/2$.

(iii): An elliptically polarized light with x-axis the major axis, in the condition of $\theta = (m+1/2) \cdot \pi$. The ellipticity $\eta = \tan(\varphi)$, and $\eta = 0$ for the special case of (ii).

(iv): An elliptically polarized light as a general case. The ellipticity $\eta = \tan(\varphi)$, and the rotation angle of the major axis with respect to x-axis is

$$\beta = \frac{1}{2}\arctan\left(\frac{2\cos\theta |E_x| \cdot |E_y|}{|E_x|^2 - |E_y|^2}\right) = \frac{1}{2}\arctan(\cos\theta \cdot \tan(2\varphi)) \tag{A-2}.$$

A schematic description is presented in FIG A3-1 with the parameters indicated. The major axis of the ellipse lies on the new x'- axis in the $x'y'$ coordinate system, which is transformed by rotating the xy coordinate with an angle β. In the $x'y'$ system, the light can be expressed as

$$\begin{pmatrix} E_x' \\ E_y' \end{pmatrix} = E_A \begin{pmatrix} \cos\varphi \\ e^{i\pi/2}\sin\varphi \end{pmatrix} \tag{A-3}$$

Applying the transformation matrix from the $x'y'$ to the xy coordinate system, the electric field in the xy system is expressed as

$$\begin{pmatrix} E_x \\ E_y \end{pmatrix} = \begin{pmatrix} \cos\beta & \sin\beta \\ -\sin\beta & \cos\beta \end{pmatrix}\begin{pmatrix} E_x' \\ E_y' \end{pmatrix} = E_A \begin{pmatrix} \cos\beta\cos\varphi + i\sin\beta\sin\varphi \\ -\sin\beta\cos\varphi + i\cos\beta\sin\varphi \end{pmatrix} \tag{A-4}$$
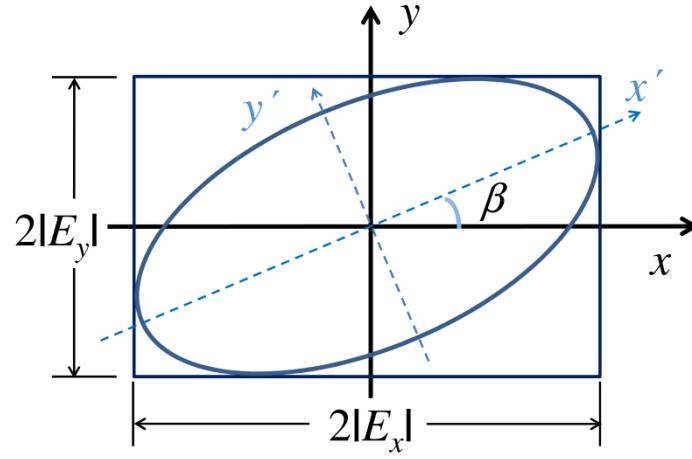
FIG A3-1: Schematic description of an elliptically polarized light.

Now the representation of the light wave in the circular system is considered. A linearly polarized wave can be treated as a superposition of a right-circularly polarized (σ^+) wave and a left-circularly polarized (σ^-) wave. Mathematically, this can be written as $E_+ = \dfrac{|E_x|}{2}(x_0 \cdot \text{Re}\{e^{i(\omega t - kz)}\} + y_0 \cdot \text{Re}\{e^{i(\pi/2 + \omega t - kz)}\})$

and $E_- = \dfrac{|E_x|}{2}(x_0 \cdot \text{Re}\{e^{i(\omega t - kz)}\} + y_0 \cdot \text{Re}\{e^{i(-\pi/2 + \omega t - kz)}\})$. The transformation matrix from the linear system based on E_x and E_y to the circular system can be found:

$$\begin{pmatrix} E_+ \\ E_- \end{pmatrix} = \frac{1}{\sqrt{2}} \begin{pmatrix} 1 & i \\ 1 & -i \end{pmatrix} \begin{pmatrix} E_x \\ E_y \end{pmatrix} \tag{A-5}$$

Then the electric field vector E can be expressed in the circular system

$$E = \begin{pmatrix} E_+ \\ E_- \end{pmatrix} = \frac{E_A}{\sqrt{2}} \begin{pmatrix} (\cos\varphi - \sin\varphi)(\cos\beta - i\sin\beta) \\ (\cos\varphi + \sin\varphi)(\cos\beta + i\sin\beta) \end{pmatrix} = \frac{E_A}{\sqrt{2}} \begin{pmatrix} (\cos\varphi - \sin\varphi)e^{-i\beta} \\ (\cos\varphi + \sin\varphi)e^{+i\beta} \end{pmatrix} \tag{A-6}$$

Here $|E_+| = \dfrac{E_A}{\sqrt{2}}(\cos\varphi - \sin\varphi) = \dfrac{1}{\sqrt{2}}(|E_x| - |E_y|)$, $|E_-| = \dfrac{E_A}{\sqrt{2}}(\cos\varphi + \sin\varphi) = \dfrac{1}{\sqrt{2}}(|E_x| + |E_y|)$, $\arg(E_+)$

$= -\beta$ and $\arg(E_-) = \beta$.

The properties of the ellipse in FIG A3-2 can be described by the following relations:

$$\beta = \frac{1}{2i} \ln \frac{E_- / |E_-|}{E_+ / |E_+|} = \frac{1}{2}(\arg(E_-) - \arg(E_+)) \tag{A-7}$$

$$\eta = \frac{|E_-| - |E_+|}{|E_-| + |E_+|} \tag{A-8}$$

$$|E_x| = \frac{1}{\sqrt{2}}(|E_+| + |E_-|) \tag{A-9}$$

$$\left|E_y\right| = \frac{1}{\sqrt{2}}\left(\left|E_-\right| - \left|E_+\right|\right) \tag{A-10}$$

In the discussion of the magneto-optics (Section 3.4), the two normal modes of the light propagation are circularly polarized, namely the σ$^+$ wave and σ$^-$ wave. The magneto-optic effects originate from the relative relations between these two modes. A schematic description is given in FIG A3-2. By changing the phase and the amplitude relation between the two circular modes, different polarization states can be formed.

(i): If the two circular modes have the same zero initial phase and the same amplitude, the composed light is linearly-polarized in x-axis direction. It is presented FIG A3-2(a);

(ii): If the two circular modes have the same non-zero initial phase and the same amplitude, the composed light is linearly-polarized in β direction. It is presented as FIG A3-2(b);

(iii): If the two circular modes have the same zero initial phase and different amplitudes, the composed light is elliptically-polarized with the major axis in x-axis direction. It is presented as FIG A3-2(c);

(iv): If the two circular modes have the same non-zero initial phase and different amplitudes, the composed light is elliptically-polarized with the major axis in β-angle direction. It is presented as FIG A3-2(d).
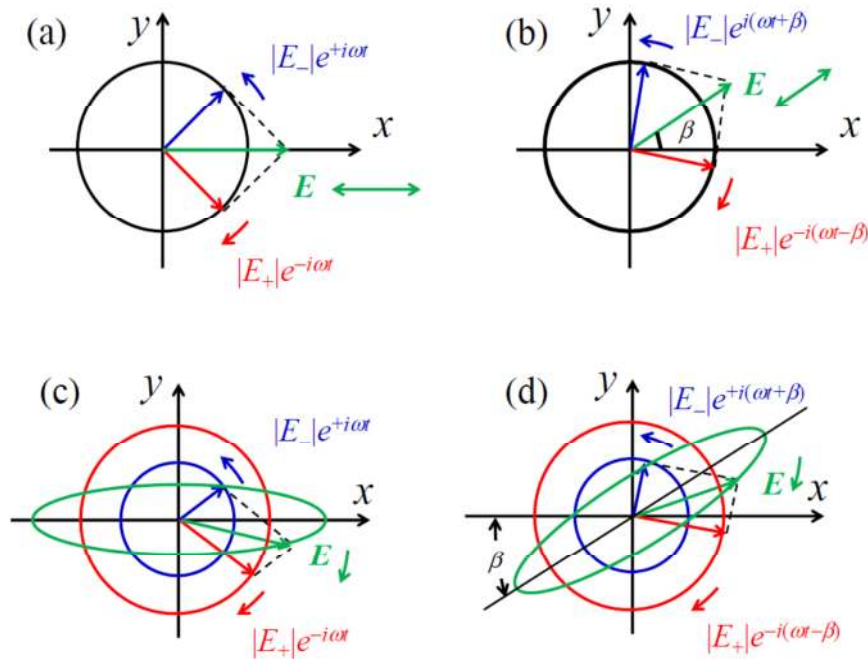
FIG A3-2: Origin of the magneto-optic effects based on the circular system. (a) A linearly-polarized light on x-axis direction: a same zero initial phase and amplitude for two circular modes; (b) A linearly-polarized light on β-angle direction: a same non-zero initial phase and a same amplitude for two circular modes; (c) A elliptically-polarized light of the major axis on x-axis direction: a same zero initial phase but different amplitudes for two circular modes; (d) An elliptically-polarized light of the major axis on β-angle direction: a same non-zero initial phases and different amplitudes for two circular modes.

BIBLIOGRAPHY

[1] http://www.itrs.net/.

[2] G. E. Moore, Electronics Magazine **38** (1965).

[3] W. Gerlach, and O. Stern, Zeitschrift für Physik **9**, 353 (1922).

[4] P. A. M. Dirac, Proc. R. Soc. Lond. **A117**, 610 (1928).

[5] P. A. M. Dirac, Proc. R. Soc. Lond. **A118**, 351 (1928).

[6] C. Kittel, *Introduction to Solid State Physics (8th edition)* (John Wiley & Sons, Inc., 2005).

[7] G. A. Prinz, Science **282**, 1660 (1998).

[8] I. Zutic, J. Fabian, and S. D. Sarma, Rev. Mod. Phys. **76**, 323 (2004).

[9] M. N. Baibich, J. M. Broto, A. Fert, F. N. V. Dau, F. Petroff, P. Eitenne, G. Creuzet, A. Friederich, and J. Chazelas, Phys. Rev. Lett. **61**, 2472 (1988).

[10] G. Binasch, P. Grünberg, F. Saurenbach, and W. Zinn, Phys. Rev. B **39**, R4828 (1989).

[11] B. Dieny, V. S. Speriosu, S. S. P. Parkin, B. A. Gurney, D. R. Wilhoit, and D. Mauri, Phys. Rev. B **43**, R1297 (1991).

[12] H. Coufal, L. Dhar, and C. D. Mee, MRS Bulletin **31**, 374 (2006).

[13] C. Tsang, R. E. Fontana, T. Lin, and D. E. Heim, IEEE Transactions on Magnetics **30**, 3801 (1994).

[14] J. Daughton, J. Brown, E. Chen, R. Beech, A. Pohm, and W. Kude, IEEE Transactions on Magnetics **30**, 4608 (1994).

[15] M. Julliere, Phys. Lett. **54A**, 225 (1975).

[16] J. S. Moodera, L. R. Kinder, T. M. Wong, and R. Meservey, Phys. Rev. Lett. **74**, 3273 (1995).

[17] http://www.mram-info.com/history.

[18] K. Inomata, in *Giant magneto-resistance devices, volume 40 of Springer series in surface sciences*, edited by E. Hirota, H. Sakakima, and K. Inomata (Springer, Berlin, 2002).

[19] S. A. Wolf, D. D. Awschalom, R. A. Buhrman, J. M. Daughton, S. v. Molnar, M. L. Roukes, A. Y. Chtchelkanova, and D. M. Treger, Science **294**, 1488 (2001).

[20] D. Awschalom, and M. Flatté, Nat Phys **3**, 153 (2007).

[21] F. Meier, and B. P. Zakharchenya, *Optical Orientation* (North-Holland, New York, 1984).

[22] P. R. Hammar, B. R. Bennett, M. J. Yang, and M. Johnson, Phys. Rev. Lett. **83**, 203 (1999).

[23] R. Fiederling, M. Keim, G. Reuscher, W. Ossau, G. Schmidt, A. Waag, and L. W. Molenkamp, Nature **402**, 787 (1999).

[24] D. Hägele, M. Oestreich, W. W. Rühle, N. Nestle, and K. Eberl, Appl. Phys. Lett. **73**, 1580 (1998).

[25] J. M. Kikkawa, and D. D. Awschalom, Nature **397**, 139 (1999).

[26] H. Ohno, D. Chiba, F. Matsukura, T. Omiya, E. Abe, T. Dietl, Y. Ohno, and K. Ohtani, Nature **408**, 944 (2000).

[27] S. Datta, and B. Das, Appl. Phys. Lett. **56**, 665 (1989).

[28] M. Sakuma, K. Hyomi, I. Souma, A. Murayama, and Y. Oka, J. Appl. Phys. **94**, 6423 (2003).

[29] A. Murayama, and M. Sakuma, Appl. Phys. Lett. **88**, 122504 (2006).

[30] L. Meier, G. Salis, C. Ellenberger, K. Ensslin, and E. Gini, Appl. Phys. Lett. **88**, 172501 (2006).

[31] S. Halm, G. Bacher, E. Schuster, W. Keune, M. Sperl, J. Puls, and F. Henneberger, Appl. Phys. Lett. **90**, 051916 (2007).

[32] A. Y. Elezzabi, M. R. Freeman, and M. Johnson, Phys. Rev. Lett. **77**, 3220 (1996).

[33] M. Goryca, D. Ferrand, P. Kossacki, M. Nawrocki, W. Pacuski, W. Maślana, S. Tatarenko, and J. Cibert, Phys. Status Solidi B **243**, 882 (2006).

[34] R. Hanson, L. P. Kouwenhoven, J. R. Petta, S. Tarucha, and L. M. K. Vandersypen, Reviews of Modern Physics **79**, 1217 (2007).

[35] L. Meier, G. Salis, I. Shorubalko, E. Gini, S. Schön, and K. Ensslin, Nature Physics **3**, 650 (2007).

[36] J. A. Gupta, R. Knobel, N. Samarth, and D. D. Awschalom, Science **292**, 2458 (2001).

[37] A. Greilich, D. R. Yakovlev, A. Shabaev, A. L. Efros, I. A. Yugova, R. Oulton, V. Stavarache, D. Reuter, A. Wieck, and M. Bayer, Science **313**, 341 (2006).

[38] F. H. L. Koppens, C. Buizert, K. J. Tielrooij, I. T. Vink, K. C. Nowack, T. Meunier, L. P. Kouwenhoven, and L. M. K. Vandersypen, Nature **442**, 766 (2006).

[39] G. D. Fuchs, V. V. Dobrovitski, D. M. Toyli, F. J. Heremans, and D. D. Awschalom, Science **326**, 1520 (2009).

[40] G. D. Fuchs, V. V. Dobrovitski, D. M. Toyli, F. J. Heremans, C. D.Weis, T. Schenkel, and D. D. Awschalom, Nature Physics **6**, 668 (2010).

[41] T. Dietl, D. D. Awaschalom, M. Kaminska, and H. Ohno, *Spintronics* (Elsevier, 2008), Vol. 82.

[42] J. Kossut, and J. A. Gaj, *Introduction to the Physics of Diluted Magnetic Semiconductors* (Springer, 2010), Vol. 144.

[43] D. D. Awschalom, D. Loss, and N. Samarth, *Semiconductor Spintronics and Quantum Computation* (Springer-Verlag, Berlin, 2002).

[44] J. K. Furdyna, and J. Kossut, *Diluted Magnetic Semiconductors* (Academic Press, 1988), Vol. 25.

[45] L. Besombes, Y. Leger, L. Maingault, D. Ferrand, H. Mariette, and J. Cibert, Phys. Rev. Lett. **93**, 207403 (2004).

[46] D. A. Bussian, S. A. Crooker, M. Yin, M. Brynda, A. L. Efros, and V. I. Klimov, Nature Materials **8**, 35 (2008).

[47] R. Beaulac, P. I. Archer, S. T. Ochsenbein, and D. R. Gamelin, Advanced Functional Materials **18**, 3873 (2008).

[48] H. Boukari, P. Kossacki, M. Bertolini, D. Ferrand, J. Cibert, S. Tatarenko, A. Wasiela, J. A. Gaj, and T. Dietl, Phys. Rev. Lett. **88**, 207204 (2002).

[49] T. Dietl, A. Haury, and Y. M. d'Aubigné, Phys. Rev. B **55**, R3347 (1997).

[50] T. Dietl, H. Ohno, F. Matsukura, J. Cibert, and D. Ferrand, Science **287**, 1019 (2000).

[51] H. Ohno, H. Munekata, T. Penney, S. v. Molnár, and L. L. Chang, Phys. Rev. Lett. **68**, 2664 (1992).

[52] A. Haury, A. Wasiela, A. Arnoult, J. Cibert, S. Tatarenko, T. Dietl, and Y. M. d'Aubigné, Phys. Rev. Lett. **79**, 511 (1997).

[53] H. Boukari, F. Perez, D. Ferrand, P. Kossacki, B. Jusserand, and J. Cibert, Phys. Rev. B **73**, 115320 (2006).

[54] T. Dietl, Nature Materials **9**, 965 (2010).

[55] T. Dietl, P. Peyla, W. Grieshaber, and Y. M. d'Aubigné, Phys. Rev. Lett. **74**, 474 (1995).

[56] M. Goryca, D. Ferrand, P. Kossacki, M. Nawrocki, W. Pacuski, W. Maślana, J. A. Gaj, S. Tatarenko, J. Cibert, T. Wojtowicz, and G. Karczewski, Phys. Rev. Lett. **102**, 046408 (2009).

[57] T. Strutz, A. M. Witowski, and P. Wyder, Phys. Rev. Lett. **68**, 3912 (1992).

[58] D. Scalbert, Phys. Status Solidi B **193**, 189 (1996).

[59] A. A. Maksimov, D. R. Yakovlev, J. Debus, I. I. Tartakovskii, A. Waag, G. Karczewski, T. Wojtowicz, J. Kossut, and M. Bayer, Phys. Rev. B **82**, 035211 (2010).

[60] S. A. Crooker, D. D. Awschalom, J. J. Baumberg, F. Flack, and N. Samarth, Phys. Rev. B **56**, 7574 (1997).

[61] M. Scheibner, T. A. Kennedy, L. Worschech, A. Forchel, G. Bacher, T. Slobodskyy, G. Schmidt, and L. W. Molenkamp, Phys. Rev. B **73**, 081308(R) (2006).

[62] S. Halm, P. E. Hohage, J. Nannen, G. Bacher, J. Puls, and F. Henneberger, Phys. Rev. B **77**, 121303(R) (2008).

[63] B. König, I. A. Merkulov, D. R. Yakovlev, W. Ossau, S. M. Ryabchenko, M. Kutrowski, T. Wojtowicz, G. Karczewski, and J. Kossut, Phys. Rev. B **61**, 16870 (2000).

[64] A. V. Scherbakov, D. R. Yakovlev, A. V. Akimov, I. A. Merkulov, B. König, W. Ossau, L. W. Molenkamp, T. Wojtowicz, G. Karczewski, G. Cywinski, and J. Kossut, Phys. Rev. B **64**, 155205 (2001).

[65] A. V. Scherbakov, A. V. Akimov, D. R. Yakovlev, W. Ossau, L. W. Molenkamp, S. Tatarenko, and J. Cibert, Solid State Communications **120**, 17 (2001).

[66] A. Abragam, *The Principles of of nuclear magnetism* (Oxford University Press, Oxford, 1961).

[67] B. E. Kane, Nature (London) **393**, 133 (1998).

[68] T. D. Ladd, J. R. Goldman, F. Yamaguchi, Y. Yamamoto, E. Abe, and K. M. Itoh, Phys. Rev. Lett. **89**, 017901 (2002).

[69] A. W. Overhauser, Phys. Rev. **92**, 411 (1953).

[70] G. Lampel, Phys. Rev. Lett. **20**, 491 (1968).

[71] W. G. Clark, and G. Feher, Phys. Rev. Lett. **10**, 134 (1963).

[72] S. E. Hayes, S. Mui, and K. Ramaswamy, J. Chem. Phys. **128**, 052203 (2008).

[73] F. Henneberger, and O. Benson, *Semiconductor Quantum Bits* (Pan Stanford Publishing, 2009).

[74] S. W. Brown, T. A. Kennedy, D. Gammon, and E. S. Snow, Phys. Rev. B **54**, R17339 (1996).

[75] B. Urbaszek, P.-F. Braun, T. Amand, O. Krebs, T. Belhadj, A. Lemaítre, P. Voisin, and X. Marie, Phys. Rev. B **76**, 201301(R) (2007).

[76] P. Maletinsky, C. W. Lai, A. Badolato, and A. Imamoglu, Phys. Rev. B **75**, 035409 (2007).

[77] D. Paget, G. Lampel, and B. Sapoval, Phys. Rev. B **15**, 5780 (1977).

[78] W. Farah, M. Dyakonov, D. Scalberg, and W. Knap, Phys. Rev. B **57**, 4713 (1998).

[79] J. Strand, X. Lou, C. Adelmann, B. D. Schultz, A. F. Isakovic, C. J. Palmstrøm, and P. A. Crowell, Phys. Rev. B **72**, 155308 (2005).

[80] I. A. Akimov, D. H. Feng, and F. Henneberger, Phys. Rev. Lett. **97**, 056602 (2006).

[81] C. W. Lai, P. Maletinsky, A. Badolato, and A. Imamoglu, Phys. Rev. Lett. **96**, 167403 (2006).

[82] D. H. Feng, I. A. Akimov, and F. Henneberger, Phys. Rev. Lett. **99**, 036604 (2007).

[83] C. Testelin, B. Eble, F. Bernardot, G. Karczewski, and M. Chamarro, Phys. Rev. B **77**, 235306 (2008).

[84] V. L. Berkovits, A. K. Ekimov, and V. I. Safarov, Sov. Phys. -JETP **38**, 169 (1974).

[85] S. K. Buratto, J. Y. Hwang, N. D. Kurur, D. N. Shykind, and D. P. Weitekamp, Bulletin of Magnetic Resonance **15**, 190 (1993).

[86] T. Machida, T. Yamazaki, K. Ikushima, and S. Komiyama, Appl. Phys. Lett. **82**, 409 (2003).

[87] M. Kawamura, T. Yamashita, H. Takahashi, S. Masubuchi, Y. Hashimoto, S. Katsumoto, and T. Machida, Appl. Phys. Lett. **96**, 031102 (2010).

[88] D. Gammon, S. W. Brown, E. S. Snow, T. A. Kennedy, D. S. Katzer, and D. Park, Science **277**, 85 (1997).

[89] H. Sanada, Y. Kondo, S. Matsuzaka, K. Morita, C. Y. Hu, Y. Ohno, and H. Ohno, Phys. Rev. Lett. **96**, 067602 (2006).

[90] G. Salis, D. D. Awaschalom, Y. Ohno, and H. Ohno, Phys. Rev. B **64**, 195304 (2001).

[91] M. Poggio, G. M. Steeves, R. C. Myers, Y. Kato, A. C. Gossard, and D. D. Awschalom, Phys. Rev. Lett. **91**, 207602 (2003).

[92] M. Poggio, and D. D. Awschalom, Appl. Phys. Lett. **86**, 182103 (2005).

[93] J. M. Kikkawa, and D. D. Awschalom, Phys. Rev. Lett. **80**, 4313 (1998).

[94] J. M. Kikkawa, and D. Awschalom, Science **287**, 473 (2000).

[95] R. I. Dzhioev, and V. L. Korenev, Phys. Rev. Lett. **99**, 037401 (2007).

[96] P. Maletinsky, M. Kroner, and A. Imamoglu, Nature Physics **5**, 407 (2009).

[97] O. Krebs, P. Maletinsky, T. Amend, B. Urbaszek, A. Lemaître, P. Voisin, X. Marie, and A. Imamoglu, Phys. Rev. Lett. **104**, 056603 (2010).

[98] M. N. Makhonin, E. A. Chekhovich, P. Senellart, A. Lemaitre, M. S. Skolnick, and A. I. Tarkakovskii, Phys. Rev. B **82**, 161309(R) (2010).

[99] V. K. Kalevich, V. D. Kul'kov, I. A. Merkulov, and V. G. Fleisher, Sov. Phys. Solid State **24**, 1195 (1982).

[100] V. A. Novikov, and V. G. Fleisher, Sov. Phys. -JETP **47**, 539 (1978).

[101] L. Vegard, Zeitschrift für Physik **5**, 17 (1921).

[102] E. Dynowska, E. Janik, J. Bak-Misiuk, J. Domagala, T. Wojtowicz, and J. Kossut, J. Alloys and Compounds **286**, 276 (1999).

[103] O. Madelung, *Semiconductors: Data Handbook* (Springer, Berlin, 2004).

[104] P. Y. Yu, and M. Cardona, *Fundamentals of Semiconductors: Physics and Materials Properties (Second Edition)* (Springer, 1999).

[105] S. L. Chuang, *Physics of optoelectronic devices* (John Wiley & Sons, Inc., 1995).

[106] J. R. Chelikowsky, and M. L. Cohen, Phys. Rev. B **14**, 556 (1976).

[107] J. K. Furdyna, J. Appl. Phys. **64**, R29 (1988).

[108] A. Abragam, and B. Bleaney, *Electronic paramagnetic resonance of transition ions* (Clarendon, Oxford, 1970).

[109] W. Maślana, Ph.D dissertation, University of Warsau (2007).

[110] Landolt-Börnstein, *Numerical data and functional relationships in science and technology* (Springer Verlag, Berlin, 1982), Vol. 17b.

[111] J. M. Hartmann, J. Cibert, F. Kany, H. Mariette, M. Charleux, P. Alleyson, R. Langer, and G. Feuillet, J. Appl. Phys. **80**, 6257 (1996).

[112] B. Kuhn-Heinrich, W. Ossau, H. Heinke, F. Fischer, T. Litz, A. Waag, and G. Landwehr, Appl. Phys. Lett. **63**, 2932 (1993).

[113] J. H. Davies, *The Physics of Low-Dimensional Semiconductors* (Cambridge University Press, 1998).

[114] L. S. Dang, G. Neu, and R. Romestain, Solid State Communications **44**, 1187 (1982).

[115] C. R. Li, B. K. Tanner, D. E. Ashenford, J. H. C. Hogg, and B. Lunn, Semicond. Sci. Technol. **13**, 746 (1998).

[116] G. Fishman, Phys. Rev. B **52**, 11132 (1995).

[117] J. Shah, *Ultrafast Spectroscopy of Semiconductors and Semiconductor Nanostructures* (Springer, 1999).

[118] U. Rössler, and H.-R. Trebin, Phys. Rev. B **23**, 1961 (1981).

[119] M. Nawrocki, and A. Twardowski, Phys. Status Solidi B **97**, K61 (1980).

[120] M. K. Kneip, Ph.D dissertation, Dortmund University of Technology (2008).

[121] J. A. Gaj, W. Grieshaber, C. Bodin-Deshayes, J. Cibert, G. Feuillet, Y. M. d'Aubigné, and A. Wasiela, Phys. Rev. B **50**, 5512 (1994).

[122] M. A. Lampert, Phys. Rev. Lett. **1**, 450 (1958).

[123] K. Kheng, R. T. Cox, Y. M. d'Aubigné, F. Bassani, K. Saminadayar, and S. Tatarenko, Phys. Rev. Lett. **71**, 1752 (1993).

[124] P. Kossacki, J. Cibert, D. Ferrand, Y. M. d'Aubigné, A. Arnoult, A. Wasiela, and S. Tatarenko, Phys. Rev. B **60**, 16018 (1999).

[125] P. Kossacki, J. Phys.: Condens. Matter **15**, R471 (2003).

[126]   J. A. Gaj, R. Planel, and G. Fishman, Solid State Communications **29**, 425 (1978).

[127]   J. M. Fatah, T. Piorek, P. Harrison, T. Stirner, and W. E. Hagston, Phys. Rev. B **49**, 10341 (1994).

[128]   W. J. Ossau, and B. Kuhn-Heinrich, Physica B **184**, 422 (1993).

[129]   W. J. Ossau, B. Kuhn-Heinrich, A. Waag, and G. Landwehr, J. Crystal Growth **159**, 1046 (1996).

[130]   B. E. Larson, K. C. Hass, H. Ehrenreich, and A. E. Carlsson, Solid State Communications **56**, 347 (1985).

[131]   B. E. Larson, K. C. Hass, H. Ehrenreich, and A. E. Carlsson, Phys. Rev. B **37**, 4137 (1988).

[132]   R. L. Aggarwal, S. N. Jasperson, P. Becla, and R. R. Galazka, Phys. Rev. B **32**, 5132 (1985).

[133]   X. Wang, D. Heiman, S. Foner, and P. Becla, Phys. Rev. B **41**, 1135 (1990).

[134]   A.K.Bhattacharjee, G. Fishman, and B. Coqblin, Physica B+C **117-118**, 449 (1983).

[135]   A. A. Kiselev, E. L. Ivchenko, A. A. Sirenko, T. Ruf, M. Cardona, D. R. Yakovlev, W. Ossau, A. Waag, and G. Landwehr, J. Crystal Growth **184/185**, 831 (1998).

[136]   M. R. Freeman, D. D. Awschalom, J. M. Hong, and L. L. Chang, Phys. Rev. Lett. **64**, 2430 (1990).

[137]   G. Bacher, A. A. Maksimov, A. Mcdonald, H. Schömig, M. K. Welsch, V. D. Kulakovskii, A. Forchel, C. R. Becker, L. W. Molenkamp, and G. Landwehr, Phys. Status Solidi B **224**, 573 (2001).

[138]   P. Kossacki, H. Boukari, M. Bertolini, D. Ferrand, J. Cibert, S. Tatarenko, J. A. Gaj, B. Deveaud, V. Ciulin, and M. Potemski, Phys. Rev. B **70**, 195337 (2004).

[139]   K. Mackay, M. Bonfim, D. Givord, and A. Fontaine, J. Appl. Phys. **87**, 1996 (2000).

[140]   K. Yang, *Laser principle and technology (in Chinese)* (Huazhong university of science and technology, 2000).

[141]   Olympus Corporations, http://www.olympusmicro.com/primer/anatomy/infinityintro.html.

[142]   J. M. Lerner, and A. Thevenon, http://www.horiba.com/us/en/scientific/products/optics.

[143]   S. Halm, Ph.D dissertation, University of Duisburg-Essen (2009).

[144]   W. Becker, *The bh TCSPC Handbook* (Becker&Hickl GmbH, Berlin, 2006).

[145]   D. D. Awschalom, and N. Samarth, Chapter 5 in *Semiconductor Spintronics and Quantum Computation*, edited by D. D. Awschalom, D. Loss, and N. Samarth, (Springer-Verlag, Berlin, 2002).

[146]   E. Beaurepaire, J.-C. Merle, A. Daunois, and J.-Y. Bigot, Phys. Rev. Lett. **76**, 4250 (1996).

[147]   M. l. Dyakonov, *Spin Physics in Semiconductors* (Springer-Verlag, Heidelberg, 2008).

[148]   M. Faraday, Philos. Trans. R. Soc. London **136**, 1 (1846).

[149]   W. Voigt, Nachr. Kgl. Ges. Wiss. Göttingen Math.-Phys. Kl. **4**, 355 (1898).

[150]   A. Cotton, and H. Mouton, Ann. Chim. Phys. (8.) **11**, 145 (1907).

[151]   J. Kerr, Philos. Mag. **3**, 321 (1877).

[152]   M. Born, and E. Wolf, *Principles of Optics* 2003).

[153]   P. E. Hohage, Ph.D dissertation, University of Duisburg-Essen (2012).

[154]   M. Heidkamp, Ph.D dissertation, RWTH Aachen (2004).

[155]   C.-Y. You, and S.-C. Shin, Appl. Phys. Lett. **69**, 1315 (1996).

[156]   C.-Y. You, and S.-C. Shin, J. Appl. Phys. **84**, 541 (1998).

[157]   L. D. Landau, and M. F. Lifshitz, *Electrodynamics of continuous media* (Pergamon, London, 1960).

[158]   Z. Q. Qiu, and S. D. Bader, Rev. Sci. Instrum. **71**, 1243 (2000).

[159]   L. Vina, L. Munoz, E. Perez, J. Fernandez-Rossier, C. Tejedor, and K. Ploog, Phys. Rev. B **54**, R8317 (1996).

[160]   L. Meier, Ph.D dissertation, ETH Zürich (2007).

[161]   S. Sugano, and N. Kojima, *Magneto-Optics* (Springer, Heidelberg, 2000).

[162]   M. D. Sturge, Phys. Rev. **127**, 768 (1962).

[163]   P. E. Hohage, G. Bacher, D. Reuter, and A. D. Wieck, Appl. Phys. Lett. **89**, 231101 (2006).

[164]   D. E. Aspnes, and A. A. Studna, Phys. Rev. B **27**, 985 (1983).

[165]   M. Tanaka, H. Shimuzu, and M. Miyamura, J. Crystal Growth **227-228**, 839 (2001).

[166]   Z. Chen, R. Bratschitsch, and S. T. Cundiff, Opt. Lett. **30**, 2320 (2005).

[167]   A. V. Kimel, F. Bentivegna, V. N. Gridenev, V. V. Pavlov, R. V. Pisarev, and T. Rasing, Phys. Rev. B **63**, 235201 (2001).

[168]   D. Paget, Phys. Rev. B **24**, 3776 (1981).

[169]   W. Maślana, P. Kossacki, M. Bertolini, H. Boukari, D. Ferrand, S. Tatarenko, J. Cibert, and J. A. Gaj, Appl. Phys. Lett. **82**, 1875 (2003).

[170]   J. Yang, Y. Zidon, and Y. Shapira, J. Appl. Phys. **91**, 703 (2002).

[171]   W.Grieshaber, C. Bodin, J. Cibert, J. Gaj, Y. M. d'Aubigné, A. Wasiela, and G. Feuillet, Appl. Phys. Lett. **65**, 1287 (1994).

[172]   R. Brazis, and J. Kossut, Solid State Communications **122**, 73 (2002).

[173]   V. P. Varshni, Physica **34**, 149 (1967).

[174]   B. S. Sundersheshu, and T. Kendelewicz, Phys. Status Solidi A **69**, 467 (1982).

[175]   G. Bacher, A. A. Maksimov, H. Schömig, V. D. Kulakovskii, M. K. Welsch, A. Forchel, P. S. Dorozhkin, A. V. Chernenko, S. Lee, M. Dobrowolska, and J. K. Furdyna, Phys. Rev. Lett. **89**, 127201 (2002).

[176]   G. Mackh, W. Ossau, D. R. Yakovlev, A. Wagg, G. Landweher, R. Hellmann, and E. O. Göbel, Phys. Rev. B **49**, 10248 (1994).

[177]   K. Mitchell, A. L. Fahrenbruch, and R. H. Bube, J. Appl. Phys. **48**, 829 (1977).

[178]   D. Keller, D. R. Yakovlev, B. König, W. Ossau, T. Gruber, A. Wagg, L. W. Molenkamp, and A. V. Scherbakov, Phys. Rev. B **65**, 035313 (2001).

[179]   G. Salis, Y. Kato, K. Ensslin, D. C. Driscoll, A. C. Gossard, and D. D. Awschalom, Nature **414**, 619 (2001).

[180]   C. D. Stanciu, F. Hansteen, A. V. Kimel, A. Kirilyuk, A. Tsukamoto, A. Itoh, and T. Rasing, Phys. Rev. Lett. **99**, 047601 (2007).

[181]   P. Redlinski, T. Wojtowicz, T. G. Rappoport, A. Libál, J. K. Furdyna, and B. Jankó, Phys. Rev. B **72**, 085209 (2005).

[182]   S. Halm, P. E. Hohage, J. Nannen, E. Neshataeva, L. Schneider, G. Bacher, Y. Fan, J. Puls, and F. Henneberger, J. Phys. D: Applied Physics **41**, 164007 (2008).

[183]   Y.-H. Fan, J. Puls, S. Halm, S. Sadofev, F. Seifert, E. Schuster, G. Bacher, W. Keune, and F. Henneberger, Appl. Phys. Lett. **95**, 223502 (2009).

[184]   A. V. Akimov, A. V. Scherbakov, and D. R. Yakovlev, in *Handbook of Semiconductor Nanostructures and Nanodevices*, edited by A. A. Balandin, and K. L. Wang (American Scientific Publishers, 2006), pp. 45

[185]   A. V. Akimov, A. V. Scherbakov, A. L. Zhmodikov, V. P. Kochereshko, D. R. Yakovlev, W. Ossau, G. Landwehr, T. Wojtowicz, G. Karczewski, and J. Kossut, Phys. Rev. B **56**, 12100 (1997).

[186]   A. V. Scherbakov, A. V. Akimov, D. R. Yakovlev, W. Ossau, A. Waag, G. Landwehr, T. Wojtowicz, G. Karczewski, and J. Kossut, Phys. Rev. B **60**, 5609 (1999).

[187]   A. V. Akimov, D. R. Yakovlev, A. V. Scherbakov, and I. A. Merkulov, J. Luminescence **125**, 1 (2007).

[188]   A. V. Scherbakov, A. V. Akimov, D. R. Yakovlev, W. Ossau, G. Landwehr, T. Wojtowicz, G. Karczewski, and J. Kossut, Phys. Rev. B **62**, R10641 (2000).

[189]   X.-J. Wang, W. M. Dennis, and W. M. Yen, Phys. Rev. Lett. **67**, 2807 (1991).

[190]   W. M. Dennis, and W. M. Yen, J. Luminescence **125**, 60 (2007).

[191]   M. K. Kneip, D. R. Yakovlev, M. Bayer, A. A. Maksimov, I. I. Tartakovskii, D. Keller, W. Ossau, L. W. Molenkamp, and A. Waag, Phys. Rev. B **73**, 035306 (2006).

[192]   M. K. Kneip, D. R. Yakovlev, M. Bayer, A. A. Maksimov, I. I. Tartakovskii, D. Keller, W. Ossau, L. W. Molenkamp, and A. Waag, Phys. Rev. B **73**, 045305 (2006).

[193]   Y. S. Chen, S. Halm, E. Neshataeva, T. Kümmell, G. Bacher, M. Wiater, T. Wojtowicz, and G. Karczewski, Appl. Phys. Lett. **93**, 141902 (2008).

[194]   J. Lambe, and C. Kikuchi, Phys. Rev. **119**, 1256 (1960).

[195]   M. Qazzaz, G. Yang, S. H. Xin, L. Montes, H. Luo, and J. K. Furdyna, Solid State Communications **96**, 405 (1995).

[196]   A. Kiel, and W. B. Mims, Phys. Rev. B **5**, 803 (1972).

[197]   E. R. Feher, Phys. Rev. **136**, A145 (1964).

[198]   M. T. Causa, M. Tovar, S. B. Oseroff, R. Calvo, and W. Giriat, Phys. Lett. **77A**, 473 (1980).

[199]   D. Ferrand, J. Cibert, A. Wasiela, C. Bourgognon, S. Tatarenko, G. Fishman, T. Andrearczyk, J. Jaroszynski, S. Kolesnik, T. Dietl, B. Barbara, and D. Dufeu, Phys. Rev. B **63**, 085201 (2001).

[200]   S. Koshihara, A. Oiwa, M. Hirasawa, S. Katsumoto, Y. Iyo, C. Urano, H. Takagi, H. Munekata, Phys. Rev. Lett. **78**, 4617 (1997).

[201]   P. Kossacki, A. Kudelski, J. A. Gaj, J. Cibert, S. Tatarenko, D. Ferrand, A. Wasiela, B. Deveaud, and T. Dietl, Physica E **12**, 344 (2002).

[202]   V. D. Kulakovskii, M. G. Tyazhlov, A. I. Filin, D. R. Yakovlev, A. Waag, and G. Landwehr, Phys. Rev. B **54**, R8333 (1996).

[203]   J. Puls, A. Hundt, H. Thomas, and F. Henneberger, Phys. Status Solidi B **241**, 568 (2004).

[204]   D. Scalbert, J. Cernogora, and C. Benoit, and A. La. Guillaume, Solid State Communications **66**, 571 (1988).

[205]   S. A. Crooker, D. D. Awschalom, J. J. Baumberg, F. Flack, and N. Samarth, Phys. Rev. Lett. **77**, 2814 (1996).

[206]   M. K. Kneip, D. R. Yakovlev, M. Bayer, T. Slobodskyy, G. Schmidt, and L. W. Molenkamp, Appl. Phys. Lett. **88**, 212105 (2006).

[207]   J. Kobak, M. Goryca, P. Kossacki, A. Golnik, G. Karczewski, T. Wojtowicz, and J. A. Gaj, Acta Physica Polonica A **116**, 907 (2009).

[208]   M. Goryca, Proc. of SPIE **7398**, 739807 (2009).

[209]   M. Goryca, P. Kossacki, M. Nawrocki, P. Wojnar, and G. Karczewski, J. Korean Physical Society **53**, 2963 (2008).

[210]   H.-P. Breuer, and F. Petruccione, *The theory of open quantum systems* (Oxoford University Press, 2007).

[211]   A. W. Overhauser, Phys. Rev. **89**, 689 (1953).

[212]   J. Strand, B. D. Schultz, A. F. Isakovic, C. J. Palmstrøm, and P. A. Crowell, Phys. Rev. Lett. **91**, 036602 (2003).

[213]   C. Awo-Affouda, O. M. J. v. t. Erve, G. Kioseoglou, A. T. Hanbicki, M. Holub, C. H. Li, and B. T. Jonker, Appl. Phys. Lett. **94** (2009).

[214]   G. Salis, A. Fuhrer, and S. F. Alvarado, Phys. Rev. B **80**, 115332 (2009).

[215]   M. K. Chan, Q. O. Hu, J. Zhang, T. Kondo, C. J. Palmstrøm, and P. A. Crowell, Phys. Rev. B **80**, 161206 (R) (2009).

[216]   B. Eble, O. Krebs, A. Lemaitre, K. Kowalik, A. Kudelski, P. Voisin, B. Urbaszek, X. Marie, and T. Amand, Phys. Rev. B **74**, 081306(R) (2006).

[217]   R. K. Kawakami, Y. Kato, M. Hanson, I. Malajovich, J. M. Stephens, E. Johnston-Halperin, G. Salis, A. C. Gossard, and D. D. Awschalom, Science **294**, 131 (2001).

[218]   M. I. D'yakonov, and V. I. Perel', Sov. Phys. -JETP **38**, 177 (1974).

[219]   C. Weisbuch, and C. Hermann, Phys. Rev. B **15**, 816 (1977).

[220]   B. Heaton, J. S. Colton, D. N. Jenson, M. J. Johnson, and A. S. Bracker, Solid State Communications **150**, 244 (2010).

[221]   Y. S. Chen, J. Huang, D. Reuter, A. Ludwig, A. D. Wieck, and G. Bacher, J. Appl. Phys. **109**, 071101 (2011).

[222]   Y. S. Chen, J. Huang, D. Reuter, A. Ludwig, A. D. Wieck, and G. Bacher, Appl. Phys. Lett. **98**, 081911 (2011).

[223]   P. Hohage, J. Nannen, S. Halm, and G. Bacher, Advances in Solid State Physics **48**, 183 (2009).

[224]   V. L. Berkovits, C. Hermann, G. Lampel, A. Nakamura, and V. I. Safarov, Phys. Rev. B **18**, 1767 (1978).

[225]   D. Paget, Phys. Rev. B **25**, 4444 (1982).

[226]   K. Ramaswamy, S. Mui, and S. E. Hayes, Phys. Rev. B **74**, 153201 (2006).

[227]   G. Salis, D. T. Fuchs, J. M. Kikkawa, and D. Awschalom, Phys. Rev. Lett. **86**, 2677 (2001).

[228]   V. K. Kalevich, V. L. Korenev, and O. M. Fedorova, JETP Lett. **52**, 349 (1990).

[229]   H. Sanada, S. Matsuzaka, K. Morita, C. Y. Hu, Y. Ohno, and H. Ohno, Phys. Rev. B **68**, 241303(R) (2003).

[230]   B. E. Kane, L. N. Pfeiffer, and K. W. West, Phys. Rev. B **46**, 7264 (R) (1992).

[231]   A. M. Song, and P. Omling, Phys. Rev. Lett. **84**, 3145 (2000).

[232]   S. Kronmüller, W. Dietsche, K. v. Klitzing, G. Denninger, W. Wegscheider, and M. Bichler, Phys. Rev. Lett. **82**, 4070 (1999).

[233]   T. Machida, S. Ishizuka, T. Yamazaki, S. Komiyama, K. Muraki, and Y. Hirayama, Phys. Rev. B **65**, 233304 (2002).

[234]   D. Gammon, A. L. Efros, T. A. Kennedy, M. Rosen, D. S. Katzer, and D. Park, Phys. Rev. Lett. **86**, 5176 (2001).

[235]   K. Ono, and S. Tarucha, Phys. Rev. Lett. **92**, 256803 (2004).

[236]   A. I. Tartakovskii, T. Wright, A. Russell, V. I. Fal'ko, A. B. Van'kov, J. Skiba-Szymanska, I. Drouzas, R. S. Kolodaka, M. S. Skolnick, P. W. Fry, A. Tahraoui, H.-Y. Liu, and M. Hopkinson, Phys. Rev. Lett. **98**, 026806 (2007).

[237]   P.-F. Braun, X. Marie, L. Lombez, B. Urbaszek, T. Amand, P. Renucci, V. K. Kalevich, K. V. Kavokin, O. Krebs, P. Voisin, and Y. Masumoto, Phys. Rev. Lett. **94**, 116601 (2005).

[238]   I. A. Merkulov, A. L. Efros, and M. Rosen, Phys. Rev. B **65**, 205309 (2002).

[239]   T. Pietra   , and M. Tomaselli, Phys. Rev. B **59**, 1986 (1999).

[240]   I. J. H. Leung, and C. A. Michal, Phys. Rev. B **70**, 035213 (2004).

[241]   W. Dong, B. Li, Q. Zhang, M. C. Tamargo, and C. A. Meriles, Phys. Rev. B **80**, 045211 (2009).

[242]   A. Nakamura, D. Paget, C. Hermann, C. Weisbuch, and G. Lampel, Solid State Communications **30**, 411 (1979).

[243]   V. Gapon, J. Puls, and F. Henneberger, Appl. Phys. Lett. **94**, 213111 (2009).

[244]   J. Kim, J. Puls, Y. S. Chen, G. Bacher, and F. Henneberger, Appl. Phys. Lett. **96**, 151908 (2010).

[245]   M. W. Wu, J. H. Jiang, and M. Q. Weng, Physics Reports **493**, 61 (2010).

[246]   H. O. H. Churchill, A. J. Bestwick, J. W. Harlow, F. Kuemmeth, D. Marcos, C. H. Stwertka, S. K. Watson, and C. M. Marcus, Nature Physics **5**, 321 (2009).

[247]   J. P. King, P. J. Coles, and J. A. Reimer, Phys. Rev. B **81**, 073201 (2010).

[248]   Y. Lu, J. Li, and I. Appelbaum, Phys. Rev. Lett. **106**, 217202 (2011).

[249]   J. J. L. Morton, A. M. Tyryshkin, R. M. Brown, S. Shankar, B. W. Lovett, A. Ardavan, T. Schenkel, E. E. Haller, J. W. Ager, and S. A. Lyon, Nature **455**, 1085 (2008).

[250]   J. Lu, M. J. R. Hoch, P. L. Kuhns, W. G. Moulton, Z. Gan, and A. P. Reyes, Phys. Rev. B **74**, 125208 (2006).

[251]   M. Gueron, Phys. Rev. **135**, A200 (1964).

[252]   A. Willig, and B. Sapoval, Solid State Communications **11**, 1077 (1972).

[253]   D. Paget, T. Amand, and J.-P. Korb, Phys. Rev. B **77**, 245201 (2008).

[254]   W. O. Putikka, and R. Joynt, Phys. Rev. B **70**, 113201 (2004).

[255]   S. A. Crooker, L. Cheng, and D. L. Smith, Phys. Rev. B **79**, 035208 (2009).

[256]   G. M. Müller, M. Römer, J. Hübner, and M. Oestreich, Phys. Rev. B **81**, 121202(R) (2010).

[257]   A. K. Paravastu, S. E. Hayes, B. E. Schwickert, L. N. Dinh, M. Balooch, and J. A. Reimer, Phys. Rev. B **69**, 075203 (2004).

[258]   P. J. Coles, and J. A. Reimer, Phys. Rev. B **76**, 174440 (2007).

[259]   P. Maletinsky, A. Badolato, and A. Imamoglu, Phys. Rev. Lett. **99**, 056804 (2007).

[260]   P. J. Coles, Phys. Rev. B **78**, 033201 (2008).

[261]   M. J. Yang, R. J. Wagner, B. V. Shanabrook, J. R. Waterman, and W. J. Moore, Phys. Rev. B **47**, 6807 (1993).

[262]   M. A. Nielson, and I. L. Chuang, *Quantum Computation and Quantum Information* (Cambridge University Press, Cambridge, 2002).

[263]   I. T. Vink, K. C. Nowack, F. H. L. Koppens, J. Danon, Y. V. Nazarov, and L. M. K. Vandersypen, Nature Physics **5**, 764 (2009).

[264]   X. Xu, W. Yao, B. Sun, D. G. Steel, A. S. Bracker, D. Gammon, and L. J. Sham, Nature **459**, 1105 (2009).

[265]   C. Latta, A. Högele, Y. Zhao, A. N. Vamivakas, P. Maletinsky, M. Kroner, J. Dreiser, I. Carusotto, A. Badolato, D. Schuh, W. Wegscheider, M. Atature, and A. Imamoglu, Nature Physics **5**, 758 (2009).

[266]   G. P. Flinn, R. T. Harley, M. J. Snelling, A. C. Tropper, and T. M. Kerr, Semicond. Sci. Technol. **5**, 533 (1990).

[267]   Y. S. Chen, M. Wiater, G. Karczewski, T. Wojtocicz, and G. Bacher, Phys. Status Solidi B **247, No. 6**, 1505 (2010).

[268]   C. P. Slichter, *Principles of Magnetic Resonance, Second Revised and Expanded Edition* (Springer, 1980).

[269]   R. G. Shulman, B. J. Wyluda, and H. J. Hrostowski, Phys. Rev. B **109**, 808 (1958).

[270]   S. K. Buratto, Ph.D dissertation, California Institute of Technology (1993).

[271]   V. L. Berkovits, and V. I. Safarov, JETP Lett. **26**, 256 (1977).

[272]   M. Eickhoff, B. Lenzmann, D. Suter, S. E. Hayes, and A. D. Wieck, Phys. Rev. B **67**, 085308 (2003).

[273]   M. H. Cohen, and F. Reif, Solid State Physics **5**, 321 (1957).

[274]   D. Gill, and N. Bloembergen, Phys. Rev. **129**, 2398 (1963).

[275]   K. A. Dumas, J. F. Soest, A. Sher, and E. M. Swiggard, Phys. Rev. B **20**, 4406 (1979).

[276]   A. K. Paravastu, and J. A. Reimer, Phys. Rev. B **74**, 045215 (2005).

[277]   J. Ishihara, M. Ono, G. Sato, S. Matsuzaka, Y. Ohno, and H. Ohno, in The 6th International Conference on the Physics and Applications of Spin Related Phenomena in Semiconductors Tokyo, Japan, 2010), p. 147.

[278]   E. Brun, R. J. Mahler, H. Mahon, and W. L. Pierce, Phys. Rev. **129**, 1965 (1963).

[279]   C. A. Michal, J. Chem. Phys. **118**, 3451 (2003).

[280]   J. H. Shirley, Phys. Rev. **138**, B979 (1965).

[281]   V. K. Kalevich, K. V. Kavokin, and I. A. Merkulov, in *Spin Physics in Semiconductors*, edited by M. l. Dyakonov (Springer, Heidelberg, 2008).

[282]   R. K. Wangsness, Phys. Rev. **104**, 857 (1956).

PUBLICATIONS

Peer-viewed journal papers:

1. <u>Y. S. Chen</u>, G. Karczewski, T. Wojctowicz, and G. Bacher, "*Sub-ns magnetization dynamics down to zero field in diluted magnetic semiconductor quantum wells*", under preparation for submission to Phys. Rev. B;

2. J. Huang, <u>Y. S. Chen</u>, A. Ludwig, D. Reuter, A.D. Wieck, G. Bacher, " *Electron-nuclei spin coupling in GaAs – free versus localized electrons*", Appl. Phys. Lett. 100, 132103 (2012);

3. <u>Y. S. Chen</u>, D. Reuter, A. D. Wieck, and G. Bacher, "*Dynamic nuclear spin resonance in n-GaAs*", Phys. Rev. Lett. 107, 107601 (2011);

4. <u>Y. S. Chen</u>, J. Huang, D. Reuter, A. Ludwig, A. D. Wieck, and G. Bacher, "*Optically detected nuclear magnetic resonance in n-GaAs using an on-chip microcoil*", Appl. Phys. Lett. **98**, 081911 (2011);

5. <u>Y. S. Chen</u>, J. Huang, D. Reuter, A. Ludwig, A. D. Wieck, and G. Bacher, "*Manipulation of Spin Dynamics of Electron-Nuclear System in n-GaAs using On-Chip Microcoil*", J. Appl. Phys. 109, 016106 (2011);

6. J. Kim, J. Puls, <u>Y. S. Chen</u>, G. Bacher, and F. Henneberger, "*Electron spin control in charged semiconductor quantum dots by electrical currents from micro-coils*", Appl. Phys. Lett. 96, 151908 (2010);

7. <u>Y. S. Chen</u>, M. Wiater, G. Karczewski, T. Wojtowicz, and G. Bacher, "*Sub-ns electrical control of spin polarization in a semiconductor by microscale current loops*", phys. stat. sol. (b) 247, 1505 (2010);

8. <u>Y. S. Chen</u>, S. Halm, T. Kümmell, G. Bacher, M. Wiater, T. Wojtowicz and G. Karczewski, "*Local Definition of Spin Polarization in a Semiconductor by Micro-scale Current Loops*", J. of Supercond. Nov. Magn. 23, 111 (2010);

9. <u>Y. S. Chen</u>, S. Halm, E. Neshataeva, T. Kümmell, G. Bacher, M. Wiater, T. Wojtowiecz, G. Karczewski, "*Local control of spin polarization in a semiconductor by microscale current loops*", Appl. Phys. Lett. 93, 141902 (2008);

Conference talks:

1. <u>Y. S. Chen</u>, J. Huang, D. Reuter, A. Ludwig, A. D. Wieck, and G. Bacher, "*Manipulation of nuclear spins in n-GaAs using an on-chip microcoil*", PASPS VI, Aug. 1st - 4th 2010, Tokyo, Japan;

2. <u>Y. S. Chen</u>, M. Wiater, G. Karczewski, T. Wojctowicz, and G. Bacher, "*Sub-ns electrical spin control in a diluted magnetic semiconductor quantum well*", DPG Spring Meeting, Mar. 22nd - 26th 2010, Regensburg, Germany;

3. <u>Y. S. Chen</u>, S. Halm, T. Kümmell, M. Wiater, G. Karczewski, T. Wojctowicz, and G. Bacher, "*Micro Coils for Spin Manipulation in Semiconductors*", DPG Spring Meeting, Feb.25th - 29th 2008, Berlin, Germany;

4. J. Puls, Y. S. Chen, V. Gapon, G. Bacher, and F. Henneberger, "*Control of the resident electron spin in CdSe quantum dots by electrical current pulses though micro-coils*", 14th International Conference on II-VI Compounds, August 23rd - 28th 2009, St. Petersburg, Russia;

5. J. Puls, Y. S. Chen, V. Gapon, G. Bacher, and F. Henneberger, "*Electron spin manipulation in self-assembled CdSe/ZnSe quantum dots by combined magnetic and optical pulses*", Spintech 5, July 7th - 11th , 2009, Cracow, Poland.

Conference posters:

1. Y. S. Chen, M. Wiater, G. Karczewski, T. Wojctowicz, and G. Bacher, "*Sub-ns electrical spin control in a diluted magnetic semiconductor quantum well*", 39th Jaszowiec ISCPS, Jun.24th -29th 2010, Krynica-Zdroj, Poland;

2. Y. S. Chen, M. Wiater, G. Karczewski, T. Wojctowicz, and G. Bacher, "*Electrical Control of Spin Polarization in a CdMnTe/CdMgTe Quantum Well on a Micrometer Scale*", 14th International Conference on II-VI Compounds, August 23rd - 28th 2009, St. Petersburg, Russia;

3. Y. S. Chen, S. Halm, T. Kümmell, M. Wiater, G. Karczewski, T. Wojctowicz, and G. Bacher, "*Electrical Control of Spin Polarization in a CdMnTe/CdMgTe Quantum Well on a Micrometer Scale*", Aug.3rd - 6th 2008, PASPS V, Foz do Iguacu, 2008;

4. J. Huang, Y. S. Chen, D. Reuter, A. Ludwig, A. D. Wieck, and G. Bacher, "*Optical pump-probe measurement of local nuclear magnetic resonance on micrometer scale in n-doped bulk GaAs*", July 25th - 30th 2010, Seoul, Korea;

5. Jungtaek Kim, J. Puls, Y. S. Chen, G. Bacher, and F. Henneberger, "*Electron Spin Control in Semiconductor Quantum Dots by Electrical Current From Micro-coils*", Quantum Dot, Apr. 26th - 30th 2010, Nottingham, UK.

ACKNOWLEDGEMENTS

The biography is not included in the online version for reasons of data protection